

EARTHQUAKE SOURCE PARAMETERS, SEISMICITY, AND TECTONICS OF  
NORTH ATLANTIC TRANSFORM FAULTS

by

JAMES LOUIS MULLER

B.S., Virginia Polytechnic Institute and State University  
(1971)

S.M., Massachusetts Institute of Technology (1982)

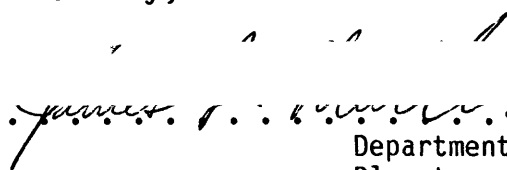
SUBMITTED TO THE DEPARTMENT OF  
EARTH AND PLANETARY SCIENCES  
IN PARTIAL FULFILLMENT OF THE  
REQUIREMENTS FOR THE DEGREE OF

DOCTOR OF PHILOSOPHY

at the

MASSACHUSETTS INSTITUTE OF TECHNOLOGY

January, 1983

Signature of Author  .....  
Department of Earth and  
Planetary Sciences

Certified by .....  
Sean C. Solomon  
Thesis Supervisor

Accepted by .....  
Theodore R. Madden  
Chairman, Department  
Graduate Committee

  
MASSACHUSETTS INSTITUTE  
OF TECHNOLOGY

MAR 14 1983



EARTHQUAKE SOURCE PARAMETERS, SEISMICITY, AND TECTONICS OF  
NORTH ATLANTIC TRANSFORM FAULTS

by

James Louis Muller

Submitted to the Department of Earth and Planetary Sciences  
Massachusetts Institute of Technology  
on January 24, 1983,  
in partial fulfillment of the requirements  
for the degree of Doctor of Philosophy

ABSTRACT

Earthquakes on oceanic transform faults provide a record of plate motion in space and time. This thesis is a study of the recent history of displacement on six transform faults on the Mid-Atlantic Ridge, as revealed by the source characteristics of teleseismically recorded earthquakes. We have investigated the seismic history of the Gibbs, Oceanographer, Kane,  $15^{\circ} 20'$ , Vema, and Doldrums transform faults, and we have determined the source parameters of twelve large earthquakes ( $M_s$  5.1 to 7.0) on these transform faults by constructing synthetic seismograms to match observed P waveforms from WWSSN long-period vertical seismograms. The approximate latitudes of the transforms studied are  $52^{\circ}\text{N}$ ,  $35^{\circ}\text{N}$ ,  $24^{\circ}\text{N}$ ,  $15^{\circ}20'\text{N}$ ,  $11^{\circ}\text{N}$ , and  $7^{\circ}\text{N}$ , respectively.

Synthetic seismograms were constructed using the method of Langston and Helmberger (1975). This technique uses the superposition of the direct P wave with the surface reflections pP and sP, with the latter phases delayed in time to account for the additional travel path. All amplitudes were adjusted to account for the radiation pattern of the earthquake, and amplitudes of the reflected phases were also corrected for reflection at the free surface. The resulting source waveforms were then convolved with an attenuation operator and corrected for geometrical spreading, and the appropriate WWSSN instrument response was applied. We modified this method to include the effects of a layered velocity structure near the source and of a finite fault, along which either unilateral or bilateral rupture proceeds horizontally. The effect of fault width (vertical dimension) was shown to be significant, though resolution of fault width is poor because of tradeoff with other source parameters and insufficient understanding of the rupture process. Synthetic seismograms were constructed using various combinations of fault parameters until waveforms were found which matched those of observed seismograms.

Synthesis of the P waveforms from twelve transform fault earthquakes indicates strike-slip mechanisms on nearly vertical faults oriented along the strike of each transform. Seismic moments for the events varied by over a factor of 100, from  $9.5 \times 10^{24}$  to  $1.3 \times 10^{27}$  dyne-cm. The focal depths varied between 1 and 6.5 km below the top of oceanic basement. Unilateral rupture propagation was indicated for the source mechanisms of six of the earthquakes studied, and was suggested for another, with a consistency of propagation direction for each transform. The predominant period of the first half cycle of the observed waveforms was generally no more than about 15 sec and varied little among the earthquakes studied, despite the broad range of moments found. Fault lengths ranged from 6 to 30 km except for one complex event, which required a multiple source with a total fault length of 60 km. Average displacements for these events ranged from 0.9 to 12 m.

We compared  $M_s$ ,  $m_b$ , and  $M_0$  values of these earthquakes and others on oceanic transform faults. By restricting the earthquake group to the transforms considered in this study, i.e., to one tectonic setting and to consistent observational procedures, we derive linear relations between  $M_s$  and  $m_b$  and between  $M_s$  and  $\log M_0$  that faithfully represent our data with little scatter. Using these relations we have estimated the total seismic moment released by earthquakes on each transform since 1920 and compared each result with the cumulative moment predicted by the transform length and the local spreading rate. Those transforms which had large earthquakes toward the beginning of historic seismic observations had an observed moment total greater than predicted, while those with early seismicity more comparable to that of the entire period showed better agreement. The historical record of large earthquakes on these transforms indicates that each transform slips in a jerky manner and along small fault segments rather than in large events involving rupture along the entire length of the transform. The repeat time for  $M_s \approx 6$  events on the part of the transform fractured by each event varied from about 30 to about 350 years. There may be some correlation between transforms of the times of occurrence of the largest earthquakes.

Thesis advisor: Sean C. Solomon, Associate Professor of Geophysics

## ACKNOWLEDGEMENTS

This work would not have been possible without the ideas, work, inspiration, and understanding of many people. Foremost of these has been my advisor, Dr. Sean C. Solomon, who provided the original concept and many of the ideas (and financial support) for this work, who insisted on my getting everything right (or as near to right as I could make it) and thus taught me how real work is done, who acted as primary reviewer of this document, and who (se patience probably wore thin enough that he) forced me to accomplish something tangible. I am grateful for all of these things. I would also like to thank Mark Murray, who compiled much of the earthquake data in the seismicity tables in Chapters 3 to 8, thus saving me lots of time and providing a seed crystal for my doing the rest of it. Thanks also go to Wai-Ying Chung, who provided the original synthetic seismogram program, to Eric Bergman, who provided programming, ideas, inspiration, and the substance of several figures presented here, to Rob Comer, Dan Davis, J. Lynn Hall, W. Roger Buck IV, Mark Willis, and Gerardo Suarez who provided necessary inspiration and idea exchange, and to Jan Nattier-Barbaro (Word Wizard), who made it real. Finally, I would like to thank my wife, Sharon J. Horovitch, Ph.D., who showed me that it can be done, and who provided the support and understanding for me to do likewise.

This research was partially supported by the National Science Foundation, Earth Sciences Section, under NSF Grants EAR 77-09965 and EAR-8115908.



# TABLE OF CONTENTS

	<u>page</u>
Abstract . . . . .	ii
Acknowledgements . . . . .	iv
Table of Contents . . . . .	v
Chapter 1. Introduction . . . . .	1
General Concept of Transform Faults	1
Geologic Setting of North Atlantic Transform Faults	2
Transform Fault Seismicity	6
Large Earthquakes on North Atlantic Transforms	8
Objectives of this Study	9
Figures	12
Chapter 2. Method of P-Wave Synthesis . . . . .	14
General Technique	14
Modifications	18
The Problem of Finite Width	21
Checks on the Validity of the Method	27
Parameters and Data Needed	30
Resolution of and Ambiguities in the Results	31
Figures	40
Chapter 3. The Seismicity and Tectonics of the Gibbs Transform Fault . . . . .	54
Seismicity	55
Major Earthquakes	56
Total Seismic Moment	59
North Atlantic Transform Behavior	61
Tables	62

	<u>page</u>
Figures	65
Chapter 4. Earthquakes and Tectonics of the Oceanographer Transform Fault . . . . .	68
Seismicity	70
The May 17, 1964 Earthquake	71
The November 18, 1970 Earthquake	80
Total Seismic Moment	82
Implications for the Oceanographer Transform	84
Tables	87
Figures	92
Chapter 5. Earthquakes and Tectonics of the Kane Transform Fault . . . . .	103
Seismicity	106
The March 12, 1977 Earthquake	107
Total Seismic Moment	109
Implications for the Kane Transform	111
Tables	112
Figures	116
Chapter 6. Earthquakes and Tectonics of the 15° 20' Transform Fault . . . . .	120
Seismicity	121
The September 24, 1969 Earthquake	122
The June 19, 1970 Earthquake	125
The December 9, 1972 Earthquake	129
Total Seismic Moment	131
Implications for the 15° 20' Transform	132
Tables	136
Figures	141

	<u>page</u>
Chapter 7. Earthquakes and Tectonics of the Vema Transform Fault . . . . .	149
Seismicity	152
The March 17, 1962 Earthquake	153
The May 14, 1976 Earthquake	157
The August 25, 1979 Earthquake	160
Total Seismic Moment	164
Implications for the Vema Transform	166
Tables	169
Figures	174
Chapter 8. Earthquakes and Tectonics of the Doldrums Transform Fault . . . . .	182
Seismicity	184
The August 3, 1963 Earthquake	186
The September 4, 1964 Earthquake	190
The April 4, 1977 Earthquake	193
Total Seismic Moment	195
Implications for the Doldrums Transform	197
Tables	199
Figures	205
Chapter 9. Characterization of General Seismic Behavior of 6 Atlantic Transforms . . . . .	212
Comparison of Earthquake Source Parameters	212
$M_S$ vs. $m_b$	214
Log $N(M_S)$ vs. $M_S$	216
$M_S$ vs. Log $M_0$	219
Total $M_0$ and Accumulated $M_0$ per Year	220

	<u>page</u>
Summary of Results	226
Tables	228
Figures	230
References . . . . .	238

## CHAPTER 1. INTRODUCTION

### GENERAL CONCEPT OF TRANSFORM FAULTS

Oceanic transforms are lateral offsets of oceanic ridges, representing a discontinuity along the ridge length of the emplacement of crustal material beneath the ocean floor. They are recognizable by lateral offsets in the seismicity and topographic expression of the adjoining ridge segments, and by fracture zones, linear topographic and magnetic features extending away from, and at right angles to, the ridge segments. The existence of fracture zones has been known for some time, but until 1965 they were regarded as transcurrent faults along which the adjoining ridge segments were moving away from each other. According to this interpretation earthquake activity should be distributed along the entire fracture zone, and the slip direction should carry the ridge segments away from each other, i.e., if the ridge were offset to the right, then the direction of earthquake motion should be right-lateral strike-slip.

Wilson (1965) noted that, according to sea-floor spreading theory, oceanic ridges represent zones along which plates of the earth's lithosphere move apart from each other. He therefore proposed that the offsets of ridge axes are zones of shear between plates moving away from the adjoining ridge segments. Wilson (1965) called this new interpretation of the ridge offsets "transform faults". According to this interpretation, the direction of slip during earthquakes on these faults should be in the opposite direction to that of the ridge offset, the seismicity along these faults should be limited to the "active" section between the adjoining ridge segments, and the long topographic

and magnetic features which extend away from the ridge segments are simply scars on the ocean floor produced when that crust had been part of the active transform. By relocating and preparing fault plane solutions for many ocean floor earthquakes, Sykes (1967) showed that most ocean floor seismic activity was indeed limited to the "active" portion of transform faults and that the direction of fault slip was opposite to that of the ridge offsets, thus confirming Wilson's (1965) interpretation. Transforms are steady-state features of constant length, which terminate sections of active emplacement of material onto the oceanic lithosphere and crust, and at which parts of the ocean floor with different age are in contact. In this thesis we take a closer look at the seismicity and source parameters of major earthquakes on several oceanic transform faults in the north and central Atlantic in order to characterize the motion on these transforms in space and time.

#### GEOLOGIC SETTING OF NORTH ATLANTIC TRANSFORM FAULTS

The general shape of the Mid-Atlantic Ridge between 5° N and 55° N, and the locations of the major transforms in this area, are shown in Figure 1.1. In the central and north Atlantic Ocean, transform faults along the Mid-Atlantic Ridge range in length from less than a few tens to several hundreds of kilometers. Common bathymetric features reported for transform faults include a deep central trough which, at its deepest point, can be as much as a thousand meters deeper than the surrounding sea floor. Another feature found sometimes on one side, and sometimes on both sides, of the transform is an elevated "transverse" ridge, running parallel to the transform valley and forming walls which can be as much as a thousand meters higher than the surrounding sea floor and 10 km wide (e.g., van Andel et al., 1971; Fleming et al., 1970; Detrick and Purdy,

1980). The troughs typically obtain their greatest depths in depressions located at the intersections of the transform and the adjacent ridge segments. The topographic expressions are present not only on the active portion of each transform, but extend several thousand kilometers away from the ridge into older ocean floor. The topographic features are accompanied by magnetic and gravitational anomalies.

Small-scale topographic features have been studied for a few of the transforms on the Mid-Atlantic Ridge. Detrick et al. (1973) and ARCYANA (1975) report that the inner walls of the transverse ridges flanking the active fault section of Fracture Zone A, a small transform in the FAMOUS area near 37° N, have scarps ranging in vertical offset from 50 cm to at least several tens of meters. Similar structures were reported by Oceanographer Transform Tectonic Research Team (1980 a,b) from work of ALVIN and ANGUS on the Oceanographer transform. Schroeder (1977) reports that the inner walls of the Oceanographer transform are made up of steep, sediment-covered scarps, individually with 100 to 1000 m of vertical relief. At least for these two transforms the inner walls seem to be made up of faulted blocks of material, whose faces have considerably greater slopes than the average slope of the inner walls. Eittreim and Ewing (1975) presented results from a seismic reflection survey of the Vema transform fault, which showed that the entire valley floor was covered with thick sediment and that this sediment was cut by a fault-like feature for the entire length of the transform. The implication was that this feature is a zone along which recent strike-slip motion has taken place. Searle (1979, 1981) presented the results of high-resolution, side-scan sonar surveys, and an analysis of the structure of the Gibbs transform using some of these data. He

concluded that the Gibbs transform was a double transform, active in the west along the northern segment and in the east along the southern segment. He also concluded that strike-slip activity was limited to a single narrow zone in the center of each active segment, but that this zone was not always delineated in the bathymetry by the location of the greatest water depth. Lonsdale and Shor (1979) examined the ridge-transform intersection at the western end of the Gibbs transform by mapping fault traces using a deep-tow instrument. Their results showed that this intersection has substantial faulting along scarps running obliquely to the spreading (or strike-slip) direction. Choukroune et al. (1978) presented the results of dives by the Cyana and Archemede, and concluded that (1) transforms show pure strike-slip activity with no new crust being formed, (2) strike-slip activity is not limited to one single well-defined fault, but (3) the zone of active strike-slip faulting is only about 300 m to 1 km wide, and (4) the vertical relief in a transform's large-scale bathymetry must be generated by vertical motion along the transform flanks, and not in the zone of active strike-slip movement.

Results have been published from several seismic refraction experiments designed to measure the crustal structure beneath Atlantic fracture zones. Two of these (Fox et al., 1976; Detrick and Purdy, 1980) were on inactive limbs of fracture zones. Fox et al. (1976) found that the basement crustal structure of the western limb of the Oceanographer Fracture Zone consisted of an upper layer with a compressional velocity of 4.4 km/sec and a thickness of 2.1 km, and a second layer with a velocity of 6.5 km/sec. They did not observe any mantle arrivals, and thus were able only to estimate the minimum thickness of the second layer



by assuming various velocities for the mantle. For assumed mantle compressional velocities of 7.0, 7.5, and 8.2 km/sec they obtained a minimum thickness for the second layer of 2.5, 3, and 4 km, respectively. Detrick and Purdy (1980) reported the results of a detailed refraction study of the eastern inactive limb of the Kane Fracture Zone. Their results showed the crust there to consist of only one layer over the mantle. The layer had a compressional velocity of 4 to 5 km/sec and a thickness of 2 to 3 km. The mantle had a compressional velocity of 7.7 to 8.0 km/sec. This result has both crustal thickness and average crustal velocities considerably lower than those of normal ocean crust. Ludwig and Rabinowitz (1980) reported results from a seismic refraction and reflection experiment in the active section of the Vema transform fault. Their results showed the transform valley to be filled with about 1500 m of sediment, and the depth to the basement ranged from 6200 to 6700 m. Below this depth they found a two-layer crust, with the first layer having a compressional velocity of 4.3 km/sec and a thickness of 2 km, and the second layer having a compressional velocity of 5.9 to 6.2 km/sec and a thickness of 2.6 km. They reported that the structure had significant variation and that it was impossible to identify any consistent layers with those of normal oceanic crust. Detrick et al. (1982) presented results of a long seismic refraction experiment on the Vema transform, which showed the structure to be similar to that of the Kane, with considerable variation, probably the result of intense fracturing.

Solomon (1973) examined the attenuation of shear waves from a large earthquake on the Gibbs transform and found greater attenuation for stations for which the ray paths passed under the western intersection of

the transform and the adjoining ridge segment than for stations whose ray paths went elsewhere. The implication was that a zone of low Q material existed beneath the western end of the Gibbs transform, possibly indicating a hotspot or zone of partial melting. Rowlett and Forsyth (1979) reported abnormally large lateral variation in P-wave travel time residuals from a distant earthquake as observed by an array of ocean-bottom seismometers at the western end of the Vema transform fault. The relative magnitude and distribution of the residuals implied that under part of the intersection of the transform and the adjoining ridge segment there must exist a zone with lower than normal seismic velocities which extends quite far into the mantle. They suggested that this might be a magma chamber or a zone of partial melting. This interpretation is similar to that of Solomon (1973).

#### TRANSFORM FAULT SEISMICITY

Earthquakes on oceanic transform faults have been shown to be strike-slip and in a direction consistent with Wilson's (1965) hypothesis of transform faults (e.g., Sykes, 1967, 1970). Isacks, Oliver, and Sykes (1968) showed that the maximum sizes of earthquakes observed on transform faults were larger than those on oceanic ridge crests, but smaller than those on island arc-subduction zone systems, probably reflecting the relative amount of lithosphere in contact at each of these boundaries. Sykes (1967) showed that transform fault earthquakes are primarily confined to the active transform section between the adjoining ridge segments. This finding has been verified by several experiments using arrays of ocean-bottom seismometers (e.g., Rowlett, 1981; Project ROSE Scientists, 1981).

Transform fault earthquakes generally occur at shallow depths. Weidner and Aki (1973) studied the surface waves from event pairs on the Mid-Atlantic Ridge, and found the focal depths of two strike-slip events to be  $6 \pm 3$  km below sea floor. Project ROSE Scientists (1981) and Trehu (1982), using a large array of ocean-bottom seismometers, found that the microearthquakes on the Orozco transform were limited to depths shallower than about 8 km.

Teleseismically determined epicenters of transform earthquakes are generally scattered over a zone that is as wide as 30 km. This may be due to poor epicentral determinations or it may indicate that seismic activity is distributed over a broad area. Epicenters determined by Project ROSE Scientists (1981) for the Orozco transform were divided into two groups. One group, near the western end of the transform, showed clear alignment along a narrow trough parallel to the slip direction between the Cocos and Pacific plates, and the first motions of these events were consistent with strike-slip faulting along the transform. The other group occurred near the center of the transform, in a topographically complicated region, and did not show any preferred alignment with the strike of the transform. One interpretation is that the microseismicity is composed of both strike-slip activity and other activity, possibly related to topographic features. This would be consistent with the interpretation of Eittreim and Ewing (1975) that the linear feature they observed in the sediments of the Vema transform represented a narrow zone of strike-slip motion. Microearthquakes at the ends of transforms on slow spreading ridges do not exhibit alignment with the transform strike, but instead are generally scattered across a diffuse area at the inner corner of transform-ridge intersections

(Rowlett, 1981); which suggests that many of these events are related to processes unique to the intersection zone.

There is evidence that the size of transform fault earthquakes is related to the dimensions and slip rate of the transform. Burr and Solomon (1978) found that (1) the maximum seismic moment for such earthquakes decreases with slip rate and increases with transform length up to lengths of about 400 km, (2) average fault width increases with transform length and decreases with slip rate, and (3) larger earthquakes generally occur toward the center of a transform. They interpreted these results as indicating that the lower boundary of seismic activity is defined by an isotherm, conservatively determined to be between 50°C and 300°C. This is consistent with the finding of shallow focal depths for transform earthquakes.

#### LARGE EARTHQUAKES ON NORTH ATLANTIC TRANSFORMS

Comparatively few large earthquakes on oceanic transform faults have been studied in detail. For the north and central Atlantic, several studies may be noted. As mentioned above, Weidner and Aki (1973) inverted Rayleigh wave amplitude and phase spectra to obtain the source characteristics of two strike-slip earthquakes from North Atlantic fracture zones which occurred on May 17, 1964 and June 9, 1970. Epicenters of these events were 35.29° N, 36.07° W, and 15.4° N, 45.9° W, respectively. Both of these events had  $m_b = 5.6$ . Weidner and Aki (1973) found seismic moment values for these events of  $1.03 \times 10^{25}$  dyne-cm and  $1.94 \times 10^{25}$  dyne-cm, respectively. Udias (1971) studied the Rayleigh wave spectra of four earthquakes, two of which were on a transform fault system we have studied here, which we call the Doldrums transform fault. His study included the determination of source parameters and seismic

moment for these events. Sykes (1967, 1970) presented fault plane solutions for several North Atlantic earthquakes, which showed the expected strike-slip motion. Tsai (1969), Wyss (1970), and Dziewonski and Woodhouse (1982) determined seismic moments for various transform fault earthquakes.

Kanamori and Stewart (1976) performed a detailed study of the surface waves and body waves from two earthquakes on the Gibbs transform which occurred on February 13, 1967 and October 16, 1974. They found seismic moments for these events of  $3.4 \times 10^{26}$  dyne-cm and  $4.5 \times 10^{26}$  dyne-cm, respectively. By assuming bilateral rupture propagation, they found fault lengths of 60 km and 72 km. With these values and assuming a fault width of 10 km, they found displacements of 160 cm and 180 cm and dislocation velocities of 23 cm/sec and 18 cm/sec, respectively. An important implication was that these events exhibited slower than normal fault movement and therefore excited much greater long-period surface waves than usual for events of this  $m_b$ . By comparing the displacements and fault lengths of these events to the total length of the transform and the rate of slippage predicted by magnetic anomalies, and by assuming that previous large earthquakes on the transform were similar to these, they concluded that the Gibbs transform slips in a jerky manner, with major events alternating between the eastern and western half. The time for one complete cycle is about 26 years, with the entire transform slipping once during this period.

#### OBJECTIVES OF THIS STUDY

Previous work on transform fault earthquakes has shown them to be strike-slip, reflecting the relative motion of plates across the transform. It has also shown them to be shallow. Burr and Solomon

(1978) showed that there is some connection between a transform fault's dimensions and slip rate and the earthquakes which occur on the transform. From the study of Kanamori and Stewart (1976), the earthquakes gave us some clues as to how the Gibbs transform behaves, although the earthquakes themselves seemed to be somewhat unusual.

In this work we examine the seismicity and largest earthquakes of several North Atlantic transforms. Our goal is to try to understand plate slip along these transforms, and in particular to focus on the following questions: What are the main source parameters of the large earthquakes? How deep in the crust or mantle do they occur? Are other earthquakes similar to those on the Gibbs transform studied by Kanamori and Stewart (1976)? Do transform earthquakes exhibit abnormally high or low stress drop or displacement? Do transforms slip smoothly or do they move in discrete, jerky episodes? What is the repeat time for seismic episodes on any section of a transform? Have entire transforms slipped at least once during the known seismic history? Is there agreement between the total seismic moment observed on any transform and that predicted by the slip rate and fault dimensions, or has the observed seismic activity been too uneven for such comparisons to be reliable?

To try to answer these questions we have constructed synthetic seismograms for comparison to the observed P waveforms from the large earthquakes on five North Atlantic transforms (Oceanographer, Kane, 15° 20', Vema, Doldrums). The technique adopted for P-wave synthesis is described in Chapter 2. On the basis of the P-wave modeling we have determined source parameters for twelve earthquakes. We have also combined data from the known seismicity of these five transforms plus the Gibbs transform with the parameters found for these large earthquakes to

estimate the observed seismic slip rate, for comparison to the rate of slip predicted from magnetic anomalies. The results are presented in Chapters 3 through 8 of this work. Finally, in Chapter 9, we examine the similarities and differences between the transforms studied and the implications of this work for transform behavior.

### Figure Captions

Figure 1.1. The Mid-Atlantic Ridge and other plate boundaries between 5° N and 55° N, and 15° W and 55° W. The major transform faults on the Mid-Atlantic Ridge are also indicated, and labelled G for the Gibbs transform, O for the Oceanographer transform, K for the Kane transform, F for the 15° 20' transform, V for the Vema transform, and D for the Doldrums transform system. This represents an interpretation of the bathymetry taken from Uchupi (1982). The plate boundaries marked with question marks are not well-known. The multiple-transform interpretation of the Gibbs and Doldrums transforms are discussed in Chapters 3 and 8, respectively.



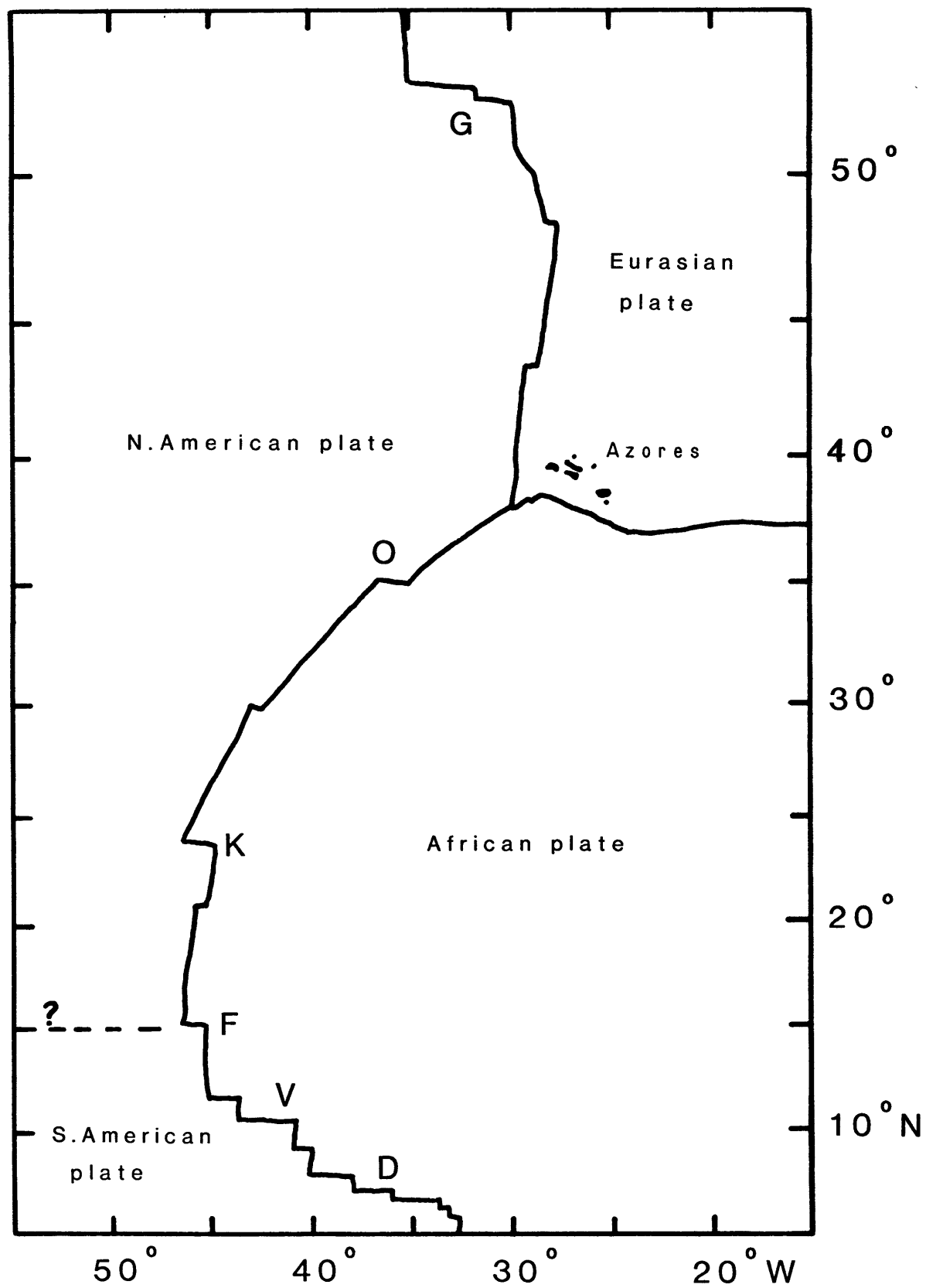


Fig. 1.1

## CHAPTER 2. METHOD OF P-WAVE SYNTHESIS

### GENERAL TECHNIQUE

We have constructed synthetic seismograms of the P-waves for comparison with the observed seismograms from the largest strike-slip earthquakes on the transform faults treated in this study. By matching the synthetic waveforms and amplitudes to observed ones we have been able to determine some of the source parameters and other features of these events.

We have used the method of Langston and Helmberger (1975), used also by Kanamori and Stewart (1976) and Chung and Kanamori (1976), with some modifications of our own. The basic approach is a time-domain superposition of the direct P, pP, and sP phases. The pP and sP phases are delayed by an amount appropriate to the event depth and adjusted in amplitude by the reflection coefficient for the top of the oceanic crust. The amplitude of each phase is corrected for the radiation pattern of the event, and the final time series is corrected for geometric spreading, attenuation, instrument response, and the effect of the free surface near the receiver.

The far-field displacement for a double-couple point source in a uniform, unattenuating medium can be expressed by (Love, 1934)

$$u_p(t) = \frac{1}{4\pi\rho v^3} \dot{M}(t-r/v) R_{\theta,\phi} \quad (2.1)$$

where  $r$  is the distance,  $\rho$  is the density,  $v$  is the wave velocity,  $R_{\theta,\phi}$  is a factor for the radiation pattern,  $\dot{M}$  is the time derivative of the seismic moment, and  $t$  is time. We can think of  $\dot{M}$  as the rate of generation of seismic moment. If we express  $\dot{M}$  as

$$\dot{M} = M_0 T(t) \quad (2.2)$$

where  $M_0$  is the scalar seismic moment and  $T(t)$  is a time series such that

$$\int T(t) dt = 1, \quad (2.3)$$

then  $T(t)$  represents a normalized displacement function with the same shape as would be observed as a direct P wave at teleseismic distances. The far field displacement expression (2.1) then becomes

$$u_p(t) = \frac{1}{4\pi\rho v^3} M_0 R_{\theta,\phi} T(t-r/v). \quad (2.4)$$

P-wave arrivals on observed seismograms are composed principally of the direct P and the surface reflections pP and sP. We can express these reflected phases by using the appropriate radiation pattern factor  $R_{\theta,\phi}$ , multiplying by the free surface reflection coefficient  $A(i_r)$ , where  $i_r$  refers to the emergent angle at the point of reflection for the phase  $i$ , and then delaying each phase  $\Delta t$  for the extra travel path length due to the event depth. The complete waveform is then the sum of these phases and can be expressed as

$$u(t) = \frac{1}{4\pi\rho v^3} M_0 \left( T(t-r/v) R_1 + T(t-r/v-\Delta t_2) R_2 A_2 + T(t-r/v-\Delta t_3) R_3 A_3 \right) \quad (2.5)$$

where the subscripts 1, 2, and 3 refer respectively to the P, pP, and sP phases.

To obtain the final synthetic seismogram we correct this expression for geometric spreading, attenuation, crustal effects at the receiver, and instrument response. The result can be expressed as

$$u_{\text{syn}}(t) = u(t) \frac{g(\Delta, h)}{a} C(i_0) * \frac{F(t/t^*)}{t^*} * I(t) \quad (2.6)$$

where  $a$  is the radius of the earth,  $g(\Delta, h)$  is the geometric spreading factor,  $C(i_0)$  is the free surface effect at the receiver,  $i_0$  is the incident angle at the receiver,  $F(t/t^*)$  is the attenuation operator,  $I(t)$

is the instrument response, \* denotes the convolution operation,  $\Delta$  is the epicentral distance to the station,  $h$  is the focal depth, and  $t^*$  is the attenuation parameter, defined as the ratio of travel time to the average quality factor  $Q$  along the ray path.

Several of the factors in the above expressions have been given in previous work. The radiation pattern factors ( $R_i$ 's) have been given by Kanamori and Stewart (1976). The free surface correction  $C(i_o)$  is given in Bullen (1965). The geometric spreading factor  $g(\Delta, h)$  is given by Kanamori and Stewart (1976) as

$$g(\Delta, h) = \left( \frac{\rho_h \beta_h}{\rho_o \beta_o} \frac{\sin i_h}{\sin \Delta \cos i_o} \left| \frac{di_h}{d\Delta} \right| \right)^{1/2} \quad (2.7)$$

where the subscripts  $h$  and  $o$  refer to the source and receiver, respectively. The incident angles for this expression were calculated using travel times from Herrin (1968) and the velocity appropriate to the depth for the source structure, and using a velocity of 6.0 km/sec for the receiver. The attenuation function  $F(t/t^*)$  corresponds to a linear, causal, constant- $Q$ , slightly dispersive earth model calculated by Carpenter (1966) from the work of Futterman (1962) and Kolsky (1956). [The paper of Carpenter (1966) has been reprinted by Toksoz and Johnston (1981).] The instrument response correction  $I(t)$  is taken from the frequency domain correction given by Hagiwara (1958). The reflection coefficients  $A_i$  are given in Ewing et al. (1957), though for potential amplitude rather than displacement amplitude. This makes no difference for the  $pP$  conversion. For the  $sP$  conversion however it means that we must also use the additional factor of

$$B_{sp} = \frac{\beta}{\alpha \sqrt{3}} \frac{\cos i_p}{\cos i_s} \quad (2.8)$$

where  $\alpha$  is the P-wave velocity and  $\beta$  the S-wave velocity in the medium where the reflection takes place,  $i_s$  is the S-wave incident angle on the surface, and  $i_p$  is the emergent angle of the reflected P-wave. Thus the sP term in (2.5) becomes  $T(t-r/v-\Delta t_3) R_3 A_3 B_{SP}$ . For all of these calculations and for the velocity models used we have assumed a Poisson solid, i.e.,  $(\alpha/\beta)^2 = 3$ .

The scalar moment is a factor which (along with several other factors) multiplies the source time function to produce the amplitudes of the final waveform. Thus the moment represents a scaling factor for the synthetic seismograms. To determine the seismic moment for an earthquake we first determine, for each station used, the moment necessary to duplicate in the synthetic waveform the amplitude of the observed waveform. (For most seismograms presented in the following chapters, this was the zero to peak amplitude of the first major signal displacement. For the waveforms which had small first arrivals followed by larger signals with opposite polarity, we usually used the amplitude of this second peak.) We then average these values to find the seismic moment of the earthquake, using the formula

$$\ln M_0 = 1/n \sum_i \ln M_{0i} \quad (2.9)$$

where  $n$  is the number of stations used and  $M_{0i}$  is the moment for station  $i$  which gave the same amplitudes for the observed and synthetic seismograms. Using this approach also allows us to express the scatter in the observed  $M_{0i}$ 's by determining the standard-deviation  $\sigma$  of  $\ln M_0$ ; thus  $\exp(\sigma)$  represents an "error factor" for  $M_0$ .

If we have any information about the fault dimensions, we can then determine the displacement  $D$  and particle velocity  $V_t$  for each earthquake using the formulas

$$M_0 = \mu L w D \quad \text{and} \quad V_t = D/R_t,$$

and we can determine the stress drop for each earthquake using the formula given by Kanamori and Anderson (1975) for a strike slip event

$$\Delta\sigma = \frac{2}{\pi} \mu \frac{D}{w} \quad (2.10)$$

where  $\mu$  is shear modulus of the material,  $D$  is the average displacement,  $w$  is the fault width,  $L$  is the fault length, and  $R_t$  is the rise time.

#### MODIFICATIONS

We have made two improvements to the previously used versions of this method for P-wave synthesis. The first is the use of a layered velocity structure near the source. In previous applications of this technique (e.g., Kanamori and Stewart, 1976) the structure near the source was assumed to be a simple half-space. In order to improve the accuracy of the focal depth determination we used a layered structure, in which the actual properties of the faulted material depend on the layer in which the event occurred. The calculation of the delays  $\Delta t_i$  for the pP and sP phases were made by tracing the reflected P from the depth of the focus up to the surface and then, as the original s or p phase, back down to the source, changing the emergent angle at each interface encountered. The final delay value was a summation of a path-length component for each layer (accounting for the extra travel path of the reflected phases), and a horizontal component (accounting for the slightly smaller epicentral distances traveled by the reflected phases to the station from the point where they reached the depth of the focus). The total delay value for either the upward or downward direction can be given by the expression

$$\Delta t = \sum_j h_j \left( 1/(v_j \cos i_j) - (\tan i_j)/p \right) \quad (2.11)$$

where  $h_j$  is the thickness of layer  $j$ ,  $i_j$  is the emergent angle in layer  $j$ ,  $v_j$  is the wave velocity in layer  $j$ , and  $p$  is the horizontal phase velocity for that epicentral distance and event depth.

In practice this summation over the  $j$  layers is actually done once, for the reflected P phase from the depth of the focus up to the point of reflection at the surface. For the complete pP delay time this value is doubled, since the upward-going p phase follows a similar path, with similar incident angles at each interface, as the reflected pP. However for the sP phase we must trace the s ray path back down from the point of reflection to the same depth as the focus. Since the s to P conversion requires a difference between incident and reflected angles we use an incident angle appropriate for the s phase. This results in different incident and refracted angles at each interface, so that the horizontal correction for the sP phase is what would be appropriate for a ray from a virtual source slightly closer to the receiver than the actual source. Figure 2.1 illustrates the geometry of these corrections. (For these calculations we have assumed that the pP and sP phases reflect off the basement-sediment interface, not the sediment-water interface; except possibly for transforms with large sediment thickness, the former is probably the stronger reflector. Thus the water depths used include actual water depth plus sediment thickness.)

The other modification we have introduced is the use of a finite fault, and the resulting variation of the apparent source time function  $T(t)$  with emergent angle and station azimuth. We assume that rupture begins at the event focus and propagates horizontally for some finite distance with a constant rupture velocity. We allow the fault to be either unilateral or bilateral, and in the latter case we assume that the

two arms of the fault are of equal length. We can then calculate the angle  $Q$  between the propagation vector and the ray to any station  $i$  by

$$\begin{aligned} \cos Q_i = & \cos \theta \cos d_i + \sin \theta \sin d_i \cos \phi \cos Az_i \\ & + \sin \theta \sin d_i \sin Az_i \sin \phi, \end{aligned} \quad (2.12)$$

where  $Az_i$  and  $d_i$  are the azimuth measured clockwise from north and emergent angle measured up from vertical, respectively, for the ray to station  $i$ ,  $\phi$  is the azimuth of the propagation vector, measured clockwise from north, and  $\theta$  is the angle of the propagation vector measured from vertical. This geometry is illustrated in Figure 2.2. We assume for all cases treated here that propagation occurs horizontally along the strike of the fault, so that  $\theta = \pi/2$ . Equation 2.10 thus reduces to  $\cos Q_i = \sin d_i \cos (\phi - Az_i)$ . (In Figure 2.2 we also show the fault dip  $\delta$ . The fault dip is used in determining the effect of finite fault width on the source time function.)

The apparent propagation time  $T_i$ , as seen at station  $i$ , for any unilateral event with fault length  $L$  and rupture velocity  $v_r$  will be

$$T_i = L (1/v_r - (\cos Q_i)/v). \quad (2.13)$$

As shown in Figure 2.3, this represents the propagation time plus (or minus, depending on the propagation direction) a correction for the extra path length required by source finiteness. For a bilateral fault the result will simply be the superposition of two simultaneous equal-length unilateral faults propagating in opposite directions. This method is similar to that used by Bollinger (1968) in examining source finiteness and directivity in the P waves from several large earthquakes, including one event studied here.

The time function corresponding to this apparent propagation time is then convolved with two other time domain functions, one representing the



rise time of the displacement, and the other representing nearly instantaneous rupture along the fault width. The rise time function is taken as a boxcar function, with a duration equal to the rise time. The fault width function is calculated in the same manner as the propagation time function  $T_i$ , except that fault width replaces fault length and  $v_r$  is assumed to be infinite in Equation 2.13, and  $Q_i$  is taken from Equation 2.12 with  $\pi/2 - \delta$  replacing  $\theta$ . Examples of source time functions for P, pP, and sP phases from a vertical fault, with dimensions similar to those required by the earthquakes studied in the following chapters, are shown in Figure 2.4. Our approach assumes that the fault plane exists in a medium characterized by a single seismic velocity even though the plane may span several layers.

As a result, the apparent source time function, and therefore the waveform, of the synthetic seismogram for each station varies with the emergent angle and azimuth of the ray to that station. This effect can be important for horizontally propagating faults (including large transform fault events), particularly for unilateral rupture. Figure 2.5 shows, for four different depths, a pair of synthetic seismograms, each of which includes one calculated using bilateral rupture and one assuming unilateral rupture in a direction away from the station. All other fault parameters were held constant for each pair. The effect of rupture direction, as well as that of focal depth, can be seen clearly.

#### THE PROBLEM OF FINITE WIDTH

The time function for fault width implies essentially infinite propagation of the rupture along one dimension of the fault, or in other words, horizontal propagation of a vertical line source. We realize that this is not a physically reasonable model for actual rupture propagation,

but there is not enough precision available in the shape of observed P-waves to justify a more detailed model. There are two significant objections to our approach that can be raised, however. One involves the calculation of the pP and sP delay times for a horizontally propagating fault. For our model of horizontal rupture along a nearly vertical fault, the initiation of rupture is assumed to take place simultaneously along a vertical line. This means that the up-going pP and sP waves begin at a different depth from the down-going direct P. If, for example, the fault has a width of 4 km and extends from the surface down to 4 km, then the pP and sP phases would arrive at a receiver simultaneously but behind the direct P phase by roughly the time required to travel vertically the extra 4 km. Such a situation is not likely because the initiation of rupture is more likely to occur at a point than along a line, and this point can be located anywhere along the fault's width. We therefore assume that the focal depth is a point source rather than a line source for the purposes of calculating the pP and sP delay times. This means that we should use, for our "fault width" convolution of the source time function, some non-rectangular function which represents the build-up of rupture away from the point of origin into the line source which will ultimately propagate horizontally. This would require, as noted above, the inclusion of a correction for wave shape which cannot be resolved from the shapes of observed P-waves. Therefore we have not included this additional complexity, even though we realize it introduces an incompatibility between two facets of our model.

The second major objection to this treatment of the fault width is more serious, and tends to obscure one of the major ambiguities inherent in this technique. If rupture is assumed to propagate along a vertical

line at a finite rupture speed, then the width function can be calculated using Equation 2.13, with fault width substituted for fault length, or

$$T_{wi} = w (1/v_r \pm |\cos Q_i|/v). \quad (2.14)$$

For the P phase, if the rupture is upward the + sign is used, and if downward, the -sign is used. For the pP and sP phases the signs should be reversed. The actual contribution of the fault width to the source time function is probably different from what we calculate using infinite  $v_r$ .

We can estimate the magnitude of this difference by assuming that the rupture speed approximately equals the shear wave velocity, so that  $v_r \approx v / \sqrt{3}$ , and by noting that the emergent angles, and therefore the angle  $Q_i$  in Equation 2.14, are usually around  $30^\circ$  for the stations used in this study. Thus, for the P phase, the minimum value possible for  $T_{wi}$  is about  $0.5 w/v_r$ , corresponding to downward rupture, and the maximum value possible is about  $1.5 w/v_r$ , corresponding to upward rupture. Since we determined the width effect by using  $T_{wi} = w (\cos Q_i)/v$ , the actual fault width might have been as large as the value we used or as little as  $1/3$  of the value we used, depending on whether rupture propagated downward or upward, respectively. Since the pP phase emerges from the source upward rather than downward, the effect of vertical rupture on the pP time length will be opposite to that of the P, i.e., if we have estimated the duration of the width component of P correctly (actual downward rupture), then we will have underestimated the duration of the width component of pP by possibly a factor of  $1/3$ . If the fault actually ruptured upward, the duration of our width contribution to P and pP could be wrong by a factor of  $1/3$  and correct, respectively. If we conjecture that an upper limit on the ratio of vertical rupture time to horizontal rupture time is 1, and that the rise time is much smaller than either,

then the duration of either the P or pP might therefore be underestimated by a factor of 2/3, as a worst case. Since each component is normalized to have  $\int T dt = 1$ , then the maximum amplitude of either component may be overestimated by this much also.

For the sP phase we have  $v_r \approx v$ , so that our calculated  $T_{wi}$  may be underestimated (and therefore  $w$  overestimated) by a factor of 1/2.2 for downward rupture (remember that sP emerges from the fault upward), while for upward rupture, our calculated  $T_{wi}$  may be overestimated by (and therefore  $w$  underestimated by) a factor of 6.5. Our calculated total duration of any sP phase may therefore be in error by a factor of perhaps 2 either larger or smaller, and likewise any sP amplitude. If rupture is bilateral vertically, with rupture starting in the center of the fault plane and propagating with a constant  $v_r$ , then there would be two equal components to the sP phase, with the upward propagation component from the top half of the fault having possibly 1/4 the duration and 4 times the amplitude of the part from the bottom half of the fault. With such a larger amplitude the top half component would probably dominate the waveform, and thus the actual fault width could be twice that indicated by the sP components of our synthetic seismograms.

Exactly what all of this does to any comparison between synthetic and observed waveforms probably varies with each event. Since the sP component usually has the larger amplitude it probably dominates the observed waveforms, and this effect may be major. For those events presented later which have slightly non-vertical fault planes, the effect may depend on the azimuth of each station. Clearly upward rupture is limited by the distance from the focal depth to sea floor, so that actual fault width cannot exceed twice that amount if there were equal-arm

bilateral vertical propagation. However, since seismic velocities increase with depth, rupture speeds may increase also, so that equal-time bilateral rupture may occur even though the lower (and therefore not as significant) portion of the fault may be larger than the top portion. The result is that, for the important sP phase, and to a lesser extent for the P and pP phases, an actual fault width may easily be more than twice the distance between the focal depth found and sea floor, if the vertical rupture was bilateral.

The nature of the spread of rupture over a finite fault can significantly affect the shape of the waveform produced. This fact should be considered whenever synthetic seismograms are constructed, and, in particular, whenever fault dimensions are inferred from source time functions. Obviously fault width cannot be clearly resolved by this method because the observed waveforms do not contain enough information. More importantly, fault orientation cannot be resolved as precisely as it would first seem because the relative sizes of the three main phases can vary with fault dimensions and the shape of the spread of rupture as well as with fault orientation. Even for synthetic seismograms calculated using a single source time function for all three phases, care must be exercised when fault dimensions are inferred because the source time functions of real earthquakes are probably not the same for these phases, and, in addition, the effects of the fault dimensions on source time functions are ambiguous. This problem exists with synthetic seismograms generated using any method, not just the one used here, and it will remain a problem until the nature of the rupture process is better understood.

These fault width effects are significant because they offer explanations for some of the characteristics of the seismograms presented

in the later chapters. One such feature is that the events presented all seem to have had time functions of 5 to 10 sec, even though the seismic moments varied by nearly two orders of magnitude. In order to produce these short time functions our model required small fault dimensions and thus produced very large displacements for the larger events. The possibility that the fault widths are larger than estimated means that the displacements may be overestimated; the effects discussed here offer an explanation of how events with very different seismic moments (corresponding to very different fault dimensions) might have similar (and short) time functions.

Another feature is that many of the events studied had some sort of precursor phase. One way to generate a "precursor" is to have a small P compared to pP and sP, a condition which can occur for some stations with a strike-slip earthquake if the fault plane is almost, but not quite, vertical. However, if the rupture was vertical and primarily upward, then the P phase could be quite long and therefore have a small amplitude, while the pP and especially the sP phase could be short and impulsive, producing a "precursor" effect with a completely vertical fault plane. Figure 2.6 shows two synthetic seismograms, one constructed using horizontal rupture propagation on a non-vertical fault, the other using upward rupture propagation on a vertical fault. For the amplitudes to be the same, the former required a seismic moment that was roughly 1.5 times that of the latter. The two waveforms also required different source dimensions so that the displacement inferred for the former was about 2.5 times that inferred for the latter.

The hypothesis that rupture begins below the surface and moves primarily upward seems to agree with the observation presented later that

most of these events had focal depths several km below the sea floor, thus allowing room to rupture upward. These possibilities will be discussed later but are presented now also in order that the lack of resolution of fault width be clearly understood.

#### CHECKS ON THE VALIDITY OF THE METHOD

As a check of our method, we computed synthetic seismograms of P waves and compared them to the results of Langston and HelMBERGER (1975). For this comparison we used their source velocity structure, which consisted of a half-space with a seismic velocity of 6.0 km/sec and a density of 2.7 g/cm<sup>3</sup>. We computed seismograms for a strike-slip earthquake, as observed at a station with an epicentral distance of 80° and on an azimuth 45° from the strike of the fault. We used two sets of source dimensions and rise times, which produced the source time functions given by Langston and HelMBERGER (1975) as representing a low stress-drop earthquake and a high stress-drop earthquake. This was a trapezoidal time function, with a rising ramp of 0.5 sec duration, a plateau of 1.5 sec duration, and a falling ramp of 0.5 sec duration for the high stress-drop case, and values of 2.0 sec, 6.0 sec, and 2.0 sec, respectively, for these variables in the low stress-drop case. Synthetic seismograms were computed for focal depths of 5, 10, 15, and 20 km. The resulting waveforms are shown in Figure 2.7 and are practically identical to the waveforms given in Figure 4 of Langston and HelMBERGER (1975).

For the oceanic earthquakes studied here there were also phases of p waves traveling upward through the 4 to 5 km of water over the transform fault, reflecting off the water surface, and traveling back down. These reflections do not influence the first 15 seconds of so of each seismogram because of the time required for the waves to travel up and back

down through the water. We do not include these water reflections in our synthetic seismograms. The observed waveforms presented in all of the following chapters have complexities after the first 15 sec or so, which we have been unable to duplicate in synthetic seismograms. We have assumed that these complexities are due partly to water reflections, and we have not given these details much consideration when matching waveforms.

The primary limitation to our method is that we do not include any phases or reflections other than P, pP, and sP. For most earthquakes complexities in the signal are introduced by the layered velocity structure near the source; reflections and phase conversions at the interfaces can introduce other phases into the final waveform. One such complexity is presence of pP and sP reflections at the sediment-water interface as well as the basement-sediment interface, particularly for transforms with an unusually thick cover of sediment like the Vema. The reflections and phase conversions at the interfaces in the oceanic crust generally do not contribute much to observed waveforms, because the amplitudes are too small. Figure 3-16 in Ewing, Jardetsky, and Press (1957) shows that, for a typical interface in an oceanic crust, the amplitude ratios of reflected or transmitted P waves from incident SV waves are only about .05 to .07 for the range of emergent angles used here. Figure 3-15 in Ewing, Jardetsky, and Press (1957) shows that for these interfaces and emergent angles the amplitude ratio of reflected P waves to incident P waves is less than .05. Another factor which would minimize the contribution of internal reflections in the layers of an oceanic crust is that the Q values for these layers may be fairly low; any multiple reflections must pass through these layers several times and



thus would have amplitudes even further reduced compared to the P, pP, and sP phases. The amplitudes of internal reflections would of course be increased if multiple reflections were superimposed with constructive interference. The magnitude of this effect would be dependent on the predominant period of the signal, layer thicknesses, and the angle from vertical of the emergent ray to each station; thus the effect could vary for each station and for each earthquake. These phase conversions and reflections could be included in our method, but it would contribute to the computational complexity which we have tried to minimize.

Another source of waveform complexity is the contribution introduced by a layered velocity structure beneath each receiver. We did not try to correct for this because each receiver would have its own structure.

Other methods of constructing synthetic seismograms have been developed which involve superposition of eigenfunctions in wavenumber space, e.g. Bouchon and Aki (1977). One major difference in the two techniques as applied to a layered structure for a transform fault is that the wavenumber superposition method includes all of the internal and water reflections, and phase conversions, expected for the structure, as discussed in the preceeding paragraph, and thus represents a complete solution. However our method offers the advantage that it is numerically simpler and requires less computer time. Because our method is a time domain synthesis, it is easier to understand the contribution to the result from each of the fault parameters, and to adjust these parameters to bring about the desired result.

We have prepared synthetic seismograms using both techniques, for (1) a simple half-space, (2) a layer of water and a crustal layer over a half-space, with the event focus in the crustal layer, and (3) a crustal

layer over a half-space, with the event focus in the mantle. The comparisons, given in Figures 2.8 and 2.9, show that the waveforms calculated from the two methods are quite similar, though the agreement is best for the simple half-space model. For each figure, all of the seismograms are plotted with the same vertical scale, so that the amplitudes calculated with the two methods could be compared. The maximum amplitudes found with each method for the half-space model differed slightly, but this was primarily due to different methods of calculating the geometric spreading factor. (This calculation involves taking the second derivative of the travel-time tables and thus is subject to numerical "noise".) When the amplitudes were corrected for this effect, the difference was no greater than 1%. The slight dissimilarity of waveforms for the other structures is presumably indicative of the effect produced by not including all reflected phases in our method. It must be remembered that the comparisons shown here for the layered structures are not valid for other combinations of focal depths, source time functions, and layer dimensions, since the interference between multiple reflections depends on these parameters. In particular the effect of the water layer shown in Figure 2.9 cannot be taken as representative of the effect for all transform fault earthquakes.

#### PARAMETERS AND DATA NEEDED

With our method the following independent variables must be given: P-wave velocity and density for each layer in the structure near the source, station azimuths and distances, event depth, fault strike and dip, slip angle, fault length and width, rise time, rupture velocity, propagation direction (bilateral or unilateral and, if unilateral, which direction), attenuation value  $t^*$  ( $t^*$  was set at 1 sec for all of the

synthetic seismograms presented here), and scalar moment. Of these, all but the velocity and density structure and station azimuths and distances are unconstrained by other considerations and therefore are, in principle, resolvable within the limits of the available observed seismograms and the ambiguities inherent in the method.

The observed seismograms used for comparisons to the synthetic seismograms were taken from the long-period vertical records of WWSSN stations, generally in Europe and North America and around the North Atlantic Ocean. The records were digitized at an interval of 0.6 sec or less, and plotted along with the synthetic seismograms, with normalized amplitudes to facilitate waveform comparison. Total moment was determined by numerically matching the maximum amplitude, taking into account which part of the waveform was being compared. Other parameters were determined by visual comparison. The epicenters used for determining distances and azimuths were taken from the Bulletins of the International Seismological Centre, and the travel times and ray parameters were calculated from the tables of Herrin (1968).

#### RESOLUTION OF AND AMBIGUITIES IN THE RESULTS

The input parameters of this scheme can be specified to any desired precision, but there are various kind of errors and ambiguities present which must be considered when the results are interpreted. These can be separated into the following general classes: numerical errors in the method, theoretical flaws in the method, ambiguities between two or more input parameters, errors and imprecision in the observed waveforms, and uncertainties in the transform fault structure.

1. Numerical errors in the method. The major source of numerical imprecision has already been mentioned, i.e., determination of geometric

spreading factors. One component of this term includes the second derivative of the travel time curve used. Figure 2.10 presents geometric spreading factors versus epicentral distances for a focal depth of 3.5 km below sea floor. The values can be seen to vary by as much as 10% about some "average" curve. Thus the actual values used for any given earthquake may average out to be high or low depending on the distribution of stations available. At closer distances ( $\Delta < 30^\circ$ ) the slope of this curve becomes large, making stations at these distances much more susceptible to errors.

Since the geometric spreading factor is a constant which multiplies the synthetic seismograms, its errors do not influence the parameters of the source time function, but do influence the seismic moment and calculations derived from it. A geometric spreading factor which is too large will mean that the resulting synthetic seismogram will also be too large, and thus the seismic moment required to match the observed amplitudes will be too small. Any results which are proportional to the seismic moment will also be too low, including total displacement and dislocation velocity, and the errors will be the same percentage as that of the moment.

2. Theoretical flaws in the method. One of these has already been discussed in the previous section, i.e., the exclusion of other phases which may contribute to the waveform. The effect of these exclusions on the results is largely unsystematic. Synthetic seismograms for pure strike-slip earthquakes less than 1 km or so from the sea floor generally show very little complexity. As seen from the expressions for radiation patterns (Kanamori and Stewart, 1976), the shapes of these waveforms show dependence on emergent angle (nearly constant over these epicentral

distances) but not on station azimuth. For these events, waveform matching does not involve any interference effects between the main phases, and thus the excluded phases probably do not contribute much. For events deeper than 1 km below sea floor, as many of those studied seem to have been, the excluded phases may contribute to the waveforms.

For many of these events the exact shape of the waveforms depends on a precise combination of fault dimensions, fault orientation and focal depth. For example the fault dip may have to be specified to a precision of  $0.5^\circ$  in order to match exactly the ratio of amplitudes between the peaks of a double-peaked waveform. Phases excluded in our synthesis may have contributed significantly to the observed waveform. Thus, while the actual dip of the fault plane was probably near that necessary for the synthetic waveform, the apparent precision required by the synthetic seismogram probably gives a false impression of the certainty of the results. It is not straightforward to put any quantitative value on how large these influences might be, though the final results for each earthquake studied probably reflect the general character of the actual faulting process.

Another significant flaw in the method is our model of a planar fault, involving a line source propagating at a fixed velocity, with either completely unilateral or completely bilateral faulting. In reality faults are probably never completely unilateral, even if the observed waveforms show extreme directionality. The choice of unilateral or bilateral faulting, for a first order approximation, makes little difference in waveform, provided the fault length is adjusted accordingly. Thus with other parameters held constant this choice makes a difference in the determined displacement (and likewise the dislocation

velocity) by up to a factor of two. Some of the earthquakes presented in the following chapters showed enough directionality in the observed waveforms that the model of a unilateral fault was required. This usually resulted in the fault length being as short as 10 to 12 km. These earthquakes may have ruptured primarily unilaterally, though some propagation of rupture in the reverse direction may have occurred if it was sufficiently short to avoid significant contribution to the waveforms. Thus the determined fault lengths for these events should be considered lower bounds, with the actual values probably slightly higher, and the determined displacements and dislocation velocities should be considered upper bounds, with the actual values slightly lower.

The problem of fault width has already been discussed extensively in a previous section. We have not used a more elaborate model because we do not feel that the results would be any more precise than those presented here.

3. Ambiguities between two or more input parameters. For the synthetic seismogram for any single station the source time function is the convolution of three rectangular functions, representing apparent time of rupture propagation along the strike, apparent rupture time due to fault width, and the time required for the dislocation process. The longest of these, usually the rupture propagation, was often 3 to 5 seconds, while the other two were usually determined or set to be 1 sec. The convolution of these functions produces a general trapezoidal shape with the corners and the beginning and end having segments with parabolic shapes, i.e., a "trapezoid" with the corners smoothed out (Figure 2.4). Since the apparent rupture time depends on the seismic velocity and the direction from which the rupture is observed, the source time function

other factors. If a rise time was decreased so that a fault length or width could be increased, in most cases it would have meant a dislocation velocity much greater than those reported for other earthquakes. If a fault length or width was decreased it usually produced a displacement value much too large for events of this magnitude, particularly when the seismic history is considered. Error in the estimated seismic moment therefore influences the resolution of the time function components indirectly, in that a seismic moment too large produces too large a displacement value, and therefore places very tight constraints on the fault dimensions and rise time, while a moment value too low places very loose constraints on these parameters. As already discussed the fault widths used in these synthetic seismograms are probably too small due to lack of resolution in the model.

4. Errors and imprecision in the observed waveforms. The fits obtained between synthetic and observed waveforms are only as significant as the resolution of the observed waveforms allows them to be. As already mentioned, WWSSN long period seismometers do not have much resolution for details as short as one second. Since the rise times used here, as well as the fault width effects, were generally about 1 second duration, the effects of changes in these parameters were generally small in the synthetic waveforms. The presence of noise in observed waveforms usually meant that the exact arrival time, and therefore the exact shape of the first-arrival slope could not be identified easily.

Signal size on the observed records was a strong influence on the apparent wave shape. Most of the waveforms studied had short signal lengths, so that even at a very fine digitizing interval, some significant features in the waveforms were represented by only a few data

used for the sP phase generally will be different from that used for the P phase, and if the fault plane is non-vertical, the source time function used for the pP phase generally will be different also. The total time of the function is the sum of lengths of the component functions, but the duration of the rising and falling edges depends on the relative size of the three components. The parabolic section at the start is the length of the shortest of the three functions, which for the seismograms presented here may have been either the rise time or the width function. Since the emerging rays covered a fairly small solid angle, any directionality introduced by a finite fault width would be observable only if the fault plane deviated much from vertical, usually not the case here. Thus the rise time and fault width effects were generally unresolvable from each other. For events with bilateral propagation the fault lengths were generally so small that directionality could not be observed within the resolvable shape of the waveforms, and the only easily resolvable parameter was total length of the source time function. (It must be remembered that long period seismometers are not particularly responsive to waveform details as short as one second.) Thus for these events ambiguity exists not only in the resolution of fault width and rise time but fault length and rupture velocity as well, and, for certain cases, focal depth.

This situation is not as bleak as it may seem, however, because the effects of these parameters influence, and are therefore constrained by, some of the results. Regardless of the details of shape, the waveforms studied here generally required time functions with total lengths less than 10 sec, often as short as 5 sec. This required that each of the three components be quite short also, though each one was constrained by



points. For some records, if only one data point were digitized incorrectly, either from operator or machine error, the results could obscure or eliminate a feature of the waveform. This is apparent in some of the digitized waveforms presented in the following chapters. In these cases we determined wave shape by referring back to the original seismograms rather than digitized waveforms. For the smaller signals, improper digitization usually meant that the size of any feature, or the maximum amplitude, was affected. For very large signals the effect was usually to obscure the shapes of the rapidly rising and falling parts of the waveform, while the relative and absolute sizes of features were recorded faithfully.

5. Uncertainties in the transform fault structure. The velocity structure beneath transform faults has been studied by several investigators, e.g., Detrick and Purdy (1980), Ludwig and Rabinowitz (1980), Detrick et al. (1983), and the results have varied. This probably indicates that there is not a single velocity structure beneath all Atlantic transforms, and that there is probably significant variation beneath each one. It is therefore impossible to be certain of the correct structure to use for each earthquake studied here.

The choice of velocity structure affects synthetic waveforms in several ways. It directly affects the bounce times calculated for pP and sP phases. A model that has velocities too large will yield a source depth that is too great, and the deeper the event, the greater the effect will be. The velocity at the source also influences the emergent angles of all three phases and the reflection coefficients of the pP and sP phases. Incorrect emergent angles will produce amplitude errors in the phases by affecting the radiation pattern coefficients. Since the

amplitude of any phase is inversely proportional to the third power of the seismic velocity at the source (see equation 2.1), velocity structure has a very large effect on the seismic moment determined. These errors can also be compounded by indirect effects if the source depth is chosen incorrectly, placing the focus in the wrong velocity layer.

Observed waveforms from some stations for the earthquakes studied here showed features indicating that the emergent rays were near nodal planes. The shapes of these could usually be reproduced in synthetic seismograms by very careful selection of fault orientation. In fact since the ratios of pP and sP to P phases for pure strike-slip earthquakes vary with emergent angle but not with azimuth, and since the stations used covered only a small range of emergent angles, these waveforms were often the greatest constraint on the selection of fault orientation. However the real precision necessary to match these waveforms is only as great as that for the emergent angles themselves, and, as pointed out, these are influenced directly by the velocity at the source, and indirectly, and sometimes more dramatically, by the choice of focal depth.

The discerning reader will notice that this section has been fairly devoid of quantitative discussion. Magnitudes and precisions of results, as far as they can be determined, will be given in subsequent chapters. The quantitative problem of resolution and precision cannot be approached systematically, since this is a forward, not an inverse, problem and the final results do not depend in any simple, let alone analytical, way on the input parameters. In most cases it was not possible to obtain perfect fits for all of the stations used, and in some cases the observed waveforms for stations very close to each other showed different

features, indicating that there was some other, possibly regional, influence on the observed waveforms. Since there was no way to quantify the validity of these conflicting requirements, some subjective judgement was needed in these cases.

### Figure Captions

Figure 2.1 Calculation of the delay times of pP and sP phases with respect to the direct P phase. The contribution from the extra path length through each layer is determined by dividing the path length by the appropriate seismic velocity. An additional correction to the teleseismic travel time is determined from the phase velocity and the total horizontal separation between source (or virtual source) and reflected ray at the focal depth.

Figure 2.2 Geometry used in determining the angle  $Q_i$  between rupture propagation vector and the ray path to station  $i$ .  $\phi$  is the strike of the fault plane, measured clockwise from N. For horizontal propagation,  $\phi$  is also the azimuth of the propagation vector.  $\delta$  is the dip of the fault plane, measured from the horizontal.

Figure 2.3 Total apparent propagation time is composed of a term for the actual time of rupture propagation and a term proportional to the difference  $L \cos Q_i$  in path lengths from each end of the fault to station  $i$ .

Figure 2.4. Example of source time functions  $T(t)$  produced by finite fault model. The source velocity structure used was that given in Table 4.2, and 4 km of water. We used a station epicentral distance of  $28^\circ$ , a station azimuth of  $N271.5^\circ E$ , a fault strike of  $N90^\circ E$ , a dip of  $90^\circ$ , a slip angle of  $180^\circ$ , a fault length of 10 km, a fault width of 5 km, a rise time of 1 sec, a focal depth of 7.5 km, and bilateral horizontal rupture propagation at a speed of 3 km/sec.

Figure 2.5. Synthetic seismograms prepared for focal depths of 6, 7, 8, and 9 km, using bilateral horizontal rupture propagation and unilateral horizontal propagation away from the station azimuth,

with a rupture propagation speed of 4 km/sec. All other source parameters were held constant. The source structure used is that given in Table 4.2, with a water depth of 4 km. The focal depths shown are with respect to the sea surface. The station's epicentral distance and the azimuth were  $40^\circ$  and  $271.5^\circ$ , respectively. The fault plane had a strike of  $N140^\circ E$ , a dip of  $89^\circ$  to the north, a slip angle of  $180^\circ$ , a length of 10 km, and a width of 5 km. The rise time was taken to be 1 sec. The instrument response used had pendulum and galvanometer periods of 15 and 100 sec, respectively, and damping factors of 0.93 and 1, respectively. The difference in waveforms in the pair for each depth is due to the different source time functions.

Figure 2.6. Synthetic seismograms showing "precursors" that are actually small P phases caused by (1) non-vertical fault dip, and (2) upward propagation of the rupture. In both cases the station used had an epicentral distance of  $62.2^\circ$  and an azimuth of  $31.9^\circ$ , the source velocity structure was that shown in Table 4.2, the water depth was 5.7 km, the fault strike was  $N91^\circ E$ , and the slip angle was  $180^\circ$ . For the first waveform, we used a fault dip of  $83^\circ$  to the north, a focal depth of 7.5 km, a fault length of 12 km, a fault width of 5 km, a rise time of 1 sec, and bilateral horizontal rupture propagation at a speed of 4 km/sec. For the second waveform we used a vertical fault, a focal depth of 10 km, a fault length and width of 10 km, a rise time of .5 sec, and upward vertical rupture propagation at a speed of 3 km/sec. The instrument response used was the same as for Figure 2.5, except that the pendulum period was 30 sec.

Figure 2.7. Synthetic seismograms determined for a strike-slip earthquake in a halfspace, for the high stress-drop and low stress-drop cases of Langston and Helmberger (1975), for focal depths of 5, 10, 15, and 20 km. The instrument response used was the same as that for Figure 2.5. These waveforms are comparable to those in Figure 4 of Langston and Helmberger (1975).

Figure 2.8. Synthetic seismograms for epicentral distances of 30°, 45°, 60°, and 75°, calculated using both our technique and wavenumber superposition. The source structure used was a simple half-space with P wave velocity of 6.00 km/sec, S wave velocity of 3.46 km/sec, density of 2.7 g/cm<sup>3</sup>. We used a focal depth of 10 km, and the high stress drop source time function of Langston and Helmberger (1975). The instrument response used was the same as for Figure 2.5. All eight seismograms are plotted with same vertical scale, so that their amplitudes can be compared. Except for the vertical scale, these are comparable to the high stress drop, 10 km depth case in Figure 2.7.

Figure 2.9. Synthetic seismograms for epicentral distances of 30°, 45°, and 60°, calculated using both our technique and wavenumber superposition. The source structure used was (1) a 4 km deep layer of water and a 5 km thick crustal layer over a half-space, and (2) a 5 km thick crustal layer over a half-space. In both cases the crustal layer had a P wave velocity of 6.0 km/sec, an S wave velocity of 3.46 km/sec, and a density of 2.7 g/cm<sup>3</sup>, while the half space had values of 8.1 km/sec, 4.68 km/sec, and 3.2 g/cm<sup>3</sup>, respectively. The water layer had a P wave velocity of 1.52 km/sec, and a density of 1.03 g/cm<sup>3</sup>. In the first case the earthquake focus

was placed in the crust, 4 km below sea floor; in the second case the focus was placed in the mantle, 10 km below the free surface. The source time function used was the same as that used in Figures 2.7 and 2.8. The instrument response used was the same as for Figure 2.5. All twelve seismograms are plotted with same vertical scale, so that their amplitudes can be compared.

Figure 2.10. Geometric spreading factors vs. epicentral distances, using the velocity structure given in Table 4.2 and a focal depth of 3.5 km below sea floor.

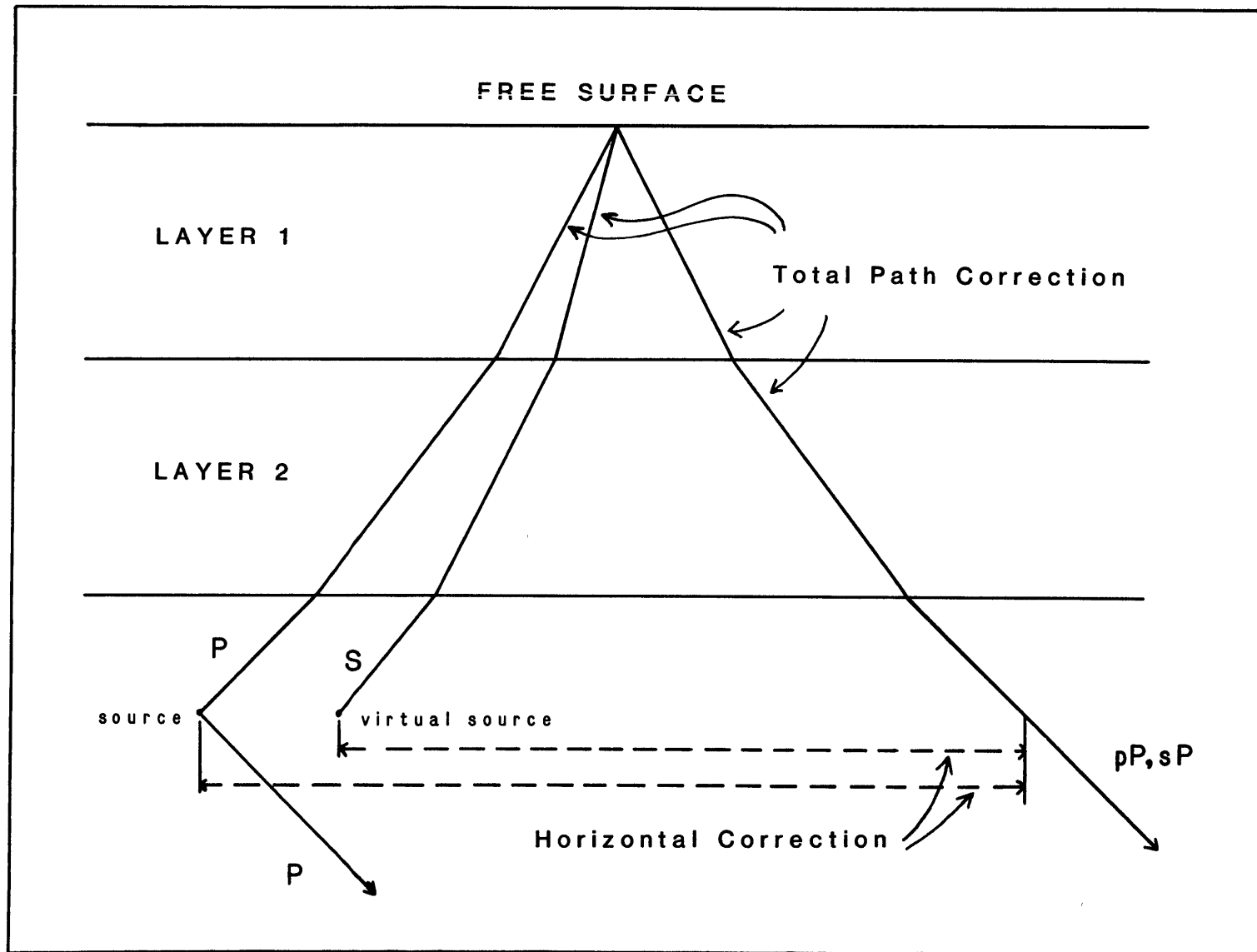


Fig. 2.1



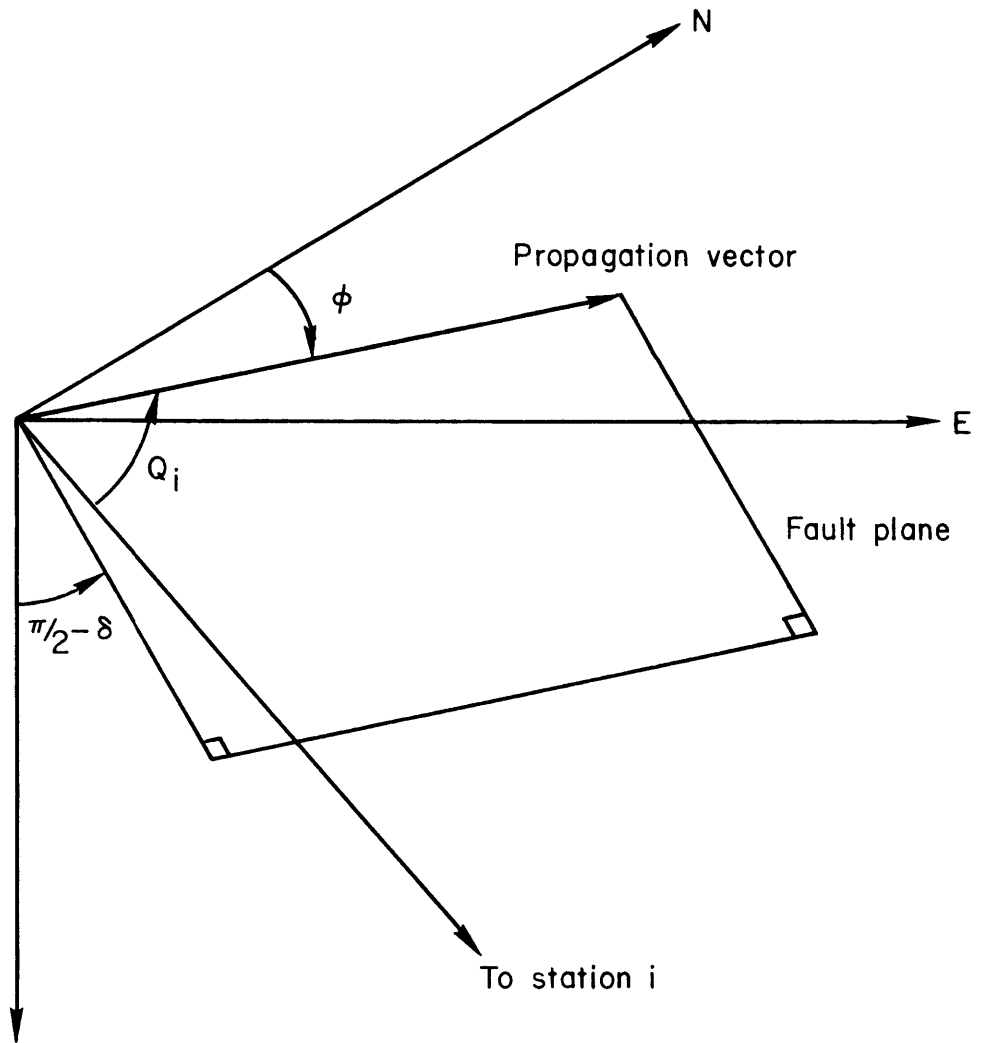


Fig. 2.2

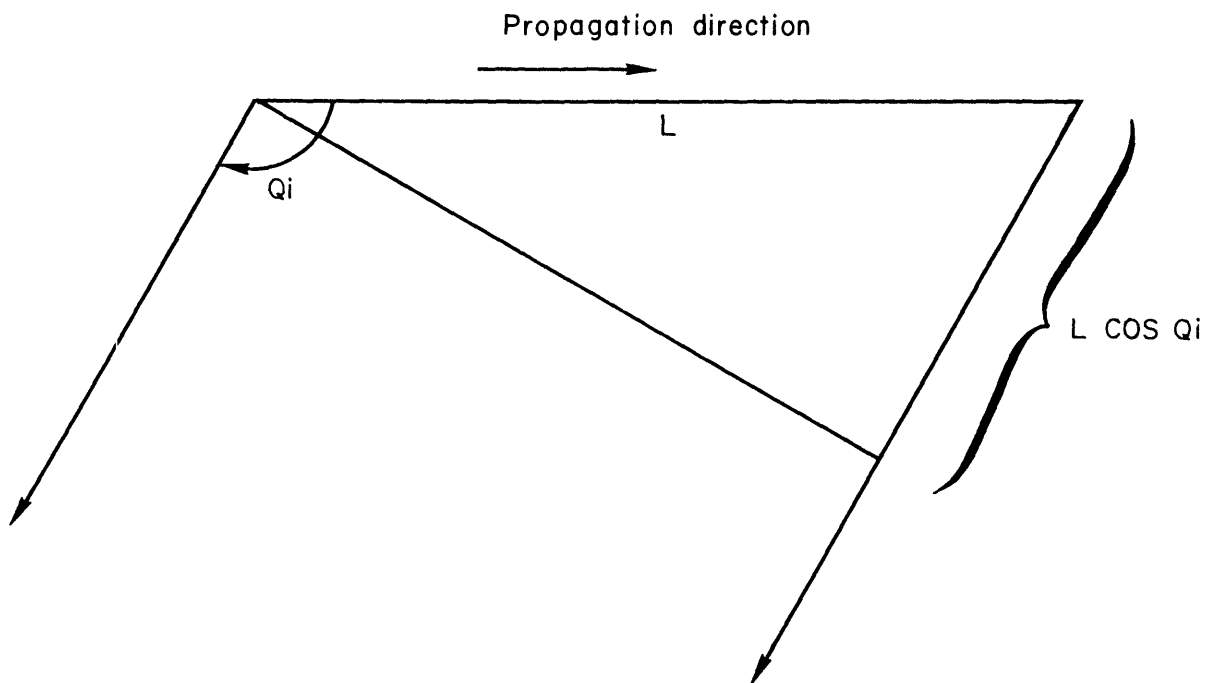


Fig. 2.3

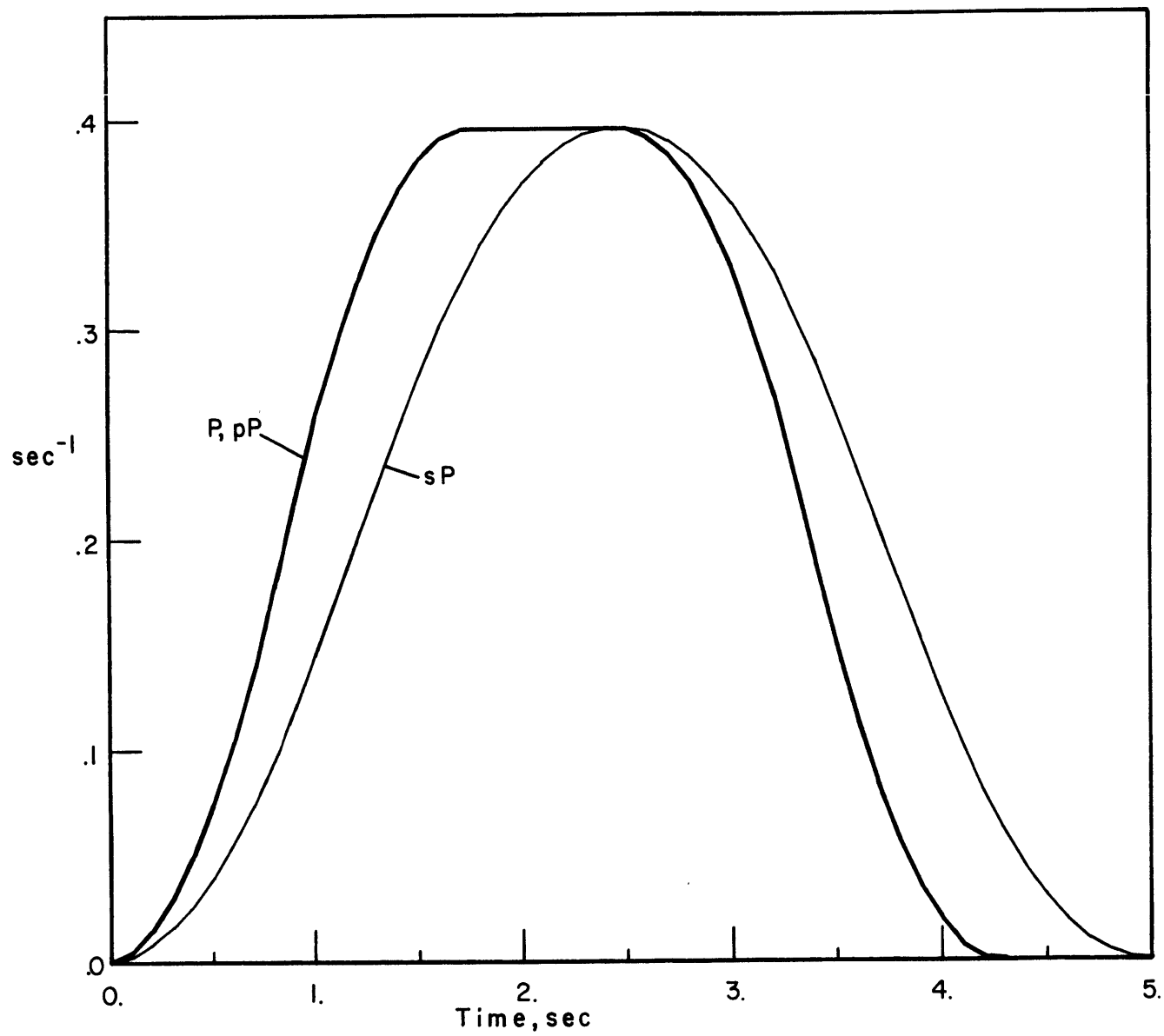


Fig. 2.4

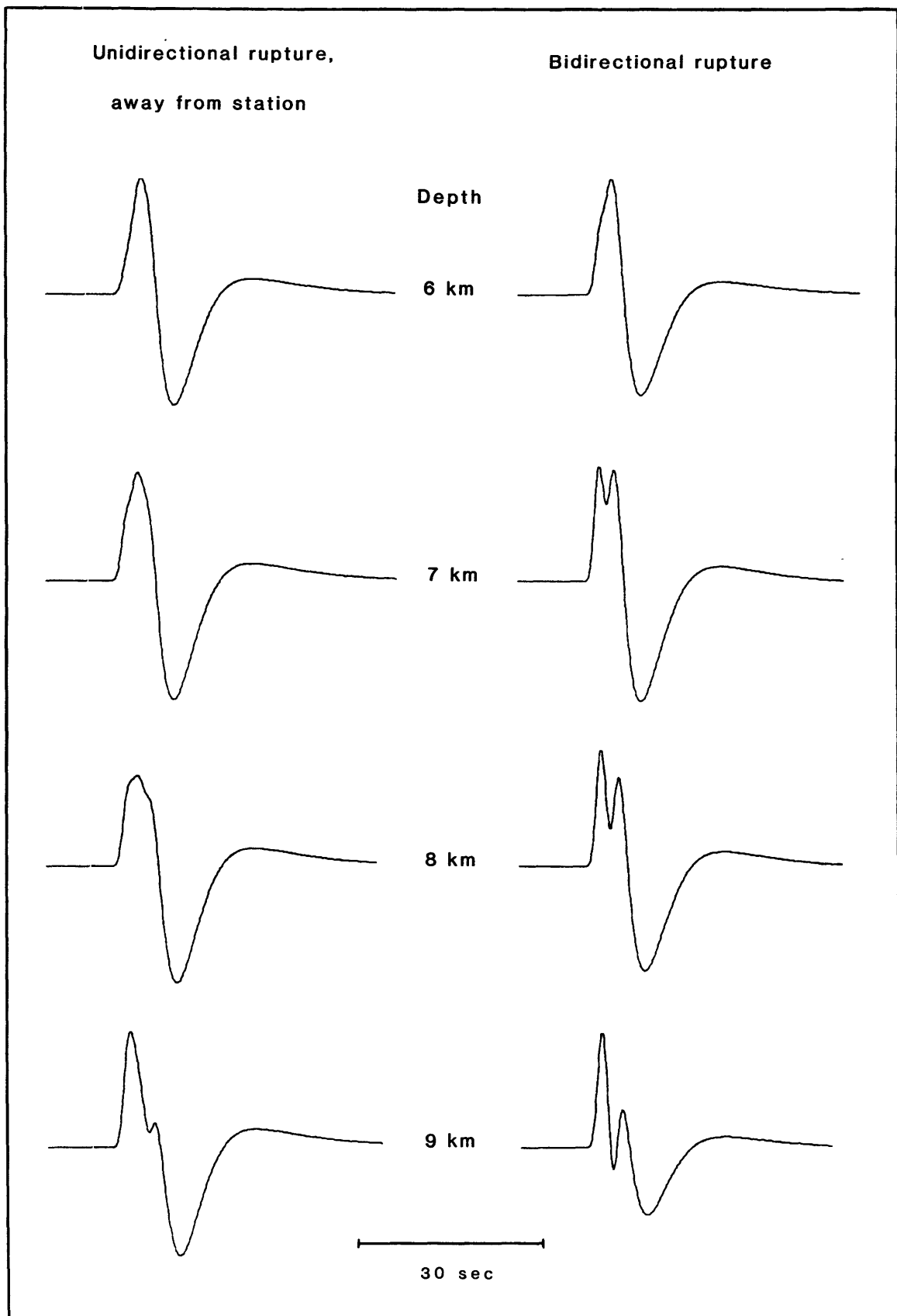


Fig. 2.5

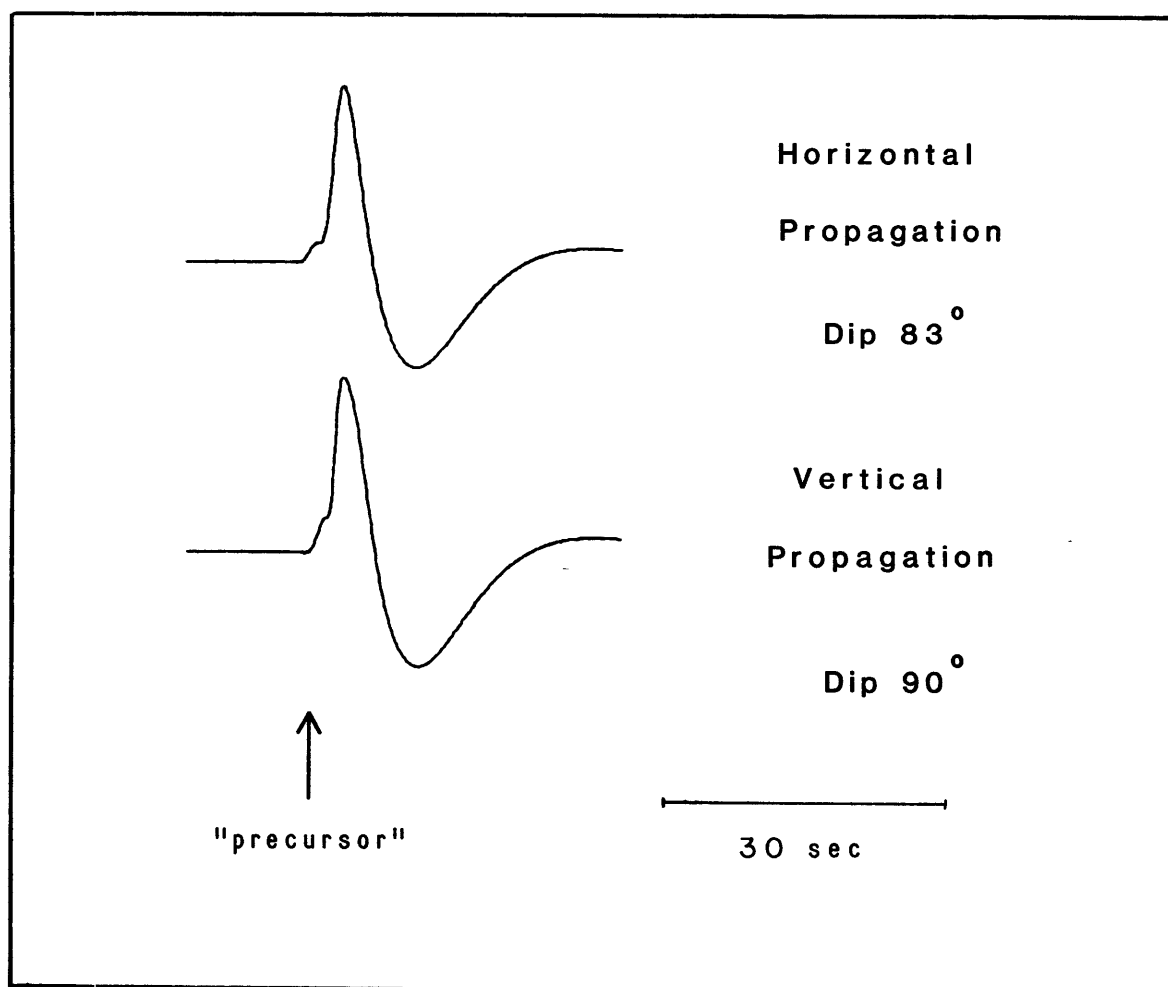


Fig. 2.6

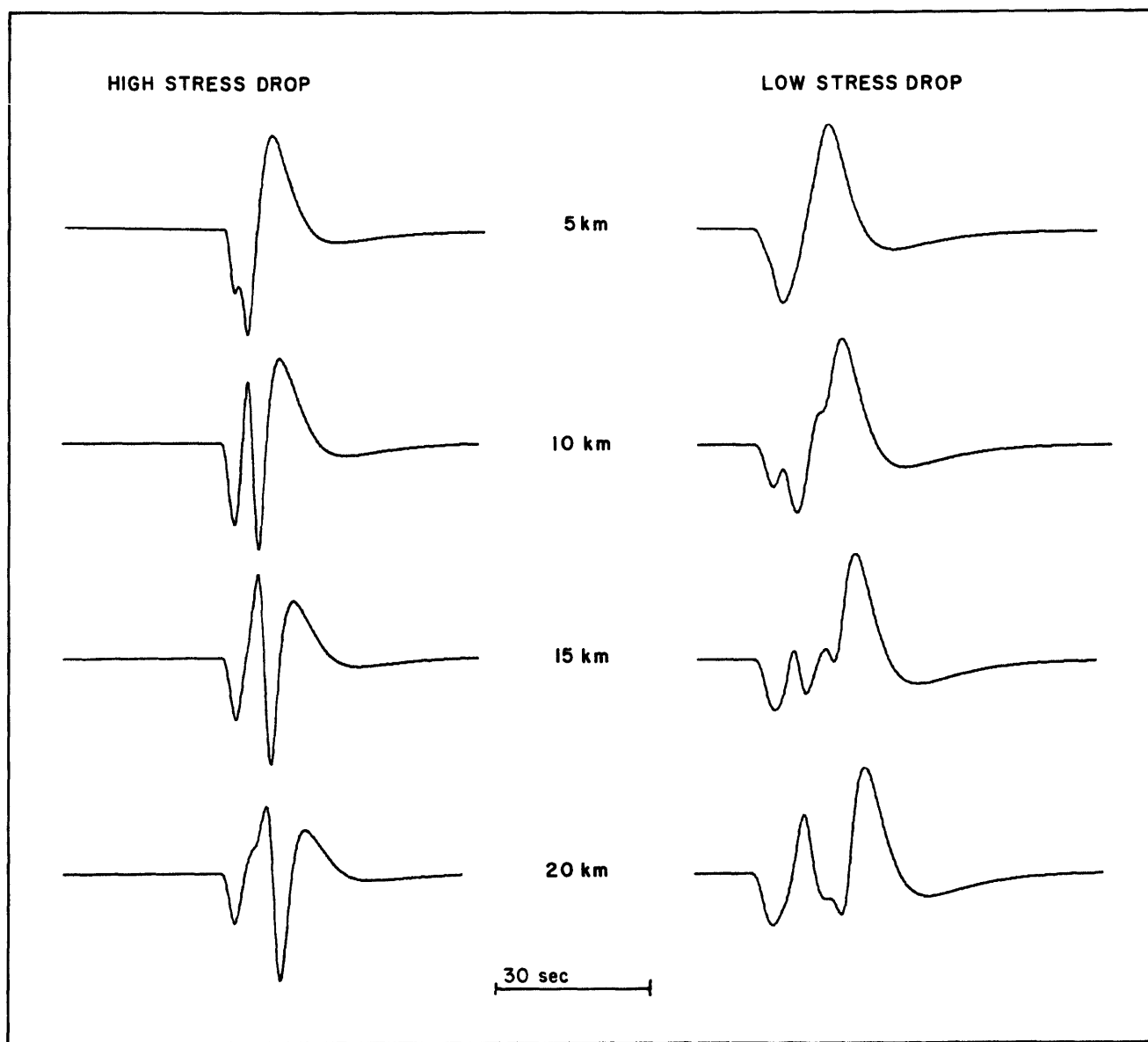


Fig. 2.7

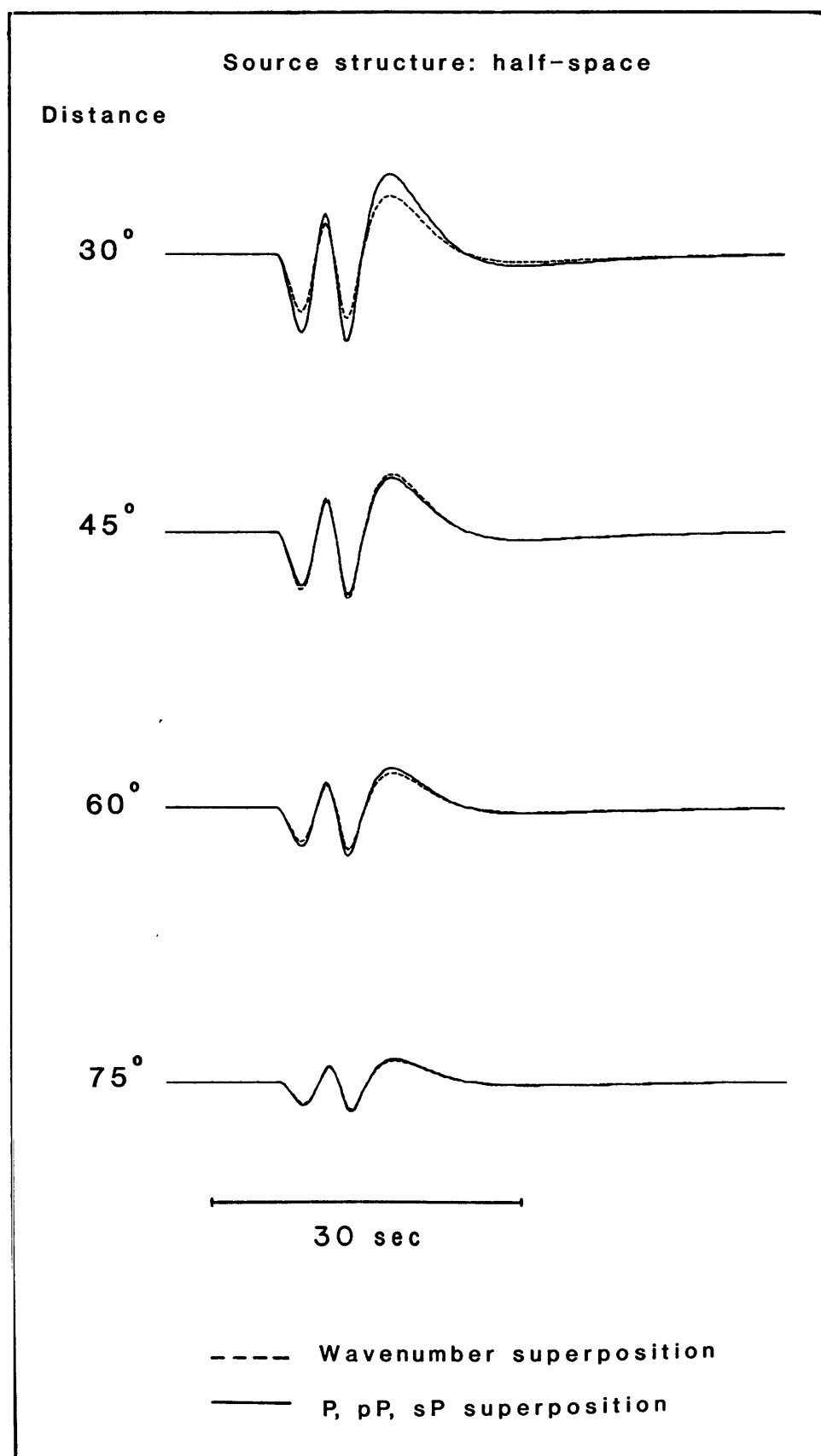


Fig. 2.3

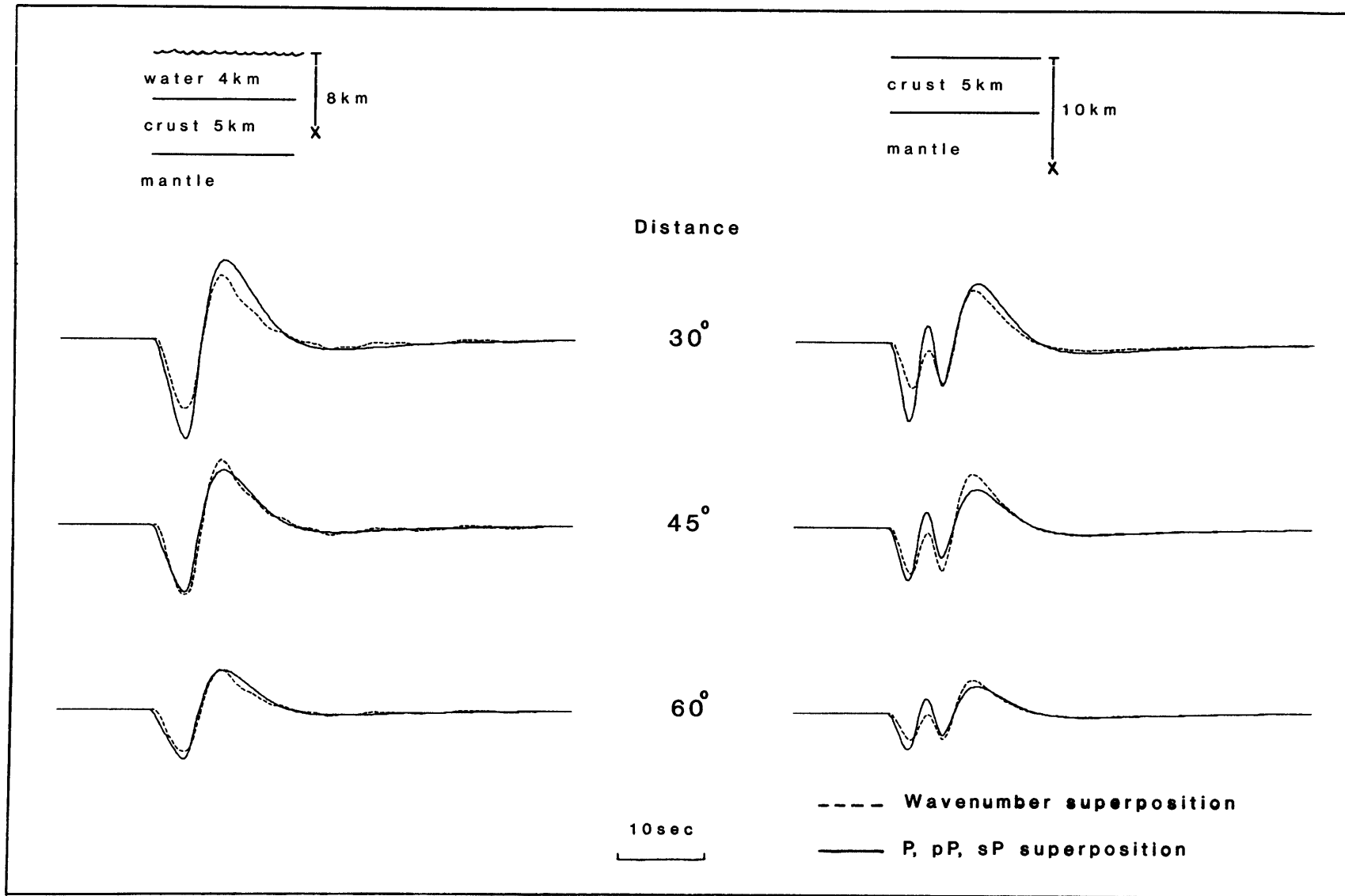


Fig. 2.9



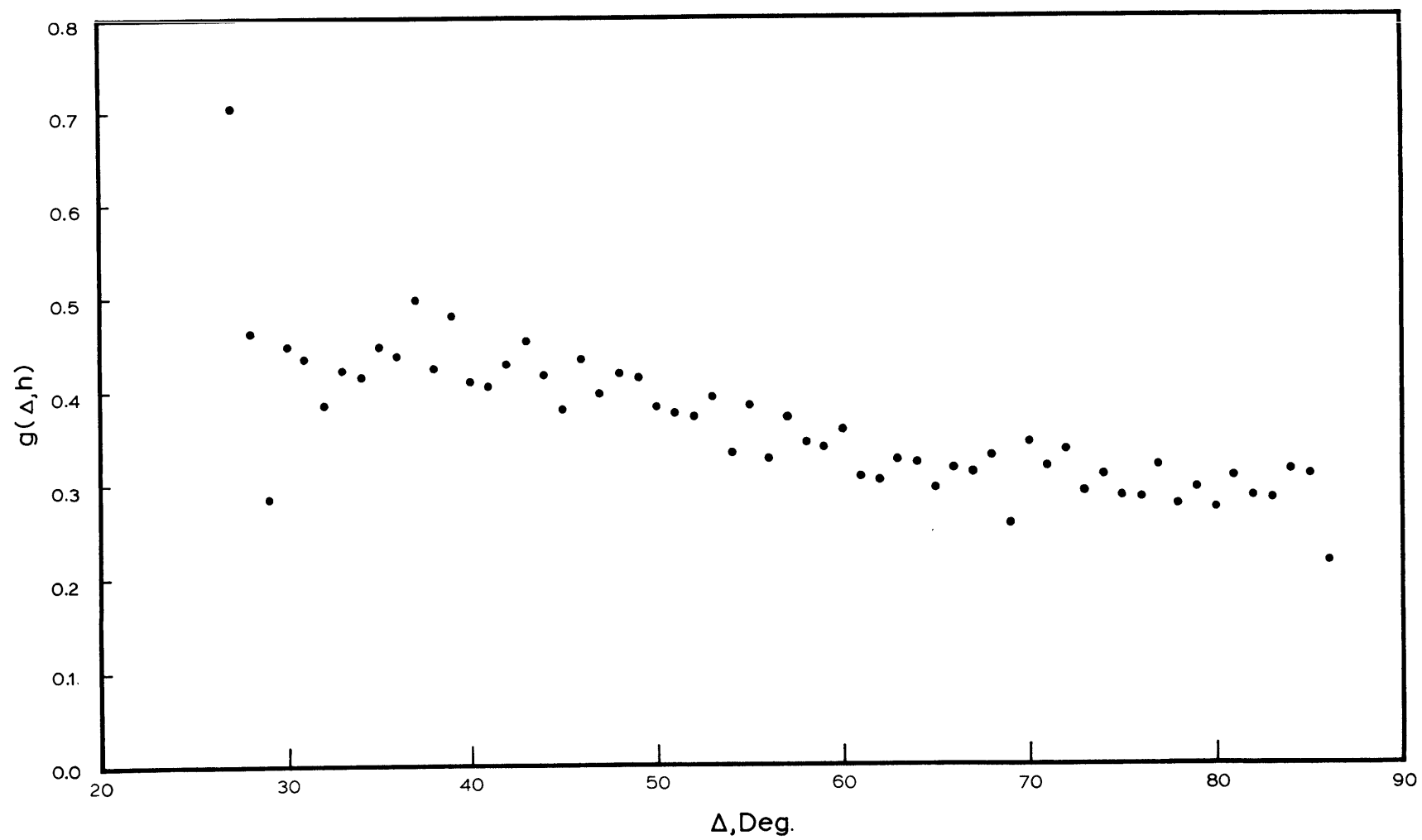


Fig. 2.10

### CHAPTER 3. THE SEISMICITY AND TECTONICS OF THE GIBBS TRANSFORM FAULT

The Gibbs transform fault is a left-lateral offset of the Mid-Atlantic Ridge about 350 km long near latitude 52°N. It was first described by Johnson (1967), and later by others, including Fleming et al. (1970), Olivet et al. (1974), and Searle (1981). The Gibbs transform fault is one of the longest in the North Atlantic and is the longest between the European and North American plates.

The bathymetry of the Gibbs transform fault, shown in Figure 3.1 (Uchupi, 1982), is dominated by two parallel trough-like depressions, with a strike of about N95°E, separated by an elevated ridge. Bathymetrically the transform's length can be divided into two segments, the eastern third and the western two thirds. The northern trough is deeper in its western segment, while the southern trough is deeper in its eastern segment. Vogt et al. (1971) interpreted this pattern of trough depths as defining a double transform, in which the eastern segment is active in the southern trough and the western segment is active in the northern trough, with the two sections separated by a small north-south spreading center joining the two active sections.

Van Andel et al. (1971) suggested that the central ridge may exist because the transform is "leaky", brought about by a 10° change in the spreading direction about 10 m.y. ago. However, Olivet et al. (1974) showed that the last change in spreading direction indicated by the sea floor magnetic record was considerably earlier (anomaly 19, approximately 43 m.y. ago) and in the wrong direction to produce a leaky transform. They concluded instead that the entire system comprises one complex

transform, and that the central ridge is made up of diapiric intrusions along the transform axis. They suggested that the long length and small slip rate of the transform brings parts of oceanic lithosphere with very different ages into juxtaposition, creating a zone of shear stress and allowing intrusions to take place along the entire length of the transform instead of at a localized spreading center. By this interpretation, the central ridge exists by virtue of its being hotter than the surrounding material.

Searle (1981) presented an analysis of the Gibbs transform based on side-scan sonar results and other geophysical data. He confirmed that there are actually two transforms, separated by a north-south striking spreading center at about  $31.75^{\circ}\text{W}$ , and that this spreading center accounts for the elevated topography between the two segments. In the southern segment the floor was sediment-free, and he identified a single continuous fault, with a strike of  $\text{N}95^{\circ}\text{E}$ , which he interpreted to be the active transform. He also noted another reflector about 1 km further south, which he took to be the base of the southern wall of the transform valley. He was able to identify an active-transform trace in the northern segment also, though the floor here was covered with sediment. The depth to the basement in both transform valleys was generally about 4000 m, while greater depths were present at the ends where the active transforms intersected with the adjoining spreading centers.

## SEISMICITY

Figure 3.1 shows the epicenters of the known earthquakes on the the Gibbs transform fault through 1981. Data for these earthquakes, given in Table 3.1, were taken from Gutenberg and Richter (1954) and Rothe (1969) for events before 1964, from the I.S.C. Regional Catalogue for events

between January 1964 and December 1979, and from the P.D.E. Monthly Listings of N.E.I.S. for events in 1980 and 1981. Table 3.1 (and similar tables in succeeding chapters) contains, for each earthquake, date and origin time, epicenter, focal depth, number of stations reporting the event,  $m_b$ ,  $M_S$ , and seismic moment ( $M_0$ ). Following Geller and Kanamori (1977), we have taken magnitudes reported before 1964 as equivalent to  $M_S$ . For each event whose  $M_S$  was not available, we determined a value from  $m_b$ , using the relation given in Chapter 9. For all events except the two studied by Kanamori and Stewart (1976) and those events we have studied we have determined  $M_0$  values from  $M_S$ , using the relation presented in Chapter 9. Those values of  $M_S$  and  $M_0$  determined from the relations in Chapter 9 are given in parentheses in Table 3.1.

As indicated by Figure 3.1, the northern trough is seismically active primarily in the western section, while the southern trough is active only in the eastern section, the center of which has been seismically quiet. At the boundary between the eastern and western segments there is a region of high seismicity which trends roughly N-S, and seems to indicate that movement along the transform crosses over between the troughs at this point. This pattern is similar to what Searle (1981) found, and supports the interpretation that the Gibbs Fracture Zone actually contains two separate transforms separated by a short spreading center segment.

#### MAJOR EARTHQUAKES

Kanamori and Stewart (1976) noted that five large earthquakes ( $M_S > 6$ ) have occurred on or near the Gibbs transform since about 1920: on September 30, 1923, June 18, 1941, December 11, 1954, February 13, 1967, and October 16, 1974. They showed that at least the last four of these

alternated between each end of the transform with an average interval between events of 13 years. The 1923 event ( $M = 6.5$ ) was located by Gutenberg and Richter (1954) at  $54^{\circ}\text{N } 32^{\circ}\text{W}$ , a location that may have been less accurate than for later events.

Kanamori and Stewart (1976) also determined the source parameters for the events in 1967 and 1974 by comparing observed Rayleigh and Love waves and P and SH waves to synthetic seismograms. They found that these earthquakes had strike-slip mechanisms with fault orientations which agreed with the bathymetrically implied direction of motion on the transform. They found that the fault lengths for these two events, assuming bilateral propagation, were about 60 km for the 1967 event and about 70 km for the 1974 event. (Bilateral faulting was supported by the similarity of waveforms observed to the east and west, and by the locations of aftershocks of the 1974 event.) These fault lengths suggest that the entire length of the fault has experienced slip at least once in the last five major earthquakes. In Figure 3.2 we have plotted the longitude for each event listed in Table 3.1 with  $M_S$  equal to or greater than 5.5 versus the year of occurrence. The pattern of the four largest events alternating between each end of the transform can be seen. Two other features of note are that all of these events tended to occur near the end of a transform segment, particularly so near the small spreading center near the middle of the transform and on the eastern portion of the transform system, and that all of the events before 1955 occurred near the western end. (A possible exception to this last point is the September 30, 1923 earthquake; if this event occurred on the Gibbs transform, its epicenter was near the eastern end of the northern transform segment.) This supports the suggestion of Kanamori and Stewart

(1976) that the large strike-slip events may fracture entire transform segments, but unilateral rupture propagation would also be implied.

Kanamori and Stewart (1976) found that the average dislocations were 160 cm for the 1967 event and 180 cm for the 1974 event, based on an assumed fault width of 10 km. If the entire transform has slipped in the last five large earthquakes, these displacements imply an average slip rate of 2.6 cm/year, which agrees well with the slip rate of 2.3 cm/year predicted by the angular velocity between the Eurasian and North American plates determined by Minster and Jordan (1978), implying that most of the slippage along the transform occurs as seismic activity. Kanamori and Stewart also suggested that these earthquakes seemed to be related to large earthquakes on the adjoining ridge segments, thus reflecting episodes of active plate movement.

Kanamori and Stewart (1976) noted that the waveforms for these two earthquakes required source time functions with unusually large rise times, thus indicating very low dislocation velocities of 23 cm/sec for the 1967 event and 18 cm/sec for the 1974 event. These values are nearly an order of magnitude lower than those previously reported for large earthquakes (e.g., Abe, 1974). Such slow particle velocities, and the implied low stress drops, for these earthquakes may be understandable if the region beneath the transform is actually composed of hot, intruded material which cannot support great stress and which slips in a partially viscous manner (Oka1 and Stewart, 1982). Such a model might suggest, however, that a large amount of slip would take place as aseismic creep, contrary to the conclusion that slip occurs regularly as faulting during earthquakes.

## TOTAL SEISMIC MOMENT

Because the transform is a plate boundary, we would expect that potential seismic moment is continuously generated by the relative motion between the plates. We can therefore compare the total moment from observed earthquakes to the moment rate calculated from the fault dimensions and the slip rate inferred from magnetic anomalies.

We have added the seismic moments for all of the earthquakes on the transform, using the  $M_0$  values given in Table 3.1. The total observed moment was  $1.25 \times 10^{27}$  dyne-cm. (Some of these events may have been normal faulting events on the spreading center between the two segments or on adjoining Mid-Atlantic Ridge segments, but since such events were generally quite small, they probably contributed very little to this total.) The largest contributions to this total came from the events in 1954, 1967 and 1974.

To this total moment sum we add a correction for the seismicity too small to be observed, using Formula (7) given in Molnar (1979)

$$\dot{M}_0^\Sigma = \frac{\alpha}{1 - \beta} M_0^{\max (1-\beta)} \quad (3.1)$$

where  $\dot{M}_0^\Sigma$  is the total rate of moment generation,  $M_0^{\max}$  is the maximum moment to be included in the summation, and  $\alpha$  and  $\beta$  are defined as

$$\alpha = 10^{(a+bd/c)} \quad \text{and} \quad \beta = b/c.$$

The quantities  $a$  and  $b$  are empirically determined values from the equation

$$\log N(M) = a - b M \quad (3.2)$$

where  $N(M)$  is the number of events with  $M_S > M$ , and  $c$  and  $d$  are empirically determined values from the equation

$$\log M_0 = c M_S + d. \quad (3.3)$$

In Chapter 9 we determine the values  $a = 1.7$ ,  $b = 0.37$ ,  $c = 1.18$ , and  $d = 18.6$ . For minimum  $M_0$  values of  $1.22 \times 10^{25}$  dyne-cm for the years from 1920 to 1963 and  $8.0 \times 10^{21}$  dyne-cm for the years from 1964 to 1981, we obtain unobserved moment rates of  $7.23 \times 10^{24}$  dyne-cm/yr and  $4.8 \times 10^{22}$  dyne-cm/yr, respectively, for these time periods. Since these time periods represent 44 yrs and 18 yrs, respectively, this means unobserved moment totals of  $3.2 \times 10^{26}$  dyne-cm and  $8.7 \times 10^{24}$  dyne-cm. Adding these values to the total observed seismic moment gives a total seismic moment of  $1.6 \times 10^{27}$  dyne-cm released by earthquakes on the two sections of the Gibbs transform since 1920.

From the transform dimensions and the slip rate we have determined the total seismic moment expected on these two transform sections since 1920, using  $M_0 = \mu L w D$  where  $\mu$  is shear modulus,  $L$  is fault length,  $w$  is fault width, and  $D$  is the total displacement for this 62 year period. For this estimate we used  $\mu = 3.5 \times 10^{11}$  dyne/cm<sup>2</sup>,  $L = 350$  km,  $w = 10$  km, and  $D = 143$  cm, calculated from the rotation vector given by Minster and Jordan (1978). The value of 10 km was used for width because that was the value used by Kanamori and Stewart (1976). The result is an expected seismic moment value of  $1.75 \times 10^{27}$  dyne-cm. This value is very close to the total moment value presented in the previous paragraph. This good agreement is not unexpected, since this calculation is almost equivalent to Kanamori and Stewart's (1976) comparison of calculated earthquake displacements to slip rate, the difference being that we included the smaller earthquakes in our moment sum. If we have chosen the fault dimensions correctly, this good agreement implies that most of the slip on the Gibbs transform occurs as earthquakes rather than aseismic creep.



## NORTH ATLANTIC TRANSFORM BEHAVIOR

The apparently unusual source parameters found by Kanamori and Stewart (1976) for the two most recent large earthquakes on the Gibbs transform urges similar investigations on other transform faults in the Atlantic. In later chapters of this work we characterize the seismic behavior of five other transforms in the North Atlantic by modeling the P waves from large transform earthquakes, and then we examine the seismicity of each transform in a way similar to that done here. The source quantities we derive for each event studied include focal depth, seismic moment, fault orientation, fault length, fault width (where possible), rise time, average displacement, average particle velocity, and average stress drop. (These parameters cannot all be determined with comparable precision.) One objective is to address the generality of results determined by Kanamori and Stewart (1976) for the Gibbs transform. Specifically, is the seismic behavior found on the Gibbs transform characteristic of other North Atlantic transforms? If not, what different styles of transform slip can we identify, and what properties of each transform determine how it behaves?

Table 3.1 Seismicity of the Gibbs Transform Fault

Date	Origin Time			Lat, °N	Lon, °W	h, km	$m_b$	$M_S$	No. of sta.	$M_0$ , $10^{25}$ dyne-cm
	h	m	s							
7/6/27	0	03	48	53	34			d		(1.6)
1/27/32	19	40	54	51.5	29.5			6		
2/28/33	22	19	24	51.5	30			d		
7/31/33	11	35	34	53	35			d		(1.6)
6/18/41	11	09	10	52	34.5			6.25		(8.7)
2/25/54	11	50	41	52.5	34.2	n		d		(1.6)
12/11/54	12	57	08	52.7	32.0	n		6.5		(17.)
3/28/55	0	59	07	52.9	34.9	n		d		(1.6)
6/11/56	8	22	06	52.3	31.8	n		5.5		(1.2)
6/5/57	7	16	17	52.8	35.0	n		5.6		(1.6)
3/2/60	21	56	25	52	30	n		5.5		(1.2)
4/30/61	7	33	53.5	52.0	31.9	38		5.6		(1.6)
6/1/64	13	24	6.1	52.6	35.0	33	4.4	(3.9)	18	(0.018)
8/17/64	22	47	31.4	52.03	30.09	25	5.0	(5.0)	63	(0.33)
8/26/64	3	18	43.7	52.12	30.12	28	5.2	d *	113	(1.6)
10/7/64	0	54	16.3	52.7	35.78	33	4.5	(4.1)	19	(0.031)
3/9/65	4	53	32.4	52.9	34.8	33	4.0	(3.2)	12	(0.0029)
7/3/65	2	22	18.1	52.73	32.05	30	5.3	(5.5)	113	(1.2)
7/3/65	5	40	58.0	52.8	32.1	33	4.0	(3.2)	12	(0.0029)
7/5/65	5	34	17.3	53.0	34.0	102	4.4	(3.9)	20	(0.018)
7/5/65	8	31	58.4	52.88	34.27	25	5.4	5.5 *	177	(1.2)
7/9/65	16	38	9.5	53.0	35.6	33	4.6	(4.3)	18	(0.053)
2/26/66	17	23	39	52.6	33.1	33	4.3	(3.7)	10	(0.011)
4/8/66	5	52	40.5	52.70	33.27	34	5.2	(5.3)	154	(0.72)
5/23/66	1	25	58.3	52.95	33.80	33	4.2	(3.6)	28	(0.0084)
5/23/66	1	29	1	52.77	33.97	101	4.6	(4.3)	45	(0.053)
11/27/66	7	00	48	52.6	34.0	33	4.4	(3.9)	18	(0.018)
2/13/67	23	14	22.3	52.82	34.25	17	5.6	6.5 **	312	34. ***
2/26/69	8	03	59	52.4	33.1		4.0	(3.2)	3	(0.0029)
9/24/69	3	58	55	52.97	32.06	35	5.3	(5.5)	53	(1.2)
9/24/69	3	58	58.0	52.61	32.01	28	5.2	(5.3)	170	(0.72)
9/24/69	4	20	51.3	52.6	31.83	18	5.3	(5.5)	179	(1.2)

Table 3.1 (cont'd)

Date	Origin Time h m s	Lat, °N	Lon, °W	h, km	$m_b$	$M_s$	No. of sta.	$M_0$ , $10^{25}$ dyne-cm
12/2/69	4 07 50	52.5	32.1	1	4.8	(4.6)	28	(0.12)
12/4/69	8 36 16	53.0	32.7	30	3.7	(2.7)	1	(0.0008)
1/31/70	4 23 0.2	52.29	31.75	33	4.4	(3.9)	21	(0.018)
5/18/70	1 30 6.2	52.27	30.13	31	4.9	(4.8)	137	(0.20)
5/13/72	13 58 50.2	52.84	35.26	33	4.1	(3.4)	22	(0.005)
11/14/72	17 51 59.4	52.8	35.8	0	4.4	(3.9)	10	(0.018)
5/27/73	21 25 6	52.9	35.3	0	4.1	(3.4)	6	(0.005)
8/7/73	20 33 33	52.57	32.2	49	4.3	(3.7)	54	(0.011)
12/5/73	17 57 11	52.63	31.39	18	4.7	(4.4)	100	(0.068)
3/23/74	16 17 56	53.0	32.1	0	4.4	(3.9)	9	(0.018)
6/7/74	19 17 16.8	52.7	35.08	0	4.5	(4.1)	12	(0.031)
10/16/74	5 36 26.5	52.64	32.15	23	4.8	(4.6)	122	(0.12)
10/16/74	5 45 11.2	52.71	32.00	41	5.7	6.9	355	45. ***
10/16/74	9 22 39.3	52.5	31.72	33	4.4	(3.9)	17	(0.018)
10/17/74	9 36 20	52.9	32.4	0			4	
10/17/74	15 36 47	52.65	34.2	65	4.4	(3.9)	19	(0.018)
11/16/74	19 24 14.1	52.64	32.15	26	4.9	4.9	172	(0.253)
11/17/74	7 39 57	52.76	31.87	84	4.3	(3.7)	38	(0.011)
11/21/74	21 43 18	52.23	31.59	20	4.7	(4.4)	73	(0.068)
11/21/74	23 16 30.5	52.2	31.6	33	4.1	(3.4)	13	(0.005)
4/12/75	4 35 4	51.9	30.5	33	4.3	(3.7)	14	(0.011)
4/12/75	13 18 29.4	52.13	30.20	33	4.7	4.1	56	(0.068)
7/17/75	11 42 41.5	52.83	34.92	23	4.4	3.9	43	(0.018)
3/26/77	0 32 4.5	52.03	30.22	33	4.5	(4.1)	37	(0.031)
10/23/77	19 26 26	52.8	31.3	33	4.4	(3.9)	27	(0.018)
10/24/77	5 58 27.1	52.19	31.54	26	5.0	(5.0)	197	(0.33)
4/10/79	10 32 59.5	52.23	31.79	42	4.8	4.6	123	(0.12)
7/2/79	20 45 4.9	52.39	31.67	10	3.9	(3.0)	22	(0.0017)
4/10/81	5 19 4.7	53.26	35.54	10	4.0	(3.2)	18	

\*  $M_s$  taken from Rothe (1969); other data taken from I. S. C. Regional Bulletin.

\*\*  $M_s$  taken from Kanamori and Stewart (1976); other data taken from I. S. C. Regional Bulletin.

\*\*\*  $M_0$  taken from Kanamori and Stewart (1976).

This table includes all events on the Mid-Atlantic Ridge between 51.5°N and 53.5°N, which includes the Gibbs transform fault. Data for the events before 1955 were taken from Gutenberg and Richter (1954). Data for events between 1955 and 1963 inclusive were taken from Rothe (1969). Data for events from 1964 to 1979 were taken from the ISC Regional Bulletin, while events in 1980 and 1981 were taken from P.D.E. reports of the U.S.G.S. For depth, n refers to "normal depth, (focus situated in the crust or at its base)", from Rothe (1969). We have taken magnitudes reported before 1964 as equivalent to  $M_S$ .  $M_S$  values shown in parentheses were determined from  $m_b$  using Equation 9.1. Except for those noted, other  $M_S$  values were taken from the same source as the other data for that event; d refers to a Gutenberg and Richter (1954) or Rothe (1969) listing as between 5.3 and 5.9, assumed here to be 5.6. The  $M_S$  values in parentheses were determined for all events whose  $M_S$  was not available from another source and whose location placed them on the Gibbs transform fault. The  $M_0$  values shown in parentheses were determined from  $M_S$  using Equation 9.2. These values in parentheses were determined for all events whose moment was not determined by Kanamori and Stewart (1976) and whose location placed them on the Gibbs transform fault.

Figure Captions.

Figure 3.1 Bathymetry of the Gibbs transform fault between  $51.5^{\circ}$  N and  $53.5^{\circ}$  N, and  $28.5^{\circ}$  W and  $37.0^{\circ}$  W, and epicenters of all known earthquakes in this area, taken from Table 3.1. The approximate locations of the ridge axes are indicated by double lines. Open circles represent epicenters taken from Gutenberg and Richter (1954) and Rothe (1969). Larger symbols are events with  $M_S > 6.0$ . Bathymetric contours, every 400 m, are taken from Uchupi (1982).

Figure 3.2 Longitude versus year of occurrence for the earthquakes on the Gibbs transform fault with  $M_S > 5.5$ .  $M_S$  is indicated for each event. Dashed lines indicate where the transform segments intersect spreading centers.

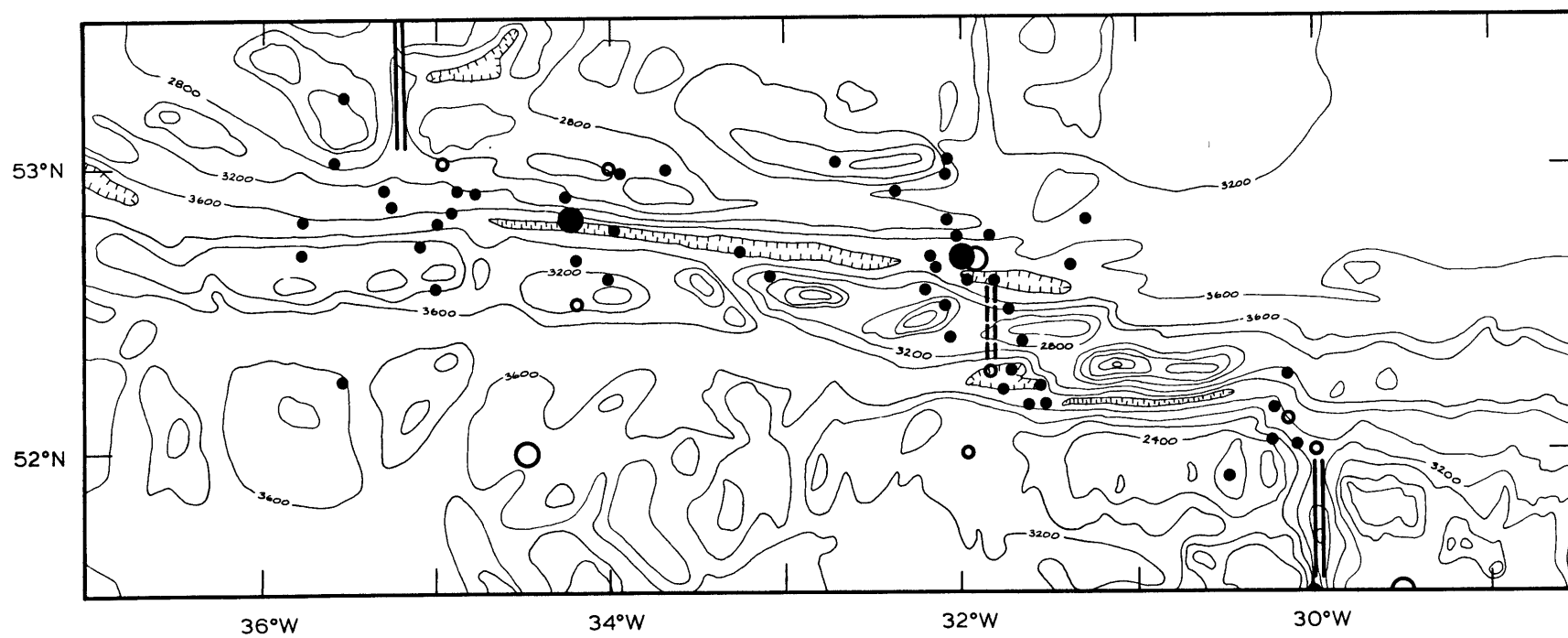


Fig. 3.1

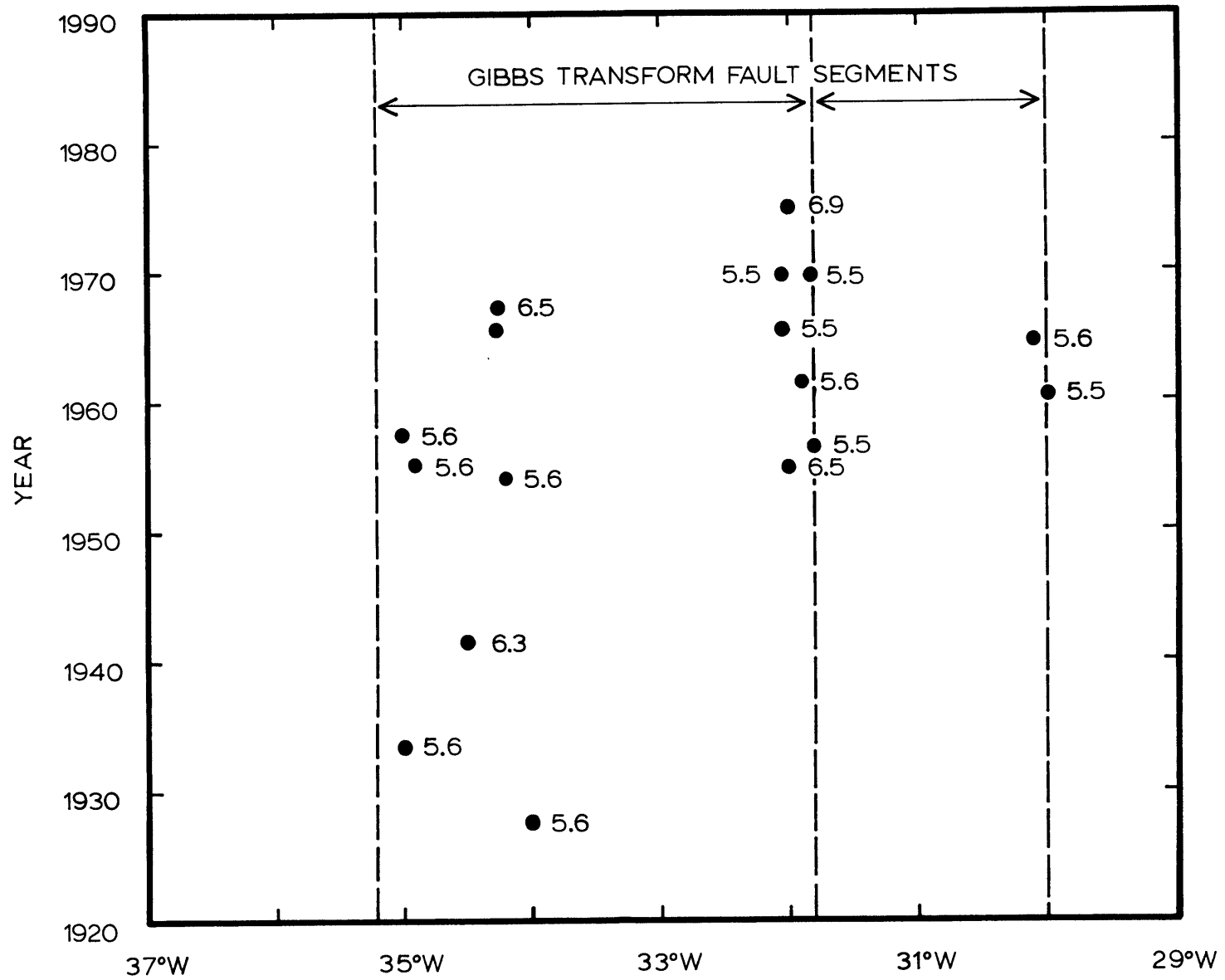


Fig. 3.2

## CHAPTER 4. EARTHQUAKES AND TECTONICS OF THE OCEANOGRAPHER TRANSFORM FAULT

The Oceanographer Fracture Zone offsets the Mid-Atlantic Ridge right-laterally by about 130 km near 35°N. Its existence as an east-west trending section of the Mid-Atlantic Ridge was first noted by Heezen et al. (1959). Sykes (1967) analyzed the first motion polarities of P waves from an earthquake which occurred on May 17, 1964 on the transform portion of the Oceanographer Fracture Zone. He showed that the motion was left-lateral strike slip on a nearly vertical fault and was therefore compatible with Wilson's (1965) concept of a transform fault. The area was surveyed in 1967 by the USCGS Oceanographer and in 1973 and 1974 by the R/V Vema. The results of the surveys were presented by Fox et al. (1969,1976) and by Schroeder (1977). The transform was also the subject of investigation by ALVIN and ANGUS, the results of which were presented by the Oceanographer Transform Tectonic Research Team (1980 a,b).

The bathymetry of the Oceanographer transform fault, shown in Figure 4.1 (Rogan, 1982), is characterized by a v-shaped valley which runs down the center of the transform, i.e., on a strike of roughly N 105° E, and by ridges which run parallel to and on each side of the the valley. The width of the valley below the 3000 m contour varies between 8 and 35 km, and the maximum depth varies between 3600 and 5000 m below sea level. At each end of the transform, where the transform intersects the adjoining ridge segment, there is a depression in the bathymetry of the basement. Similar depressions have been reported at the ends of other transform faults in the North Atlantic, e.g., the Kane transform fault, and are believed to be caused by the loss of hydrostatic pressure due to



the viscosity of the upward moving mantle material (Sleep and Biehler, 1970). The ridges which flank the transform valley rise to depths shallower than 2000 m below sea level, with the southern ridge higher in the west and the northern ridge higher in the east. Schroeder (1977) reports that when the effects of sediment are removed from the bathymetric data, the walls of the valley appear to be made up of scarps which vary in vertical offset from 100 to 1000 m. He suggests that these scarps are actually fault envelopes containing numerous fault planes which may dip very steeply; this inference is supported by direct observations of similar fault envelopes in the FAMOUS area (ARCYANA, 1975). The southern wall is dominated by a peak at its western end, near where the transform ridge merges with the eastern flank of the adjoining spreading center. This peak creates an apparent bend in the bathymetric trend of the transform valley and may be related to a source of seismic stress concentration at this point. A similar peak exists at the eastern end of the northern wall, though the trend of the transform valley is considerably less affected here than by its counterpart to the west.

Results of work with ALVIN and ANGUS in the transform valley, presented by the Oceanographer Transform Tectonic Research Team (1980a, b), suggest that the crust in the valley itself is thin, perhaps less than 1000 m thick. The results also showed that the walls of the valley exhibit apparently dip-slip faulting, creating a stair-step effect which determines the valley-wall topography, and that the zone of active strike-slip motion is only several hundred meters wide along the center of the valley floor.

## SEISMICITY

All known earthquakes on the Oceanographer transform fault are listed in Table 4.1, and the epicenters are shown in Figure 4.1. This list includes all earthquakes between  $34^{\circ}$  N and  $36^{\circ}$  N, and between  $34^{\circ}$  W and  $37.5^{\circ}$  W. The sources for the data in Table 4.1 were the same as for Table 3.1.

Several of the earthquake epicenters displayed in Figure 4.1 are considerably to the west of the western end of the active transform section. We believe that these events were mislocated. Events of this size and frequency represent a source of significant displacement, and would probably be accompanied by smaller events, yet ocean-bottom seismometer surveys of the microearthquake seismicity at other ridge-transform intersections, including the eastern end of the Oceanographer transform (e.g., Rowlett, 1981), show very little or no seismicity on the inactive side of ridge-transform intersections. We suspect that the epicenters in Figure 4.1 to the north and south of the Oceanographer transform occurred on the smaller transform segments just to the north and south of the Oceanographer transform, and that the sections of the Mid-Atlantic Ridge adjacent to the Oceanographer transform have been seismically quiet for events of  $m_b \gtrsim 4$ .

There are seven events in Table 4.1 with  $M_S > 5.5$  whose locations indicate that they occurred on the Oceanographer transform. Figure 4.2 shows the longitudes of the epicenters of these events plotted versus year of occurrence. The largest event observed on the Oceanographer transform ( $M_S = 6.4$ ) occurred on May 17, 1964, along the same part of the transform as, and only 5 years after, the then largest known event ( $M_S = 6.2$ , on March 19, 1959), which had been preceded by only 15 months by another large event ( $M_S = 6.0$ , December 23, 1957). Prior to that there had been only one event as large as  $M_S = 6.0$ , that of December 4, 1932.

The apparent gap in seismicity between 1932 and 1955, (and between 1932 and 1957, if we look only at events with  $M_S = 6.0$ ) is interesting, in that it suggests that the rate of seismic slip on the transform is not constant on a time scale equal to the length of time for which we have seismic records. This differs from Kanamori and Stewart's (1976) conclusion that the Gibbs transform slips at regular intervals, with similarly sized earthquakes. In Chapter 9, we will discuss this feature in the behavior of all of the transforms studied here.

Sykes (1967) prepared a fault-plane solution for the May 17, 1964 earthquake from P wave first motions, which showed left-lateral strike-slip motion on a nearly vertical fault-plane with a strike of  $86^\circ$ . Weidner and Aki (1973) inverted Rayleigh wave amplitude and phase spectra for this event and found a similar fault-plane solution but with a fault strike of  $91^\circ$ , a seismic moment of  $1.94 \times 10^{25}$  dyne-cm, and a focal depth of  $6 \pm 3$  km below the sea floor. Figure 4.3 shows the fault-plane solutions obtained by both Sykes (1967) and Weidner and Aki (1973).

#### THE MAY 17, 1964 EARTHQUAKE

We have studied the May 17, 1964 event by computing synthetic P wave seismograms using the method described in Chapter 2 for comparison to the observed P wave seismograms from 20 WWSSN stations. Observed records were digitized over a time length large enough to include that entire portion of the P wave, generally about 60 sec. Synthetic seismograms were then constructed to provide a visual match to the observed seismograms, with particular attention given to predominant periods, slopes of rising and falling portions of the waveforms, and the existence and shape of any features in the early portion of each waveform. Features after about 10 sec into the observed waveforms were ignored

because they were probably influenced by water reflections which we did not include in our synthesis. The source structure used for the synthetic seismograms is given in Table 4.2. This structure, with a slightly thinner than normal oceanic crust, was taken from the refraction survey of Ludwig and Rabinowitz (1980) in the Vema Fracture Zone.

Station data for the earthquake are given in Table 4.3.

The results of the synthesis, and the fault-plane solution used to calculate the synthetic seismograms, are shown in Figure 4.4, along with the position of each station used on the lower focal hemisphere. The most significant feature of the seismograms for this event is that the waveforms recorded at the stations in the western hemisphere look quite different from those recorded at stations in the eastern hemisphere. Except for station BEC, the waveforms observed to the west all had a double-peaked initial pulse, and many also had a small precursory phase ahead of the main arrival. The waveforms observed to the east all had a smooth, highly emergent initial pulse, and a predominant period of this pulse perhaps 50% longer than those observed to the west. These features must of course be reflected in the parameters used to construct synthetic seismograms, so that the source time function used for each hemisphere should be different. In our synthetic seismograms we obtained the double-peak waveforms for the western hemisphere stations by making the focal depth sufficiently large that the P phases separated from the pP and sP phases. The longer, smoother waveforms observed to the east were then produced in our synthetic seismograms by making the rupture propagation unilateral from east to west, resulting in a merging of the double peaks into one.

We also considered an alternate set of fault parameters for these

waveforms by using a multiple source, with a second source located to the east of and later than the first. We discuss this alternate source discription later in this chapter.

The fault-plane solution shown in Figure 4.4 has a fault strike of N 97° E, a dip of 89.5° to the north, and a slip angle of 4°, using the convention of Kanamori and Stewart (1976). The fault strike was originally chosen to be N 97° E because that is close to the average strike of the active part of the transform. However a change in the strike of only 5° in either direction makes it difficult to obtain simultaneous fits of the waveforms for more than just a few stations. For stations in North America better fits of the waveforms could generally be obtained by decreasing the dip, thus moving the fault plane closer to the emergent directions of the rays to these stations. The limiting factors to this are the waveforms and amplitudes observed at SHA and ATL, for which compressional first-arrivals must be maintained, and for which the amplitudes of the synthetic seismograms become too small if the dip is decreased too much. The synthetic seismograms calculated for both of these stations show the effects of this compromise. The fit of the waveform for BEC could be improved by moving the dip of the fault plane the other direction, so that it dips to the south. However this would cause a deterioration in the fits for most of the North American stations. (We suspect that the poor fit obtained for BEC may be due to the proximity of the station to the epicenter.) We have given the dip to a precision of 0.5°, because that was necessary to obtain a satisfactory fit at SHA and ATL. However since emergent angles depend on the poorly known velocity structure, the actual uncertainty on the dip of the fault plane is probably closer to  $\pm 5^\circ$ , even though the relative angle between

rays and fault plane is more constrained. The slip angle can be varied about  $3^\circ$  in either direction from that given without significant variation in the synthetic waveforms, other than a change in the relative amplitudes for stations to the east compared with those to the west.

The depth we found for this event was 4.0 km below sea floor. This value is similar to that found by Weidner and Aki (1973), who placed this event at 6 km below sea floor, but admitted a range of 3 to 10 km. The value determined here is more precise because the synthetic P waveforms vary strongly with changes in depth of only a kilometer, while the surface wave radiation pattern from a strike-slip earthquake is relatively insensitive to changes in depth within the upper 10 km of a typical ocean floor structure. Figure 4.5 shows two synthetic seismograms calculated for the same station for this event, one using a focal depth of 4.0 km below sea floor and the other using a depth of 5.0 km below sea floor, with other parameters held constant. To some extent, the effect on the waveform of increasing the focal depth can be compensated by increasing the fault length and rise time so that the shape of the source time function and the ratio of its length to the delay times of the pP and sP phases is constant. While this will maintain a constant waveform shape, it will change the predominant periods of the waveform, in this case making the waveform too long. We believe that the depth presented here is precise to about  $\pm 1$  km, subject to the velocity structure used.

The rise time used was 1 sec. Propagation was taken to be horizontal and unilateral, east to west, in order to reproduce the difference between the observed seismograms from the eastern and western hemispheres. The rupture propagation velocity used was 4 km/sec rather

than the more commonly used value of 3 km/ sec. With a fault length of 12 km, a rupture velocity of 3 km/sec would have lengthened all of the source time functions by 1 sec, thus requiring either a shorter fault length incompatible with the observed difference between waveforms to the east and the west, or a much shorter (i.e., zero) rise time, or a zero fault width, or some combination of these effects. Though we obtained our fits with the value of 4 km/sec, we do not claim to have determined rupture propagation velocity, and we recognize that this value is greater than the shear wave velocity in the crust. The overall length of the source time functions necessary to match the observed seismograms was about 3 to 3.5 sec to the west and about 4.5 to 5 sec to the east; an increase in either the rise time or fault dimensions, or a decrease in the propagation velocity, would have made the source time functions unacceptably long.

If we assume completely unilateral propagation, we can constrain the fault length because the difference between eastern and western time functions is proportional to the fault length. The fault length which gave the best fits between observed and synthetic seismograms was 12 km, with a subjectively-determined uncertainty of about  $\pm 2$  km. As discussed in Chapter 2, it is possible that there was a bilateral component to the rupture even though the propagation was primarily unilateral. If so, the actual fault length may have been somewhat larger, though probably less than twice as large. The width was set at 5 km because a larger value, say, 10 km as used by Kanamori and Stewart (1976), produced source time functions which were too long. This value for width is compatible with the depth determined (4 km below sea floor) in that we might expect

rupture to extend at least from the point of origin upward to include the top of the igneous crust, and possibly downward also. Since the fault plane is nearly vertical, the effect of this fault width is to add approximately 1 sec to the length of the source time function for all stations. The effect of minor variations in the fault width could easily be absorbed by variations in the rise time or propagation velocity, and thus width is not well-constrained.

The observed difference in the waveforms from east to west could not be explained by a difference in attenuation using bilateral propagation. Increasing the value of  $t^*$  for stations to the east lengthens the waveforms but not nearly enough to match the observed waveforms. In addition, an increase in  $t^*$  smooths out the details in the region of maximum displacement of the first motion so that the synthetic waveforms are not nearly as "peaky" as the observed ones. With the values used for these synthetic seismograms we were able to match not only the "peakiness" and predominant period but also the general asymmetry in the maximum amplitude portion of the first motion in all of the observed seismograms from stations in the eastern hemisphere. We were unable to match the slow emergence of the waveforms at the eastern stations.

We found a seismic moment for this event of  $8.3 \times 10^{25}$  dyne-cm, a value somewhat greater than the  $1.94 \times 10^{25}$  dyne-cm found by Weidner and Aki (1973). Table 4.3 gives the values of moment found for each station. The  $2\sigma$  lower limit for  $M_0$  was  $1.7 \times 10^{25}$  dyne-cm and the upper limit for  $M_0$  was  $4.0 \times 10^{26}$  dyne-cm. One station, SHA, was considerably outside of the  $2\sigma$  range, i.e., differing by a factor of 12.3 compared to the  $2\sigma$  error of a factor of 4.8. (If the value for SHA is discarded, the moment for this event reduces to  $7.1 \times 10^{25}$  dyne-cm.) This error was probably



due to the proximity of the ray path to one of the nodal planes, where the amplitudes vary most rapidly with changes in the relative angle between ray and nodal plane; the amplitudes for such stations are strongly dependent on the velocity structure used, as the emergent angles vary with velocity at the source. All of these values are larger than the  $M_0$  value found by Weidner and Aki (1973), though their value is slightly inside of the  $2\sigma$  range presented here.

As explained in Chapter 2, the seismic moment value is susceptible to other errors than the statistical scatter discussed above. Of particular concern is the dependence of maximum amplitude on the phasing of the P, pP, and sP. In synthesizing a double peak for the stations to the west, we required a depth so that the pP and sP phases, which arrived close enough together compared to the signal length that they acted as one phase, to begin motion in the same direction as the initial motion of the P phase just after the P phase had begun to change direction. This destructive phasing influences amplitudes in a way strongly dependent on the depth and signal length. Another serious source of error is the inverse proportionality of the calculated amplitudes on the cube of the seismic velocity at the source.

Using the above values for scalar moment and fault dimensions, and using a value for shear modulus  $\mu$  of  $3.5 \times 10^{11}$  dyne/cm<sup>2</sup>, we calculate that the average displacement for this event was about 4 m. Dividing this by the rise time of 1 sec produces a dislocation velocity of 4 m/sec. This value is close to the range of previously reported dislocation velocities (Brune, 1970; Kanamori, 1972; Abe, 1974), and does not agree with the exceptionally low dislocation velocities (0.1 to 0.2 m/sec) determined by Kanamori and Stewart (1976) for two large events on the Gibbs transform.

Our value of dislocation velocity is determined to no better than a factor of 2 however, because the value for rise time could be varied between 0.5 and 1.5 sec without significant change in the synthetic seismograms.

Since the values of displacement and dislocation velocity were determined from the fault dimensions and total moment, which have their own uncertainties, we have confidence only in the order of magnitude determined for dislocation velocity.

We have determined the stress drop for this earthquake using the formula described in Chapter 2 for a strike-slip event,

$$\Delta\sigma = \frac{2}{\pi} \mu \frac{D}{W} . \quad (2.10)$$

We used the calculated displacement value presented earlier and those values for  $\mu$  and fault width used for the synthetic seismograms. We obtained a stress drop of about 200 bars, which is high compared to the range of stress drops presented by Kanamori and Anderson (1975) for inter-plate events. Since stress drop is proportional to seismic moment, if our moment value is too large, as suggested by the discrepancy between our value and that of Weidner and Aki (1973), our stress drop value might be too large also. With this formula, for any given moment and fault length, the stress drop is inversely proportional to the square of the fault width. Thus imprecision in the fault width by, say, a factor of 2, would mean the stress drop could be anywhere between 50 bars and 800 bars.

The suggestion of high stress drop and unilateral propagation on a 12 km fault is noteworthy considering the teleseismic location of the event, which placed it just north of an irregularity in the bathymetry about 15 to 20 km east of the western end of the transform; see Figure 4.1. (The epicenter may have been mislocated to the north because of a large number

of seismic stations whose azimuths were to the north.) This bathymetric feature may be related to a local stress concentration or asperity on the transform. (Two of the three preceding large earthquakes on the Oceanographer Fracture Zone (1957 and 1960) were located east of the 1964 epicenter, and may have released the strain on those sections of the fault. (Why the 1960 event did not similarly release the strain in the vicinity of the 1964 epicenter is not clear.) Our interpretation is that the 1964 event began at a stress concentration or fault asperity related to the local bathymetry and propagated westward toward the junction of the fault and the adjoining ridge segment.

As mentioned earlier, we were able to generate waveforms similar to those observed by using a very different set of source parameters. For this we placed the focal depth right at sea floor, so that the P, pP, and sP phases were not separated in time. We then modeled the double peak observed in the western hemisphere by using a multiple source, with a second source located to the east of and later than the first. By adjusting the spatial and temporal separations we were able to create two peaks to the west by having the arrivals separated while the two signals arrived simultaneously to the east. We computed synthetic seismograms for two stations, STU to the east, and OGD to the west. The results are shown in Figure 4.6. For these seismograms we assumed bilateral faulting on faults which were each 7 km long, a rupture propagation velocity of 3 km/sec, fault strikes of  $95^\circ$ , dips of  $90^\circ$ , slip angles of  $0^\circ$ , fault widths of 5 km, and rise times of 0.5 sec. The second source was located 7 km east of the first, on an azimuth of  $N 95^\circ E$  relative to the first, and occurred 2.5 sec later. The moment for the second source was set at twice that of the first. The synthetic waveforms do not fit those observed as

well as do those prepared from a single source, in that the synthetic waveform is too long for OGD and too short for STU. It was difficult to correct both of these problems simultaneously. For this reason and because the two additional parameters create too many degrees of freedom to allow any real precision in the results, we did not try to generate synthetic seismograms for other stations. We present this result to illustrate that the observed waveforms could be explained (although not necessarily equally well) by at least two source models. In the single source model, the propagation is continuous from east to west, while in the double source model, propagation is discrete, from west to east.

#### THE NOVEMBER 18, 1970 EARTHQUAKE

Figure 4.7 shows a fault plane solution, constructed from both P-wave polarities and S-wave polarization angles, for the event which occurred on the Oceanographer transform on November 18, 1970 ( $m_b = 5.1$ ). This fault plane solution is quite similar to that of the 1964 event; in fact, the polarities in Figure 4.7 can be accommodated very well by the same fault plane solution as that found for the 1964 event.

The 1970 event also displayed some form of "precursory" (or multiple event) activity. For example, the short period, vertical seismogram for station DUG (epicentral distance  $59.3^\circ$ , azimuth  $300^\circ$ ) showed the arrival of a small signal, followed by a larger signal about 5 sec later. The travel-time residual for DUG listed by I.S.C. for this event was -5.1 sec, almost exactly the time difference between the two arrivals. This suggests that the epicenter and origin time determined by I.S.C. for this event probably corresponded to this second arrival, implying that many stations must have reported the second arrival and not the first. A histogram of the residuals reported by I.S.C. for their epicenter is shown

in Figure 4.8. For most events in the North Atlantic, the scatter is generally only a few seconds. Large scatter could result if two (or more) signals arrived at most stations, but because of differing amplitudes, some stations reported the first arrival time while others reported a later one. Such might be the case with two nearly simultaneous events separated by perhaps 50 km; however, this could also be the result of source finiteness creating different ratios of P, pP, and sP amplitudes for stations in different directions.

We have calculated synthetic P-waves, using the method presented in Chapter 2, for comparison to observed seismograms from 3 WWSSN stations for this earthquake. Only one of these stations (CAR) had an epicentral distance greater than  $30^\circ$ , and we therefore did not use the waveforms from the other two stations to constrain our results. It was, in fact, impossible to match all three waveforms simultaneously. Station data are given in Table 4.4, and the results of the synthesis are given in Figure 4.9. For these calculations we used the velocity structure given in Table 4.2. The fault plane solution found and the location on the lower focal hemisphere of the stations used are also shown in Figure 4.9. We used a fault strike of  $N 98^\circ E$ , a fault dip of  $90^\circ$ , i.e., a vertical fault, and a slip angle of  $180^\circ$ . This fault plane solution represents right-lateral strike-slip motion, and is similar to that shown in Figure 4.7.

Since we had only one station whose waveforms we trusted, we used bilateral horizontal rupture, rather than unilateral rupture as was required with the May 17, 1964 earthquake. We also used a more conservative rupture speed of 3 km/sec, on a fault that was 6 km long and 5 km wide. Focal depth was set at 10.5 km below sea level, or 6.5 km below the sea floor, placing this event slightly below the base of the

crust. This depth, with the fault dimensions given above, reproduced in the synthetic waveforms the detailed character of the observed waveform for station CAR. This depth is also sufficient to account for multiple arrivals observed in short-period, vertical seismograms, e.g., DUG, mentioned earlier. The seismic moment necessary to match the amplitudes for station CAR for this earthquake was  $9.5 \times 10^{24}$  dyne-cm. As will be shown in Chapter 9, this value is probably high considering the size of the event. This moment, with the fault dimensions used, produced an average displacement of 0.9 m. Since we used a rise time of 1 sec, this means a particle velocity of 90 cm/sec. None of these source parameters can be considered to be uniquely determined.

#### TOTAL SEISMIC MOMENT

Using the method explained in Chapter 9, we have calculated moments from the  $M_S$  values for all of the earthquakes listed in Table 4.1 which we believe occurred on the Oceanographer transform and for which we have not determined a moment value here. These values are given in parentheses in Table 4.1. Summing the moment values given in Table 4.1 gives us a value of  $3.5 \times 10^{26}$  dyne-cm for the total observed seismic moment since about 1920 (about the earliest events listed by Gutenberg and Richter, 1954).

To this moment sum we add a correction for the seismicity too small to be observed, using Formula (7) given in Molnar (1979), Equation 3.1 in this work. For this we use  $a = 1.8$ ,  $b = .47$ ,  $c = 1.18$ , and  $d = 18.6$ ; these values are determined in Chapter 9. For minimum  $M_0$  values of  $1.58 \times 10^{25}$  dyne-cm for the years from 1920 to 1963 and  $1.1 \times 10^{23}$  dyne-cm for the years from 1964 to 1981, we obtain unobserved moment rates of  $4.32 \times 10^{24}$  dyne-cm/yr and  $2.18 \times 10^{23}$  dyne-cm/yr, respectively, for these

time periods. Since these time periods represent 44 yrs and 18 yrs, respectively, this means unobserved moment totals of  $1.9 \times 10^{26}$  dyne-cm and  $3.9 \times 10^{24}$  dyne-cm. Adding these values to the total observed seismic moment gives a total seismic moment value of  $5.4 \times 10^{26}$  dyne-cm released by earthquakes on the Oceanographer transform since 1920. A little less than one third of this total was released by only two earthquakes, those of March 19, 1959, and May 17, 1964.

From the transform dimensions and the slip rate we have determined the total seismic moment expected on these two transform sections since 1920, using  $M_0 = \mu L w D$  where  $\mu$  is shear modulus,  $L$  is fault length,  $w$  is fault width, and  $D$  is the total displacement for this 62 year period. For this we used  $\mu = 3.5 \times 10^{11}$  dyne/cm<sup>2</sup>,  $L = 130$  km,  $w = 5$  km, and  $D = 150$  cm, calculated from the rotation vector given by Minster and Jordan (1978). We used 5 km for width because that was the value we used in the synthetic seismograms for the May 17, 1964 event. The result is an expected seismic moment value of  $3.4 \times 10^{26}$  dyne-cm.

This value is only slightly less than the total moment value presented in the previous paragraph, a result which suggests that most of the slippage on the transform occurs as earthquake activity. However the near equality between expected and observed total moments should not be judged as too significant, since there are several sources of uncertainty in these values. One uncertainty is the value of the expected moment calculated from slip rate. The least well known quantity in this is probably the fault width, which we may have chosen incorrectly by a factor or 2. If the seismic thickness for the whole transform is not uniform, and the average is therefore different from the 5 km we found for one earthquake, our expected moment sum would be in error. There is, in

addition, the uncertainty in the moment values determined for each earthquake.

#### IMPLICATIONS FOR THE OCEANOGRAPHER TRANSFORM

From the observations presented in this chapter we can draw some inferences in general about the seismic processes occurring on the Oceanographer transform fault, and in particular about the largest event observed on the transform. The 1964 earthquake was definitely strike-slip, with a vertical fault plane whose strike was parallel to the topographically-inferred direction of the transform. The rupture propagation of this earthquake was primarily, if not completely, unilateral, with the predominant direction from east to west, though west to east propagation is also possible if the event were composed of two (or more) discrete sources. The depth of this earthquake was  $4 \pm 1$  km below the sea floor if the source was a single event, placing the focus near the base of the crust; a greater focal depth can be excluded while a shallower depth, e.g., at the sea floor, is possible if the rupture were of the discrete west-to-east type mentioned above. Stress drop, displacement, and dislocation velocity for this event do not appear to have been particularly abnormal for events of this size. Comparison of this event to the events on the Gibbs transform fault studied by Kanamori and Stewart (1976) shows this one to be more "normal"; the events on the Gibbs transform required source time functions with total lengths of 17 and 22 sec, implying low stress drops and low dislocation velocities. A source time function this long is incompatible with the P waveforms observed for this event, for which the source time functions were in the range of 4 to 5 sec.

One implication of the 1964 event is that the Oceanographer transform fault releases its slip in a jerky manner. This event had a displacement



of about 4 m, while the displacement calculated from the slip rate for the last 62 years is only about 1.5 m. While there is significant imprecision in the displacement calculated for the 1964 event, the actual displacement for this event was probably much larger than that expected from the slip rate. These figures suggest that the repeat time for an earthquake similar to the 1964 event on this part of the transform is about 170 years, and a recurrence time for large events ( $M_S > 6.0$ ) on the whole transform is about 15 to 20 years. This last result is supported by the seismicity listed in Table 4.1, which shows 4 events with  $M_S > 6.0$  since 1920. The short (12 km) fault length for the 1964 event is considerably less than the transform length, which allows for a large number of events to take place before this section of the transform fractures again. Three of the four events with  $M_S > 6.0$  listed in Table 4.1 occurred between 1957 and 1964, though their epicenters were separated by only  $0.3^\circ$  of longitude. If the fault lengths for the first two events were more than 10 to 15 km, then such close proximity of three large events in space and time would not be possible unless either (1) each one did not completely release the strain on that part of the transform, or (2) the rate of slip on the transform is extremely uneven. We consider both of these possibilities unlikely, and, considering the short time functions necessary to match the observed waveforms, believe that short, non-overlapping fault lengths are the best explanation. We observed this sort of behavior on the  $15^\circ 20'$  transform as well (see Chapter 6).

In all, the transform has not slipped uniformly in the last 62 years. While there has been fairly steady background seismicity, there have been only a few events large enough to release a significant amount of strain, of which the 1964 event was probably the largest. If a fault length of about 12 km is representative of the earthquakes on the Oceanographer

transform with  $M_S > 6.0$ , then there have only been enough of these events to fracture less than half of the transform length since 1920.

Table 4.1. Seismicity of the Oceanographer Transform Fault

Date	Origin Time h m s	Lat, °N	Lon, °W	h, km	$m_b$	$M_s$	No. of sta.	$M_0, 10^{25}$ dyne-cm
7/3/26	18 09 53	35.5	36			d		(1.6)
12/4/32	4 04 00	35.5	36.5			6		(4.5)
5/6/55	11 39 58	35.3	36.8			d		(1.6)
2/10/57	5 47 59	35.5	34.6			5.8		
12/23/57	12 34 08	35.2	35.8			6		(4.5)
3/19/59	8 25 32	35.1	36.1			6.2		(7.6)
6/8/60	16 19 48	35.0	35.0			5.9		(3.5)
5/17/64	19 26 21.6	35.35	36.08	33	5.6	6.3 *	210	8.3
8/16/65	4 36 37.1	35.4	35.75	16	4.6	(4.3)	71	(0.053)
8/16/65	19 53 18.3	35.2	35.1	52	4.7	(4.4)	49	(0.068)
8/17/65	0 22 25.5	35.0	35.0	33	4.4	(3.9)	28	(0.018)
7/15/66	2 26 15.4	35.4	36.35	33	4.6	(4.3)	24	(0.053)
12/12/67	11 50 08	35.0	35.3	33	4.3	(3.7)	10	(0.011)
5/2/68	7 33 50	35.8	35.3		4.0		4	
7/21/69	17 38 29.8	35.35	36.05	33	4.9	4.8	101	(0.195)
8/4/69	13 47 00.0	35.60	36.58	33	4.7	(4.4)	20	(0.068)
11/5/70	20 36 14	34.78	37.09	54	5.0		45	
11/18/70	12 23 15.6	35.14	35.90	18	5.1	(5.1)	218	0.95
7/2/71	3 35 49.2	35.32	36.39	33	4.7	(4.4)	82	(0.068)
6/17/72	6 00 4.4	35.27	35.45	0			10	
7/5/72	4 06 13.0	35.47	36.61	26	4.4	(3.9)	36	(0.018)
11/26/72	8 00 42.1	35.40	36.46	25	5.0	(5.0)	71	(0.329)
5/8 73	0 26 11.9	35.78	34.62	33	4.0		13	
2/2/74	3 37 26	35.65	34.51	41	4.9		77	
3/6/74	5 11 04.1	35.00	35.24	33	4.4	(3.9)	15	(0.018)
3/10/74	20 14 42.6	35.3	37.5	33	4.5	(4.1)	12	(0.031)
4/17/74	0 32 21.4	35.2	35.37	28	5.0	5.0	136	(0.33)
9/9/74	17 58 10	34.6	36.63	56	5.0	4.5	42	
5/24/75	2 37 38.9	34.4	36.84	33	4.6		12	
3.26.76	11 08 09	35.5	34.2	33	4.7		27	
1/16/77	10 34 54.2	35.44	37.07	10	4.9	(4.8)	56	(0.20)
3/28/77	13 00 16	34.69	36.75	28	4.8		41	
4/29/80	16 02 45.6	35.32	36.33	10	5.1	4.7	88	(0.15)
7/14/80	4 24 24.4	35.14	35.45	10	5.2	5.1	105	(0.43)
1/9/81	7 51 28.3	35.18	35.21	10	4.9	5.0	33	(0.33)

\*  $M_s$  value taken from Rothe (1969), other data taken from I. S. C. Regional Bulletin.

(Table 4.1, cont'd)

This table includes all events on the Mid-Atlantic Ridge between 34°N and 36°N and 34°W and 37.5°W, which includes the Oceanographer transform fault. Data for the events before 1955 were taken from Gutenberg and Richter (1954). Data for events between 1955 and 1963 inclusive were taken from Rothe (1969). Data for events from 1964 to 1979 were taken from the ISC Regional Bulletin, while events in 1980 and 1981 were taken from P.D.E. reports of the U.S.G.S. We have taken magnitudes reported before 1964 as equivalent to  $M_S$ .  $M_S$  values shown in parentheses were determined from  $m_b$  using Equation 9.1. Except for those noted, other  $M_S$  values were taken from the same source as the other data for that event; d refers to a Gutenberg and Richter (1954) or Rothe (1969) listing as between 5.3 and 5.9, assumed here to be 5.6. The  $M_S$  values in parentheses were determined for all events whose  $M_S$  was not available from another source and whose location placed them on the Oceanographer transform fault. The  $M_0$  values shown in parentheses were determined from  $M_S$  using Equation 9.2. These values in parentheses were determined for all events whose moment was not determined in this study and whose location placed them on the Oceanographer transform fault.

Table 4.2. Source structure used for synthetic seismograms for all events except the one on March 12, 1977.

	<u>Layer</u>	<u>Thickness, km</u>	<u><math>V_p</math>, km/sec</u>	<u><math>\rho</math>, g/cm<sup>3</sup></u>
1.	crust	2.2	4.3	2.8
2.	crust	2.6	5.9	2.8
3.	mantle	Half-space	7.8	3.2

$V_p$  is P wave velocity,  $\rho$  is density. This structure was determined by Ludwig and Rabinowitz (1980) for the Vema Fracture Zone.

Table 4.3. Station data used for synthetic seismograms  
for the earthquake of May 17, 1964.

Station	Distance, degrees	Azimuth, degrees	Magnification	$10^{25} M_0$ , dyne-cm
BEC	23.9	271.1	1500	16 *
MAL	25.6	77.6	750	8.1 *
TOL	25.7	70.3	1500	5.6 *
ESK	30.1	38.2	1500	5.0
OGD	30.6	292.4	3000	7.2
SCP	33.1	292.2	750	8.8
STU	35.7	53.7	750	4.4
AAM	37.3	295.4	1500	7.6
CAR	37.4	236.2	3000	4.9
KON	38.2	36.0	1500	2.8
TRI	38.7	59.0	3000	4.9
ATL	39.6	281.6	1500	15
FLO	42.9	291.3	1500	10
SHA	43.5	279.2	1500	102
MNN	43.9	300.6	3000	5.3
RCD	51.1	301.4	750	16
ALQ	56.4	291.7	3000	5.4
BOZ	56.4	305.3	3000	7.8
TUC	60.7	290.5	1500	17
BKS	66.7	300.7	3000	6.8

\*  $M_0$  values not used to find "average" for this event.

For all stations we used  $T_p = 30$  sec,  $T_g = 100$  sec,  $H_p = .93$ ,  $H_g = 1.0$ , where  $T_p$ ,  $T_g$ ,  $H_p$ , and  $H_g$  refer to the seismometer and galvanometer periods and damping factors, respectively.

Table 4.4. Station data used for synthetic seismograms  
for the earthquake of November 18, 1970.

<u>Station</u>	<u>Distance, degrees</u>	<u>Azimuth, degrees</u>	<u>Magnification</u>	$10^{25} \overset{M_0}{\text{dyne-cm}}$
MAL	25.5	77.2	1500	1.5 *
TOL	25.6	69.9	1500	1.9 *
CAR	37.4	236.6	3000	.95

\*  $M_0$  values not used to find "average" for this event.

For all stations we used  $T_p = 15$  sec,  $T_g = 100$  sec,  $H_p = .93$ ,  $H_g = 1.0$ , where  $T_p$ ,  $T_g$ ,  $H_p$ , and  $H_g$  refer to the seismometer and galvanometer periods and damping factors, respectively.

### Figure Captions

Figure 4.1 Bathymetry of the Oceanographer transform fault between  $34^{\circ}$  N and  $36^{\circ}$  N, and  $34^{\circ}$  W and  $37.5^{\circ}$  W, and epicenters of all known earthquakes in this area, taken from Table 4.1. The approximate locations of the ridge axes are indicated by double lines. Open circles represent epicenters taken from Gutenberg and Richter (1954) and Rothe (1969). Larger symbols are events with  $M_S > 6.0$ . Contour intervals are every 1000 m below sea level, taken from Rogan (1982).

Figure 4.2 Longitude versus year of occurrence for the earthquakes on the Oceanographer transform fault with  $M_S > 5.5$ .  $M_S$  is shown for each event. Dashed lines indicate where the transform intersects adjacent spreading centers. The bar for the 1964 event indicates the fault length and propagation direction used for the synthetic seismograms.

Figure 4.3 Fault plane solutions for the May 17, 1964, Oceanographer transform earthquake, obtained by Sykes (1967) (solid line) and Weidner and Aki (1973) (dashed line).

Figure 4.4 Results of fits of synthetic (upper) to observed (lower) seismograms of P waves from the May 17, 1964 earthquake. Positions on lower focal hemisphere of stations used for synthesis and fault plane solution obtained are also shown. Closed circles for station locations represent compressional first-arrival polarities, open circles represent dilatational polarities. The vertical scales were normalized so that all seismograms would have equal maximum amplitudes.

Figure 4.5 Synthetic P-wave seismograms for the May 17, 1964 earthquake, calculated for station OGD using focal depths of 8 km and 9 km below sea level (4 and 5 km below sea floor), keeping other parameters



constant, and using the source velocity structure for the Kane Fracture Zone given in Table 5.2. A comparison of this figure to Figure 4.4 (station OGD) shows the effect of changing the velocity structure.

Figure 4.6 Synthetic seismograms for the May 17, 1964 earthquake, calculated for stations STU and OGD using a double source. Fault parameters are described in the text.

Figure 4.7 Fault plane solution for the earthquake of November 18, 1970 on the Oceanographer transform fault, obtained from P wave first motions and S wave polarities. Open circles represent dilational arrivals; closed circles represent compressional arrivals. Smaller symbols represent questionable readings. Arrows represent the direction of S wave polarization. Arrows pointing inward represent downward SV motion; arrows pointing outward represent upward SV motion.

Figure 4.8 Histogram of P-wave residuals reported by I.S.C. for the earthquake of November 18, 1970 on the Oceanographer transform fault.

Figure 4.9 Results of fits of synthetic (upper) and observed (lower) seismograms of P waves from the November 18, 1970 earthquake. Positions on lower focal hemisphere of stations used for synthesis, and fault plane solution obtained are also shown. Closed circles for station locations represent compressional first-arrival polarities. Open circles represent dilatational polarities obtained on the synthetic seismograms; polarities of the actual first-arrivals for these stations is uncertain. The vertical scales were normalized so that all seismograms would have equal maximum amplitudes.

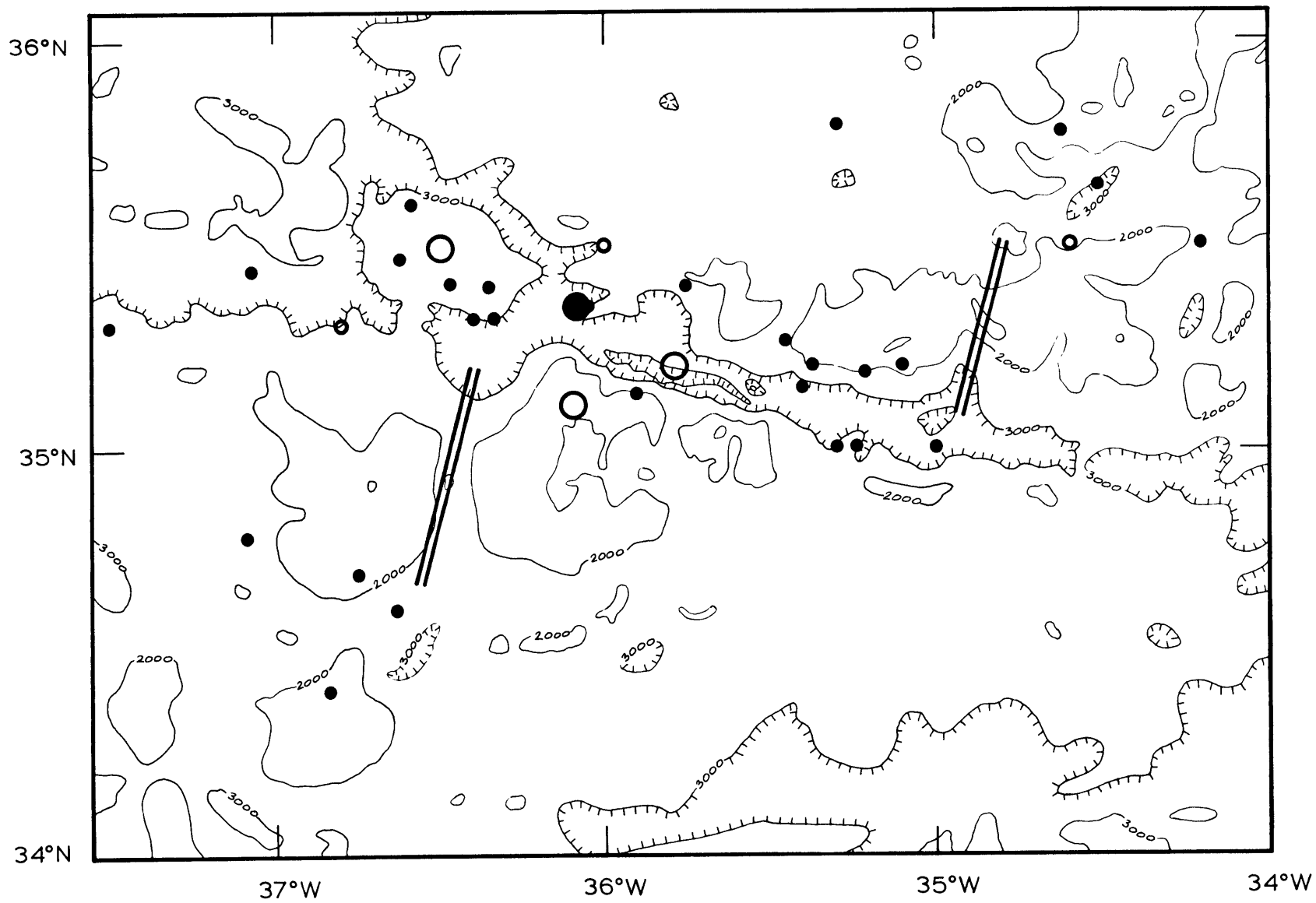


Fig. 4.1

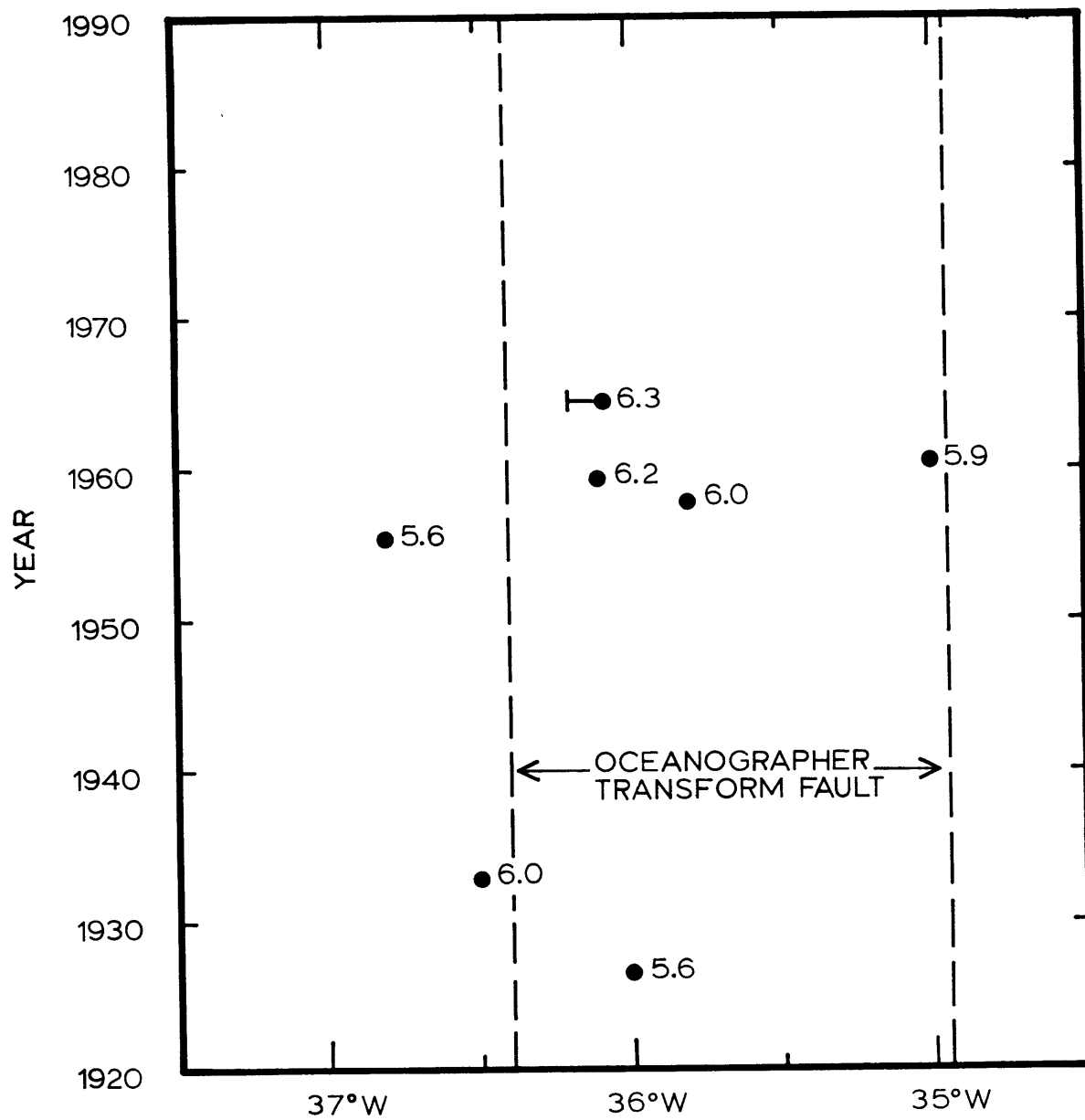


Fig. 4.2

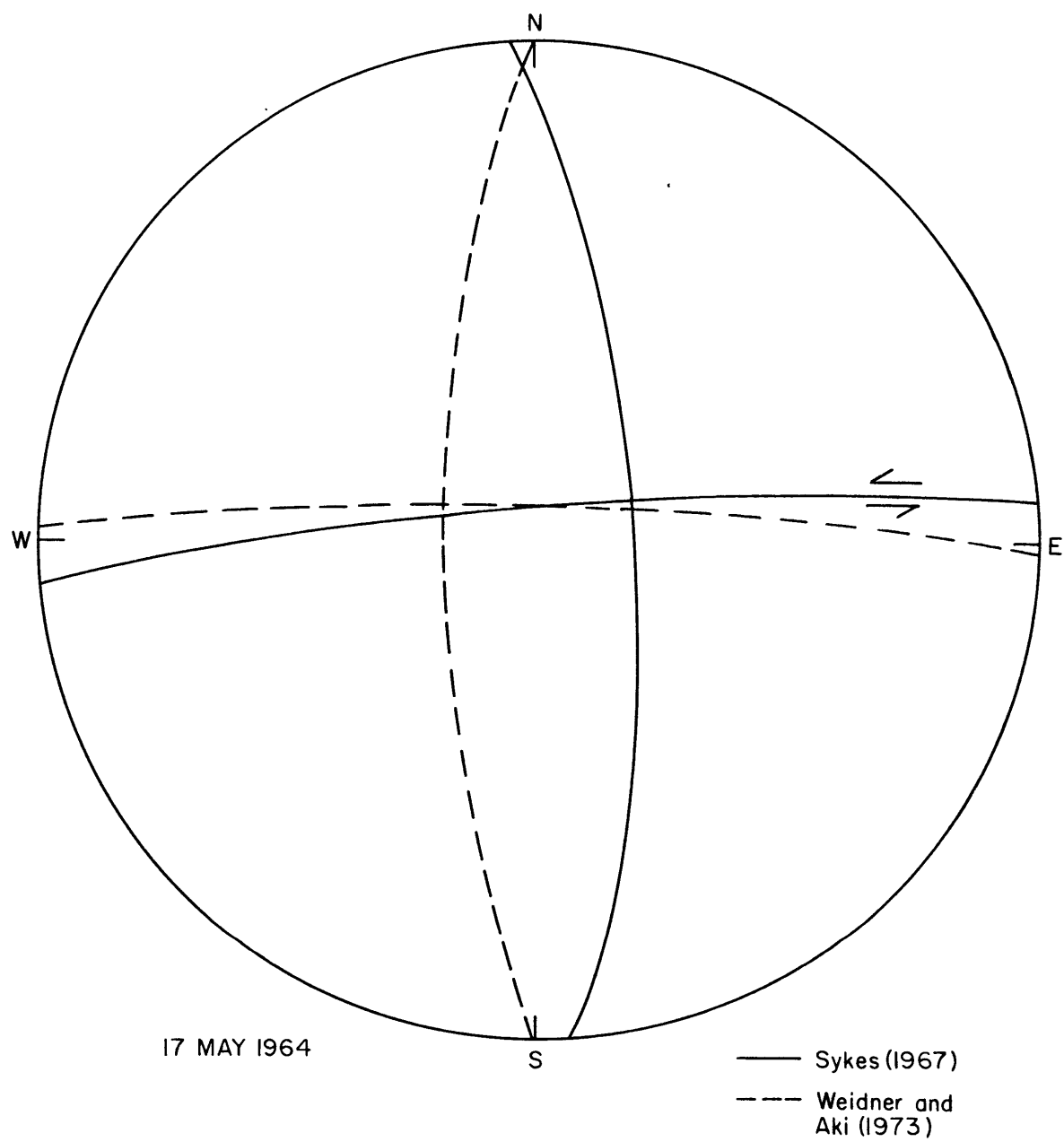


Fig. 4.3

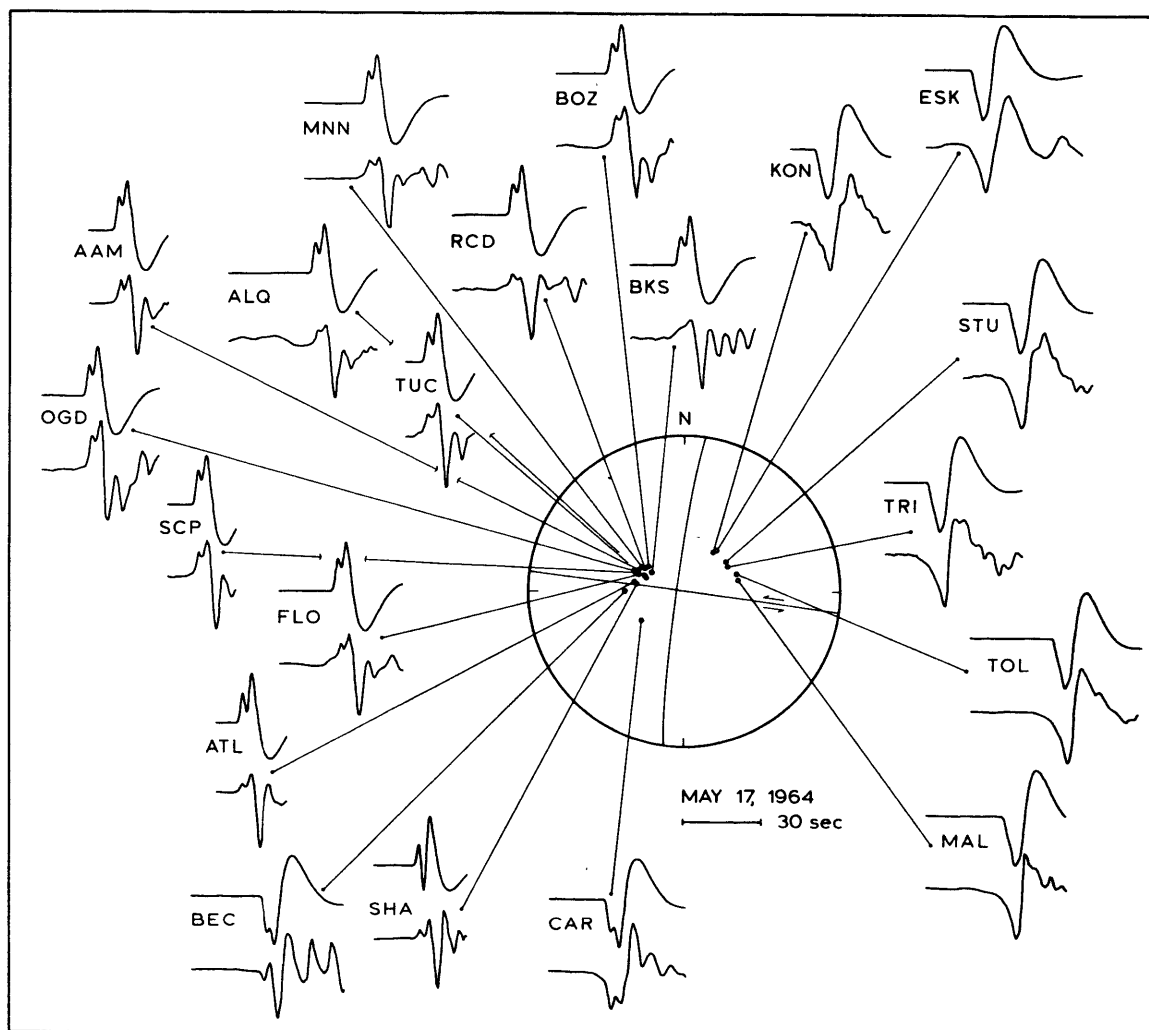


Fig. 4.4

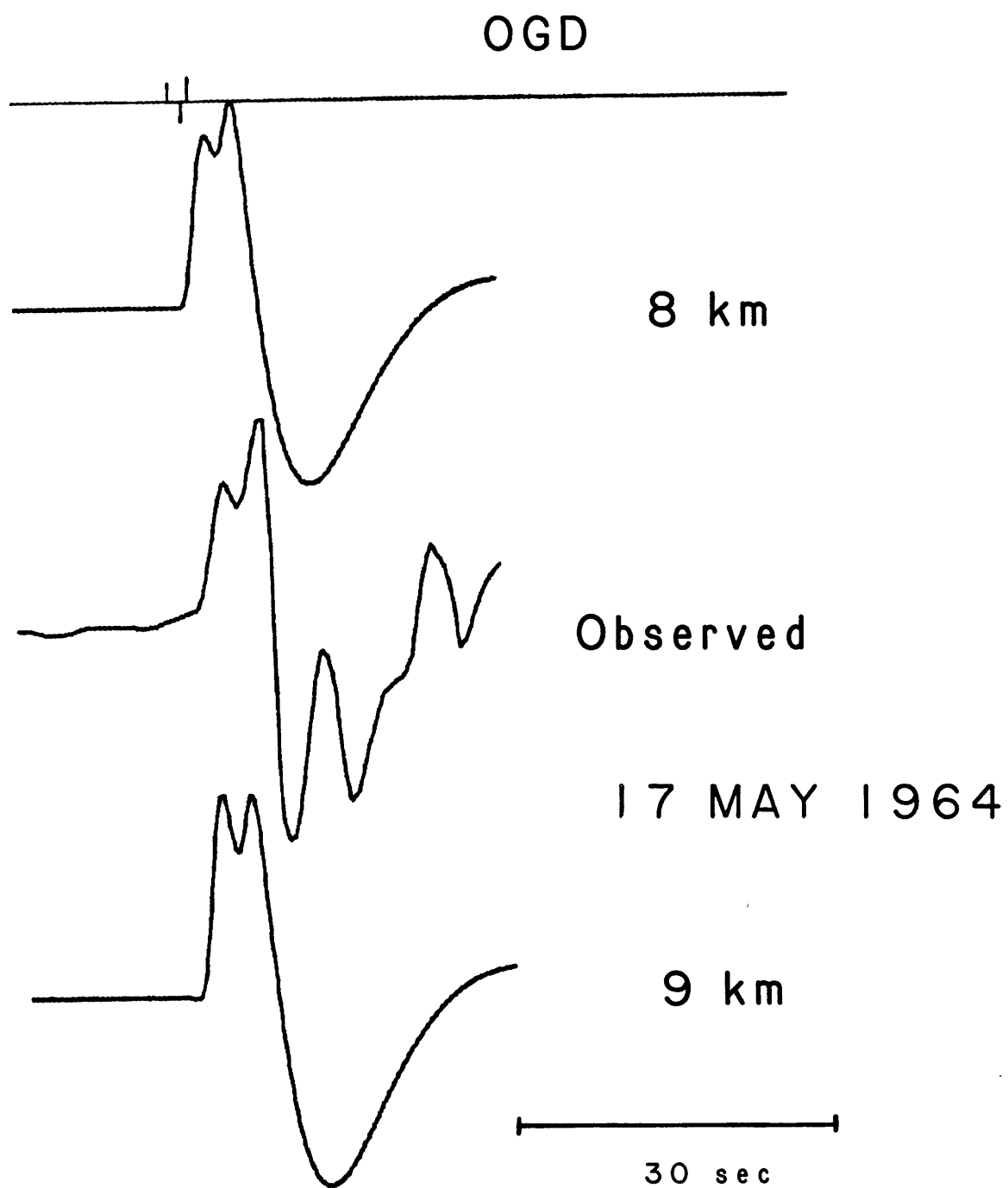


Fig. 4.5

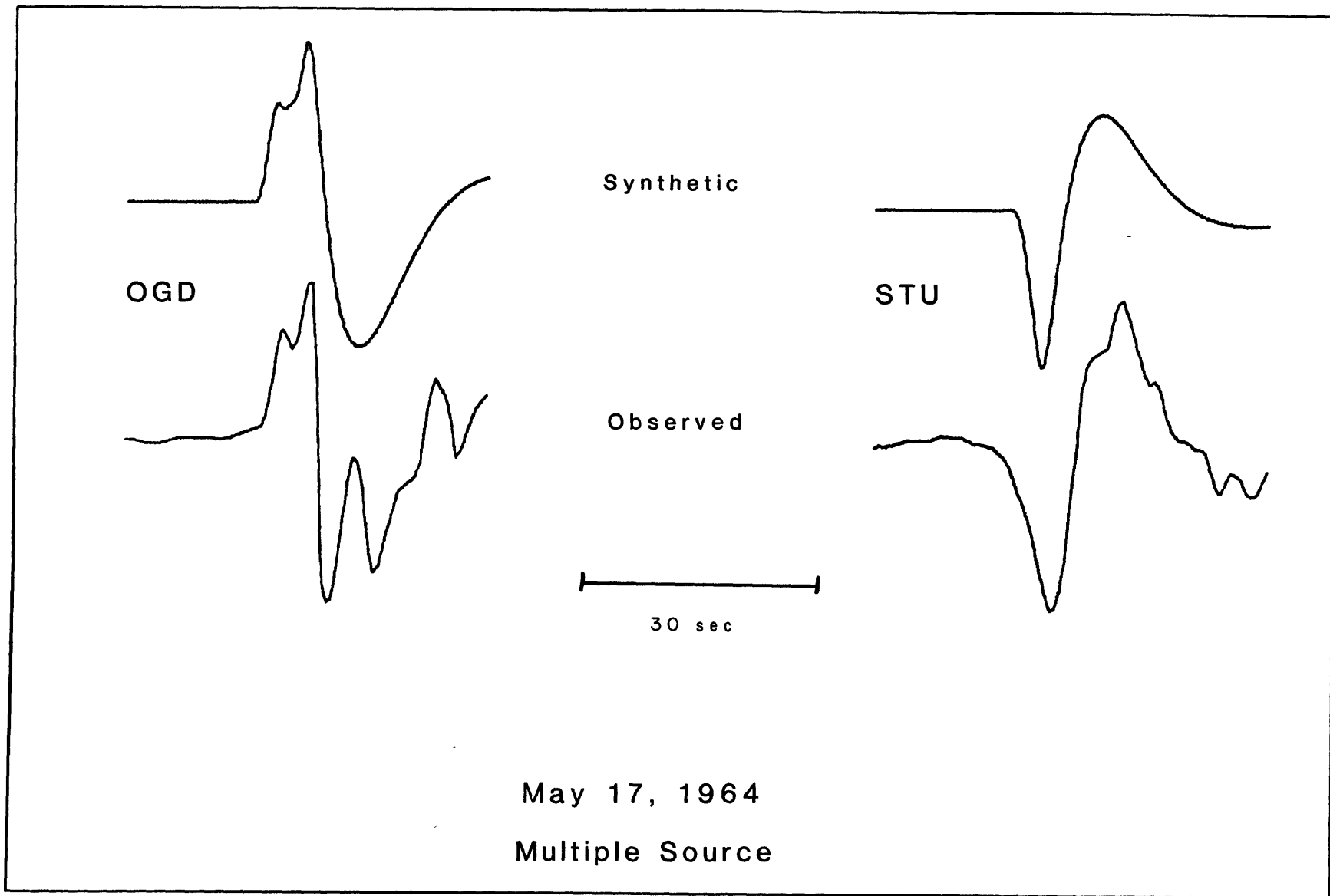


Fig. 4.6

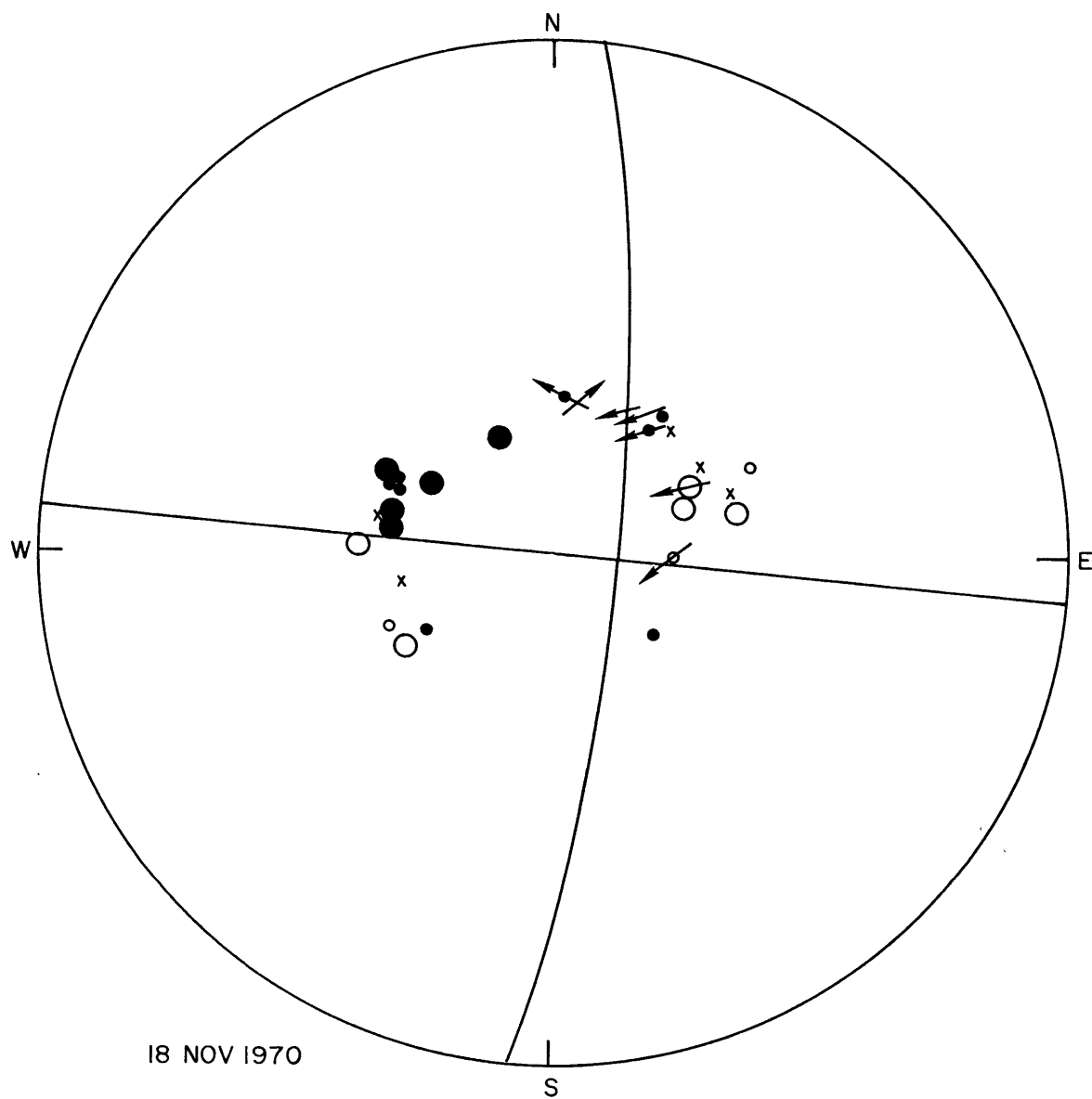


Fig. 4.7



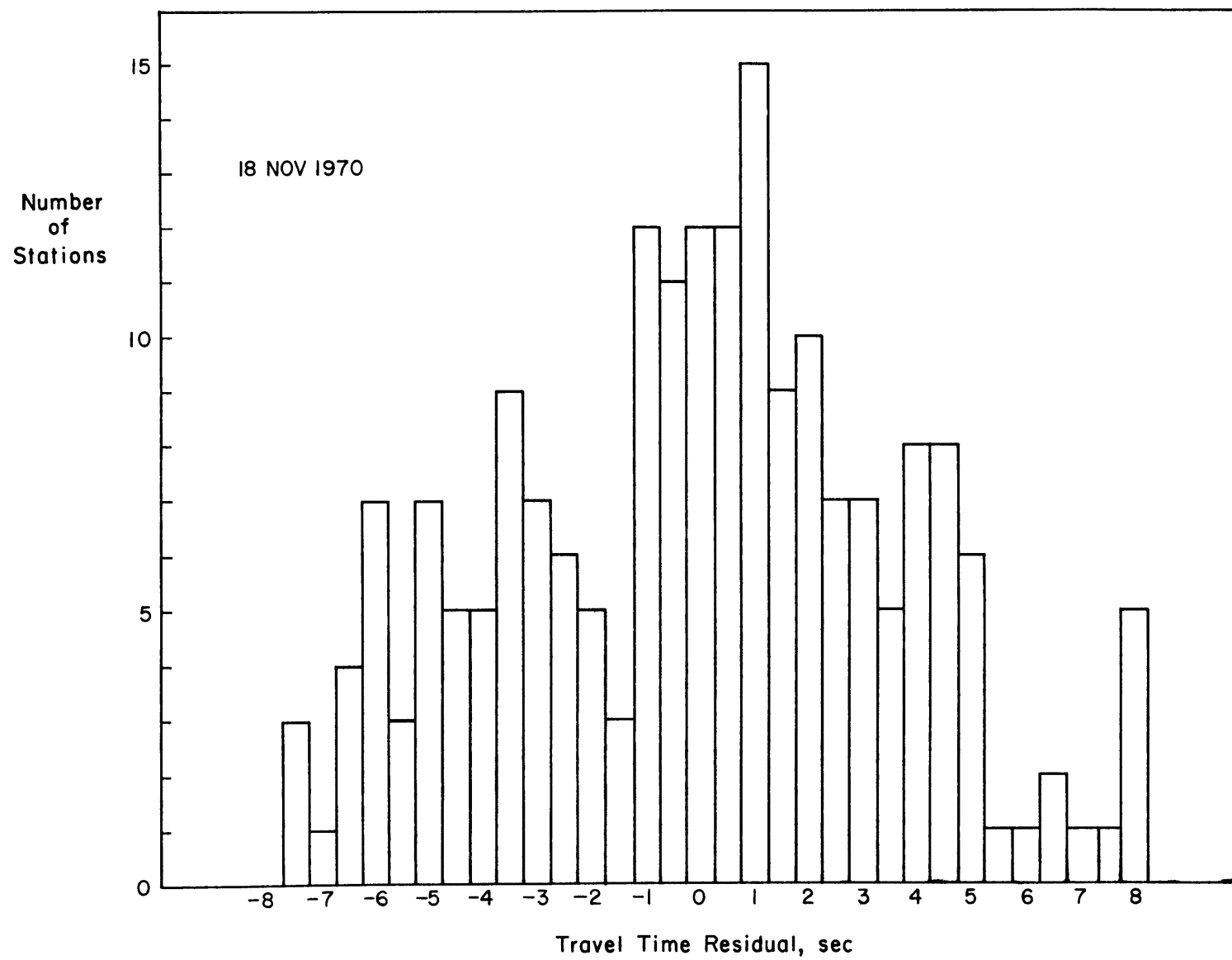


Fig. 4.8

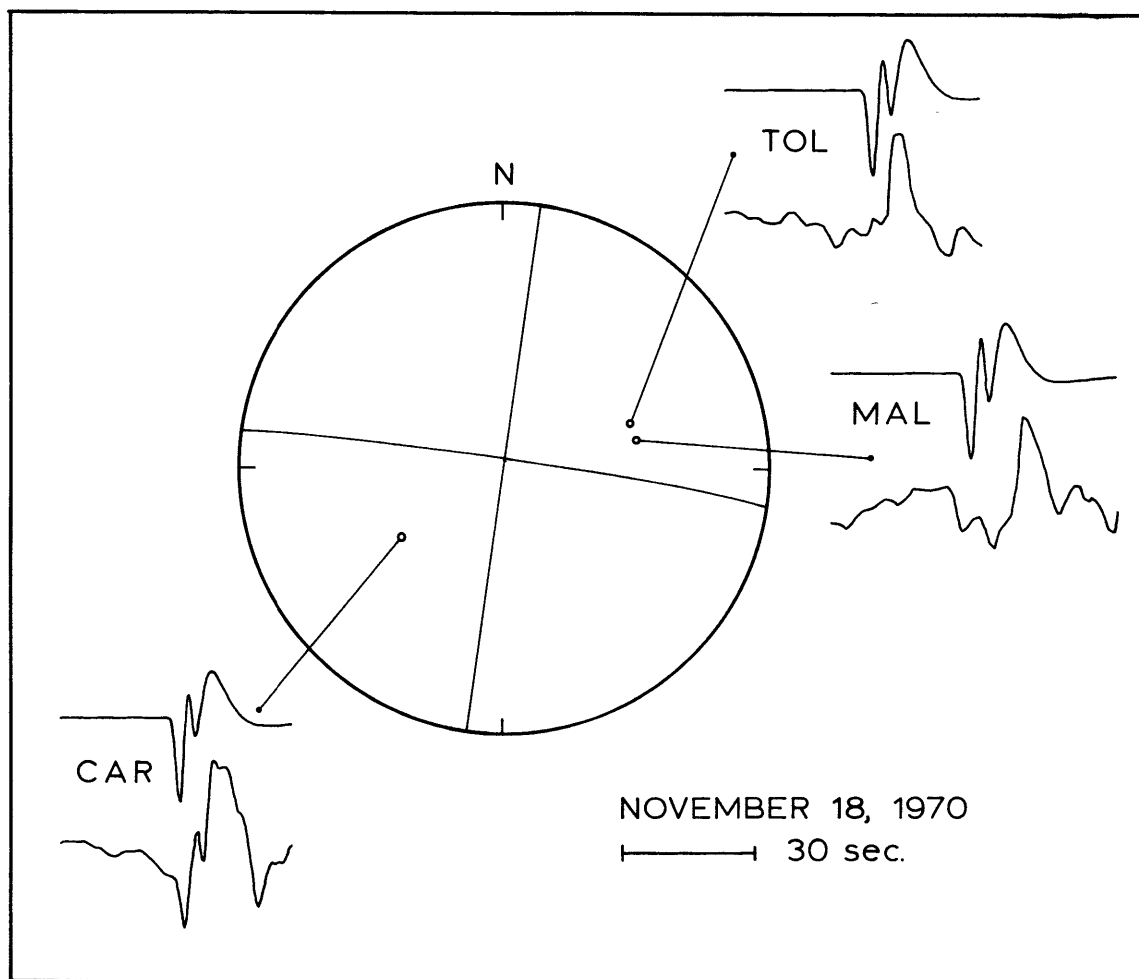


Fig. 4.9

## CHAPTER 5. EARTHQUAKES AND TECTONICS

### OF THE KANE TRANSFORM FAULT

The Kane transform fault is a 150 km long left-lateral offset of the Mid-Atlantic Ridge at about 24° N. It was first noted as an offset in the seismicity of the Mid-Atlantic Ridge by Sykes (1967), who also presented a fault plane solution from an earthquake there showing the expected right-lateral motion. The Kane Fracture Zone has been thoroughly surveyed with respect to its bathymetry (Rabinowitz and Purdy, 1976, Purdy et al., 1979), its seismic velocity structure (Detrick and Purdy, 1980), and its gravity features (Louden and Forsyth, 1983). Schouten et al. (1979) discussed the history of the Kane transform, as interpreted from magnetic anomalies. Rona and Gray (1980) presented the results of a narrow-beam bathymetric and magnetic survey on a section of the Mid-Atlantic Ridge which included the Kane transform. They observed that transforms could be separated into two classes by size; those with total offset greater than about 50 km, of which the Kane transform is one, are generally oriented along small circles about the pole of rotation between the plates, while smaller transforms often display asymmetry about the ridge axis, and are not necessarily oriented along small circles of rotation. Bryan et al. (1981) presented the results of dredging in the Kane transform, which showed that there was no evidence of volcanic activity within the transform.

The bathymetry of the Mid-Atlantic Ridge from 23°N to 24.5°N, from Detrick and Purdy (1980), is shown in Figure 5.1. The transform is characterized by a sediment-free central valley which has a depth generally between 4000 m and 4500 m below sea level, a width which varies

from 5 to 20 km, and walls with slopes of  $15^{\circ}$  to  $25^{\circ}$ . The edges of the transform are paralleled by transverse ridges which rise to heights of 1000 to 2500 m above the central valley floor. The height of each transverse ridge varies considerably along its length, with a maximum height obtained in a peak where the transverse ridge intersects the ridge of the adjacent spreading center. The strike of the transform, as indicated by the bathymetry, is about  $N 99^{\circ} E$ . The depth of the central valley reaches a maximum between 5500 and 6000 m in depressions at either end of the transform, where the central transform valley intersects the axial valleys of the adjoining ridge segments.

Detrick and Purdy (1980) presented the results of a seismic refraction experiment on the inactive arm of the Kane Fracture Zone east of the active transform. In this experiment, an array of 8 receivers was arranged in a T pattern, with the top of the T (7 receivers) crossing the fracture zone valley at right angles to its strike, and the stem of the T (2 receivers) along the center of the fracture zone valley. The results indicated that there was no significant difference in the crustal structure on either side of the fracture zone, despite the 10 million year age difference. The results also indicated that the fracture zone itself had an anomalously thin crust, possibly only 2 or 3 km, and a compressional wave velocity at shallow depths of only about 4 km/sec, lower than the value for normal oceanic crust. Detrick and Purdy also noted that the signals recorded at the two receivers in the valley floor looked quite different from each other, possibly suggesting variability of the seismic characteristics along the fracture zone. They proposed that the crust of the fracture zone is made up of a volcanic or plutonic layer which is thinner than normal oceanic crust, and that this structure

is limited to a zone in the center of the fracture zone valley perhaps only 10 km wide. They suggested that this thinner crust, by isostasy, could account for the greater depth of the fracture zone floor.

Louden and Forsyth (1982) studied the correlation between gravity and topography profiles across the fracture zone, using spectral analysis. Their results showed that either the density structure or the crustal thickness varied over the entire area studied. If the variation were assumed to be in crustal thickness, then the variation could be by as much as a factor of two. They also concluded that there was no evidence for general thinning of the crust beneath the fracture zone floor. Since there was correlation between the topography and gravity profiles only for the longest wavelengths, they concluded that the topography was not locally compensated, and that it must therefore be supported by stresses in the lithosphere. Their interpretation was that there must be one crustal formation process governing the local topography and another governing crustal thickness. Finally they concluded that, though the resolution was poor, there was evidence for the existence of a gravitational edge-effect, as expected across the fracture zone from thermal models of cooling of the oceanic lithosphere. Their results are noteworthy in that Ludwig and Rabinowitz (1980), in a seismic refraction study of the Vema Fracture Zone, found results suggesting a highly variable crustal thickness, with no appreciable crustal thinning beneath the fracture zone floor. Since the experiment of Detrick and Purdy (1980) was in only one limited portion of the fracture zone, it is possible that their finding of a thin crust was caused by the fortunes of instrument placement over a variable structure.

This is supported by the fact that the two receivers recorded signals with very different appearances.

## SEISMICITY

The epicentral locations of all of the known earthquakes on the Kane transform are shown in Figure 5.1. These data were taken from the same sources as the data for the other transforms (see Figure 3.1). Epicentral and other data for these earthquakes are listed in Table 5.1. The location of the transform is indicated by both the bathymetry and the seismicity. The epicenters are scattered somewhat to the north of the transform axis, as they are on most of the North Atlantic transforms, and the seismicity has been scattered fairly evenly along the transform's length.

There have been few large earthquakes on the Kane transform compared to most of the other transforms we studied. The largest event on the Kane transform since 1935 was an  $M_S = 6.4$  event on May 19, 1963, for which Sykes (1967) determined a fault plane solution showing the expected right lateral strike-slip motion on a vertical fault with a strike of  $N 103^\circ E$ . Another large event ( $M_S = 6.3$ ) occurred on March 26, 1980. The third largest event occurring after 1935 was an  $M_S = 5.6$ ,  $m_b = 5.4$  event on March 12, 1977 near the eastern end of the transform. There was a sequence of three large events in 1922, 1924, and 1925, another single event in 1935 (whose epicenter was reported as latitude  $23^\circ N$ , slightly south of the transform, but which we suspect was probably a transform earthquake), and no other events large enough to be recorded until that of 1963. Figure 5.2, showing the year of these epicenters plotted against the longitude of each event, clearly illustrates this gap in

large event seismicity. The earlier epicenters are probably not as well-determined as the later ones, but it is possible that the entire transform may have fractured in the four earthquakes from 1922 to 1935. This possibility and the large gap in the large event seismicity from 1935 to 1963 will be discussed in Chapter 9. We have studied the 1977 earthquake, but we were unable to obtain records for the earthquakes of 1963 or 1980. This last event should be a good candidate for further study, when its records become available, because it was not preceded by any other large events which might obscure its waveforms.

#### THE MARCH 12, 1977 EARTHQUAKE

We have calculated synthetic seismograms for comparison with seismograms from the March 12, 1977 earthquake observed at 5 WWSSN stations. This is too few stations, and this event is actually too small, for us to study this event thoroughly, but we can still obtain reasonable estimates of some of the source parameters. The source velocity structure, shown in Table 5.2, was taken from Detrick and Purdy (1980), and the water depth used was 4 km. Data for the stations used are presented in Table 5.3. Only two of the five stations used have an epicentral distance greater than the requisite  $30^\circ$ , so we used only these two stations to find the total moment, though we did make an attempt to match the waveforms for all five stations.

The waveform results are shown in Figure 5.3, along with the adopted fault plane solution and the location on the lower focal hemisphere of the stations used. The fault strike we used was  $N 99^\circ E$ , about equal to that of the Kane transform. The best fitting waveforms were obtained with a fault dip of  $89^\circ$  to the north, and a slip angle of  $180^\circ$ . The fault length we used was 10 km and the fault width was 5 km. Rupture was

taken to be bilateral because we did not have the records from stations to both the east and west that would be necessary to recognize any directivity. Rupture velocity was taken to be 3 km/sec because a higher velocity was not required in order to match these few waveforms. The rise time was taken to be 0.5 sec because the waveforms were impulsive, requiring short source time functions, though perhaps this effect could have been obtained with a smaller fault width instead. We used a focal depth of 5.5 km below sea level, 1.5 km below sea floor. None of these values are well determined because of the small number of stations used, but the fault plane solution does represent the expected right-lateral strike slip motion, and the fault dimensions and focal depth used are typical of what we used for the other small events studied. If we had used the same velocity structure as we used for the other events, it would have required a focal depth of 1.4 km below sea floor, and a seismic moment about 25% smaller.

The moment value for this earthquake, as determined using only stations BOG and LPB, was  $1.3 \times 10^{25}$  dyne-cm, with BOG's value being low, and LPB's being high, by a factor of 1.2. As will be shown in Chapter 9, this moment value correlates well with the  $M_s$  of this event, when compared to the other events studied, even though the moment was determined using only a few stations. This moment value and fault dimensions imply a total displacement of 73 cm, and for a rise time of 0.5 sec, a dislocation or particle velocity of 150 cm/sec. Since the transform is about 150 km long this fault length represents strain release on about 1/15 of the transform's length. The total spreading rate for the Kane transform, as calculated from Minster and Jordan's (1978) relative rotation vector between the North American and African



plates, is 2.4 cm/yr, so that the displacement calculated for this earthquake represents the release of strain accumulated over, and therefore a recurrence time for this part of the transform of, 30 years. This value is similar to the number of years (42) elapsed since the 1935 earthquake, also on the eastern end of the transform, which suggests, but does not require, that these two events fractured the same parts of the transform. The stress drop for this earthquake, determined as described in Chapter 2 using values of  $\mu$  and fault width as used for the synthetic seismograms and the calculated displacement, was about 33 bars, a fairly low value. A greater fault length would have meant a smaller displacement, and therefore a lower stress drop. Had we used a smaller fault width, it would have meant a greater displacement, and thus a greater stress drop.

#### TOTAL SEISMIC MOMENT

We can compare the total seismic moment from the observed earthquakes with that predicted by the Minster and Jordan (1978) relative rotation vector for the North American and African plates. For this we calculate moments from the  $M_S$  values for all of the other earthquakes on the transform, using the method explained in Chapter 9. These values are given in parentheses in Table 5.1. To the sum of these moments we add the moment found for the earthquake studied here, which gives a value of  $1.5 \times 10^{27}$  dyne-cm for the total observed seismic moment since about 1920 (about the earliest events for the North Atlantic listed by Gutenberg and Richter, 1954). Over half of this total can be accounted for by the  $M_S$  7.1 event in 1922 reported by Gutenberg and Richter (1954), though the magnitude of this earthquake may not be directly comparable to the more recent values. After this earthquake, the events in 1924 and 1925

contribute most to this total. Even if the magnitudes for these three events are greatly over-estimated, this seismic episode still dominates the known seismic history.

To this total moment sum we add a correction for the seismicity too small to be observed, using Formula (7) given in Molnar (1979) (Equation 3.1 of this work). Following procedures used earlier, with  $a = 2.4$  and  $b = 0.60$  in equations 3.2 and 3.1, and using minimum  $M_0$  values of  $8.7 \times 10^{25}$  dyne-cm for the years from 1920 to 1963 and  $8.4 \times 10^{22}$  dyne-cm for the years from 1964 to 1981, we obtain unobserved moment rates of  $9.0 \times 10^{24}$  dyne-cm/yr and  $2.9 \times 10^{23}$  dyne-cm/yr, respectively, for these time periods. Since these time periods represent 44 yrs and 18 yrs, respectively, this means unobserved moment totals of  $4.0 \times 10^{26}$  dyne-cm and  $5.3 \times 10^{24}$  dyne-cm. Adding these values to the total observed seismic moment gives a total seismic moment value of  $1.9 \times 10^{27}$  dyne-cm released by earthquakes on the Kane transform since 1920.

From the transform dimensions and the slip rate we have determined the total seismic moment expected on the Kane transform since 1920, using  $M_0 = \mu L w D$  where  $\mu$  is shear modulus,  $L$  is fault length,  $w$  is fault width, and  $D$  is the total displacement for this 62 year period. For this we used  $\mu = 3.5 \times 10^{11}$  dyne/cm<sup>2</sup>,  $L = 150$  km,  $w = 5$  km, and  $D = 149$  cm, calculated from the rotation vector given by Minster and Jordan (1978). The value of 5 km was used for width because that is the value we used for the synthetic seismograms. The result is an expected seismic moment value of  $3.9 \times 10^{26}$  dyne-cm. This value is about one fifth of the total value presented in the previous paragraph.

There are several factors which may contribute to this error. One is the value of 5 km we used for the transform width. From the

discussion in Chapter 2, we see that the actual width of the transform may easily be as great 10 km, producing an expected moment total of  $7.8 \times 10^{26}$  dyne-cm, which reduces the discrepancy to a factor of about 2.4. Another source of error is that the magnitudes for the earthquakes taken from Gutenberg and Richter (1954) may be larger what would have been determined today. A third effect, and probably the most significant, is that the large events of 1922-1925 may have released strain accumulated for a long time before our seismic records begin. This last possibility is supported by the seismic history.

#### IMPLICATIONS FOR THE KANE TRANSFORM

We have seen that the large event seismicity on the transform is episodic in nature, that the transform is capable of producing three large earthquakes in 4 years, and then going for several decades without producing another. We will discuss this topic further in Chapter 9. From the fault lengths used in our synthetic seismograms it appears that the transform does not necessarily slip along its entire length in each seismic episode, though it may have done so during the 4 events from 1922 to 1935. From the recurrence time we found for the 1977 event, it is possible that this event fractured a part of the transform that also slipped in either 1924 or 1935. It is extremely unlikely, however, that the same part of the transform slipped in both 1924 and 1935, unless the slip on the transform is very uneven. We can therefore conclude that the fault lengths are at most a few tens of km, and thus only a small fraction of the transform's length. This is similar to what we found for the Oceanographer transform. Finally, we can see from the seismic moment totals, that the smaller length of this transform, compared to most of the others we studied, seems to be reflected in the lower seismicity.

Table 5.1 Seismicity of the Kane Transform Fault

Date	Origin Time h m s	Lat, °N	Lon, °W	h, km	$m_b$	$M_s$	No. of sta.	$M_0, 10^{25}$ dyne-cm
1/9/22	05 09 34	24	46			7.1		(81)
10/14/24	05 00 19	24	45			6.5		(17)
8/12/25	06 58 45	24	46	60		6.5		(17)
5/23/35	17 58 59	23	45			6.25		(8.7)
5/19/63	21 35 47	23.8	46	10		6.4		(13)
11/22/64	00 02 32.6	23.86	45.35	32	4.8	(4.6)	62	(0.12)
1/15/65	21 26 41.0	23.81	44.91	16	4.9	(4.8)	48	(0.20)
5/1/66	22 23 22.2	23.87	45.33	33	4.6	(4.6)	57	(0.12)
11/18/66	19 43 39	24.08	46.24	59	4.7	(4.4)	65	(0.068)
11/18/66	21 17 33	23.1	46.3	33	4.5		15	
11/19/66	05 29 50.3	24.34	45.91	33	4.4	(3.9)	7	(0.018)
11/19/66	08 34 16	24.10	45.9	33	4.5	(4.1)	12	(0.031)
11/19/66	17 41 06	24.04	46.44	112	4.8	(4.6)	37	(0.12)
11/20/66	00 59 50.8	24.09	46.43	33	5.1	(5.1)	31	(0.43)
9/20/67	17 14 36.0	23.8	45.1	33	4.5	(4.1)	18	(0.031)
3/14/68	19 30 23.5	23.66	44.89	33	4.3	(3.7)	8	(0.011)
3/16/68	00 17 03.6	23.0	45.1	33	4.3		17	
6/22/68	17 27 11.5	23.63	44.92	33	4.4	(3.9)	22	(0.018)
9/23/68	08 53 50.5	23.91	45.4	33	4.5	(4.1)	17	(0.031)
12/11/68	20 28 14.3	24.10	45.48	33	4.8	(4.6)	38	(0.12)
1/1/69	13 04 11.3	24.07	45.72	33	4.5	(4.1)	28	(0.031)
7/1/70	16 18 43.3	23.83	45.60	32	5.1	(5.1)	122	(0.43)
11/29/70	11 35 34.9	23.90	44.89	33	4.4	(3.9)	23	(0.018)
5/31/71	08 17 16	23.84	45.03	37	4.9	5.3	99	(0.72)
7/7/71	11 27 35.2	23.60	44.85	33	4.6	(4.3)	37	(0.053)
8/12/71	01 25 55	24.0	45.70	41	4.2	(3.6)	16	(0.0084)
11/21/71	15 05 37.1	23.86	45.99	33	4.8	(4.6)	39	(0.12)
5/15/74	16 50 35	24.0	43.2	0	4.3	(3.7)	11	(0.011)
1/13/75	04 38 31.7	23.70	47.41	33	4.5	(4.1)	22	(0.031)
6/23/75	05 43 57	24.0	45.01	0	4.7	(4.4)	13	(0.068)
7/13/75	04 30 36.3	23.39	44.88	33	4.6		17	
7/13/75	05 12 53.1	23.28	45.04	33	4.8		19	
7/22/75	09 43 55.1	23.12	44.78	33	4.5		19	
7/23/75	02 34 55.1	23.25	45.07	33	4.7	3.9	46	
10/27/75	23 53 58	23.7	45.2	33	4.3	(3.7)	10	(0.011)
3/11/77	02 57 53.3	24.2	45.26	33		5.6	15	

Table 5.1 (cont'd)

Date	Origin Time h m s			Lat, °N	Lon, °W	h, km	$m_b$	$M_s$	No. of sta.	$M_0$ 10 <sup>25</sup>
3/12/77	02	57	50.7	23.79	45.17	28	5.4	5.6	315	1.3
3/30/77	21	24	25.0	23.56	45.04	33	4.7		27	(0.068)
3/30/77	21	36	12.5	23.36	45.00	33	4.6		43	
3/30/77	21	42	28.4	23.45	44.87	33	4.9		17	(0.20)
3/30/77	21	49	07	23.6	45.01	33	4.5		13	(0.031)
3/26/80	20	43	37.9	23.87	45.56	10	5.9	6.35	261	(9.9)
4/8/81	6	37	42.3	23.71	45.21	10	4.5	4.25	43	(0.04)

This table includes all events on the Mid-Atlantic Ridge between 23°N and 24.5°N, which includes the Kane transform fault. Data for the events before 1955 were taken from Gutenberg and Richter (1954). Data for events between 1955 and 1963 inclusive were taken from Rothe (1969). Data for events from 1964 to 1979 were taken from the ISC Regional Bulletin, while events in 1980 and 1981 were taken from P.D.E. reports of the U.S.G.S. We have taken magnitudes reported before 1964 as equivalent to  $M_s$ .  $M_s$  values shown in parentheses were determined from  $m_b$  using Equation 9.1. Other  $M_s$  values were taken from the same source as the other data for that event; d refers to a Gutenberg and Richter (1954) or Rothe (1969) listing as between 5.3 and 5.9, assumed here to be 5.6. The  $M_s$  values in parentheses were determined for all events whose  $M_s$  was not available from another source and whose location placed them on the Kane transform fault. The  $M_0$  values shown in parentheses were determined from  $M_s$  using Equation 9.2. These values in parentheses were determined for all events whose moment was not determined in this study and whose location placed them on the Kane transform fault.

Table 5.2. Source structure used for synthetic seismograms for event on the Kane transform on March 12, 1977.

	<u>Layer</u>	<u>Thickness, km</u>	<u><math>V_p</math>, km/sec</u>	<u><math>\rho</math>, g/cm<sup>3</sup></u>
1.	crust	2.4	4.7	2.8
2.	mantle	Half-space	7.8	3.3

$V_p$  is P wave velocity,  $\rho$  is density. This structure was taken from Detrick and Purdy (1980).

Table 5.3. Station data used for synthetic seismograms  
for the earthquake of March 12, 1977.

<u>Station</u>	<u>Distance, degrees</u>	<u>Azimuth, degrees</u>	<u>Magnification</u>	<u><math>10^{25} M_0</math>, dyne-cm</u>
BEC	19.2	300.7	1500	1.5 *
SJG	20.3	257.9	750	1.1 *
CAR	24.5	241.2	3000	1.2 *
BOG	33.7	240.1	3000	1.1
LPB	45.9	211.3	1500	1.5

\*  $M_0$  values not used to find "average" for this event.

For all stations we used  $T_p = 15$  sec,  $T_g = 100$  sec,  $H_p = .93$ ,  $H_g = 1.0$ , where  $T_p$ ,  $T_g$ ,  $H_p$ , and  $H_g$  refer to the seismometer and galvanometer periods and damping factors, respectively.

### Figure Captions.

Figure 5.1 Bathymetry of the Kane transform fault between  $23^{\circ}$  N and  $24.5^{\circ}$  N, and  $44.5^{\circ}$  W and  $47^{\circ}$  W, and epicenters of all known earthquakes in this area, taken from Table 5.1. The approximate locations of the ridge axes are indicated by double lines. Open circles represent epicenters taken from Gutenberg and Richter (1954) and Rothe (1969). Larger symbols are events with  $M_S > 6.0$ . Contour intervals are every 500 m below sea level, taken from Detrick and Purdy (1980).

Figure 5.2 Longitude versus year of occurrence for the earthquakes on the Kane transform fault with  $M_S > 5.5$ .  $M_S$  is indicated for each event. Dashed lines indicate where the transform intersects adjacent spreading centers. The bar for the 1977 event indicates the fault length used for the synthetic seismograms.

Figure 5.3 Results of fits of synthetic (upper) to observed (lower) seismograms of P waves from the March 12, 1977 earthquake on the Kane transform. Positions on lower focal hemisphere of stations used for synthesis and fault plane solution obtained are also shown. Closed circles for station locations represent compressional first-arrival polarities, open circles represent dilatational polarities. The vertical scales were normalized so that all seismograms would have equal maximum amplitudes.



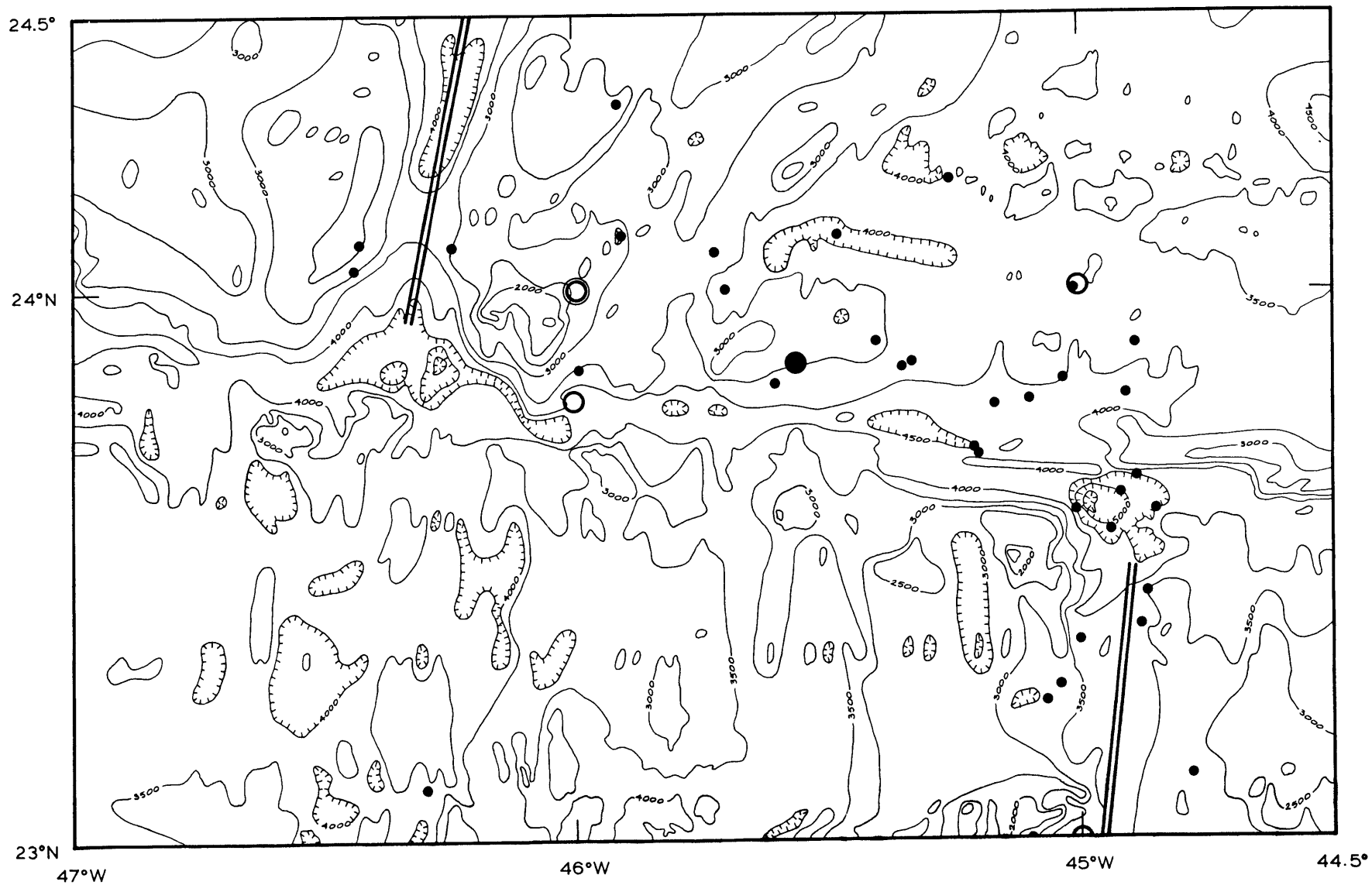


Fig. 5.1

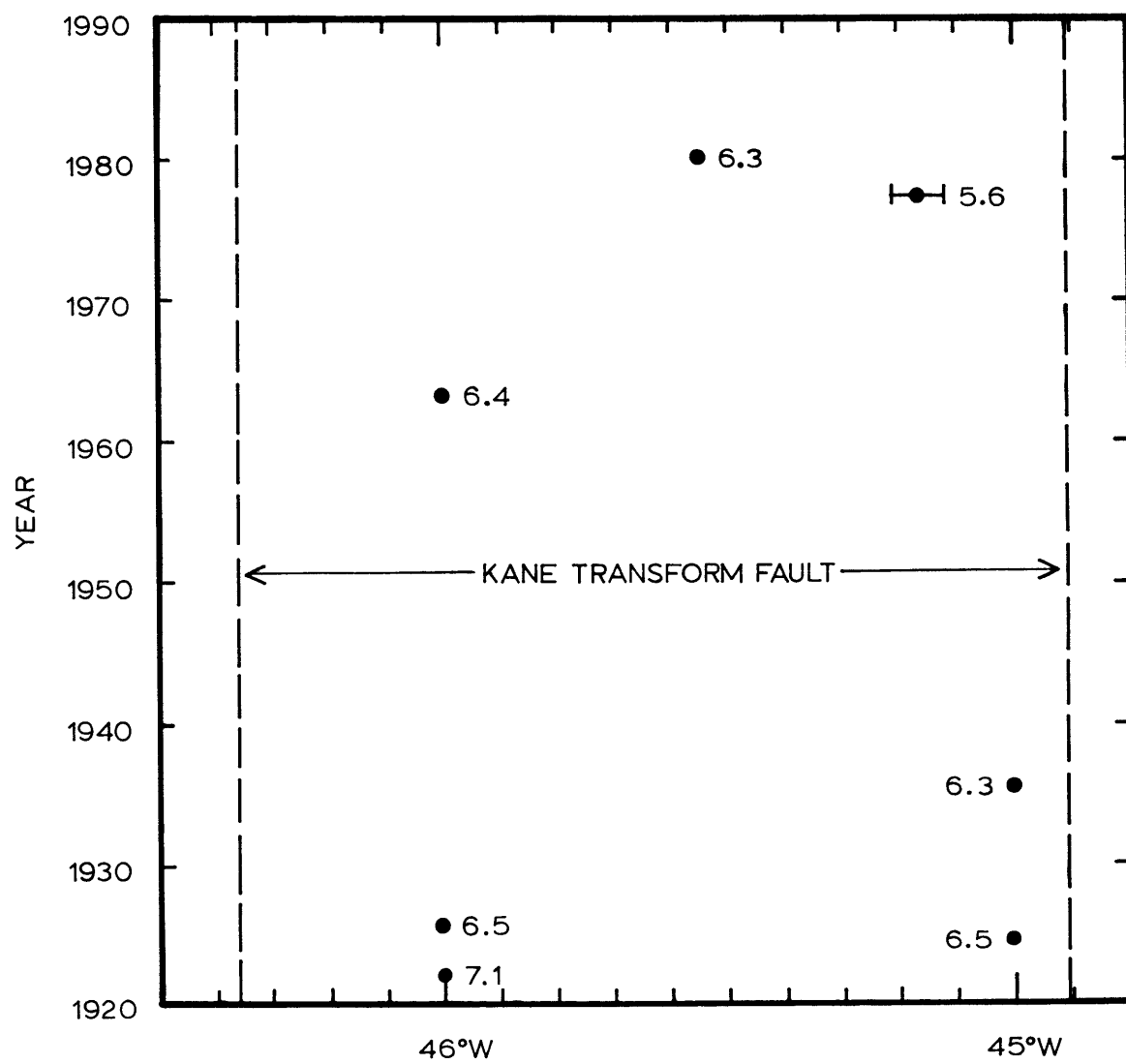


Fig. 5.2

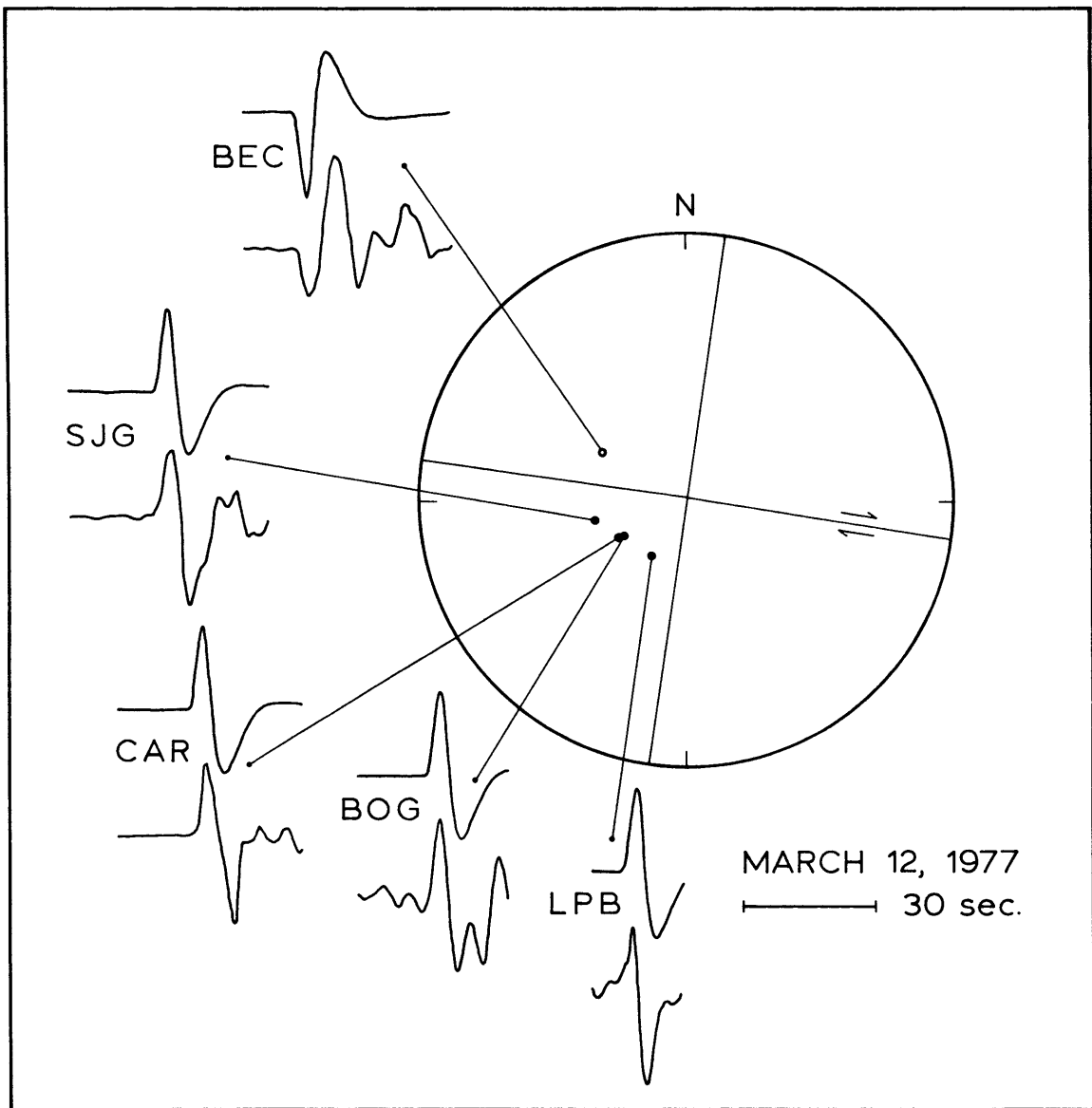


Fig. 5.3

## CHAPTER 6. EARTHQUAKES AND TECTONICS OF THE 15° 20' TRANSFORM FAULT

The 15° 20' transform fault, named by its latitude, is a 155 km long left-lateral offset of the Mid-Atlantic Ridge. Its existence was suggested by Sykes (1967) because the location of earthquake epicenters shows an offset in the Mid-Atlantic Ridge there. The area was surveyed as part of the KROONVLAG Project, the results of which were published and interpreted by Collette et al. (1974 a,b). They reported that while the magnetic signature of the transform is not very large, the transform is clearly defined by the bathymetry. They also reported the determination of a fault plane solution of an earthquake on the transform (reported as Rutten, in press, and as near as I have determined, still unpublished) which indicated right-lateral pure strike-slip motion on a fault with a strike of 95°, in accordance with the direction of offset of the ridge. (The earthquake presented was described as being located at 15.2° N, 45.7° W, with a magnitude of 5.8; they did not report the date or origin time for this event so that identifying it is difficult. We suppose that it was the largest of the three events on September 24, 1969.) Except for this study there has been little marine geophysical work in this part of the Atlantic.

Figure 6.1 shows the bathymetry of the area between 14.5° N and 16° N, and 44° W and 48° W, taken from Uchupi, (1982), indicating the ridge offset and the transform with a strike of about N98°E. The bathymetry of the transform is similar to that of other transforms in that there is a central trough, bounded on both sides by elevated ridges. The trough in the 15° 20' transform generally slopes downward to the east, with its shallowest part near the western end of the active transform. The Uchupi

(1982) map does not show the presence of bathymetric depressions near the intersections of the active transform with the adjacent ridge segments, a feature also different from other North Atlantic transforms.

The northern wall is generally higher than the southern wall, particularly near the western end, where it reaches a topographic high of 2200 m below sea level in a peak just to the east of the adjacent ridge segment. Both of the walls, like the central trough, are generally higher in the west, with the average and maximum heights toward the east.

#### SEISMICITY

The epicenters of all of the known earthquakes on the  $15^{\circ} 20'$  transform are shown in Figure 6.1. These data were taken from the same sources as the data for the other transforms (see Figure 3.1). Epicentral and other data for these earthquakes are listed in Table 6.1. The bathymetry and epicentral data plotted on Figure 6.1 indicate that the active transform extends from about  $47^{\circ}\text{W}$  to about  $44.9^{\circ}\text{W}$ . There are two curious clusterings of seismic activity, one just to the north of the center of the transform, and one near the western end of the transform, on the "inside" corner of the transform-ridge intersection and near the region of highest elevation. This latter clustering may indicate a stress concentration, or at least a greater structural complexity, in this region.

In Figure 6.2 we have plotted longitude vs. year for all of the events listed in Table 6.1 with  $M_S > 5.5$ . Major seismic activity (i.e., earthquakes with  $M_S > 6.0$ ) has occurred in only three episodes, one with two events in 1929 and 1930, one event in 1940, and an episode with two events, in 1965 and 1969. Events with  $M_S$  between 5.5 and 6.0 occurred in 1958, 1962, 1970, 1972, and 1978. On September 24 and 25, 1969 there was

a sequence of five earthquakes on the  $15^{\circ} 20'$  transform, all located between  $45.4^{\circ}\text{W}$  and  $46^{\circ}\text{W}$ . The main shock ( $m_b = 5.8$ ) was the first in the sequence. After this sequence there were only three events on the transform through 1970, all occurring within these same longitude limits; the second event in 1970 was the largest of these three ( $m_b = 5.5$ ). There have been only 12 earthquakes within these limits for the known seismic history of the transform. This series of 8 events in 1969 and 1970 thus clearly represents a major episode of slip on the transform. There are no obvious relationships between any of the other larger events. There was a large gap in the seismicity between 1940 and 1958, similar to that found for the other transforms discussed in this study. The epicenters for the events in 1929, 1930, and 1940 are probably not as well-determined as those of later events, though it appears from the sizes and locations that a large part of the transform may have been fractured by these three earthquakes.

#### THE SEPTEMBER 24, 1969 EARTHQUAKE

In this section we present a study of the largest of the events on September 24, 1969, hereafter referred to as the 1969 event. Figure 6.3 shows first-arrival polarities of observed P waves from the 1969 event, compiled by Solomon (unpublished). These polarities require the earthquake to be right-lateral strike-slip, with a fault strike of about  $100^{\circ}$  to  $105^{\circ}$ , measured clockwise from north, a fault dipping nearly vertically, and a slip angle of nearly  $180^{\circ}$ , indicating horizontal slip.

We have prepared synthetic seismograms for comparison with seismograms from the 1969 earthquake observed at 17 WWSSN stations. The source velocity structure used, listed in Table 4.2, was the same as that used for most of the other earthquakes in this study. Data for the

stations used are presented in Table 6.2. We used an epicentral distance for station QUE of  $99.5^\circ$  even though the actual distance was  $101^\circ$ , because at about this distance, ray paths begin entering the earth's core, and we wished to avoid this transition in the travel-time tables. Waveform synthesis is not valid for stations with epicentral distances greater than  $100^\circ$ ; we included station QUE because it was at a good location on the lower focal hemisphere to help determine the fault orientation, and it had a clean waveform. We did not place as much emphasis on this waveform as those from the other stations, and we did not use this station when we determined the seismic moment for this event.

The synthetic waveforms determined are presented in Figure 6.4. The fault plane solution used, along with the positions of the stations on the lower focal hemisphere, are also shown in Figure 6.4. The fault strike of  $N 98^\circ E$  was chosen because that is the strike of the transform indicated by the bathymetry, and a different value was not required by the observed waveforms. The fault dip used was  $90^\circ$ , i.e., a vertical fault, chosen because there was no significant difference between the waveforms observed in the northwestern and southwestern quadrants. The waveforms observed to the northeast were slightly different from those observed to the northwest, requiring a model of unilateral faulting and a slip angle of  $181^\circ$ , though because of the lack of precision in the results, purely horizontal motion cannot be excluded. This fault plane solution agrees with almost all of the data shown in Figure 6.2.

The waveforms observed to the east generally required shorter time functions than those to the west. Some of the waveforms observed in the west had a very slight "wiggle" just after the first maximum amplitude

was reached, a feature not present in the waveforms to the east; this effect was similar to, but not as large, as that observed for the May 17, 1964 earthquake on the Oceanographer transform. As for that event, we used unilateral faulting, in this case with rupture propagating from west to east at a rupture speed of 3 km/sec, and we placed the focus deep enough compared to the total signal lengths for the main phases to separate very slightly. The focal depth used was 5 km, or 1 km below sea floor. For this we could have used a value smaller by perhaps 0.2 km, or larger by as much as 1 km and still obtained satisfactory waveforms. The fault length used was 15 km, or about one tenth of the transform's length, and the fault width used was 5 km. We could not have used a larger fault length in our model without making the source time functions too long, though the actual fault length may have been longer, if the rupture had a small bilateral component. As discussed in Chapter 2, the fault width may have been larger, possibly by a factor of two or more, though this would require that the focal depth was a bit greater so that at least half of the vertical rupture could be upward rather than downward.

The seismic moment values determined for each station are listed in Table 6.2. The "average" value, determined according to the method given in Chapter 2, using all stations except QUE, was  $1.7 \times 10^{26}$  dyne-cm, with a "standard deviation" factor (i.e.,  $x/\tau$ ) of 1.7; this is, therefore, one of the larger events in this study, as expected from the reported  $m_b$ . Using these values for seismic moment and fault dimensions we calculate the average slip for this event to be 6.3 m, and for a rise time of 1 sec, the particle velocity is 6.3 m/sec. Using Minster and Jordan's (1978) relative rotation vector between the South American and African



plates, we calculate a total slip rate for this transform of 3.1 cm/yr, which means that this earthquake released slip accumulated over, and thus has a recurrence time of, about 200 years. If we use Minster and Jordan's (1978) rotation vector for the North American and African plates, we obtain a slip rate for the transform of 2.8 cm/yr, and the earthquake's recurrence time is about 230 years. Minster and Jordan (1978) place the North American/South American boundary at about  $15^{\circ}$ , but discuss one earthquake at a latitude of  $19.8^{\circ}$  N which seems to reflect motion between the North and South American plates, implying that the  $15^{\circ}$   $20'$  transform may be between the South American and African plates.

A recurrence time of 200 yrs for earthquakes on this part of the transform is 5 times greater than the 40 years between this event and two large events which occurred on the center of the transform in 1929 and 1930. (The South American-African rotation vector implies a displacement of only 1.3 m for 40 years.) Using the formula given in Chapter 2, we calculate that the stress drop for this earthquake was 280 bars, a value in the range of what we found for the other earthquakes studied. If all of the possible error in displacement were due to an error in fault length (a very unlikely possibility), then the stress drop value would have been 56 bars. If all of the error were due to the fault width value, then the stress drop would have been only 11 bars.

#### THE JUNE 19, 1970 EARTHQUAKE

The second of the three earthquakes in 1970 occurred on June 1, and was the second largest earthquake in the sequence of 1969-1970. The epicenter reported by I. S. C. for this event was  $0.14^{\circ}$  to the west of the large 1969 earthquake, and as stated in the previous section, the frequency of closely spaced events during this period suggests that they

were related.

Weidner and Aki (1973) studied this 1970 earthquake by inverting the Rayleigh waves to obtain the source moment tensor. The fault plane solution they obtained had a fault strike of N 96° E, a fault dip of 70° to the south, and a slip angle of 4°, representing right-lateral strike-slip motion, as expected from the direction of ridge offset. The precision of these values, however, was no more than about 10°. They also presented a fault plane solution, obtained from P wave first arrival polarities, which showed a similar orientation but with a fault plane considerably more vertical. They found a seismic moment value for this event of  $1.03 \times 10^{25}$  dyne-cm, and a focal depth between 3 and 10 km.

We have computed synthetic seismograms for comparison to observed P wave seismograms from this earthquake for 15 WWSSN stations. The station data used are given in Table 6.3; the source velocity structure used is given in given in Table 4.2. The results of the fits between synthetic and observed seismograms, along with fault plane solution used, and the positions of the stations on the lower focal hemisphere, are shown in Figure 6.5. The fault plane solution had a fault strike of 100°, a value close to the bathymetrically inferred strike of the transform, a fault dip of 90°, and a slip angle of 180°. Like the 1969 earthquake, the observed waveforms from the stations to the east were generally shorter and more detailed than those to the west, and we reproduced this effect by using unilateral rupture, propagating horizontally from west to east. The fault plane solution given above was chosen because it provided the best reproduction of the multiple-peaked waveforms observed to the east. This solution is different from that of Weidner and Aki (1973) in that the fault dip is vertical in our solution, though the difference is not

significant, considering the lack of precision in both solutions. Like the results for the Oceanographer transform event of May 17, 1964, we obtained the best results when we used a rupture speed of 4 km/ sec, though we do not believe this necessarily reflects the actual rupture speed during the earthquake. As can be seen in Figure 6.5, and as for most of the events studied here, we were unable to exactly reproduce the waveforms for all of the stations using one set of fault parameters, so that our results represent a somewhat subjective judgement of which features were more significant.

We used a fault length of 10 km, about 6.5 % of the transforms length, and a fault width of 6 km. Since the rupture was taken as horizontal and unilateral, this fault length should be taken as a lower bound, and the actual length may have been perhaps 1.5 times this value, though a value much larger than this would have produced time functions too long, even with a high rupture speed. A lower rupture speed would have produced longer time functions, possibly allowing the use of 5 km for the fault width, but we found the values presented here gave better waveforms for all of the stations. We found the focal depth to be 7 km below sea level, i.e., 3 km below sea floor, and this value could not be varied more than about 0.5 km larger or smaller without significantly changing the synthetic waveforms. This focal depth combined with the fault dimensions and rupture speed produced the multiple-peak waveforms seen in the eastern stations. As mentioned in previous chapters however, this type of waveform is extremely sensitive to small changes in the fault parameters, so that the actual values required by the synthetic seismograms, e.g., a fault width of 6 km instead of, say, 5 km, may not necessarily reflect those of the actual earthquake.

We found a seismic moment for this event, using all stations except BOG and SJG, of  $2.7 \times 10^{25}$  dyne-cm, with a "standard deviation" factor of 1.5. The values found for each station are listed in Table 6.3. Our moment value for this earthquake is larger than that found by Weidner and Aki (1973) by a factor of 2.6 compared to our  $2\sigma$  factor of 2.2. (Our value for the May 17, 1964 event on the Oceanographer transform was larger than theirs for that event also, which suggests that our technique may produce moment values systematically higher than theirs.) This value of seismic moment, with the fault dimensions used, gives an average displacement for this event of 1.3 m, a value which compares well with the other values found in this study when the event sizes are considered, and a stress drop of 58 bars, a value slightly low compared to the others found in this study. As for most of the other events studied we used a rise time of 1 sec, which produces a dislocation velocity of 130 cm/sec.

For the slip rate calculated from Minster and Jordan's (1978) rotation pole for the South American and African plates, this displacement value represents the release of strain accumulated over 42 years. Since this event occurred only 9 months after the large 1969 event, it clearly could not have ruptured the same part of the transform, even though it occurred in roughly the same place, unless the 1969 event did not release all of the accumulated strain on this part of the transform. We consider this unlikely, and note that the orientation between the epicenters, with the 1970 event about 15.6 km to the west of the 1969 event, agrees well with our model of the second event rupturing from west to east over a length of 10 (or slightly more) km. Both of the events appear to have ruptured in the same direction, possibly due to similar stress fields, and the rupture for the 1970 event appears to have stopped when it reached the area fractured by the 1969 event.

## THE DECEMBER 9, 1972 EARTHQUAKE

On December 9, 1972 a large earthquake occurred near the eastern end of the  $15^{\circ} 20'$  transform. I. S. C. located the epicenter at  $15.25^{\circ}$  N and  $45.15^{\circ}$  W, and gave it an  $m_b$  of 5.5, making it roughly the same size as the 1970 event. Since it occurred only 2 years after the 1970 event it may have been related to the 1969-1970 sequence, though it was far enough to the east that it probably did not fracture the same parts of the transform. Though there have been smaller events on this part of the transform, the only other known events in this area with  $M_s$  greater than 5.5 occurred in 1940 ( $M = 6$ , Gutenberg and Richter, 1954) and 1962 ( $M =$  "d" presumed to be 5.6, Rothe, 1963).

We have calculated synthetic seismograms for comparison to observed P wave seismograms from this earthquake for 8 WWSSN stations. The station data used are shown in Table 6.4, and the source velocity structure used is given in Table 4.2. The synthetic seismograms calculated are shown in Figure 6.6, along with the positions of the stations on the lower focal hemisphere and the fault plane solution used for the synthetic seismograms. We used a fault strike of  $N 100^{\circ} E$ , the same value used for the 1970 event, a fault dip of  $89^{\circ}$  to the north, and a slip angle of  $180^{\circ}$ . This solution represents the expected right-lateral strike-slip motion. As for the other events studied, the values presented here offered what we thought was the best fit of synthetic to observed seismograms. There is enough uncertainty in the results so that the actual fault dip might have been  $90^{\circ}$ , i.e., a vertical fault, rather than  $89^{\circ}$ .

We used only three stations to the east of the event, so that the certainty of any east-west directivity is not great, but the waveform

recorded at TOL was shorter than those recorded at the western hemisphere stations. The waveform recorded at JER appeared to be slightly shorter also, though the wave shape was slightly different, and the emergent angle was so small that directivity would not necessarily be apparent anyway. Partly because of these stations, and partly because of the rupture required by the other two events on this transform we studied, we used unilateral horizontal rupture, propagating from west to east. For this event we used a rupture velocity of 3 km/sec because a higher value was not required. The fault dimensions which produced the best fits were a length of 12 km and a width of 5 km. Some ambiguity exists in these values, particularly since so few stations were available. For the synthetic seismograms we obtained the best fits with a focal depth of 6 km below sea level, or 2 km below sea floor.

Using all of the stations except SJG and NAT, whose epicentral distances were less than  $30^\circ$ , we obtained a seismic moment for this event of  $2.8 \times 10^{25}$  dyne-cm, with a "standard deviation" factor of 1.6. Values for each station are listed in Table 6.4. For these fault dimensions and moment, we obtained a displacement for this event of 1.3 m, and for a rise time of 1 sec, a particle velocity of 130 cm/sec. This last value is even less well determined than for most of the other events studied because the small number of stations meant that the fault dimensions, and in particular the rise time, could not be constrained well. For the slip rate calculated from Minster and Jordan's (1978) rotation vector for the South American and African plates, this displacement represents strain accumulated over 42 years. We calculate a stress drop for this event of 58 bars. These values for displacement, recurrence time, and stress drop are the same as those found for the 1970 earthquake.

## TOTAL SEISMIC MOMENT

We can compare the total seismic moment from the observed earthquakes with that predicted by the Minster and Jordan (1978) relative rotation vector for the South American and African plates. For this we calculate moments from the  $M_S$  values for all of the other earthquakes on the transform, using the method explained in Chapter 9. These values are given in parentheses in Table 6.1. To the sum of these values we add the moments found for the three earthquakes studied here, which gives a value of  $6.8 \times 10^{26}$  dyne-cm for the total observed seismic moment since about 1920 (about the earliest events listed by Gutenberg and Richter, 1954). The largest contributions to this total come from the large events in 1929, 1965 and 1969.

To this total moment sum we add a correction for the seismicity too small to be observed, using Formula (7) given in Molnar (1979) (Formula 3.1 in this work). For this we use  $a = 2.0$ ,  $b = 0.52$ ,  $c = 1.18$ , and  $d = 18.6$ , determined in Chapter 9. For minimum  $M_0$  values of  $1.58 \times 10^{25}$  dyne-cm for the years from 1920 to 1963 and  $8.0 \times 10^{22}$  dyne-cm for the years from 1964 to 1981, we obtain unobserved moment rates of  $3.7 \times 10^{24}$  dyne-cm/yr and  $2.0 \times 10^{23}$  dyne-cm/yr, respectively, for these time periods. Since these time periods represent 44 yrs and 18 yrs, respectively, this means unobserved moment totals of  $1.6 \times 10^{26}$  dyne-cm and  $3.8 \times 10^{24}$  dyne-cm. Adding these values to the total observed seismic moment gives a total seismic moment value of  $8.5 \times 10^{26}$  dyne-cm released by earthquakes on the  $15^\circ 20'$  transform since 1920.

From the transform dimensions and the slip rate we have determined the total seismic moment expected on the  $15^\circ 20'$  transform since 1920, using  $M_0 = \mu L w D$  where  $\mu$  is shear modulus,  $L$  is fault length,  $w$  is

fault width, and  $D$  is the total displacement for this 62 year period. For this we used  $\mu = 3.5 \times 10^{11}$  dyne/cm<sup>2</sup>,  $L = 155$  km,  $w = 5$  km, and  $D = 190$  cm, calculated from the rotation vector given by Minster and Jordan (1978). The value of 5 km was used for width because the value used in the synthetic seismograms ranged from 5 to 6 km. The result is an expected seismic moment value of  $5.2 \times 10^{26}$  dyne-cm. This value is about two thirds of the total moment value presented in the previous paragraph, and considering the possible errors, the agreement is quite good. Had we used a width greater than 5 km for the expected moment value, as suggested by the inadequacy of our fault model, then the agreement would have been even better. The implication of this is that most of the strain generated on the transform by relative motion of the plates is released as seismic activity.

#### IMPLICATIONS FOR THE 15° 20' TRANSFORM

A noteworthy feature of the earthquakes on this transform is that two of them required unilateral horizontal rupture, and the remaining one seemed to also. The direction of rupture for all three events was west to east, even though two of them occurred near the center of the transform and one, the 1972 event, occurred near the eastern end. It may be that the mode of rupture is to begin in an area of greatest stress and move in the direction of diminishing strength. Since the bathymetry of the western end of the fault seems to be more complicated than that of the eastern end, and since the average elevation is highest near the western end and decreases to the east, it may be that the prevailing stress field also decreases from west to east, thus producing a consistent rupture direction.



It appears that the seismicity of the transform progresses at **uneven** rates, as indicated by the clustering of events in the center of the transform in 1969 and 1970. The implication is that most of the transform, or at least the central portion which is probably cooler than the ends, remains locked until enough stress is built up to cause an earthquake. That the fault lengths are generally limited to 10 to 20 km suggests that the stress release on the transform occurs in small localized events.

It appears, from the event pairs on this transform alone, that the fault lengths could not have exceeded a few tens of km, and that the displacements for these events are at least on the order of a meter. If the displacement of the 1970 event had been small enough for its recurrence time to be only 9 months, as required if it had fractured the same part of the transform as the 1969 event, then the fault area (length x width) would have been 55 times the values presented here, so that the the entire transform slipped a very small amount. The 1969 event would presumably have had such a larger area as well. This is simply not possible because of the short time functions of the observed seismograms.

Complete rupture of the transform in each of the 1969 and 1970 events would also mean that all of the potential seismic moment for the 1970 event must have been generated during only 9 months. This is similar to what we observed on the both the Oceanographer and Kane transforms, where, after a long dormant period, several large events occurred within a few years along the same portion of the transform. Potential seismic moment is presumably generated by strain at a steady rate; moment is released in large earthquakes at intervals which can vary by a factor of 50 or more, even though the long-term average of released

seismic moment agrees to better than an order of magnitude with the slip-determined generation rate. If each large event fractures the entire transform, then either (1) the displacements must vary, in accordance with the varying recurrence times and the resulting accumulated strain, or (2) each event does not totally release the strain on the transform, regardless of how much strain has accumulated, or (3) the slip rate is not constant, but varies so that the recurrence times can vary also. The first case is not likely, since, historically, the moments of these large events do not vary directly with the length of time since the last event. The second case is not likely because the strain available, and therefore the stress field, for events which follow long dormant periods would be greater. Unless a mechanism is in effect which limits the slip to a maximum value, these earthquakes should be larger, again disagreeing with the historical record. The third case seems unlikely because of the large scale of plate boundaries, though we can not rule it out at this time. We will discuss this possibility in Chapter 9 in more detail and with additional information, and conclude for now that the fault lengths must have been short because of the short time functions.

It is obvious from the results of the 1969-1970 event pair, from the results for the other events presented in this study, and from the coincidence of the admittedly imprecise epicenters of the two large events in 1929 and 1930 on this transform, that the major contributor to the moments for these earthquakes is not large fault lengths, but, rather, either large displacements, large fault widths, or both. Since the fault lengths do not seem to exceed a few tens of km, we suppose that the fault widths are probably not much greater than that either. The

focal depths are generally shallow while the short signal durations require (in addition to short fault lengths) possibly at least half of the vertical rupture to be upward, a fact which limits the fault widths to about 10 km or so. The comparison of total observed moment to slip rate for each transform (Chapters 3 -8) also suggests that the average width for each transform is no more than a few 10's of km or so. Thus the displacements may be less than we have determined, though probably by no more than a factor of two to four, and our largest calculated recurrence times, possibly high at about 200 years, must therefore be at least 50 years. This is indeed short enough for the events in 1969 and 1970 to have fractured the same parts of the transform as those in 1929 and 1930, and the earlier and later events on the other transforms may also have fractured the same parts of those transforms. (This is, in fact, about the length of time for which we have seismic records, a necessary feature if our comparisons of observed seismic moment totals to slip rates are to be valid.)

Table 6.1 Seismicity of the 15° 20' Transform Fault

Date	Origin Time			Lat, °N	Lon, °W	h, km	m <sub>b</sub>	M <sub>s</sub>	No. of sta.	M <sub>0</sub> , 10 <sup>25</sup> dyne-cm
	h	m	s							
7/6/29	9	46	15	14.5	46			6.5		(17)
2/28/30	0	57	56	15	46			6		(4.5)
3/4/40	19	59	05	15.25	45			6		(4.5)
9/23/62	12	02	35	14.7	45.1	32		d		(1.6)
9/20/58	10	34	00	15.5	45.8	n		d		(1.6)
9/13/64	10	29	19.4	15.25	45.0	33	4.3	(3.7)	17	(0.011)
6/2/65	17	43	34.1	15.93	46.70	0	4.8	(4.6)	19	(0.12)
6/2/65	23	00	49	15.3	46.8	33	4.3	(3.7)	6	(0.011)
6/2/65	23	40	23.1	15.93	46.69	27	5.8	6.0 *	209	(4.5)
6/3/65	08	33	13.4	15.4	46.4	33	4.2	(3.6)	7	(0.008)
6/3/65	09	32	57.9	15.86	45.9	33	4.3	(3.7)	18	(0.011)
6/3/65	15	11	29.1	16.0	46.8	45	4.4	(3.9)	17	(0.018)
6/3/65	21	38	56.8	15.82	46.57	136	4.3	(3.7)	14	(0.011)
6/4/65	00	48	17.5	16.0	46.1	33	4.4	(3.9)	13	(0.018)
12/8/66	22	24	15.8	15.19	45.19	33	4.5	(4.1)	13	(0.031)
4/1/67	10	58	08	16	47		4.6	(4.3)	11	(0.053)
4/29/67	09	58	52	15.66	45.9	33	4.4	(3.9)	10	(0.018)
6/12/67	00	48	34	16	46		4.7	(4.4)	9	(0.068)
3/1/68	22	06	44.3	14.63	45.04	33	4.6		36	
3/1/68	23	00	23	14.68	45.08	9	4.7		56	
9/16/68	00	48	33.1	14.60	45.18	33	4.4		23	
7/15/69	20	30	03.0	14.56	45.01	33	4.4		15	
9/24/69	18	03	19.9	15.30	45.78	37	5.8	(6.4)	281	17
9/24/69	19	00	57	15.31	45.73	29	4.5	(4.1)	27	(0.031)
9/24/69	22	26	14	15.51	45.96	12	4.4	(3.9)	13	(0.018)
9/25/69	00	44	31.3	15.1	45.4	33	4.6	(4.3)	13	(0.053)
9/25/69	04	40	9.6	15.33	45.53	33	4.2	(3.6)	20	(0.008)
3/7/70	14	03	42	15.2	45.8	35			7	
6/19/70	14	25	20	15.34	45.92	43	5.5	(5.8)	238	2.7
9/1/70	07	23	14	15.38	45.89	10	4.4	(3.9)	29	(0.018)
1/24/71	10	08	29.4	15.18	44.96	33			8	
7/17/71	03	23	56	15.31	45.26	52	4.6	(4.3)	27	(0.053)
1/11/72	03	04	16	15.23	46.58	25	4.5	(4.1)	52	(0.031)
1/24/72	09	41	32.0	15.32	45.81	33	4.8	(4.6)	66	(0.12)
2/5/72	04	18	43.0	14.56	45.07	33	5.0		65	
12/9/72	06	44	40	15.25	45.15	25	5.5	5.7	235	2.8
1/14/73	08	41	03.9	14.74	45.14	0			16	
1/14/73	08	55	18	14.82	45.11	25	4.7		25	
1/14/73	08	57	29.3	14.88	45.03	33	4.8		31	
8/26/73	07	33	19.3	15.10	44.89	0	4.2	(3.6)	13	(0.008)
12/2/73	09	27	19	15.3	47.4	0	4.3	(3.7)	8	(0.011)
4/22/74	15	26	40.4	15.13	45.22	22	4.5	(4.1)	52	(0.031)
5/27/74	12	18	25	15.81	46.75	38	4.8	(4.6)	56	(0.12)
7/7/74	00	35	21.7	15.2	45.1	33	4.3	(3.7)	7	(0.011)
10/22/74	06	08	04	14.91	45.05	50	4.7		44	
12/31/74	07	00	50.9	15.82	46.92	33	4.3	(3.7)	9	(0.011)
12/27/75	12	57	20.7	15.62	46.41	33	4.8	(4.6)	18	(0.12)
6/2/76	02	41	50.5	15.71	46.57	33			7	

Table 6.1 (cont'd)

Date	Origin Time			Lat, °N	Lon, °W	h, km	$m_b$	$M_S$	No. of sta.	$M_0$ 10 <sup>25</sup>
	h	m	s							
6/19/77	18	12	44.4	15.45	46.61	33	4.6	(4.3)	19	(0.053)
6/19/77	18	17	37.6	15.47	46.67	22	5.2	4.6	136	(0.12)
6/26/77	10	27	10.6	15.26	44.88	33	4.6	(4.3)	37	(0.053)
12/12/77	07	38	17.4	15.44	46.71	33	4.8	(4.6)	8	(0.12)
9/30/78	10	25	39.0	15.50	46.69	10	5.4	(5.7)	15	(2.1)
5/17/79	3	47	3.1	15.70	46.49	10	4.6	(4.3)	18	(0.053)
10/14/79	4	13	34.9	15.95	47.02	33			6	

\*  $M_S$  taken from Rothe (1969); other data taken from I. S. C. Regional Bulletin.

This table includes all events on the Mid-Atlantic Ridge between 14.5°N and 16°N, which includes the 15° 20' transform fault. Data for the events before 1955 were taken from Gutenberg and Richter (1954). Data for events between 1955 and 1963 inclusive were taken from Rothe (1969). Data for events from 1964 to 1979 were taken from the ISC Regional Bulletin. For depth, n refers to "normal depth, (focus situated in the crust or at its base)", from Rothe (1969). We have taken magnitudes reported before 1964 as equivalent to  $M_S$ .  $M_S$  values shown in parentheses were determined from  $m_b$  using Equation 9.1. Except for those noted, other  $M_S$  values were taken from the same source as the other data for that event; d refers to a Gutenberg and Richter (1954) or Rothe (1969) listing as between 5.3 and 5.9, assumed here to be 5.6. The  $M_S$  values in parentheses were determined for all events whose  $M_S$  was not available from another source and whose location placed them on the 15° 20' transform fault. The  $M_0$  values shown in parentheses were determined from  $M_S$  using Equation 9.2. These values in parentheses were determined for all events whose moment was not determined in this study and whose location placed them on the 15° 20' transform fault.

Table 6.2. Station data used for synthetic seismograms  
for the earthquake of September 24, 1969.

<u>Station</u>	<u>Distance, degrees</u>	<u>Azimuth, degrees</u>	<u>Magnification</u>	<u><math>10^{25} M_0</math>, dyne-cm</u>
LPB	38.5	215.8	1500	16
ATL	39.2	304.5	3000	7.7
PTO	41.2	43.9	1500	19
SHA	41.6	299.1	1500	12
AAM	42.2	317.3	1500	11
OXF	43.6	304.2	3000	7.6
TOL	43.8	47.7	1500	21
LPA	51.3	192.8	750	67
ESK	51.6	29.6	1500	18
LOR	51.9	41.3	1500	28
STU	55.8	41.0	750	19
GOL	57.1	307.6	1500	11
ATU	64.7	55.0	1500	20
NUR	67.2	30.4	1500	19
IST	68.7	51.6	1500	16
KEV	69.8	20.7	1500	17
QUE	101.2 **	54.5	6000	4.1 *

\*  $M_0$  values not used to find "average" for this event.

\*\* Value actually used in synthesis was 99.5°.

For all stations we used  $T_p = 15$  sec,  $T_g = 100$  sec,  $H_p = .93$ ,  $H_g = 1.0$ , where  $T_p$ ,  $T_g$ ,  $H_p$ , and  $H_g$  refer to the seismometer and galvanometer periods and damping factors, respectively.

Table 6.3. Station data used for synthetic seismograms  
for the earthquake of June 19, 1970.

<u>Station</u>	<u>Distance, degrees</u>	<u>Azimuth, degrees</u>	<u>Magnification</u>	$10^{25} \frac{M_0}{\text{dyne-cm}}$
SJG	19.6	280.9	750	35 *
BOG	29.6	251.9	3000	3.6 *
QUI	35.7	247.3	3000	4.7
OGD	35.7	321.5	6000	1.7
BLA	37.5	312.1	1500	2.2
ATL	39.1	304.5	3000	2.0
PTO	41.3	44.0	1500	4.1
MAL	42.5	52.0	1500	3.7
OXF	43.4	304.2	3000	1.5
TOL	43.9	47.8	1500	4.2
FLO	45.4	309.8	1500	1.7
TRI	58.1	45.5	3000	3.8
IST	68.8	51.6	1500	3.2
HLW	71.6	63.2	3000	2.2
JER	74.6	60.8	3000	3.4

\*  $M_0$  values not used to find "average" for this event.

For all stations we used  $T_p = 15$  sec,  $T_g = 100$  sec,  $H_p = .93$ ,  $H_g = 1.0$ , where  $T_p$ ,  $T_g$ ,  $H_p$ , and  $H_g$  refer to the seismometer and galvanometer periods and damping factors, respectively.

Table 6.4. Station data used for synthetic seismograms  
for the earthquake of December 9, 1972.

<u>Station</u>	<u>Distance, degrees</u>	<u>Azimuth, degrees</u>	<u>Magnification</u>	$10^{25} \frac{M_0}{\text{dyne-cm}}$
SJG	20.3	281.0	750	19 *
NAT	22.6	152.9	1500	1.2 *
BOG	30.3	252.6	3000	2.4
OGD	36.3	321.0	3000	1.3
LPB	38.9	216.6	1500	4.1
ARE	40.9	220.6	1500	2.4
TOL	43.4	47.4	1500	3.5
JER	74.1	60.8	3000	4.9

\*  $M_0$  values not used to find "average" for this event.

For all stations we used  $T_p = 15$  sec,  $T_g = 100$  sec,  $H_p = .93$ ,  $H_g = 1.0$ , where  $T_p$ ,  $T_g$ ,  $H_p$ , and  $H_g$  refer to the seismometer and galvanometer periods and damping factors, respectively.



### Figure Captions

Figure 6.1 Bathymetry of the 15° 20' transform fault between 14.5° N and 16° N, and 44° W and 48° W, and epicenters of all known earthquakes in this area, taken from Table 6.1. The approximate locations of the ridge axes are indicated by double lines. Open circles represent epicenters taken from Gutenberg and Richter (1954) and Rothe (1969). Larger symbols are events with  $M_S > 6.0$ . Contour intervals are every 800 m below sea level, taken from Uchupi (1982).

Figure 6.2 Longitude versus year of occurrence for the earthquakes on the 15° 20' transform fault with  $M_S > 5.5$ .  $M_S$  is shown for each event. Dashed lines indicate transform intersects adjacent spreading centers. The bars for the events of 1969, 1970, and 1972 indicate the fault lengths and rupture directions used for the synthetic seismograms.

Figure 6.3 Fault plane solution, from P wave first-arrival polarities, of the September 24, 1969 earthquake on the 15° 20' transform, determined by Solomon (unpublished). Closed circles represent compressional arrivals and open circles represent dilatational arrivals.

Figure 6.4 Results of fits of synthetic (upper) to observed (lower) seismograms of P waves from the September 24, 1969 earthquake on the 15° 20' transform. Positions on lower focal hemisphere of stations used for synthesis and fault plane solution obtained are also shown. Closed circles for station locations represent compressional first-arrival polarities and open circles represent dilatational polarities. The vertical scales were normalized so that all seismograms would have equal maximum amplitudes.

Figure 6.5 Results of fits of synthetic (upper) to observed (lower) seismograms of P waves from the June 19, 1970 earthquake on the  $15^{\circ} 20'$  transform. Positions on lower focal hemisphere of stations used for synthesis and fault plane solution obtained are also shown. Closed circles for station locations represent compressional first-arrival polarities and open circles represent dilatational polarities. The vertical scales were normalized so that all seismograms would have equal maximum amplitudes.

Figure 6.6 Results of fits of synthetic (upper) to observed (lower) seismograms of P waves from the December 9, 1972 earthquake on the  $15^{\circ} 20'$  transform. Positions on lower focal hemisphere of stations used for synthesis, and fault plane solution obtained are also shown. Closed circles for station locations represent compressional first-arrival polarities, open circles represent dilatational polarities, and crosses represent observed polarities which were either susceptible to misinterpretation or in disagreement with the corresponding synthetic polarity. The vertical scales were normalized so that all seismograms would have equal maximum amplitudes.

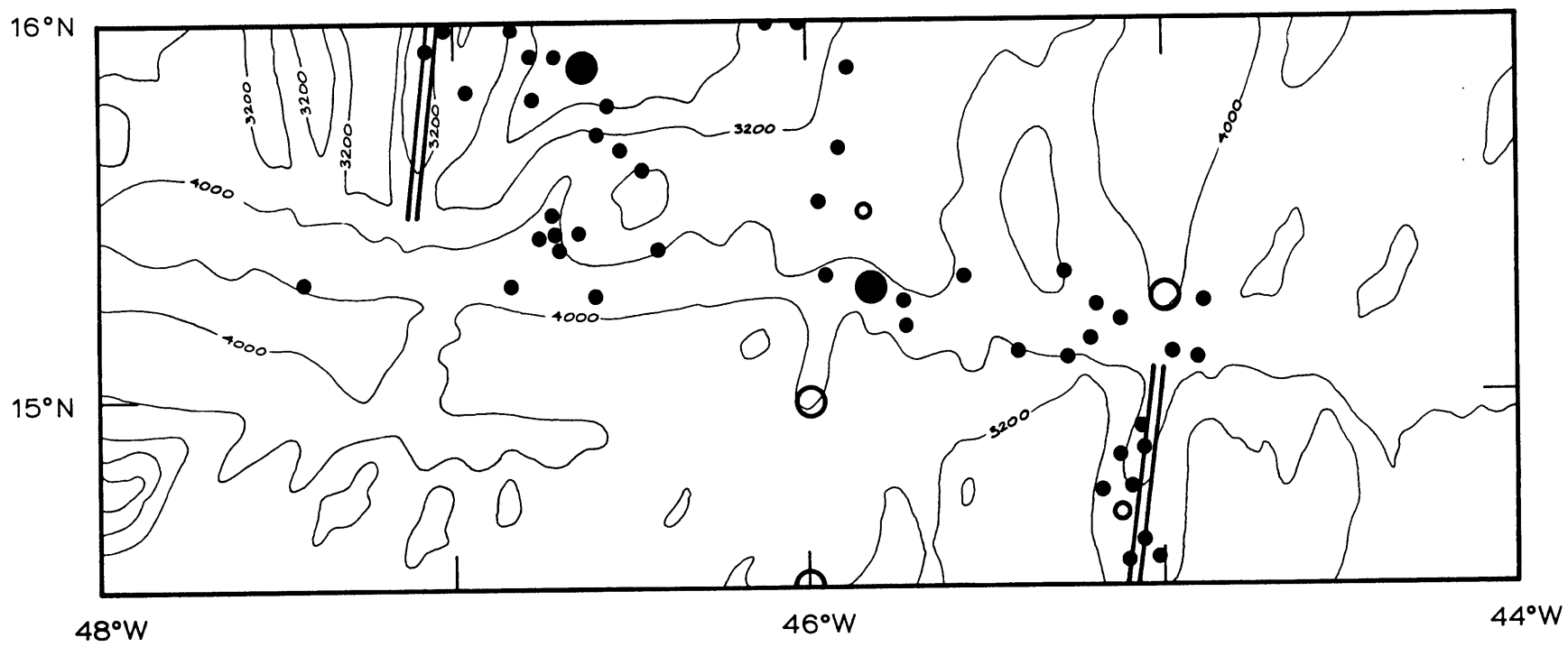


Fig. 6.1

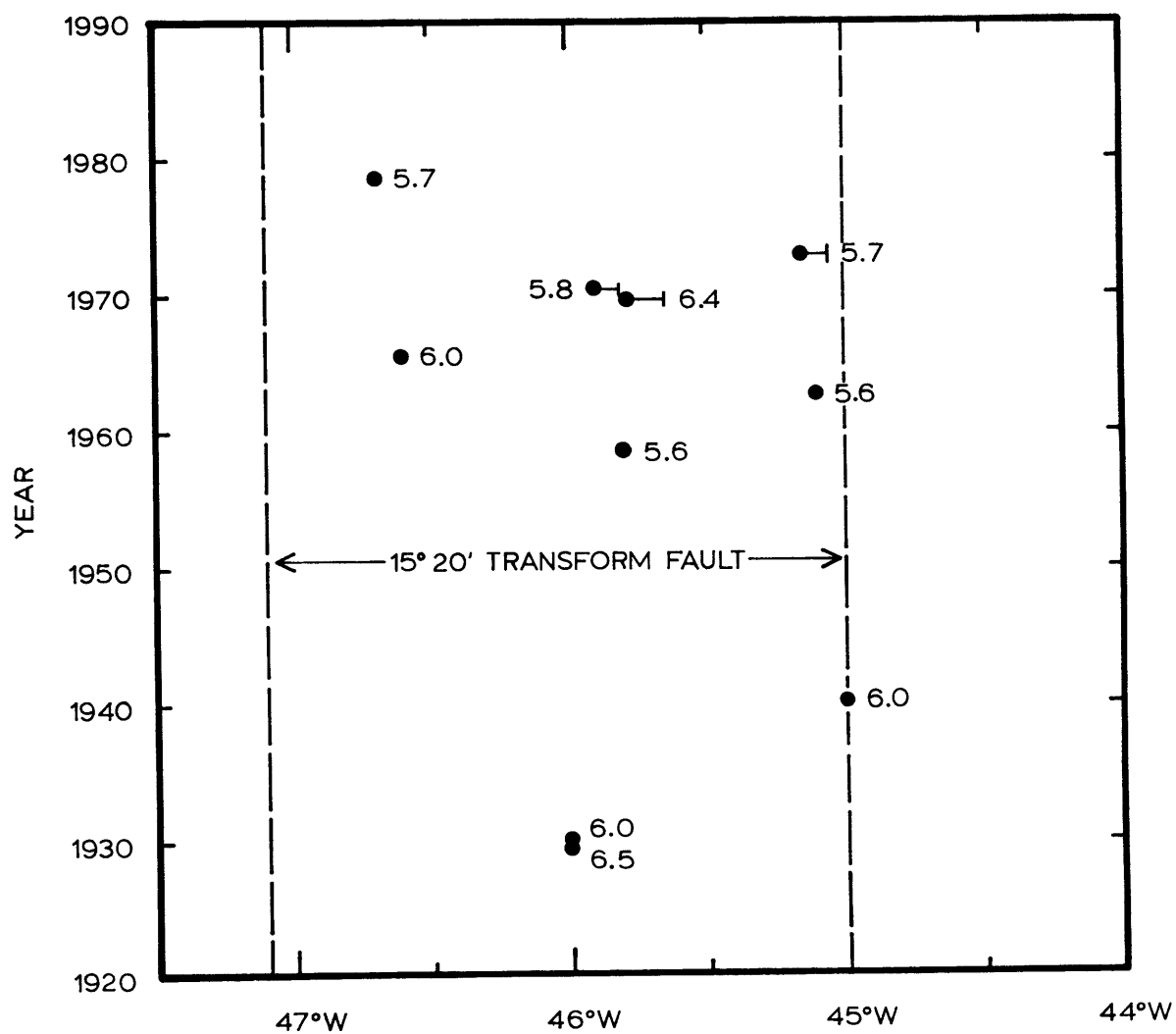


Fig. 6.2

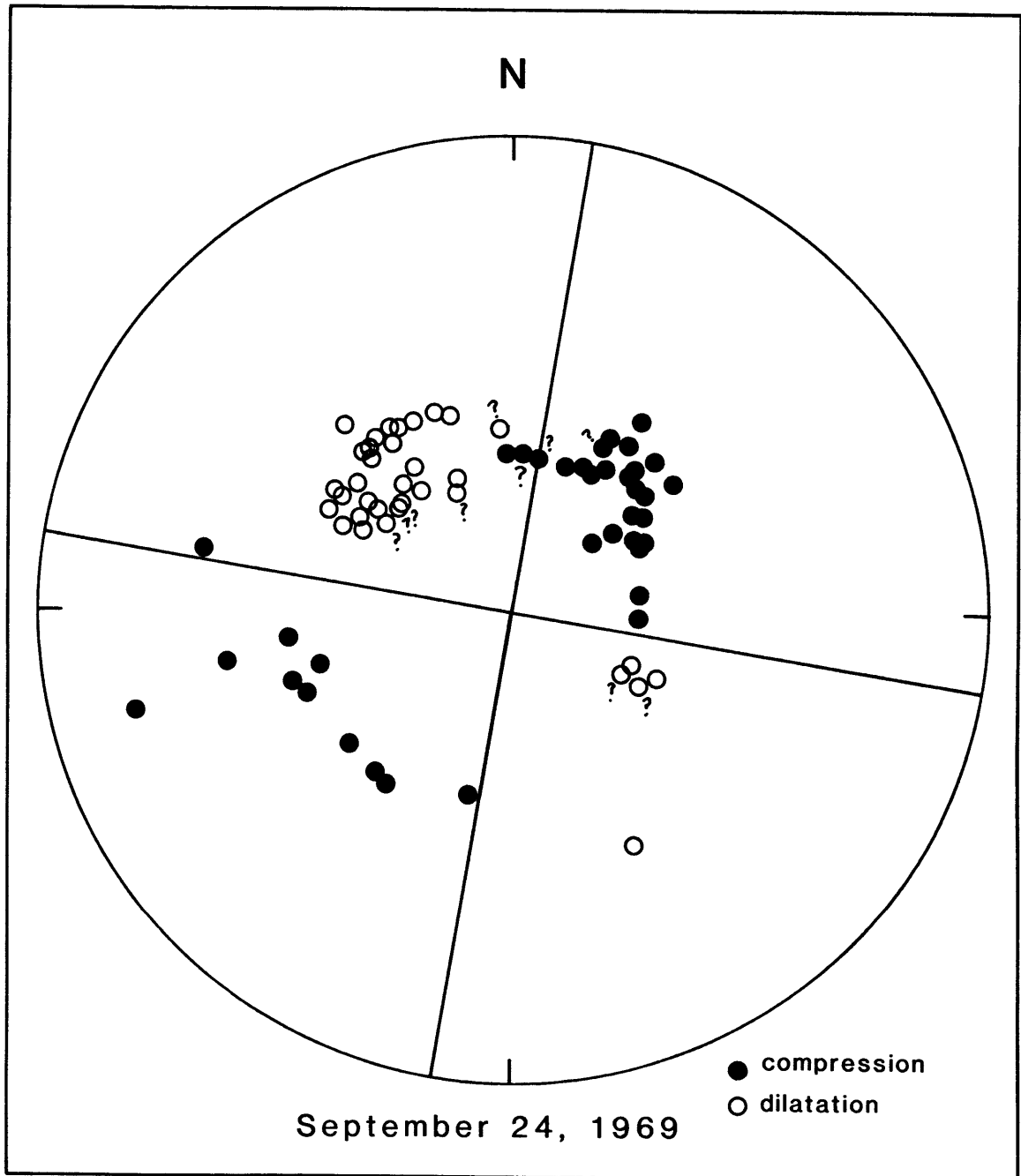


Fig. 6.3

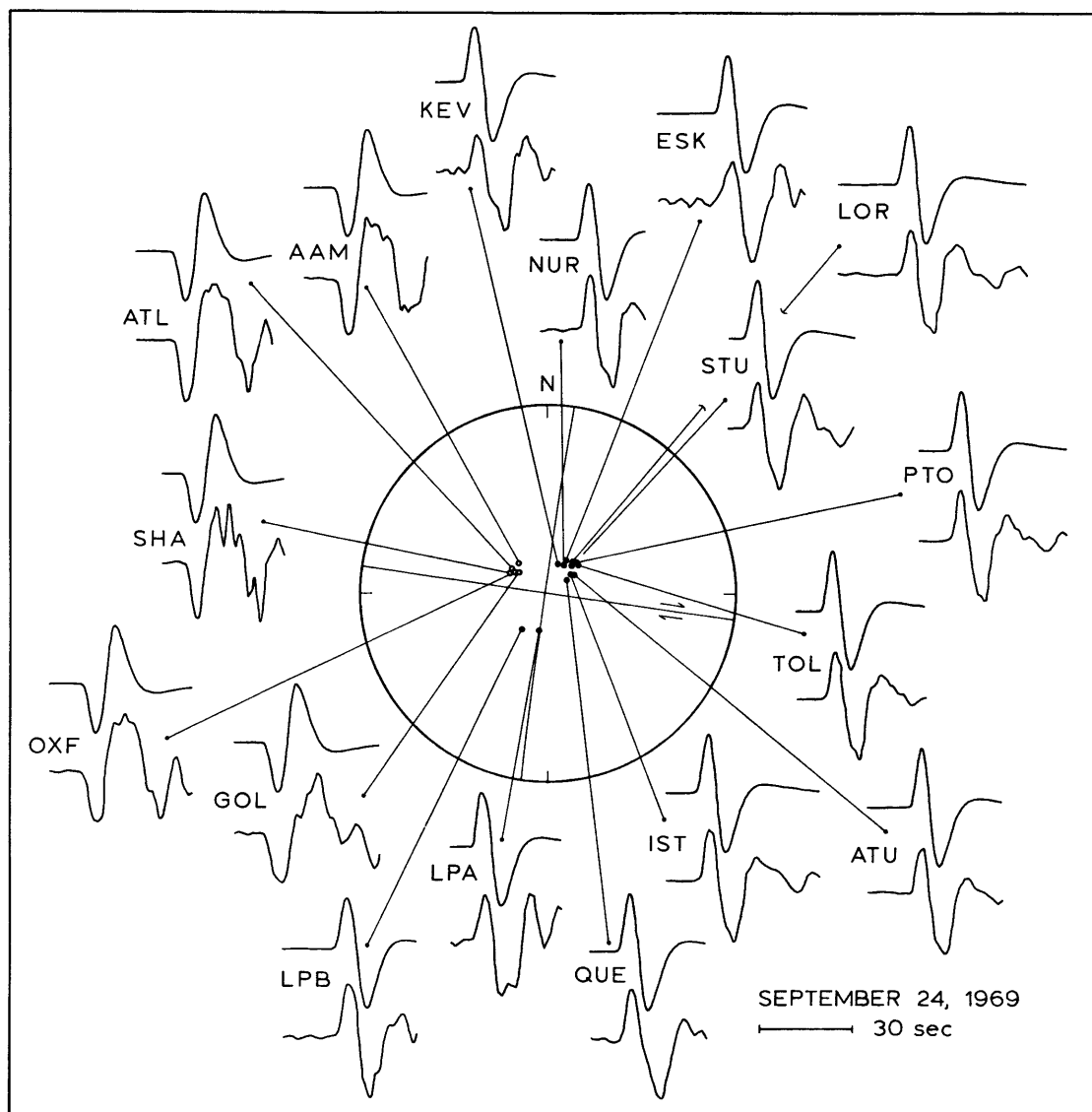


Fig. 6.4

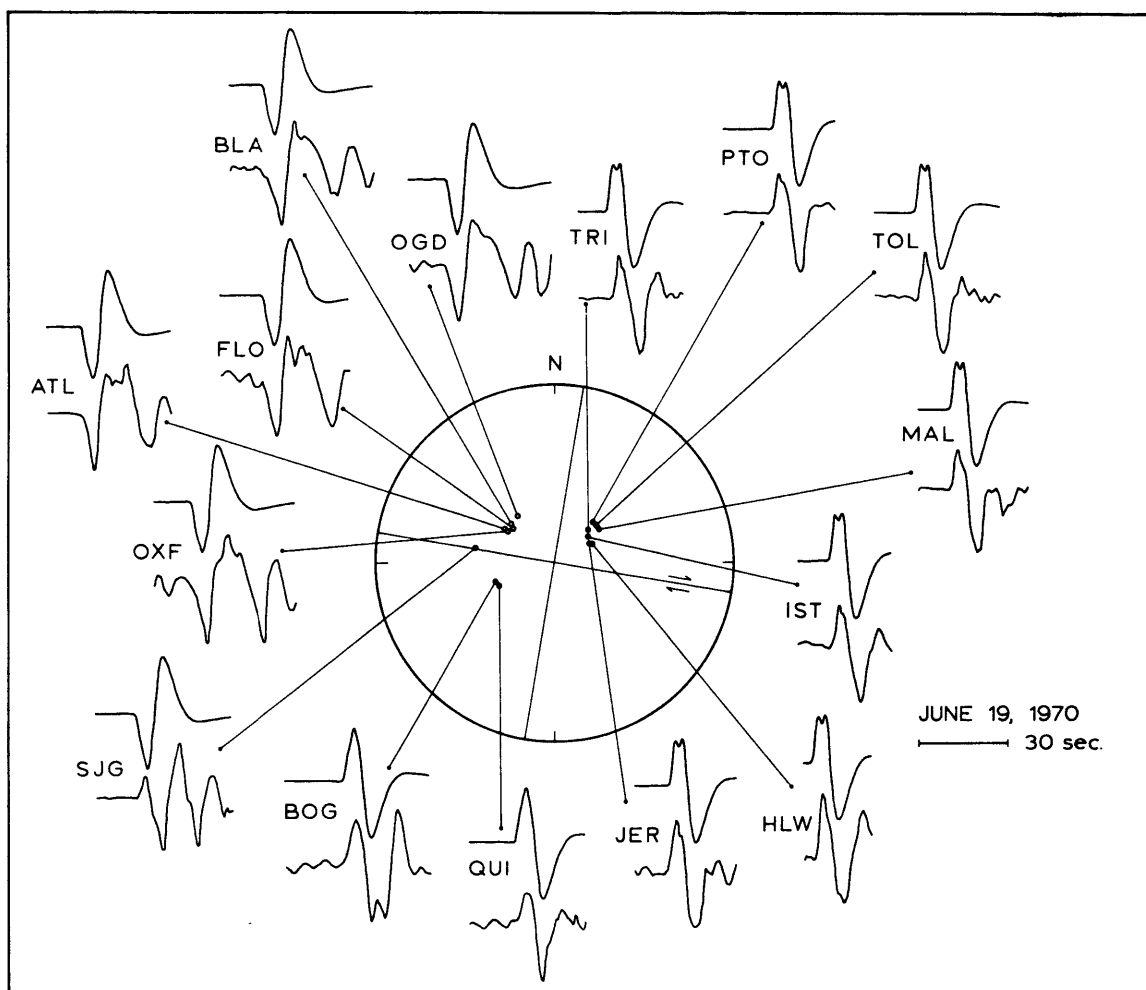


Fig. 6.5

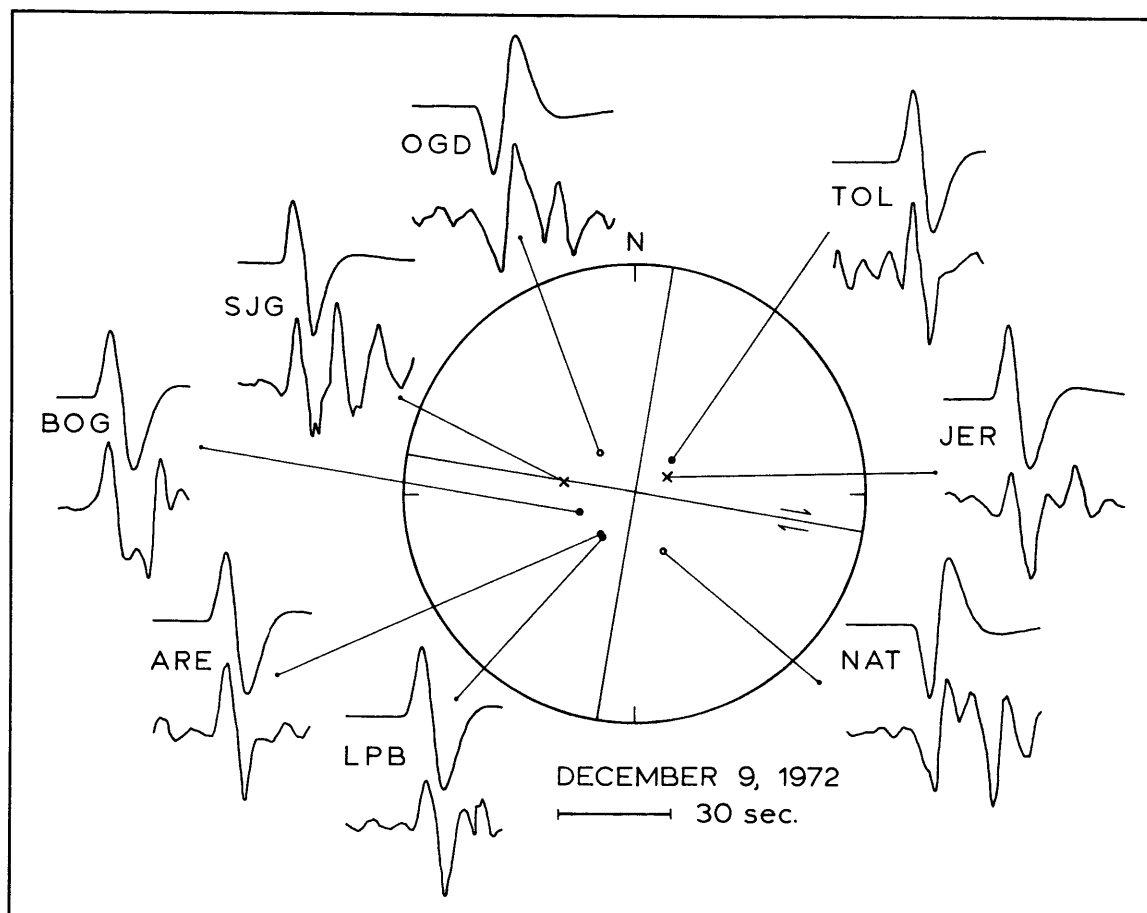


Fig. 6.6



## CHAPTER 7. EARTHQUAKES AND TECTONICS OF THE VEMA TRANSFORM FAULT

The Vema transform fault is a 320 km long left-lateral offset of the Mid-Atlantic Ridge at about 11° N. It was surveyed by the R. V. Vema in 1956 and described by Heezen et al. (1964). Van Andel et al. (1971) reviewed the results of all previous surveys of the Vema transform fault, and presented bathymetric, magnetic and heat flow details. They proposed a model of the transform in which re-orientation occurred because of a change in spreading direction about 10 m.y. ago, with slow spreading taking place along the edges of the valley and not in the center. The bathymetry of the Mid-Atlantic Ridge from 10°N to 13°N, from Uchupi (1982), is shown in Figure 7.1. The transform is characterized by a central valley which has a depth of about 5000 m below sea level, an average width of about 20 km, and walls with slopes of about 15°. The southern edge of the transform is paralleled by a transverse ridge which rises to heights of 3000 m above adjacent sea floor, and in places is within about 600 m of sea level. This wall has an average width of about 30 km and a length of about 400 km. A similar wall exists on the northern edge of the valley, but is not as high, rising to about 2000 m above the sea floor. Heat flow values are uniformly high in the valley trough and vary over the adjacent ridge segments (van Andel et al., 1971). Similar results were reported by Langseth and Hobart (1976), who offered a model for the thermal structure in a transform fault which predicts uniform heat flow.

Eittreim and Ewing (1975) presented the results of seismic reflection profiles which showed flat-lying sediments in the valley floor and a disturbance in the center which they interpreted as an active fault

trace running the entire length of the transform. This was present in every profile except one, where there was no sediment in the expected area due to an uplift in the basement at that point. The existence of this fault suggested that recent displacement along the transform has occurred on a single strike-slip fault along the center of the transform, and not at the northern or southern edges of the transform. Robb and Kane (1975) showed two gravity and magnetic anomaly profiles recorded across the transform by the R/V Unitedgeo I in 1971. They concluded that there is probably a mass excess beneath the southern wall and a smaller excess beneath the northern wall, and that observed anomalies in the transform valley itself were due to shallow sources. They also concluded that the southern wall is partially composed of rocks with low magnetization. On the basis of dredge hauls in the Vema and Romanche fracture zones, Bonatti and Honnorez (1976) concluded that the northern wall of the Vema transform valley is probably an exposed section of "normal" oceanic crust, while the southern wall represents crustal generation by processes that are restricted to fracture zones, and that these processes include diapiric intrusions of mantle-derived serpentinized peridotite, intense tectonization, minor basaltic volcanism, and hydrothermal activity. These processes are similar to those proposed by Fox et al. (1976) to explain features of the Oceanographer Fracture Zone.

Rowlett and Forsyth (1979, 1983) and Rowlett (1981) presented the results of an ocean-bottom seismometer survey and seismic reflection profiles from the western end of the Vema transform. The reflection data showed that a depression exists in the basement bathymetry at the western end of the transform, similar to what has been observed in other transforms with less sediment, but that this depression is probably not a

steady-state feature. A fault trace was apparent in the reflection data, presumably defining the active transform zone, and the transition between this zone and the adjacent spreading center appeared to be only 1 to km wide. The ocean-bottom seismometer experiment included observations of microearthquakes and one teleseism, an intermediate depth earthquake in southern Peru. The microearthquakes were concentrated along the eastern (inner) wall of the bathymetric depression at the intersection of the ridge and the active transform. (This was also observed at the intersections of other transforms in the Atlantic Ocean.) The P-wave arrivals for the teleseism showed anomalies from expected values calculated from Jeffreys-Bullen tables. The anomalies ranged from 1.31 sec to 1.81 sec, with the largest anomalies observed at the stations located in the center of the depression. The deviation in the observed anomalies was too great to be explained by differences in crustal thickness, but rather required low velocities in the upper mantle immediately beneath the depression, possibly due to extension of the ridge-upwelling into the end of the transform valley.

Ludwig and Rabinowitz (1980) give the results of seismic reflection surveys crossing the transform valley and seismic refraction surveys running parallel to the valley down the valley center and southern wall. Their results showed that the seismic velocity structure beneath the valley was variable and could not be correlated easily with a "typical" ocean floor structure. They calculated that the sediment in the valley is possibly as much as 1500 m thick, and thus the depth to basement may be between 6200 m and 6700 m below sea level. They detected what they interpreted to be oceanic layer 3 beneath the valley floor, with a P-wave velocity between 5.9 km/sec and 6.2 km/sec and a thickness of about 2.6

km, both of which are less than "normal" for oceanic crust. They found that the crustal thickness was maintained at near normal values by the presence of a layer above layer 3 with a velocity of 4.3 km/sec and a thickness of 2 km. This structure is similar to that found by Fox et al. (1976) from seismic refraction profiles on the Oceanographer transform fault. Results of a seismic refraction experiment in the Vema transform valley were reported by Detrick et al. (1982), who found a velocity structure quite similar to that of Ludwig and Rabinowitz (1980). That the crust may be thinner than normal is supported by gravity data from the adjoining ridge median valley (Prince and Forsyth, 1981).

#### SEISMICITY

The known earthquakes on the Vema transform fault are listed in Table 7.1, and the epicenters are shown in Figure 7.1. This list includes all earthquakes between 10.5°N and 12.0°N and between 40°W and 45°W; the events which occurred near 12°N were listed because they apparently represent the seismicity on another transform fault at this latitude. These data were taken from the same sources as Table 3.1. The epicenters of the events which occurred prior to 1964 are not as well determined as the epicenters of the more recent events.

Major seismic activity (i.e., with  $M_S > 6$ ) has occurred during the years of 1925-1927, 1962, 1975, and 1979. In Figure 7.2 we have plotted longitude vs. year for all of the events listed in Table 7.1 with  $M_S > 5.5$ . These earthquakes have occurred during three episodes, spanning the years 1925-1929, 1955-1963, and 1975-1979, and each episode included at least one event with  $M_S > 6$  (in fact, with  $M_S > 6.6$ ). In each episode, events occurred on both ends of the transform. The episode of 1925-1929 had three very large events, and the resulting stress release may have

been a factor in the 26 year gap before the episode of 1955-1963. It is noteworthy that each of the two larger events on the transform just to the north of the Vema (in 1954 and 1979) seems to herald the start of one of these episodes. The episodic nature of the seismicity will be discussed further in Chapter 9.

The August 25, 1975 event was preceded by about 7 minutes by a large earthquake in Chile ( $m_b = 5.7$ ). Thus the seismic arrivals for the transform event were obscured by the surface waves from the Chilean event. According to I.S.C. only 28 stations reported arrival times for this 1975 transform event with  $m_b = 5.7$ , while 307 stations reported arrival times for the very similar transform event in 1976 with  $m_b = 5.5$ . Therefore both the magnitude and epicenter for the 1975 earthquake are likely to have large uncertainties.

#### THE MARCH 17, 1962 EARTHQUAKE

The largest earthquake ( $M_s = 7.0$ ) on the Vema transform since the episode of 1925-1929 occurred on March 17, 1962. It was the fourth of the five events in the 1955-1963 sequence, and it occurred near the western end of the transform. Sykes (1967) determined a fault plane solution for the earthquake and showed the motion to be right-lateral strike-slip, as expected from the concept of a transform fault on a left-lateral offset of the Mid-Atlantic Ridge. The nodal plane interpreted as the fault plane was nearly vertical, with a strike of  $N90^\circ E$ , in agreement with the spreading direction of the adjacent ridge. This was the largest earthquake which we studied.

We have computed synthetic seismograms for comparison to long-period vertical seismograms from 9 WWSSN stations for the March 17, 1962 earthquake. (Fortunately a number of WWSSN stations were operational

this early in 1962.) Station data are given in Table 7.2. We used the crustal velocity structure given in Table 4.2, taken from a seismic profile along the Vema Fracture Zone (Ludwig and Rabinowitz, 1980), and a depth to oceanic basement of 5.7 km.

Results of the synthesis, along with the positions on the lower focal hemisphere of the stations used and the fault plane solution which produced the best fits, are shown in Figure 7.3. The fault plane had a strike of N 85° E and a dip of 82.5° to the north. The slip angle used was 183°. The depth determined for this event was 7.8 km below sea level, or 2.1 km below the basement floor, and near the boundary between the top two layers of the crust. The precision of this depth value necessary to produce the waveforms shown in Figure 7.3 was about  $\pm 0.2$  km; considering the uncertainties in the fault model, fault dimensions, and velocity structure, however, the true uncertainty is probably closer to about  $\pm 1$  km.

The most significant feature of these seismograms is the apparent wrong polarity of the first arrivals for stations BEC, GEO, ALQ, and IST. We produced synthetic waveforms to match the observed seismograms by using a non-vertical fault plane and slightly non-horizontal displacement, thus increasing the ratio of pP amplitudes to those of the P phases. The use of a fault strike which deviated from that of the transform also helped the fits for North American stations, though the main motivation for this choice was to improve the fit at the nodal stations, i.e., ALQ, BHP, and IST. We were unable to obtain a good fit for station BHP.

Another interesting feature of the observed waveforms for this earthquake is that they had large amplitudes and short time durations.

In fact the time duration for the displacement to reach its first maximum and return to zero for most stations was less than 10 sec, about the same as that for the 1976 event ( $M_S = 5.7$ , studied in the next section) even though the 1962 event had a seismic moment about 24 times greater!

Figure 7.4 shows a comparison of the observed P waveforms for these two earthquakes for all 5 of the stations which were used for both events. The maximum amplitudes have been normalized so that the wave shapes may be compared easily, but the horizontal scale is the same for all 10 seismograms. The total signal lengths for each event are about the same for three of the stations, and only for LPB is the difference more than a factor of perhaps 1.5. Short time functions such as these required that, for our model, these two events have similarly small fault dimensions, and thus much larger displacements for the 1962 event than for the 1976 event. An alternate explanation for these waveforms is offered by the discussion of fault width in Chapter 2. Though a similar, non-vertical fault dip was necessary for both events, it is possible that the waveform features observed for both events could have been produced by source finiteness effects on completely vertical faults. Upward or partially bilateral vertical rupture could have produced the "wrong" polarities of the apparent first motions as well as some of the "precursory" phenomena observed for the 1962 event. Some deviation of the fault plane from vertical was probably necessary in order to make the waveforms different between North and South America, though not as much deviation as suggested by these synthetic seismograms. We suspect also that, because of this uncertainty in the nature of the faulting process, the actual fault strike for the 1962 event was probably closer to that of the transform than the value used for our synthesis.

The total moment found for this event was  $1.3 \times 10^{27}$  dyne-cm, making it the second largest value we found in this study (the largest being for the more complex 1979 event on the Vema transform, presented later in this chapter). The values found for each station are shown in Table 7.2; the "standard deviation" factor for these is 2.9. It should be noted that the moment value found is dependent on the fault orientation used; had we used a more vertical fault plane, the moment would have been smaller. The fault length used was 30 km, with bilateral horizontal rupture at a speed of 3 km/sec, and the fault width used was 10 km. Since the fault was nearly vertical and rupture was bilateral, the effects for fault length, fault width, and rise time are not very separable. This length of 30 km is slightly less than 1/10 of the total transform length. Had we used a higher rupture speed, say 4 km/sec, the fault length could have been set higher, in this case 40 km.

The displacement found for the 1962 earthquake was 12 m, which represents relative plate motion for 375 years according to Minster and Jordan's (1978) relative rotation vector between the South American and African plates. For a rise time of 2 sec, this means a dislocation velocity of 600cm/sec. For the reasons discussed in Chapter 2 about the uncertainty in the fault dimensions, which is probably most severe for very large events such as this one, and because the seismic history of this transform suggests that it may have fractured completely during the seismic episode of 1925-1929, we suspect that these figures for displacement and dislocation velocity are too high by at least a factor of 2, and that the fault length was probably a greater fraction of the transform's length than indicated by our results. However, even if the error for displacement is as large as a factor of 3, it still produces a



displacement about equal to that found for the 1964 earthquake on the Oceanographer transform, and a particle velocity on the order of a few meters per second.

The calculated value for displacement and the value for fault width we used produce a value for stress drop for this event of 267 bars. This value is similar to that found for the 1964 earthquake on the Oceanographer transform, and, similarly, an error in the fault width of a factor of 2 could produce a stress drop as great as 1000 bars or as low as 50 bars.

#### THE MAY 14, 1976 EARTHQUAKE

The seismic episode of 1975-1979 involved as many as three large earthquakes. We did not study the first of these because it was preceded by a large earthquake in Chile, whose surface waves obscured the arrivals of the transform earthquake.

We have computed synthetic P-waves for the May 14, 1976 earthquake for comparison to observed seismograms from the records of 15 WWSSN stations. Station data are given in Table 7.3. The adopted velocity structure and the depth to oceanic basement are the same as for the 1962 event.

The results of the synthesis are given in Figure 7.5, along with the fault plane solution found and the location on the lower focal hemisphere of the stations used. The fault strike was taken as the strike of the Vema transform fault, i.e.,  $N 91^{\circ}E$ . The best fitting waveforms were obtained with a fault dip of  $81^{\circ}$  to the north and a slip angle of  $182^{\circ}$ . An interesting feature of the observed waveforms was the small apparent first motion and seemingly wrong polarity at the North American stations and at stations IST and ATU. Except for the amplitudes, these waveforms

look quite similar to those from the 1962 event (note stations GEO and IST in Figure 7.4). Another noteworthy feature was that the waveforms observed at the stations in South America were slightly shorter than those observed at stations in the northern hemisphere. Both of these features were treated in the synthetic seismograms by using a non-vertical fault plane, though the waveforms produced for the South American stations are still not quite as short as those observed. The ratios of  $pP$  and  $sP$  to  $P$  necessary for these waveforms could have been produced with vertical rupture though the fault dip must still be non-vertical to produce a different effect for stations in North and South America. This fault plane solution is similar to that found for the March 17, 1962 event.

The fault length was found to be 15 km and the fault width used was 5 km. Rupture was taken to be bilateral because no directionality was apparent in the observed waveforms; rupture velocity was taken to be 3 km/sec because that value has been used by others (e.g., Kanamori and Stewart, 1976) and a higher velocity was not required to produce the short duration of the source time functions. Rise time was taken to be 1 sec. The observed waveforms had fairly impulsive arrivals so that the total effect of the rise time and fault width could not be greatly increased, even though there is ambiguity between these components of the source time function and the rupture time over the fault length.

As discussed in Chapter 2, there normally is very little resolution between rise time and fault width. In this case the fact that the fault plane was not vertical meant that the effect of the fault width was seen differently between stations to the north and the south. Since the southern hemisphere stations "saw" the fault plane from a position closer

to the plane's normal, the width effect was diminished for these stations, though not enough to produce the observed difference between stations to the north and those to the south. The fact that the waveforms observed in the southern hemisphere were still shorter than those synthesized might suggest that the fault plane should have dipped even less than  $81^\circ$ ; however, a smaller dip would have changed the wave shapes to produce poorer fits to those observed. Perhaps this means that the seismic velocity used at the source should have been higher, so that the emergent angles would have been larger, thus allowing both a slightly smaller dip and emergent rays more normal to the fault plane for stations in the southern hemisphere. The synthetic seismograms required that the fault dip be within about  $1^\circ$  of  $81^\circ$ . Because of uncertainties in the velocity structure the actual uncertainty in the fault dip is actually greater than  $1^\circ$ , but it is probable that the fault plane could not have been vertical to produce the observed waveforms.

The focal depth was found to be 7.5 km below sea level, which places the focus in the uppermost non-sedimentary layer of the crust, 1.8 km below the basement-sediment boundary, and 0.4 km above the next deepest layer. As for the 1962 results, the actual uncertainty in the depth is probably about  $\pm 1$  km. This depth was chosen because it produced the best relative size between the largest amplitude peaks and the smaller first-motion peaks for the stations with the more detailed waveforms. The focal depth for this event could not be made as deep as the base of the crust (10.5 km below sea floor) or as shallow as the sediment-basement boundary.

The moment values determined for each of the stations used are listed in Table 7.3. The "average" was  $3.1 \times 10^{25}$  dyne-cm, with a

"standard deviation" factor of 1.4. Stations CAR, SJG, and BEC were not used to find the average because their epicentral distances were less than  $30^\circ$ . This moment value and the inferred fault dimensions imply a total displacement of 1.2 m, and for a rise time of 1 sec, a particle velocity of 120 cm/sec. This last value is similar to that found for the other events studied here. Since the transform is about 320 km long this event represented strain release on about 1/20 of the transform's length. The only way for this fraction to be increased and still produce the required short source time functions would be to further reduce the fault width and/or rise time, to use a higher rupture velocity, or introduce a finite vertical rupture speed, and thus allow the fault width to be greater. The total spreading rate for the Vema transform, as calculated from Minster and Jordan's (1978) relative rotation vector between the South American and African plates, is 3.1 cm/yr, so that the displacement calculated for this earthquake represents the release of strain accumulated over, and therefore a recurrence time for this part of the transform of, 36 years.

Using the calculated displacement and the values of  $\mu$  and fault width as used for the synthetic seismograms, we have obtained a stress drop for this earthquake of about 53 bars. This value is in the range of those found for the other earthquakes studied here, and is subject to similar uncertainties.

#### THE AUGUST 25, 1979 EARTHQUAKE

The final earthquake on the Vema transform fault treated in this study occurred on August 25, 1979. The large size of the event ( $m_b = 6.0$ ,  $M_s = 6.6$ ) may be related to the fact that the transform had no large earthquakes during the subsequent 2 1/2 years. Whereas the earthquake in

1976 occurred near the western end of the transform, the August 1979 event and a smaller preceeding one ( $m_b = 4.7$  on February 11, 1979) occurred on the eastern part. Interestingly, the 1979 events were preceeded by a large earthquake ( $m_b = 5.7$ ,  $M_s = 5.6$ ) earthquake on the transform to the north of the Vema transform, as part of the pattern noted earlier in this chapter.

We have computed synthetic seismograms for comparison to the observed P waves from 13 WWSSN stations for this earthquake. Station data are given in Table 7.4; the velocity structure used, given in Table 4.2, was the same as for the other events on the Vema transform. Because these observed waveforms were taken from film (microfiche) records that were much smaller than those of the earlier events, the digitization interval was larger, and therefore the digitization was less faithful to the original waveforms than those from the earlier events.

The results of the fits, the positions of the stations used, and the fault plane solution used for the synthetic seismograms are shown in Figure 7.6. Obtaining good fits between observed and synthetic waveforms was more difficult for this earthquake than for any of the others studied. The most significant feature of these waveforms is that all of those from stations in the eastern hemisphere had a multiple peak character, with the second pulse several times larger than the first but with roughly the same time length, while those from stations in the western hemisphere had only one major peak and rebound. This is similar to the pattern found for several other events studied here, e.g., the 1964 event on the Oceanographer transform, though in those cases the more detailed waveforms were single primary pulses with two peaks, while in this case the two pulses are separated in time enough for the waveform

displacement to show a zero crossing before the second pulse begins. A further complication of these waveforms is that those observed at stations in the northwestern quadrant had the rising portion of the main pulse interrupted by a shoulder-like feature, while the waveforms observed from the southwestern quadrant were devoid of this feature. The full set of waveforms, particularly those from the eastern stations, proved impossible to duplicate in synthetic seismograms using a single source. We could only come close to the waveforms such as those observed to the east by making the focal depth deep enough to separate the three main phases, but this produced a similar effect for all of the other stations as well. Since the eastern waveforms look like a multiple source, we modelled this earthquake using two sources. A difference in time duration of the first pulse between waveforms observed to the northwest and to the southwest was evident, just as for the other two earthquakes on the Vema transform which we studied, though for the 1979 event the northwestern waveforms were not as irregular in their polarity or shape. We were not able to model this difference successfully for the 1979 earthquake.

The fault orientation we used for the synthetic seismograms has a fault strike of N 90°E, a dip of 90°, and the slip angle used was 180°, representing pure strike-slip motion on a vertical fault. We constructed these synthetic waveforms by superimposing two sources, with the second one having twice the moment of the first. For the stations to the east, we placed the second source 8 sec after the first, and for stations to the west, the second source was set at 3 sec after the first. We can interpret this to mean that the second source was 5.5 sec later than, and 20 to 25 km (about 2.5 sec of travel time) to the west of the first.

This interpretation is not unique because other positions in space and time between the two events could produce similar delays, though this interpretation does have a distance between the events that roughly corresponds to the fault lengths we found. The focal depth we used for this event (pair) was 8.0 km, i.e., 2.3 km below basement floor, and very near the values found for the other two events on the Vema transform. That the event was several km below sea floor was necessary to produce the observed waveforms, though a different fault length would have led to a slightly different value for focal depth.

One of the problems introduced by the use of a multiple source is an increase in the number of required input variables in a system that has insufficient resolution. We have simplified the problem by assuming that the two sources are identical except for total moment. We used a fault length for each source of 20 km, with bilateral horizontal rupture at 3 km/sec, and a fault width of 5 km. Since the second source was taken to have twice the moment of the first, and since the fault dimensions between two events can apparently vary substantially without producing a very different source time function, as suggested in Chapter 2 and by the waveforms from other earthquakes, we prefer the interpretation that the second source probably had a fault length of about 40 km, thus making a total length of 60 km. (We prefer this interpretation because it implies equal displacement for the two sources.) This total length is about 1/5 of the total transform length, and about twice the fault length we found for the larger earthquake in 1962, which was probably underestimated. As mentioned before, the fault lengths found here are compatible with the model of two related events separated by about 25 km.

The total seismic moment values we found for each station for this event (pair) are given in Table 7.4. The "average" for these is  $2.1 \times 10^{26}$  dyne-cm, with a "standard deviation" factor of 1.6. This seismic moment and these fault dimensions produce a displacement value of 2.1 m, and, for a rise time of 1 sec, a particle velocity of 210 cm/sec. This displacement value represents strain accumulated over 65 years. This figure is somewhat smaller than what is suggested by the results from the other earthquakes studied here, though with the uncertainties inherent in this method, that is not surprising. The particle velocity, which is even less well-determined, is within the range found for other earthquakes, however. Following the procedure in Chapter 2, we determine the average stress drop for the earthquake to be about 90 bars.

#### TOTAL SEISMIC MOMENT

We can compare the total seismic moment from the observed earthquakes with that predicted by the Minster and Jordan (1978) relative rotation vector for the South American and African plates. For this we calculate moments from the  $M_S$  values for all of the other earthquakes on the transform, using the method explained in Chapter 9. These values are given in parentheses in Table 7.1. To the sum of these values we add the moments found for the three earthquakes studied here, which gives a value of  $6.5 \times 10^{27}$  dyne-cm for the total observed seismic moment since about 1920, the approximate time of the earliest Atlantic events listed by Gutenberg and Richter (1954). Most of this can be accounted for by the three events (1925-29) reported by Gutenberg and Richter (1954), which may have magnitude values not directly comparable to the more recent events. After these three the two largest events studied here (1962 and 1979) contribute most to this total.



To this total moment sum we add a correction for the seismicity too small to be observed, using Formula (7) given in Molnar (1979) (Formula 3.1 in this work). For this we use  $a = 2.6$ ,  $b = 0.61$ ,  $c = 1.18$ , and  $d = 18.6$ , determined in Chapter 9. For minimum  $M_0$  values of  $1.67 \times 10^{25}$  dyne-cm for the years from 1920 to 1963 and  $7.4 \times 10^{22}$  dyne-cm for the years from 1964 to 1981, we obtain unobserved moment rates of  $4.92 \times 10^{24}$  dyne-cm/yr and  $3.61 \times 10^{23}$  dyne-cm/yr, respectively, for these time periods. Since these time periods represent 44 yrs and 18 yrs, respectively, this means unobserved moment totals of  $2.3 \times 10^{26}$  dyne-cm and  $6.9 \times 10^{24}$  dyne-cm. Adding these values to the total observed seismic moment gives a total accumulated seismic moment value of  $6.7 \times 10^{27}$  dyne-cm released by earthquakes on the Vema transform since 1920. From the transform dimensions and the slip rate we have determined the total seismic moment expected on the Vema transform since 1920, using

$$M_0 = \mu L w D$$

where  $\mu$  is shear modulus,  $L$  is fault length,  $w$  is fault width, and  $D$  is the total displacement for this 62 year period. For this we used  $\mu = 3.5 \times 10^{11}$  dyne/cm<sup>2</sup>,  $L = 320$  km,  $w = 10$  km, and  $D = 194$  cm, calculated from the rotation vector given by Minster and Jordan (1978). The value of 10 km was used for width because the synthetic seismogram results suggest that this may be a minimum value for this transform. The result is an expected seismic moment value of  $2.2 \times 10^{27}$  dyne-cm. This value is about one third of the total value presented in the previous paragraph, and considering the possible errors, the agreement is good.

There are several factors which may contribute to this factor of three difference. The magnitudes for the earthquakes given by Gutenberg and Richter (1954) may be larger than modern  $M_S$  values. Alternatively,

since the recycle time for large earthquakes seems to be at least three times the span between the beginning of our records (1920) and the very large earthquakes in the seismic episode of 1925-1929, these three events may have released strain accumulated for some time before 1920. Since these three events contribute the most to the seismic moment total, the total could be therefore be nearly a factor of three too large from this effect alone. Either of these two possibilities is consistent with the large size of the 1925-1929 earthquakes. Another possible error is in the value of 10 km for the fault width used to determine the expected seismic moment. The large  $M_S$ 's reported for events on the Vema transform and the unusually high displacements found for the events studied here suggest that the average transform width may be greater than the 10 km used here, even if the 5 km used for the event in 1976 is valid for the western end. Finally there is the possibility that our seismic moments are systematically too large.

#### IMPLICATIONS FOR THE VEMA TRANSFORM

Though some of the results we have presented here are not as precise as our synthetic seismograms might indicate, we can still draw several firm conclusions about motion on the Vema transform. We have seen that seismic slip on the transform is episodic in nature, though the magnitude of each episode and the length of time between episodes are variable. From the fault lengths determined in our synthetic seismograms it appears that the transform does not necessarily slip along its entire length in each seismic episode, though it may have done so in the episode of 1925-1929.

One feature we found for all of the earthquakes studied on the Vema transform is the apparent asymmetry between the waveforms seen in the

northern and southern hemispheres, a feature which required that the fault planes be slightly non-vertical for two of the events and which we were unable to match for the third. The bathymetry of the Vema transform is also asymmetric, with the wall on the southern side being generally both higher and narrower than the wall to the north. This may be related to the observed asymmetry in the earthquake waveforms though the exact connection is not obvious. It may be that the transform fault is non-vertical and that the basement of the southern wall extends slightly beneath the northern wall. This is not unreasonable as the basement structure necessary to support the two walls is probably different, both thermally and dynamically. Thermal differences could, of course, alter the radiation pattern of an earthquake, so that a vertical fault plane might appear to be non-vertical. Nevertheless, it is clear that the Vema transform has some basic differences between north and south.

Finally, it appears that we have not seen enough of the transform's history to obtain a complete picture of its seismic behavior. If both the 1979 event and the events in 1925 and 1929 fractured primarily the eastern half of the transform then the recurrence time of 65 years predicted by the displacement of the 1979 event agrees well with the historical record. The picture on the western part of the transform is not as clear, since (1) the 1976 event was smaller, and therefore not as significant, as the 1927 and 1962 events, and perhaps the 1975 event, (2) the displacement of the 1962 event was probably not as great as we determined, and (3) the location of the 1927 event, though probably not well determined, does not coincide with that of the 1962 event as well as those on the eastern part of the transform. The proximity of the 1920's earthquakes to the start of our records, the difference between the

observed and expected total moment values, and the long recurrence time calculated for the 1962 event suggest that the transform has been overpopulated with large events releasing strain accumulated for many years before 1920. If the average fault length of the 6 largest earthquakes is 30 km, then there has been only enough fault length from these events to fracture half of the transform's length. While it may be that our fault lengths are too small, they are probably not consistently so by a factor of two, since the contribution of fault length to an earthquake's source time function is stronger than that of the fault's width.

Table 7.1 Seismicity of the Vema Transform Fault

Date	Origin Time			Lat, °N	Lon, °W	h, km	$m_b$	$M_s$	No. of sta.	$M_0, 10^{25}$ dyne-cm
	h	m	s							
10/13/25	17	40	34	11	42			7.5		(290)
9/3/27	19	47	45	11	44			6.9		(57)
2/22/29	20	41	46	11	42			7.2		(130)
7/26/54	22	09	56	11.9	43.8	n		6.3		
3/5/55	19	28	31	10.7	43.6	n		5.9		(3.8)
10/20/57	12	04	22	10.8	42.1	n		5.8		(2.9)
3/9/61	3	53	08.7	10.9	41.7	27		d		(1.7)
3/17/62	20	47	32.3	10.9	43.2	n		7.0		130
6/9/63	20	37	47.1	10.6	41.8	11		d		(1.7)
1/4/66	15	04	50.9	11.4	44.0	33	4.5	(4.1)	16	(0.029)
1/22/66	19	02	48.8	10.89	43.44	33	4.3	(3.7)	7	(0.0097)
12/14/66	06	42	30	10.8	43.23	76	4.5	(4.1)	61	(0.029)
4/5/67	20	41	09	10.95	43.45	30	4.7	(4.4)	31	(0.064)
8/4/67	15	31	18.6	10.5	40.3	33	4.2	(3.6)	8	(0.0074)
11/2/68	08	29	00	10.78	43.57	36	4.8	(4.6)	52	(0.11)
6/4/69	20	35	08.5	11.93	43.80	20	4.8		79	
6/5/69	20	39	58	10.68	41.03	25	5.1	(5.1)	143	(0.43)
8/6/69	15	41	51.5	10.78	43.17	36	5.2	(5.3)	139	(0.74)
8/5/70	09	09	02	11.87	43.76	51	5.2		139	
12/30/70	01	46	26.7	10.49	41.82	33	4.3	(3.7)	15	(0.0097)
1/14/71	11	18	10.9	11.29	43.71	23	4.9	(4.8)	53	(0.19)
5/11/71	22	29	14	10.4	44.0	33			9	
8/27/72	19	38	05.9	10.6	42.54	33	4.5	(4.1)	37	(0.029)
8/27/72	19	38	42.9	10.82	42.31	0	4.7	(4.4)	8	(0.064)
3/15/73	07	34	47.9	10.8	43.3	0	4.7	(4.4)	48	(0.064)
5/21/73	02	48	47	10.1	40.5	0	4.3		6	
2/28/74	17	32	42	10.9	43.38	44	4.6	(4.3)	21	(0.047)
6/4/74	15	14	06	10.82	42.56	51	4.9	5.0	108	(0.33)
6/26/74	18	43	19	10.5	43.7	51	4.7	(4.4)	35	(0.064)
6/26/74	18	54	18.4	10.9	43.36	34	4.6	(4.3)	32	(0.049)
7/7/74	07	42	44	11.6	44.9	33	4.6		8	
11/2/74	01	03	39	10.33	40.96	52	4.9	(4.8)	51	(0.19)
1/14/75	08	17	30.1	10.90	41.16	33	4.4	(3.9)	17	(0.017)
8/25/75	21	49	26	10.1	44	33	5.7	(6.2)	28	(8.5)
5/14/76	06	25	33	10.79	43.51	21	5.5	5.7	307	3.1
6/27/77	23	28	56.7	10.68	42.80	33	4.8	4.2	83	(0.037)
8/27/77	03	06	18	10.97	42.7	33	4.7	(4.4)	10	(0.064)
6/15/78	0	40	12	10.81	43.25	37	5.0	4.6	172	(0.11)
7/11/78	18	18	23	10.84	43.42	33	4.8	4.6	80	(0.11)
1/28/79	19	45	21	11.92	43.70	15	5.7	5.6	324	
2/11/79	6	18	19.0	10.59	41.08	0	4.7	(4.4)	13	(0.064)
8/25/79	8	44	4.5	10.72	41.68	13	6.0	6.6	436	22

This table includes all events on the Mid-Atlantic Ridge between 10°N and 12°N, which includes the Vema transform fault. Data for the events before 1955 were taken from Gutenberg and Richter (1954). Data for events between 1955 and 1963 inclusive

were taken from Rothe (1969). Data for events from 1964 to 1979 were taken from the ISC Regional Bulletin. For depth, n refers to "normal depth, (focus situated in the crust or at its base)", from Rothe (1969). We have taken magnitudes reported before 1964 as equivalent to  $M_S$ .  $M_S$  values shown in parentheses were determined from  $m_b$  using Equation 9.1. Other  $M_S$  values were taken from the same source as the other data for that event; d refers to a Gutenberg and Richter (1954) or Rothe (1969) listing as between 5.3 and 5.9, assumed here to be 5.6. The  $M_S$  values in parentheses were determined for all events whose  $M_S$  was not available from another source and whose location placed them on the Vema transform fault. The  $M_0$  values shown in parentheses were determined from  $M_S$  using Equation 9.2. These values in parentheses were determined for all events whose moment was not determined in this study and whose location placed them on the Vema transform fault.

Table 7.2. Station data used for synthetic seismograms  
for the earthquake of March 17, 1962.

<u>Station</u>	<u>Distance, degrees</u>	<u>Azimuth, degrees</u>	<u>Magnification</u>	$10^{26} \frac{M_0}{\text{dyne-cm}}$
BEC	29.2	320.7	1500	186 *
PDA	31.2	27.6	750	6.9
BHP	35.8	270.4	750	7.0
LPB	36.6	222.5	1500	3.2
GEO	41.1	318.7	750	12
MAL	43.5	47.1	750	131
ALO	61.9	303.8	3000	17
COP	62.2	31.9	1500	8.7
IST	69.7	50.2	750	12

For all stations we used  $T_p = 30$  sec,  $T_g = 100$  sec,  $H_p = .93$ ,  $H_g = 1.0$ , where  $T_p$ ,  $T_g$ ,  $H_p$ , and  $H_g$  refer to the seismometer and galvanometer periods and damping factors, respectively.

\* $M_0$  value not used to find "average" for this event.

Table 7.3. Station data used for synthetic seismograms  
for the earthquake of May 14, 1976.

<u>Station</u>	<u>Distance, degrees</u>	<u>Azimuth, degrees</u>	<u>Magnification</u>	$M_0$ , $10^{25}$ dyne-cm	
CAR	23.0	271.5	3000	2.4	*
SJG	23.1	291.0	750	6.1	*
BEC	23.9	321.0	1500	33	*
BOG	30.9	260.9	3000	3.3	
LPB	36.4	222.2	1500	2.1	
WES	39.8	327.3	3000	3.3	
OGD	40.7	323.2	3000	3.0	
GEO	40.9	318.8	750	7.8	
BLA	42.3	314.6	1500	3.6	
SCP	42.5	329.7	1500	3.4	
PTO	43.1	39.3	1500	2.4	
ANT	43.2	217.3	3000	2.1	
MAL	43.7	47.2	1500	2.6	
ATU	65.5	53.2	1500	3.6	
IST	69.8	50.2	1500	2.8	

\*  $M_0$  values not used to find "average" for this event.

For all stations we used  $T_p = 15$  sec,  $T_g = 100$  sec,  $H_p = .93$ ,  $H_g = 1.0$ , where  $T_p$ ,  $T_g$ ,  $H_p$ , and  $H_g$  refer to the seismometer and galvanometer periods and damping factors, respectively.



Table 7.4. Station data used for synthetic seismograms  
for the earthquake of August 25, 1979.

<u>Station</u>	<u>Distance, degrees</u>	<u>Azimuth, degrees</u>	<u>Magnification</u>	<u><math>10^{25} M_0</math>, dyne-cm</u>
BEC	30.2	319.0	1500	14
LPB	37.6	224.3	1500	15
ARE	40.0	227.9	1500	9.1
MAL	42.4	46.2	1500	47
BLA	43.7	313.7	1500	13
LPA	47.9	198.0	750	15
ESK	53.7	26.2	750	23
JCT	57.2	299.3	1500	21
TRI	58.5	42.7	3000	34
COP	61.4	31.5	1500	32
ATU	64.1	53.0	1500	35
IST	68.5	50.1	1500	25
DUG	68.8	309.0	3000	22

For all stations we used  $T_p = 15$  sec,  $T_g = 100$  sec,  $H_p = .93$ ,  $H_g = 1.0$ , where  $T_p$ ,  $T_g$ ,  $H_p$ , and  $H_g$  refer to the seismometer and galvanometer periods and damping factors, respectively.

### Figure Captions

Figure 7.1 Bathymetry of the Mid-Atlantic Ridge between  $10^{\circ}$  N and  $13^{\circ}$  N, including the Vema transform fault, and epicenters of all known earthquakes between  $10^{\circ}$  N and  $12^{\circ}$  N, and  $40^{\circ}$  W and  $46^{\circ}$  W, as listed in Table 7.1. The approximate locations of the ridge axes are indicated by double lines. Open circles represent epicenters taken from Gutenberg and Richter (1954) and Rothe (1969). Larger symbols are events with  $M_S > 6.0$ . Contour intervals are every 800 m below sea level, taken from Uchupi (1982).

Figure 7.2 Longitude versus year of occurrence for the earthquakes on the Vema transform fault with  $M_S > 5.5$ .  $M_S$  is shown for each event. Dashed lines indicate where the transform intersects adjacent spreading centers. The bars for the events of 1962, 1976, and 1979 indicate the fault lengths and rupture directions used for the synthetic seismograms.

Figure 7.3 Results of fits of synthetic (upper) to observed (lower) seismograms of P waves from the March 17, 1962 earthquake on the Vema transform. Positions on lower focal hemisphere of stations used for synthesis and fault plane solution obtained are also shown. Closed circles for station locations represent compressional first-arrival polarities, open circles represent dilatational polarities, and crosses represent stations for which either the observed or synthetic waveforms indicate questionable polarities. The vertical scales were normalized so that all seismograms would have equal maximum amplitudes.

Figure 7.4 Observed waveforms from all stations used for the study of both the March 17, 1962 and May 14, 1976 earthquakes on the Vema transform. The vertical scales have been adjusted so that the maximum amplitudes are equal; the horizontal (time) scale is the same for all waveforms. The total signal durations for the two events were roughly the same length for all stations except LPB, even though the moment for the 1962 event was a factor of 24 larger than the moment of the 1976 event.

Figure 7.5 Results of fits of synthetic (upper) to observed (lower) seismograms of P waves from the May 14, 1976 earthquake on the Vema transform. Positions on lower focal hemisphere of stations used for synthesis and fault plane solution obtained are also shown. Closed circles for station locations represent compressional first-arrival polarities, open circles represent dilatational polarities, and crosses represent stations for which either the observed or synthetic waveforms indicate questionable polarities. The vertical scales were normalized so that all seismograms would have equal maximum amplitudes.

Figure 7.6 Results of fits of synthetic (upper) to observed (lower) seismograms of P waves from the August 25, 1979 earthquake on the Vema transform. Positions on lower focal hemisphere of stations used for synthesis and fault plane solution obtained are also shown. Closed circles for station locations represent compressional first-arrival polarities and open circles represent dilatational polarities. The vertical scales were normalized so that all seismograms would have equal maximum amplitudes.

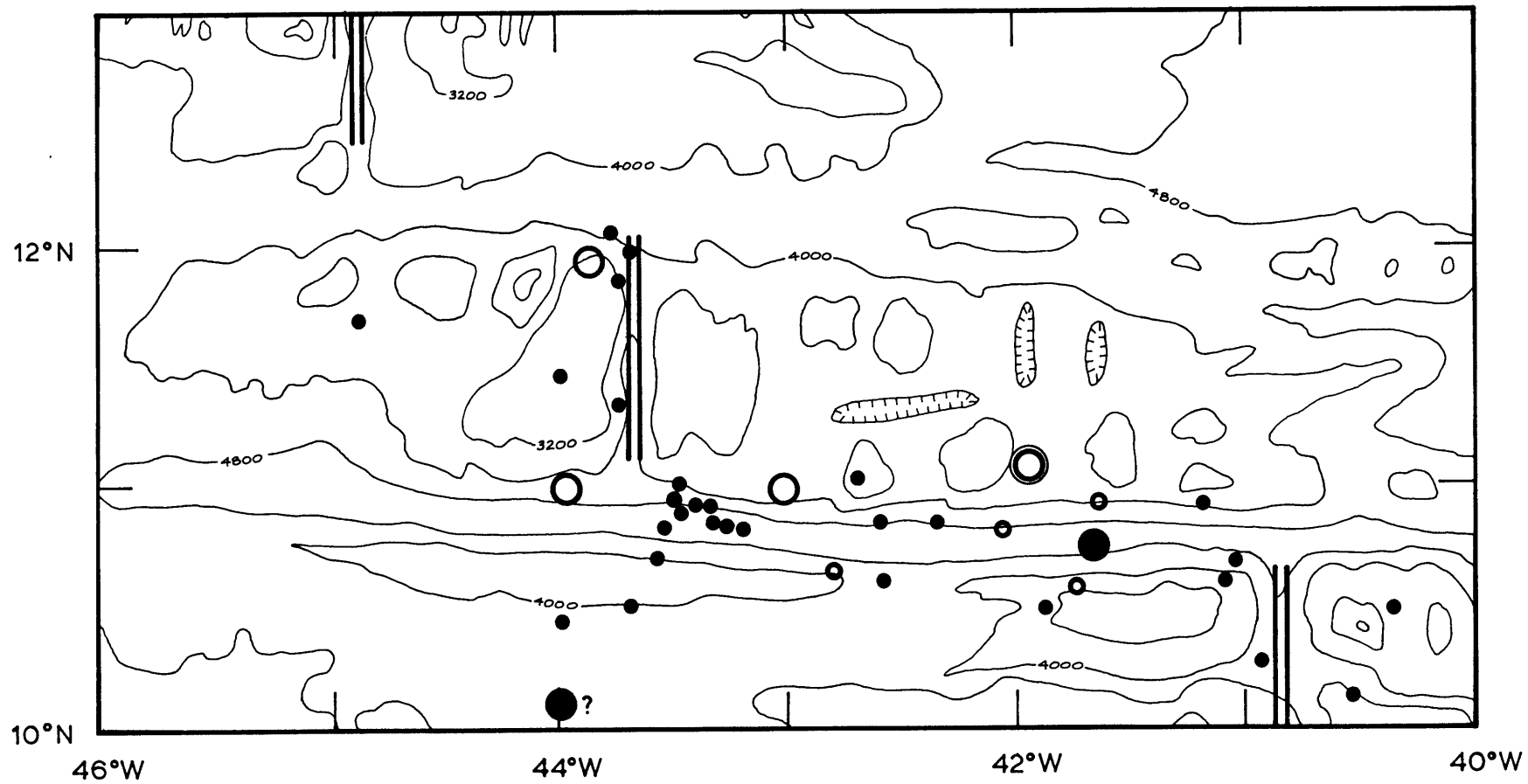


Fig. 7.1

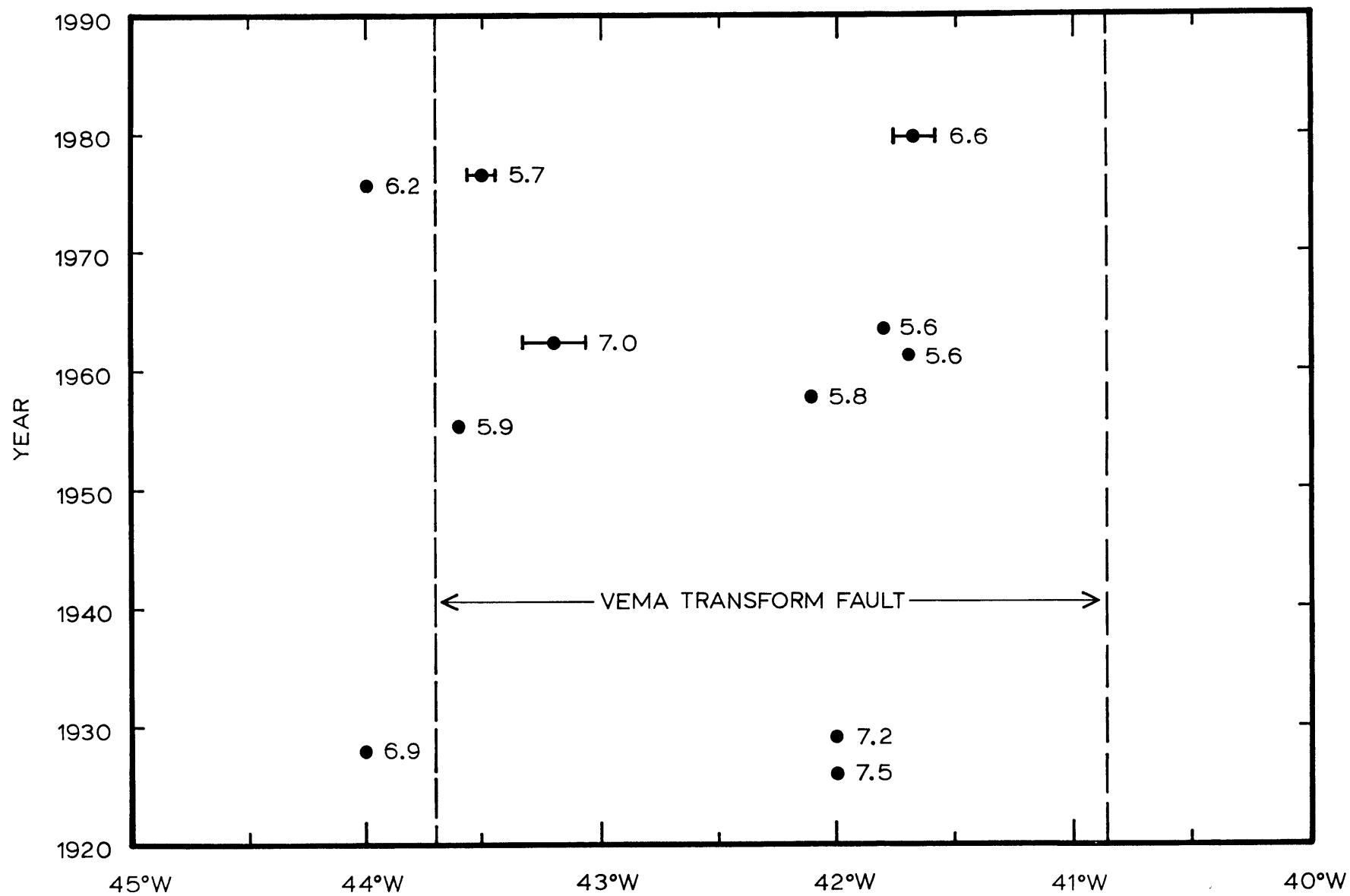


Fig. 7.2

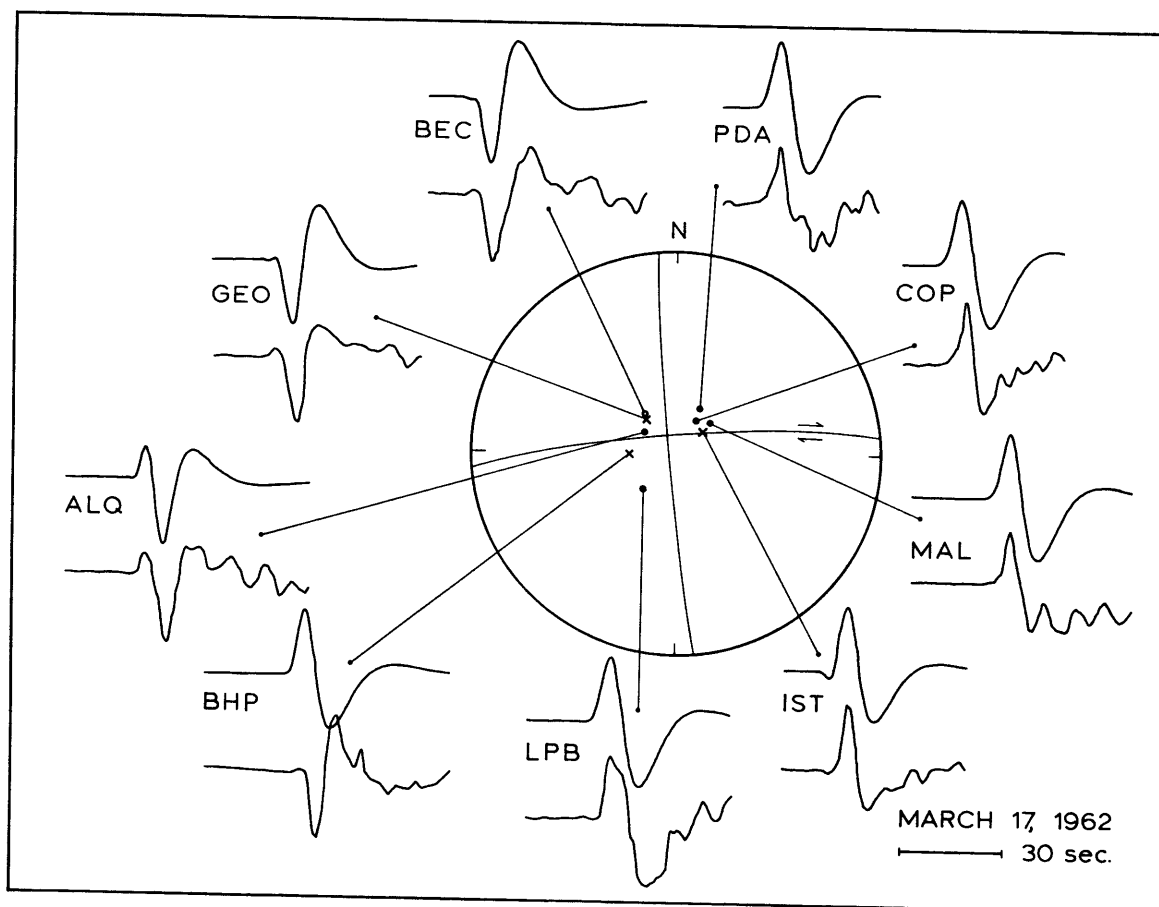


Fig. 7.3

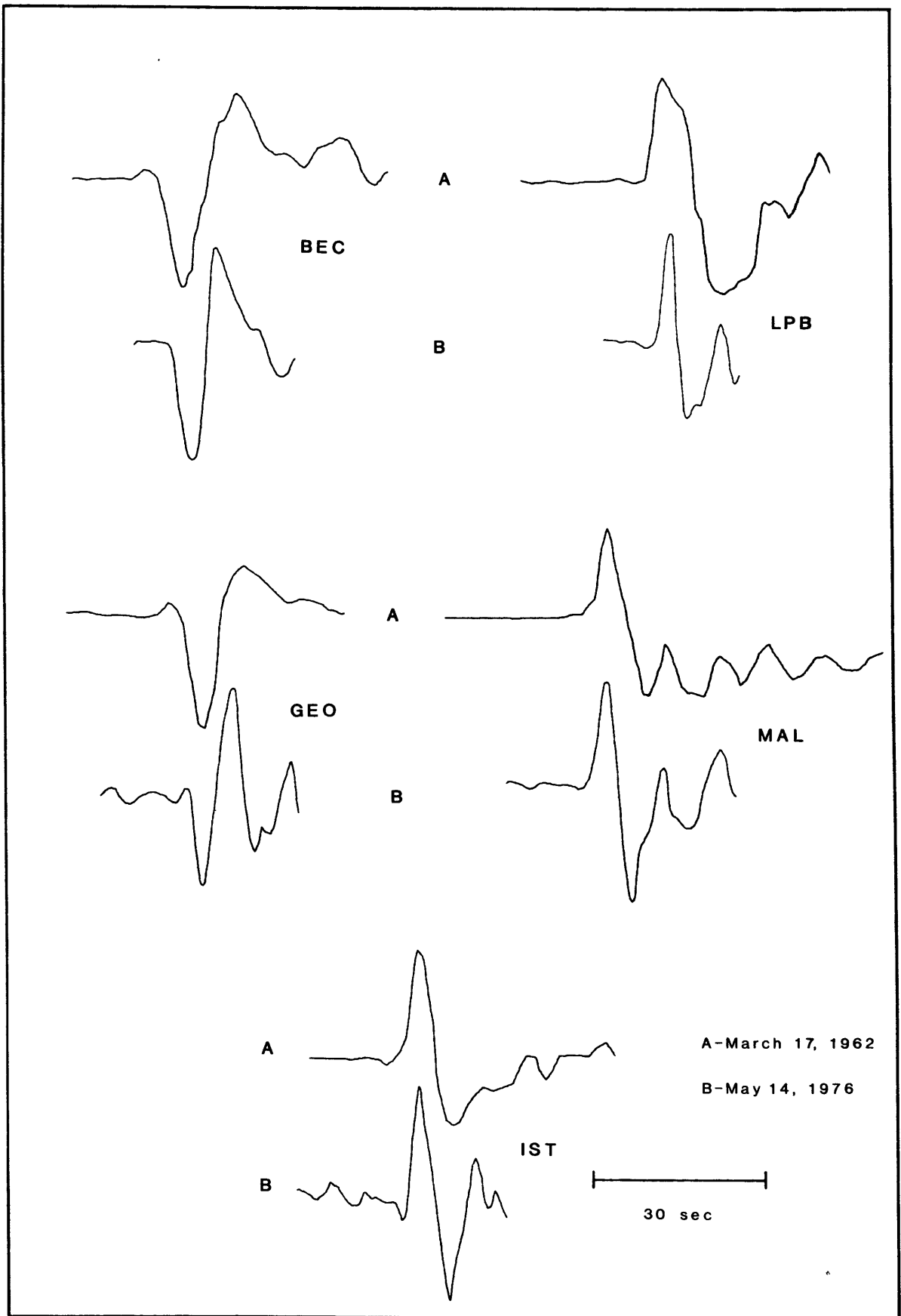


Fig. 7.4

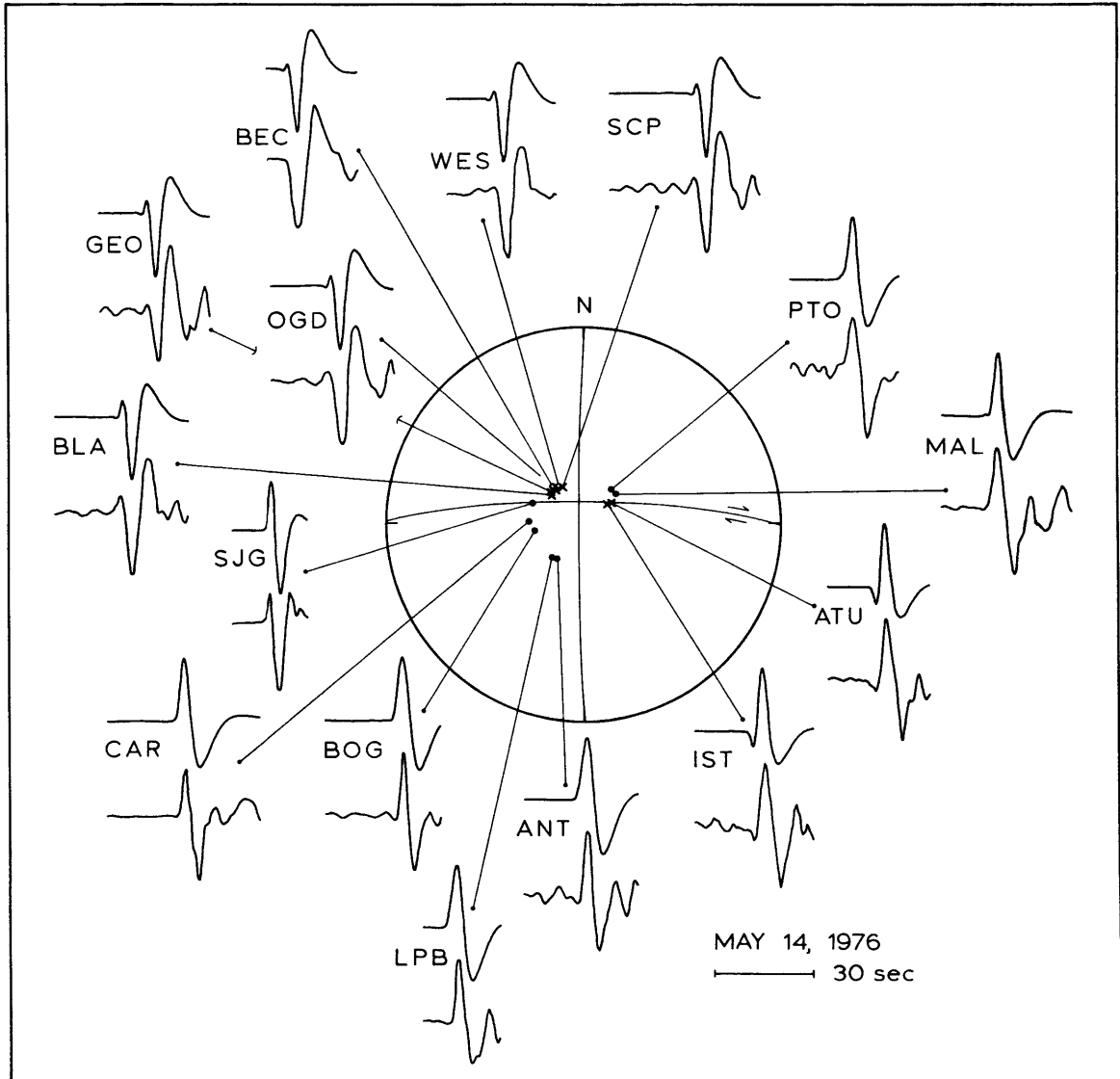


Fig. 7.5



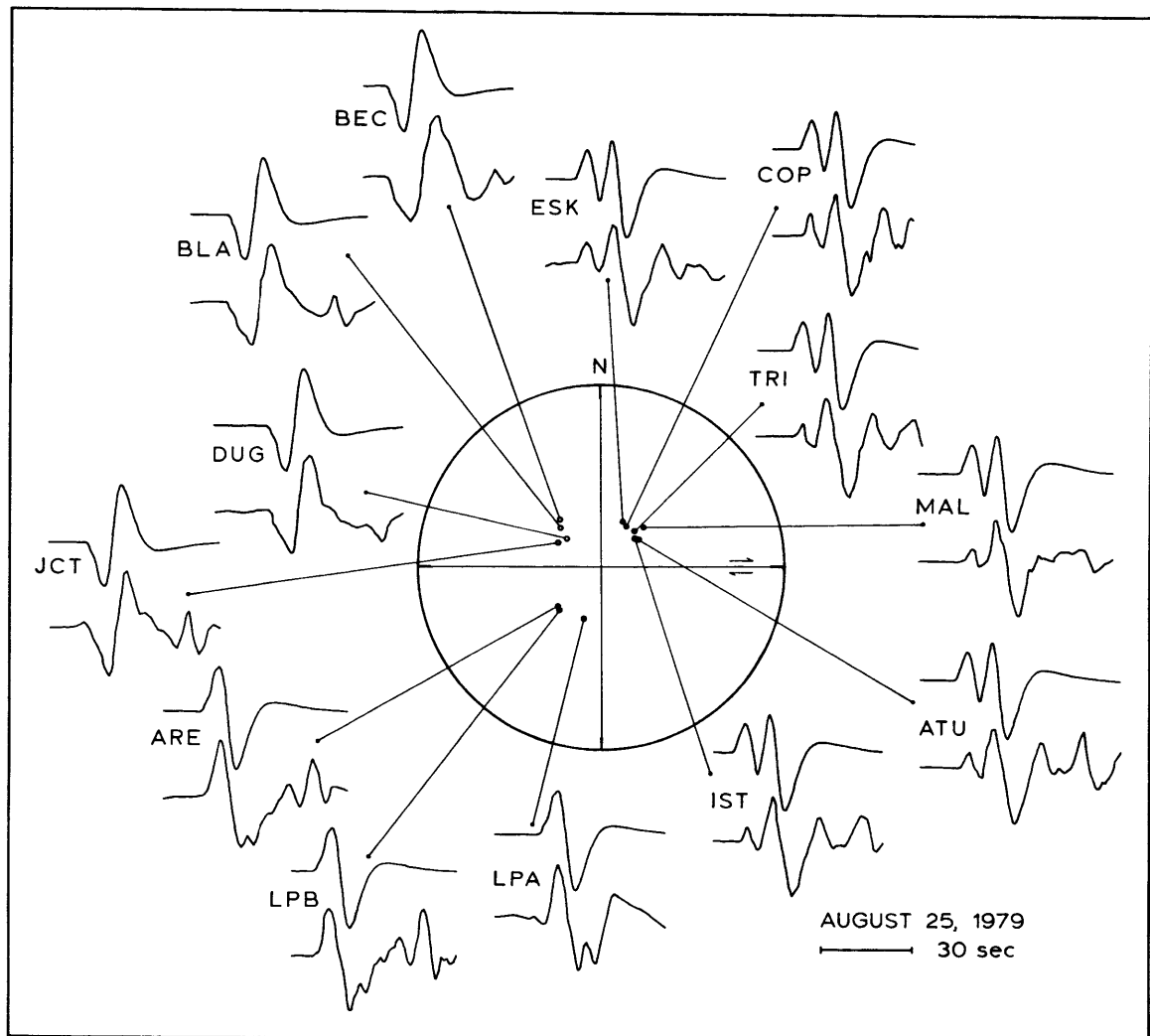


Fig. 7.6

## CHAPTER 8. EARTHQUAKES AND TECTONICS

### OF THE DOLDRUMS TRANSFORM FAULT

The Doldrums transform fault is the designation adopted here for one or more offsets in the Mid-Atlantic Ridge between latitudes  $6^{\circ}$  and  $8^{\circ}$  N, recognizable in the regional bathymetry and seismicity. This part of the Mid-Atlantic Ridge roughly marks the northern edge of the central Atlantic section characterized by an average ratio of ridge length to transform length significantly less than 1, caused by the bending of the South American-African plate boundary to parallel the corresponding shape of these two land masses. It is this shape which produces the large equatorial transforms such as the St. Paul's and Romanche transforms. The Doldrums transform has been indicated on several bathymetric maps of this part of the Atlantic (e.g., Perry et al., 1981). A fracture zone in this part of the Atlantic was noted by Heezen et al. (1964), who assigned letters as names for other fracture zones around the Vema Fracture Zone. By their scheme, this became the "Z" fracture zone, and hence the transform could be called the Z transform. Okal and Stewart (1982) used the names Doldrums Fracture Zone and Guinea transform fault in connection with an earthquake at  $7.4^{\circ}$  N. Uchupi (1982) gave the name Doldrums to a fracture zone at about  $9^{\circ}$  N. We will use the name Doldrums to avoid confusing any mathematicians.

Figure 8.1 shows the bathymetry of the Doldrums transform region, taken from Uchupi (1982). Very little geophysical work has been done on this part of the Mid-Atlantic Ridge, as can be seen from the coarseness of the bathymetric detail in Figure 8.1, particularly in the eastern portion. The most obvious feature of the bathymetry is that this "transform" probably consists of several transforms separated by very

short ridge segments. In order to determine the actual plate boundary, we have considered the epicentral locations of the earthquakes in this area, which are also shown in Figure 8.1. Data for these earthquakes are given in Table 8.1. We suppose, as is probable for most of the Atlantic Ocean, that the epicenters are systematically mislocated to the north because of a high population of seismic stations in North America and Europe. With this in mind, we interpret the plate boundary between latitudes  $6.0^{\circ}$  N and  $8.0^{\circ}$  N as having four separate transforms. In order, from the north, these transforms lie roughly between  $8.0^{\circ}$  N,  $40.3^{\circ}$  W and  $7.9^{\circ}$  N,  $37.8^{\circ}$  W for the first;  $7.6^{\circ}$  N,  $37.8^{\circ}$  W and  $7.6^{\circ}$  N,  $36.3^{\circ}$  W for the second;  $7.2^{\circ}$  N,  $36.3^{\circ}$  W and  $7.2^{\circ}$  N,  $34.1^{\circ}$  W for the third, and  $6.9^{\circ}$  N,  $34.1^{\circ}$  W and  $6.9^{\circ}$  N,  $33.4^{\circ}$  W for the fourth. This interpretation is shown along with the bathymetry in Figure 8.1. The epicentral locations indicate that the adjoining ridge segment to the north is probably not at longitude  $38.4^{\circ}$  W, as suggested by the bathymetry. We have therefore assumed that this transform ends at the next likely place to the west indicated by the bathymetry.

We suppose, because the transforms are so long while separated by very short ridge segments, that the behavior of this area may be very different from that of transforms to the north. One could think of this as one long transform, with "leaky" sections at three places along the length, thus making the average temperature higher than would be normal for a transform of this length. Alternatively one could think of this as a zone of sea floor spreading, in which the emplacement is spread out over a broad area in a slightly organized way, making this area colder than normal oceanic ridge. We will focus our attention on the inner two of these transforms, treating them as one long fault, with the

recognition that this is a purely arbitrary division. The total length of this two transform system is about 410 km.

## SEISMICITY

The seismic history of the area, listed in Table 8.1, includes an extraordinary number of large earthquakes. The larger events ( $M_S > 6$ ) are shown plotted on a graph of longitude vs. time in Figure 8.2. The events listed begin with a large ( $M = 7.4$ ) event in 1918. After this there was a sequence of large events, in 1928, 1929, and 1932, on the westernmost of our two transforms, and a period of high activity on the eastern transform, which lasted from 1934 to 1945. After this the area was free of large events until activity began again with small events in 1958 and 1959, followed by two larger events in 1963, one on each transform segment. This seismically quiet period is similar to what we found for the other transforms studied. The epicenters of the events before about 1964 or so are probably not as well-determined as those of the later events. A noticeable feature of the period before 1945 is that events with  $M_S > 6$  are numerous compared to the later period. This may suggest that the earlier magnitudes were determined in a way that makes them systematically larger than the more recent values. That there are so many events compared to the number of events on the other transforms studied in this work is not surprising considering the greater length of this transform system and the slightly higher slip rate.

Sykes (1967) determined fault plane solutions for the two large earthquakes which occurred on this transform system in 1963: on August 3 ( $M_S = 6.9$ ) and November 17 ( $M_S = 6.6$ ). The results showed right-lateral strike-slip motion, with fault strikes of N100°E and N98°E, respectively. Both faults were nearly vertical, the first dipping 79° to the south and

the second dipping  $86^\circ$  to the north. The epicenter of the August event is probably on the eastern segment of the double transform we are considering, while the epicenter of the November event is on the western segment.

Bollinger (1968) studied the P waveforms for the earthquake of August 3, 1963, which he used as an example of an earthquake with both nodal planes nearly vertical. He was attempting to measure fault lengths from P wave pulse durations using a method similar to what is presented in Chapter 2 of this work, though a method for more complete waveform synthesis had not been developed at that time. He found a fault length of 11 km, using unilateral horizontal rupture at a speed of 2.5 km/sec. He did not give the direction of this rupture though the longer signal durations to the west indicate that the direction was probably west to east.

Wyss (1970) gave epicentral data, magnitude, energy, seismic moment, apparent stress, and apparent strain for a number of transform fault earthquakes, including the events on this transform of August 3, 1963 and November 17, 1963. He found moment values for these events of  $2.0 \times 10^{26}$  dyne-cm and  $1.4 \times 10^{26}$  dyne-cm, respectively.

Udias (1971) also studied these same two earthquakes by examining the directivity of the surface waves. Using a rupture speed of 1.5 km/sec, he obtained fault lengths of  $32 \pm 2$  km and  $27 \pm 6.7$  km, respectively, for these events. He also calculated the seismic moment and average displacement to be  $1.2 \times 10^{26}$  dyne-cm and 105 cm for the August 3 event, and  $3.8 \times 10^{25}$  dyne-cm and 48 cm for the November 17 event. His seismic moment value for the August event is similar to that found by Wyss (1970), but his value for the November event is considerably smaller.

Okal and Stewart (1982) studied one earthquake on this transform system, which occurred on April 4, 1977. Our interpretation of the plate boundary indicates that this event occurred on the third from the north of the four transforms described above. They made comparisons of  $m_b$  to  $M_S$  values for earthquakes on a number of different transforms, and concluded that this transform was an "intermediate" type.

We have studied three earthquakes on this system, two on the eastern transform segment, and one on the western segment. The events we studied were those on August 3, 1963, September 4, 1964, and April 4, 1977. We did not study the November 17, 1963 event because there were too few records available, nor the October 21, 1970 event because it was too small.

#### THE AUGUST 3, 1963 EARTHQUAKE

We have calculated synthetic P-waves, using the method presented in Chapter 2, for comparison to observed seismograms from 11 WWSSN stations for the  $M_S = 6.9$  earthquake of August 3, 1963. Fortunately data for 1963 were available from these stations. Station data are given in Table 8.2, and the results of the synthesis are given in Figure 8.3. We used the velocity structure given in Table 4.2. The fault plane solution found and the location on the lower focal hemisphere of the stations used are also shown in Figure 8.3. The fault strike was taken as the strike of the Doldrums transform fault implied by the bathymetry, i.e., N95°E. We used a fault dip of 90°, i.e., a vertical fault, and a slip angle of 180°. This fault plane solution represents right-lateral strike-slip motion, and is similar to that found by Sykes (1967) for this event.

The waveforms for the stations to the west had some detail at

periods shorter than the predominant period, indicating either some sort of surface interaction or a source-finiteness effect, and the waveform for station GDH ( which we were unable to fit) was uniquely detailed. The waveforms for the three stations to the east were slightly shorter than those to the west, similar to the findings of Bollinger (1968), and seemed to be less complex, though the amplitudes were so large and the predominant periods were so short that the exact shapes of the waveforms were difficult to determine. Bollinger (1968) found unilateral rupture for this event, based on the waveform durations from more stations than we had available, and Udias (1971) also found west to east propagation for this event, using the spectra of Rayleigh waves. Because we did not trust the shapes of our digitized waveforms for the eastern stations, we did not assume unilateral rupture. That the eastern waveforms seemed to be shorter indicates to us that rupture may have been unilateral horizontally, west to east, though this should normally have resulted in the waveforms being more detailed, not less.

We used bilateral horizontal rupture with a rupture speed of 4 km/sec on a fault that was 18 km long and 4 km wide. These small fault dimensions and this rupture speed were dictated by the very short time functions required, despite the large apparent size of the event. In this respect, this event was similar to the large 1962 earthquake on the Vema transform. This fault length is greater than the value of 11 km found by Bollinger (1968) but smaller than the value of 32 km found by Udias (1971). Since Bollinger's (1968) result was based on unilateral rupture, it should be taken as a lower bound on what the actual fault length could have been. Had we assumed unilateral faulting, our fault length value would have been about 9 km, close to that of Bollinger

(1968). Our value of 18 km is still considerably lower than that of Udias (1971); his fault length and rupture speed would have produced source time functions of at least 21 sec, from the fault length alone, if the rupture were completely unilateral, and 11 sec if it were completely bilateral. While this last value is compatible with the observed P waveforms, a rupture time of 21 sec would be too long by a factor of 2. Thus we should consider 32 km as an upper bound on the fault length, acceptable only if we also accept a substantial amount of bilateral horizontal rupture. Our fault length of 18 km is only about 4.4% of the total transform length.

We used a focal depth of 7.5 km below sea level, or 3.5 km below basement floor. This, and the fault dimensions given above, reproduced in the synthetic waveforms the detailed character of the observed waveforms for the western stations. Our model also produced the same features in the synthetic seismograms for the eastern stations, though these features were not present in the observed records. As mentioned before, however, we did not fully trust the shapes of the waveforms for this limited number of stations. This focal depth is similar to what we found for most of the other events studied. The depth could not be varied by more than about  $\pm 0.2$  km without making a noticeable change in the waveforms, though the true uncertainty in the depth is probably closer to  $\pm 2$  km.

The total seismic moment we found for this earthquake was  $3.0 \times 10^{26}$  dyne-cm, which, though slightly higher, compares reasonably well to the values found by Wyss (1970) and Udias (1971). The "standard deviation" factor for the seismic moment was 1.3. This moment and the fault dimensions used produced an average displacement of 12 m and a stress



drop of 670 bars, both very high values. The rise time used was 1 sec, which produces a particle velocity of 12 m/sec, also an unusually high value. This high displacement value is due primarily to the fact that, like the large 1962 earthquake on the Vema transform, a large seismic moment was paired with P waves whose short predominant periods implied small fault dimensions. Our fault length may have been shorter than the actual fault length, though probably by no more than a factor of 2, particularly since we used bilateral faulting. Any remaining error in the fault area must be accounted for by error in our fault width. If we suppose that the displacement value of 12 m is large by, say, a factor of 4.5, and that a factor of 1.5 can be accounted for by an error in our fault length, then this means that the actual fault width must have been greater by a factor of 3.

The Minster and Jordan (1978) rotation pole for the South American and African plates predicts a slip rate on this transform system of 3.4 cm/yr. This means that the displacement for this earthquake represents strain accumulated by plate motion over a period of 350 yrs. If we treat this as an upper bound, with a potential error of a factor of 4, we obtain a possible recycle time for this part of the transform of as little as 90 yrs. It is difficult to judge the seismic history which might have influenced this portion of the transform because many of the major events in this area may have occurred on either of the two sections. However from the general frequency of events we can suppose that at least some of the events in the historical record occurred on the same section as this one. Since there have certainly been events on this section of the transform system in recent times, this implies that either the fault lengths were indeed short enough so that there were still

recently-unfractured portions of the transform segment, or the displacement of this event is overestimated even at 3 m, let alone 12 m. As was discussed in Chapter 6 for the  $15^{\circ} 20'$  transform, the more likely explanation is that the fault lengths actually are limited to at most a few tens of kilometers, and that the displacements occurring during each large earthquake represent at least several decades of slip along the transform.

#### THE SEPTEMBER 4, 1964 EARTHQUAKE

On September 4, 1964 an earthquake with  $m_b = 5.4$  occurred on the western transform segment. This event occurred 9.5 months later than, and about 35 to 40 km to the east of the  $m_b = 5.9$ ,  $M_s = 6.6$  earthquake of November 17, 1963, which suggests that the two events were related, possibly even fracturing adjacent parts of the transform. This is in general agreement with our observation that fault lengths for events of this size are possibly 15 to 30 km. If these events did fracture adjacent parts of the transform, we might expect to see some quality of unilateral faulting from west to east for the September 4, 1964 event.

We have computed synthetic P-waves, using the method presented in Chapter 2, for comparison to observed seismograms from 15 WWSSN stations for the September 4, 1964 earthquake. Station data are given in Table 8.3, and the results of the synthesis are given in Figure 8.4. We used the velocity structure given in Table 4.2. The fault plane solution found and the locations on the lower focal hemisphere of the stations used are also shown in Figure 8.4. The fault strike was taken as the strike implied by the bathymetry, i.e.,  $N 95^{\circ} E$ . We used a fault dip of  $84^{\circ}$  to the south, and a slip angle of  $192^{\circ}$ . This fault plane solution represents right-lateral strike-slip motion, with the southern side

downdropped slightly, and it is not as simple a solution as the one used for the August 3, 1963 event. As can be seen from the observed waveforms in Figure 8.4, many of the stations had apparently dilatational first-arrival polarities, including stations in the expected compressional quadrants, such as TOL and NUR to the northeast, and LPB, BOG, and possibly QUI and LPA in the southwestern quadrant. By using the fault plane solution given we were able to match the apparent polarities at most of the stations. The similarity of the waveform from TOL to those of QUI and LPB suggests that the fault plane solution should have been symmetric about the fault strike, though this constraint made it impossible to obtain as many satisfactory fits. We did not obtain a good fit for AAE. This station was near one nodal plane, and its amplitude was quite small compared to the other stations, even though its waveform appears impulsive; a very small change in the slip angle (or a fault dipping slightly to the north) could accomodate the polarity at AAE, though at the expense of the other stations.

The slip angle used,  $192^\circ$ , is quite removed from the  $180^\circ$  expected for a pure strike-slip earthquake. Synthetic waveforms in either of the compressional quadrants can be made to appear more dilatational by moving either of the nodal planes in that direction. Since this has the opposite effect on the alternate quadrant, it requires that the other nodal plane be moved so as to produce the opposite effect, so that the final result is to move the B axis towards the center of either of the dilatational quadrants. We chose to move the B axis to the southeast, resulting in the waveforms shown, though other solutions to this problem are possible. Since source finiteness can also influence the relative sizes of the P, pP, and sP phases, some of the features of the observed

waveforms may be due to this effect, and the deviation from pure strike-slip of the fault plane solution adopted here may be more than was actually present in the earthquake.

We used bilateral horizontal rupture, with a rupture speed of 3 km/sec on a fault that was 10 km long and 5 km wide. We did not use unilateral faulting because the observed waveforms did not show any obvious directivity. Because the waveforms were quite short, we used a rise time of only 0.5 sec, which also made the source finiteness slightly more influential on the final source time functions. This value is not well constrained, but was chosen because fitting the observed waveforms was slightly easier.

We used a focal depth of 5.5 km below sea level, 1.5 km below basement floor, because the observed waveforms were generally featureless, showing no significant depth-induced characteristics. The fault plane solution used produced relative amplitudes between the three main phases that varied among the stations more than for most of the other events studied. The resulting dominance of one phase over the others, particularly with the small observed amplitudes, tended to obscure the depth signature anyway, reducing the precision available. We estimate the focal depth to be anywhere from 0 to 3 km below sea floor.

The total seismic moment we found for this earthquake was  $1.8 \times 10^{25}$  dyne-cm, with a "standard deviation" factor of 2.2. This moment and the fault dimensions used produced an average displacement for this earthquake of 100 cm, and a stress drop of 46 bars. Since we used a rise time of 0.5 sec, this means a (highly unconstrained) particle velocity of 200 cm/sec. These values are within the range found (and believed acceptable) for the other events studied. This displacement represents strain accumulated

for, and therefore a recurrence time for this part of the transform of, 30 years, in good agreement with the 28 years since the last large earthquake in this area in 1936.

Since we did not find evidence of unilateral faulting, and since the total signal lengths and fairly small moment imply a fault length shorter than 35 km, we conclude that the fault plane for this event probably did not intersect that of the November 17, 1963 earthquake. This is also suggested by the fact that our fault plane dipped to the south, while that of the November 17, 1963 event, from Sykes (1967), dipped to the north.

#### THE APRIL 4, 1977 EARTHQUAKE

On April 4, 1977 an  $m_b = 5.6$ ,  $M_s = 6.0$  earthquake occurred near the center of the easternmost of our two transform segments. As can be seen in Figure 8.2, this portion of the transform had not experienced a large ( $M_s > 6$ ) event since 1941, though an  $M_s = 5.6$  earthquake on July 13, 1964 occurred nearby. This earthquake of 1977 was the largest on this transform system since most of the WWSSN stations became operational in 1964, and the largest event on this transform for which we have epicentral data reported by I. S. C. As noted above, Okal and Stewart (1982) commented on this event.

We have computed synthetic P-waves for comparison to observed seismograms from 17 WWSSN stations for the April 4, 1977 earthquake. Station data are given in Table 8.4, and the results of the synthesis are given in Figure 8.5. For these calculations, we used the same velocity structure as was used for the other events studied. The fault plane solution found and the locations on the lower focal hemisphere of the stations used are also shown in Figure 8.5. The fault strike was taken

as that suggested by the bathymetry, i.e., N 95° E. We used a fault dip of 90°, i.e., a vertical fault, and a slip angle of 181°. This fault plane solution represents almost pure right-lateral strike-slip motion with a very slight downdrop of the northern side. The slip angle of 181° was chosen because it produced better synthetic waveforms than 180°, but this does not mean that the actual slip angle was significantly different from 180°.

All of the observed waveforms had a depth character, a small wiggle in the region of the first maximum amplitude. This feature was generally more pronounced for the stations to the east, particularly for stations JER and HLW. The predominant period of the waveforms to the east was also generally shorter than those to the west, though it was quite short for all of the observed waveforms. In order to produce as much azimuthal dependence as reasonably possible, and to generate short source time functions, we used unilateral horizontal faulting, from west to east, in our synthetic seismograms, with a rupture speed of 4 km/sec, a fault length of 10 km, and a fault width of only 3 km. This fault width is smaller than the 5 km value we used for most of the other earthquakes studied, and was chosen to minimize the contribution of fault width to the source time functions. As explained in Chapter 2, the actual width contribution to the source time functions can vary depending on the nature of vertical rupture, so that the actual fault width for this event may have been possibly a factor of 2 greater than what we used. We combined these fault dimensions and rupture speed with a rise time of 0.8 sec and a focal depth of 7.8 km below sea level, 3.8 km below basement floor, to produce the features of the observed waveforms. (The observed seismogram from BEC was apparently either recorded with the wrong

polarity or reproduced upside down, since both its waveform and its time marks are the wrong direction; for our modelling we have assumed that the actual displacements were reversed from what is shown on the seismogram.)

The total seismic moment we found for this earthquake was  $5.3 \times 10^{25}$  dyne-cm, with a "standard deviation" factor of 1.6. This moment and the fault dimensions used produced an average displacement for this earthquake of 500 cm, and a stress drop of 380 bars. Since we used a rise time of 0.8 sec, this means a particle velocity of 630 cm/sec. This displacement represents strain accumulated for, and therefore a recurrence time for this part of the transform of, about 150 years. This is about 4 times larger than the 36 years since the last large earthquake in this area in 1941. We suppose that possibly half of this discrepancy could be due to an underestimated fault width. If there were a bilateral component to the horizontal rupture, then possibly another factor of 1.5 could be due to an underestimated fault length. It is certainly possible that this earthquake fractured the same parts of the transform as the event in 1941, though the fault length of this event was short enough so that it may not have.

#### TOTAL SEISMIC MOMENT

We can compare the total seismic moment from the observed earthquakes with that predicted by the Minster and Jordan (1978) relative rotation vector for the South American and African plates. For this we limit our attention to the central two transforms of the four in this system. We have calculated moments from the  $M_S$  values for all of the other earthquakes on these two transforms, using the method explained in Chapter 9. These values are given in parentheses in Table 8.1. To the sum of these values we add the moments found for the three earthquakes

studied here, which gives a value of  $3.8 \times 10^{27}$  dyne-cm for the total observed seismic moment since 1918.

To this total moment sum we add a correction for the seismicity too small to be observed, using Formula (7) given in Molnar (1979) (Formula 3.4 in this work). For this we use  $a = 4.3$ ,  $b = 0.92$ ,  $c = 1.18$ , and  $d = 18.6$ ; these values are determined in Chapter 9. For minimum  $M_0$  values of  $1.58 \times 10^{25}$  dyne-cm for the years from 1918 to 1963 and  $8.0 \times 10^{22}$  dyne-cm for the years from 1964 to 1981, we obtain unobserved moment rates of  $1.07 \times 10^{25}$  dyne-cm/yr and  $3.3 \times 10^{24}$  dyne-cm/yr, respectively, for these time periods. Since these time periods represent 46 yrs and 18 yrs, respectively, this means unobserved moment totals of  $4.9 \times 10^{26}$  dyne-cm and  $5.9 \times 10^{25}$  dyne-cm. Adding these values to the total observed seismic moment gives a total seismic moment value of  $4.3 \times 10^{27}$  dyne-cm released by earthquakes on the two central sections of the Doldrums transform since 1918.

From the transform dimensions and the slip rate we have determined the total seismic moment expected on these two transform sections since 1920, using  $M_0 = \mu L w D$  where  $\mu$  is shear modulus,  $L$  is fault length,  $w$  is fault width, and  $D$  is the total displacement for this 64 year period. For this we used  $\mu = 3.5 \times 10^{11}$  dyne/cm<sup>2</sup>,  $L = 410$  km,  $w = 5$  km, and  $D = 218$  cm, calculated from the rotation vector given by Minster and Jordan (1978). The value of 5 km was used for width because that was the largest of the three values used in the synthetic seismograms for this transform system. The result is an expected seismic moment value of  $1.5 \times 10^{27}$  dyne-cm.

This value is about one third of the total moment value presented in the previous paragraph. Had we used a width greater than 5 km for the



expected moment calculation, as suggested by the inadequacy of our fault model, then the agreement would have been better. Also the two largest contributions to the observed moment totals came from the large events in 1918 and 1942. Since there have been no events this large since 1964 it may be that, as also suggested by the seismic history on the other transforms studied, the earlier magnitudes are systematically larger than modern ones. Over-estimation of the earlier magnitudes may account for some of the excess of moment released over moment expected. However, the most likely explanation is that since most of the observed seismic moment was released in one large event at the beginning of our period of observation, it must have released moment accumulated before this time.

#### IMPLICATIONS FOR THE DOLDRUMS TRANSFORM

We have seen that the strain on this transform system has been released primarily by seismic activity, involving three major episodes. The first consisted of one very large event in 1918 (and possibly others earlier), the second consisted of a group of events progressing generally from west to east (or north to south) lasting from about 1928 to 1945, followed by a quiet period from 1945 to about 1958, when the third episode of large events began. We will discuss this pattern further in Chapter 9. From the fault lengths used in our synthetic seismograms it appears that the transform did not slip along its entire length in one or two major earthquakes, though it may have done so in the entire episode of 1929-1945.

From calculated displacements we have determined recurrence times for three large events, and they range from several tens to several hundreds of years. Thus it is possible that any portion of this transform system has fractured more than once during the time of our

seismic observation, though probably not more than once since 1964. The fault lengths we found were short enough (several tens of km) so that events occurring near each other in both time and position along the transform need not have had overlapping fault areas.

Table 8.1 Seismicity of the Doldrums Transform Fault

Date	Origin Time h m s	Lat, °N	Lon, °W	h, km	$m_b$	$M_s$	No. of sta.	$M_0, 10^{25}$ dyne-cm
5/20/18	14 36 0	7.5	36			7.4		(180)
8/31/28	5 14 34	8	37			d		(1.6)
1/27/29	16 07 12	8	37			6.5		(17.)
5/31/32	8 37 18	7	38			6		(4.5)
7/23/34	18 21 26	7.25	34.5			6		(4.5)
8/22/37	11 31 44	7	36			6		(4.5)
11/5/39	2 2 5	7	34			6		(4.5)
3/21/41	7 57 59	7	35			6.5		(17)
11/28/42	10 38 45	7.5	36			7.1		(81)
6/1/45	22 24 7	7.5	34.5			6		(4.5)
6/8/58	21 9 24	7.2	34.3	n		5.7		(2.1)
9/25/58	7 20 0	8.1	39.3	n		6.7		
11/24/59	20 6 35	7.6	36.8	n		5.7		(2.1)
5/9/60	16 27 26	6.5	33.5	n		d		
8/3/63	10 21 36.6	7.7	35.8	n		6.9		30.
11/17/63	0 48 2.6	7.6	37.4	n		6.6		(22)
7/13/64	21 02 32.4	7.44	34.71	33	5.2	5.6 *	109	(1.6)
8/14/64	21 27 43.7	7.7	36.96	33	4.7	(4.4)	85	(0.068)
9/4/64	3 28 36.4	7.75	37.07	38	5.4	5.6 *	169	1.8
10/26/64	8 49 56.0	7.9	37.6	33	4.3	(3.7)	8	(0.011)
11/27/64	14 27 55.2	7.4	36.88	33	4.7	(4.4)	24	(0.068)
6/5/65	12 09 5.1	7.8	35.9	33	4.1	(3.4)	14	(0.0050)
6/14/65	16 47 26.3	8.27	37.94	63	5.2	5.8 *	88	
6/21/65	13 20 34.6	7.5	34.6	33	4.3	(3.7)	20	(0.011)
7/26/65	18 23 1.8	8.0	39.13	33	4.7		31	
12/17/65	9 8 7.8	8.5	39.3	33	4.5		13	
1/8/66	20 0 36.3	8.04	36.80	33	4.4	(3.9)	18	(0.019)
5/28/66	12 57 24	7.4	34.6	33	4.4	(3.9)	14	(0.018)
5/28/66	20 35 27.8	7.3	34.5	33	4.4	(3.9)	27	(0.018)
6/3/66	20 02 53.2	7.46	35.92	33	4.7	(4.4)	14	(0.068)
6/4/66	6 57 47	7.2	35.7	33	4.3	(3.7)	12	(0.011)
6/14/66	11 54 57.0	7.90	37.29	36	4.7	(4.4)	57	(0.068)
10/7/66	21 0 47.6	8.26	39.29	33	4.7		16	
1/10/67	22 7 51.2	8.11	39.76	33	4.2		9	
3/7/67	7 18 34	7.87	36.6	28	4.4	(3.9)	29	(0.018)
5/10/67	7 58 9.1	7.97	38.01	33	4.2	(3.6)	8	(0.0084)
6/26/67	9 16 41	7.9	38.4	33	4.3	(3.7)	19	(0.011)
6/28/67	21 50 27.3	8.0	36.7	33	4.6	(4.3)	13	(0.054)
7/6/67	19 19 50.2	8.19	38.52	41	5.1		178	
7/25/67	5 25 25.3	7.2	37.0	33	4.3	(3.7)	19	(0.011)
8/4/67	6 01 10.6	7.47	36.32	33	4.9	(4.8)	106	(0.19)
9/6/67	0 44 24	7	35		4.6	(4.3)	6	(0.053)
1/8/68	20 22 19	8.09	38.07	59	5.3		185	
1/9/68	1 25 41	8	38		4.2		2	
1/16/68	1 58 28.9	8.30	38.21	33	4.1		9	
1/24/68	0 59 22	8.19	38.15	28	5.0		101	
9/20/68	12 30 17.3	8.5	40.4	33	4.4		17	
1/31/69	2 25 16.8	7.53	34.64	33	4.2	(3.6)	12	(0.008)

Table 8.1 (continued)

Date	Origin Time h m s	Lat, °N	Lon, °W	h, km	$m_b$	$M_s$	No. of sta.	$M_0, 10^{25}$ dyne-cm
2/1/69	20 03 28	7.16	33.98	45	4.7	(4.4)	71	(0.068)
3/5/69	17 12 19	8.1	36.4	33	4.2	(3.6)	6	(0.0086)
3/30/69	2 53 42.0	8.11	38.88	33	4.6		43	
7/20/69	10 46 10	7.1	34.3	1	4.7	(4.4)	51	(0.068)
10/6/69	0 47 26.7	7.58	35.91	30	4.2	(3.6)	23	(0.0084)
11/8/69	9 43 48	6.6	35.3	25	4.2	(3.6)	3	(0.0086)
12/23/69	12 4 30.3	7.2	34.68	57	4.6	(4.3)	32	(0.053)
10/21/70	15 50 5.3	7.68	37.57	28	5.2	5.5	197	(0.72)
11/1/70	22 33 45.1	8.43	34.59	33	4.7		25	
11/11/70	3 43 34.8	7.44	35.86	33	4.5	(4.1)	16	(0.031)
11/22/70	12 36 6	8.1	35.8	20	3.9	(3.0)	1	(0.0018)
1/1/71	18 45 41.5	8.16	37.78	33	4.8		24	
3/6/71	0 18 12.0	7.86	36.8	33			11	
6/15/71	1 40 48.0	7.52	34.71	33	4.3	(3.7)	8	(0.011)
7/11/71	12 51 31.4	7.8	37.7	33	4.4	(3.9)	20	(0.018)
9/4/71	23 06 13.9	7.3	34.9				0	
10/15/71	21 58 40	7.7	37.11	43	4.8	(4.6)	112	(0.12)
12/29/71	3 55 49.4	7.33	36.07	33	4.7	(4.4)	19	(0.068)
3/17/72	8 45 44	8.0	37.8	0	4.2		4	
4/8/72	4 55 5.3	8.09	38.87	30	5.3	5.2	204	
8/29/72	22 15 20.7	7.6	38.8	0			6	
10/29/72	3 09 19.5	7.71	36.76	0	5.0	(5.0)	49	(0.33)
4/2/73	19 25 0.0	7.27	34.35	27	4.9	(4.8)	108	(0.19)
4/3/73	20 04 51	7.50	36.32	57	4.9	(4.8)	125	(0.19)
6/26/73	12 11 7	8.3	40.7	0	4.5		10	
7/19/73	18 5 37.5	8.04	37.95	33	4.4		9	
10/9/73	19 06 03	7.35	35.14	38	4.8	(4.6)	90	(0.12)
11/20/73	15 29 57.2	7.6	36.48	0	4.6	(4.3)	9	(0.053)
3/5/74	1 58 10.6	7.58	36.9	0	4.6	(4.3)	9	(0.053)
4/22/74	1 47 27.0	8.3	37.0	0	4.5	(4.1)	9	(0.032)
4/23/74	17 38 39.7	7.35	35.33	35	4.6	(4.3)	49	(0.053)
1/21/75	2 08 59.8	7.45	34.66	33	4.5	(4.1)	15	(0.031)
2/13/75	18 12 36.5	6.6	37.4	0	4.4	(3.9)	9	(0.019)
4/22/75	1 34 59	7.9	36.8	0			4	
5/1/75	22 50 17	7.6	34.3	0			5	
6/17/75	2 17 08	8.2	38.9	0	4.4		4	
10/24/75	5 12 55	7.0	36.06	71	4.6	(4.3)	45	(0.053)
11/5/75	5 17 37.8	7.29	34.24	28	4.8	(4.6)	69	(0.12)
11/6/75	2 02 3.6	7.8	38.22	0	4.5	(4.1)	9	(0.031)
11/26/75	21 18 37.0	7.84	38.91	33	4.7	(4.4)	26	(0.068)
2/23/76	7 46 6.6	8.01	37.96	33	5.0		27	
5/4/76	4 9 23.2	8.23	38.17	22	5.0	5.0	80	
5/4/76	4 40 45	8.10	38.09	13	5.4	5.5	217	
5/20/76	6 47 42.9	7.8	36.8	33	4.5	(4.1)	9	(0.031)
1/5/77	23 07 46.1	7.35	35.66	33			12	
1/25/77	6 34 55.8	7.60	37.16	33	5.1	(5.1)	66	(0.43)
3/7/77	10 39 21.4	7.48	36.04	33	5.0	(5.0)	139	(0.33)
4/4/77	17 52 20.4	7.39	34.87	36	5.6	6.0	383	5.3

Table 8.1 (continued)

Date	Origin Time h m s	Lat, °N	Lon, °W	h, km	$m_b$	$M_s$	No. of sta.	$M_0$ , $10^{25}$ dyne-cm
3/23/78	14 52 20.3	7.63	37.31	10	4.8	(4.6)	55	(0.12)
5/7/78	22 44 46.2	8.18	38.25	33	4.5	4.2	23	
8/20/78	21 21 28.1	7.48	34.71	27	4.6	(4.3)	68	(0.053)
10/6/78	3 35 23	7.6	36.9	33	4.7	(4.4)	7	(0.068)
11/5/78	6 39 38.5	8.11	38.60	25	5.1	5.1	181	
1/19/79	23 40 26.1	7.77	37.01	10	4.6	(4.3)	19	(0.053)
5/21/79	8 19 10.4	7.10	34.00	12	4.9	4.7	73	(0.20)
6/6/79	8 31 7.6	8.16	38.44	10	4.6	4.3	68	
6/10/79	6 49 55.3	8.14	38.12	31	5.8	6.0	361	
12/31/79	20 48 23.7	7.05	33.94	10	4.9	(4.8)	18	(0.19)
1/14/80	17 20 30.2	7.47	34.80	10	5.0	(5.0)	14	(0.33)
7/26/80	12 53 40.7	7.10	34.04	10	5.2	5.3	134	(0.72)
7/31/80	10 06 3.4	7.61	36.00	10	4.4	(3.9)	14	(0.018)
1/10/81	7 51 59.3	8.33	40.12	10	4.3		6	
3/5/81	22 44 43.4	8.25	38.04	10	4.6		35	
4/22/81	23 16 54.1	7.39	36.30	10	5.1	4.9	20	(0.43)
5/18/81	19 35 4.8	7.50	36.94	10	4.7	(4.4)	8	(0.068)
6/16/81	2 57 44.3	7.46	34.59	10	4.8	4.7	12	(0.20)

This table includes all events between latitudes 6.5°N and 8.5°N and longitudes 33.5°W and 41.0°W on the Doldrums transform fault system. Data for the events before 1955 were taken from Gutenberg and Richter (1954). Data for events between 1955 and 1964 inclusive were taken from Rothe (1969). Data for events from 1964 to 1979 were taken from the ISC Regional Bulletin, while events in 1980 and 1981 were taken from P.D.E. reports of the U.S.G.S.  $M_s$  values with asterisks were taken from Rothe (1969), other data taken from the I.S.C. Regional Bulletin. For depth,  $n$  refers to "normal depth, (focus situated in the crust or at its base)", from Rothe (1969). We have taken magnitudes reported before 1964 as equivalent to  $M_s$ .  $M_s$  values shown in parentheses were determined from  $m_b$  using Equation 9.1. Except for those noted, other  $M_s$  values were taken from the same source as the other data for that event;  $d$  refers to a Gutenberg and Richter (1954) or Rothe (1969) listing for  $M$  between 5.3 and 5.9, assumed here to be 5.6. The  $M_s$  values in parentheses were determined for all events whose  $M_s$  was not available from another source and whose location placed them on either of the two Doldrums transform segments under study (longitudes 34.1 to 37.8°W). The  $M_0$  values shown in parentheses were determined from  $M_s$  using Equation 9.2. These values in parentheses were determined for all events whose moment was not determined in this study and whose location placed them on either of the two doldrums transform segments under study here.

Table 8.2. Station data used for synthetic seismograms  
for the earthquake of August 3, 1963.

<u>Station</u>	<u>Distance, degrees</u>	<u>Azimuth, degrees</u>	<u>Magnification</u>	<u><math>10^{26} \frac{M_0}{\text{dyne-cm}}</math></u>
BEC	36.5	316.7	1500	2.0
MAL	40.8	39.8	1500	4.2
QUI	43.2	261.8	1500	3.9
GEO	48.5	316.6	1500	2.5
SCP	50.0	318.4	750	2.7
SHA	54.0	302.6	1500	3.1
AAM	54.5	317.5	1500	2.6
FLO	58.0	311.4	1500	2.2
WIN	59.8	121.4	3000	3.8
GDH	62.8	353.0	1500	2.6
IST	66.2	48.4	1500	4.4

For all stations we used  $T_p = 30$  sec,  $T_g = 100$  sec,  $H_p = .93$ ,  $H_g = 1.0$ , where  $T_p$ ,  $T_g$ ,  $H_p$ , and  $H_g$  refer to the seismometer and galvanometer periods and damping factors, respectively.

Table 8.3. Station data used for synthetic seismograms  
for the earthquake of September 4, 1964.

<u>Station</u>	<u>Distance, degrees</u>	<u>Azimuth, degrees</u>	<u>Magnification</u>	<u><math>10^{25} \frac{M_0}{\text{dyne-cm}}</math></u>
CAR	29.6	277.6	3000	2.1 *
BOG	36.9	267.4	3000	8.8
LPB	39.1	231.7	1500	1.6
ARE	41.7	234.6	1500	1.1
QUI	42.1	261.1	1500	7.2
TOL	43.5	37.5	1500	2.7
NNA	44.1	244.0	3000	1.5
LPA	46.8	203.7	750	0.81
BLA	49.0	313.4	6000	0.86
SHA	52.8	302.7	1500	1.1
AAM	53.5	317.9	1500	0.82
FLO	56.9	311.6	1500	0.67
RCD	67.6	314.5	750	3.8
NUR	69.6	27.7	3000	1.9
AAE	74.9	82.7	750	3.5

\*  $M_0$  values not used to find "average" for this event.

For all stations we used  $T_p = 30$  sec,  $T_g = 100$  sec,  $H_p = .93$ ,  $H_g = 1.0$ , where  $T_p$ ,  $T_g$ ,  $H_p$ , and  $H_g$  refer to the seismometer and galvanometer periods and damping factors, respectively.

Table 8.4. Station data used for synthetic seismograms  
for the earthquake of April 4, 1977.

<u>Station</u>	<u>Distance, degrees</u>	<u>Azimuth, degrees</u>	<u>Magnification</u>	<u><math>10^{25} \frac{M_0}{\text{dyne-cm}}</math></u>
WES	47.4	323.3	3000	3.4
TRI	56.6	39.1	3000	4.9
TOL	42.5	35.7	1500	3.6
SCP	50.7	318.0	1500	3.9
OGD	48.7	319.9	1500	3.8
NNA	46.0	245.5	3000	2.4
MAL	40.3	39.1	1500	5.7
LPB	40.6	233.8	1500	4.7
JER	69.2	58.9	3000	5.8
HLW	65.7	60.7	3000	5.3
GEO	49.2	316.2	750	7.8
COP	60.9	28.4	1500	6.4
CAR	31.8	278.0	3000	18
BOG	39.1	268.2	3000	8.8
BEC	37.2	315.9	1500	4.0
ATL	52.5	306.7	3000	3.7
AAE	72.8	82.8	1500	9.7

For all stations we used  $T_p = 15$  sec,  $T_g = 100$  sec,  $H_p = .93$ ,  $H_g = 1.0$ , where  $T_p$ ,  $T_g$ ,  $H_p$ , and  $H_g$  refer to the seismometer and galvanometer periods and damping factors, respectively.



### Figure Captions

Figure 8.1 Bathymetry of the Doldrums transform fault region between latitudes  $6^{\circ}$  N and  $10^{\circ}$  N, and longitudes  $33^{\circ}$  W and  $42^{\circ}$  W, and epicenters of all known earthquakes in this area between latitudes  $6^{\circ}$  N and  $8.5^{\circ}$  N, taken from Table 8.1. The approximate locations of the ridge axes, as discussed in the text, are indicated by double lines. Open circles represent epicenters taken from Gutenberg and Richter (1954) and Rothe (1969). Larger symbols are events with  $M_S > 6.0$ . Contour intervals are every 800 m below sea level, taken from Uchupi (1982).

Figure 8.2 Longitude versus year of occurrence for the earthquakes on the Doldrums transform fault system with  $M_S > 5.5$ .  $M_S$  is shown for each event. Dashed lines indicate where the transform segments intersect adjacent spreading centers. Bars for the events of 1963, 1964, and 1977 indicate the fault lengths and rupture directions used for the synthetic seismograms.

Figure 8.3 Results of fits of synthetic (upper) to observed (lower) seismograms of P waves from the August 3, 1963 earthquake. Positions on lower focal hemisphere of stations used for synthesis and fault plane solution obtained are also shown. Closed circles for station locations represent compressional first-arrival polarities, open circles represent dilatational polarities, and crosses represent stations with unusually complex, perhaps nodal, waveforms. The vertical scales were normalized so that all seismograms would have equal maximum amplitudes.

Figure 8.4 Results of fits of synthetic (upper) to observed (lower) seismograms of P waves from the September 4, 1964 earthquake. Positions on lower focal hemisphere of stations used for synthesis and fault plane solution obtained are also shown. Closed circles for station locations represent compressional first-arrival polarities, open circles represent dilatational polarities, and crosses represent stations with questionable polarities. The vertical scales were normalized so that all seismograms would have equal maximum amplitudes.

Figure 8.5 Results of fits of synthetic (upper) to observed (lower) seismograms of P waves from the April 4, 1977 earthquake. Positions on lower focal hemisphere of stations used for synthesis and fault plane solution obtained are also shown. Closed circles for station locations represent compressional first-arrival polarities, open circles represent dilatational polarities, and crosses represent stations with questionable polarities. The observed seismogram from BEC was apparently either recorded with the wrong polarity or reproduced upside down, since both its waveform and its time marks are the wrong direction; for our modelling we have assumed that the actual displacements were reversed from what is shown on the seismogram. The vertical scales were normalized so that all seismograms would have equal maximum amplitudes.

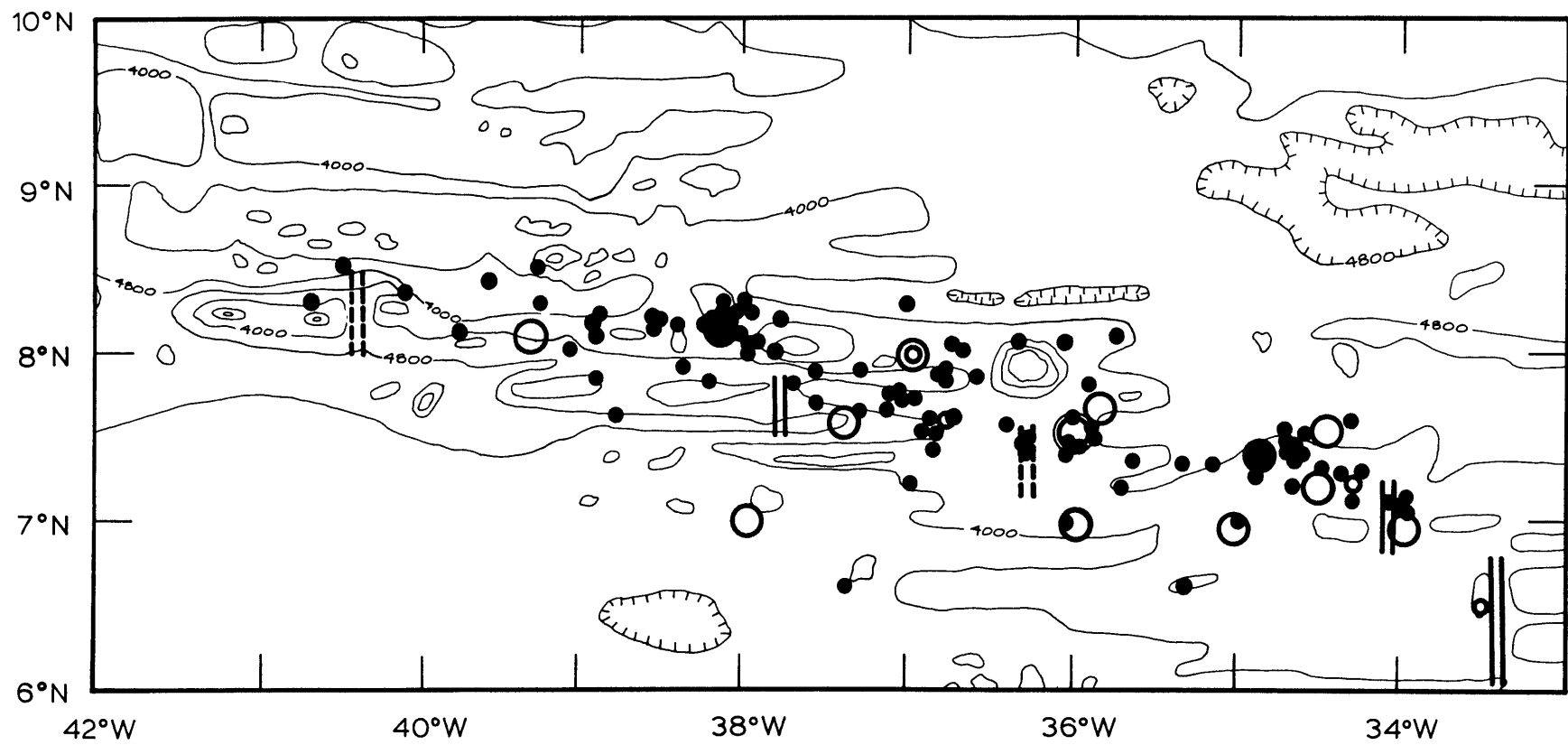


Fig. 8.1

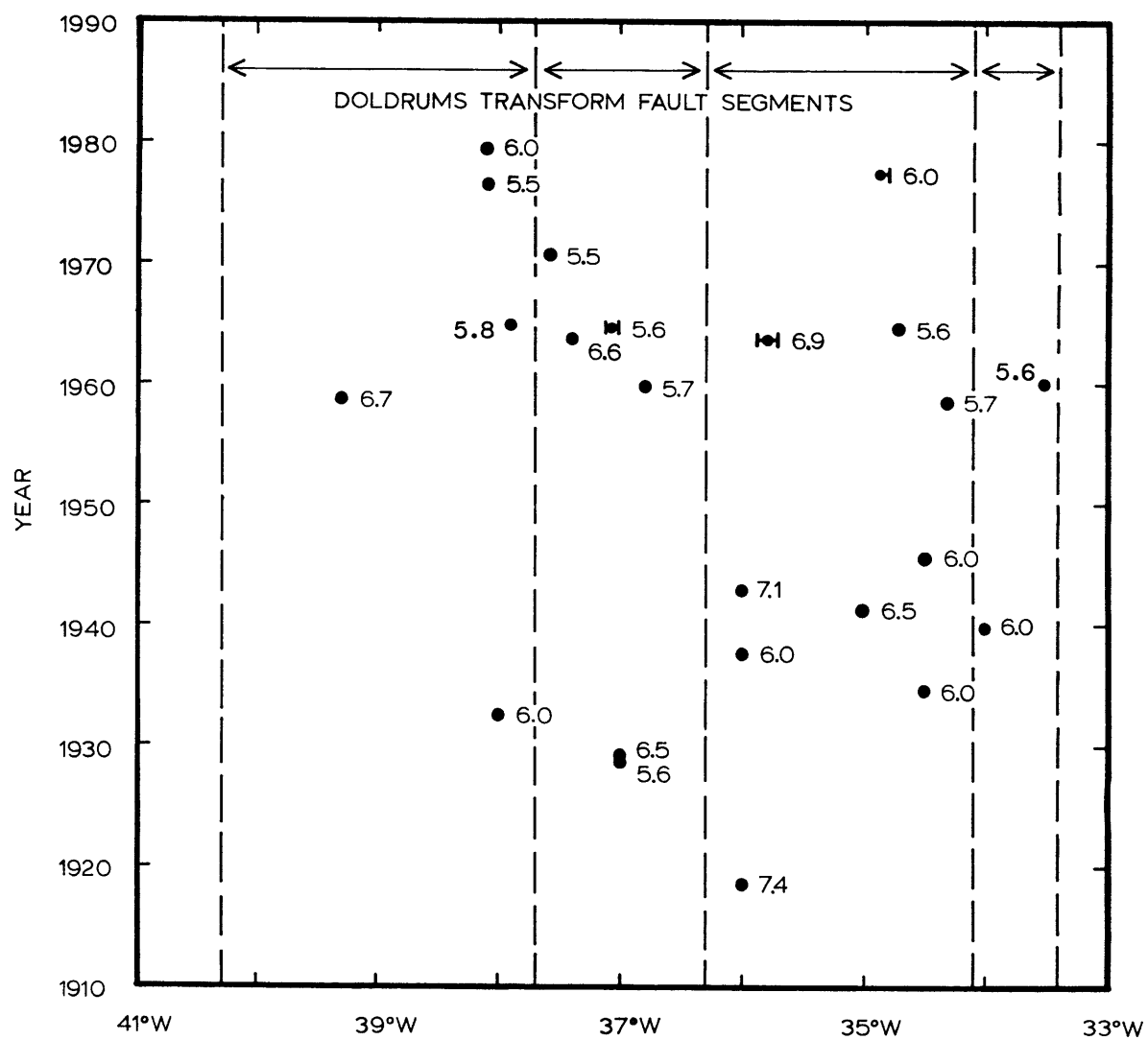


Fig. 8.2

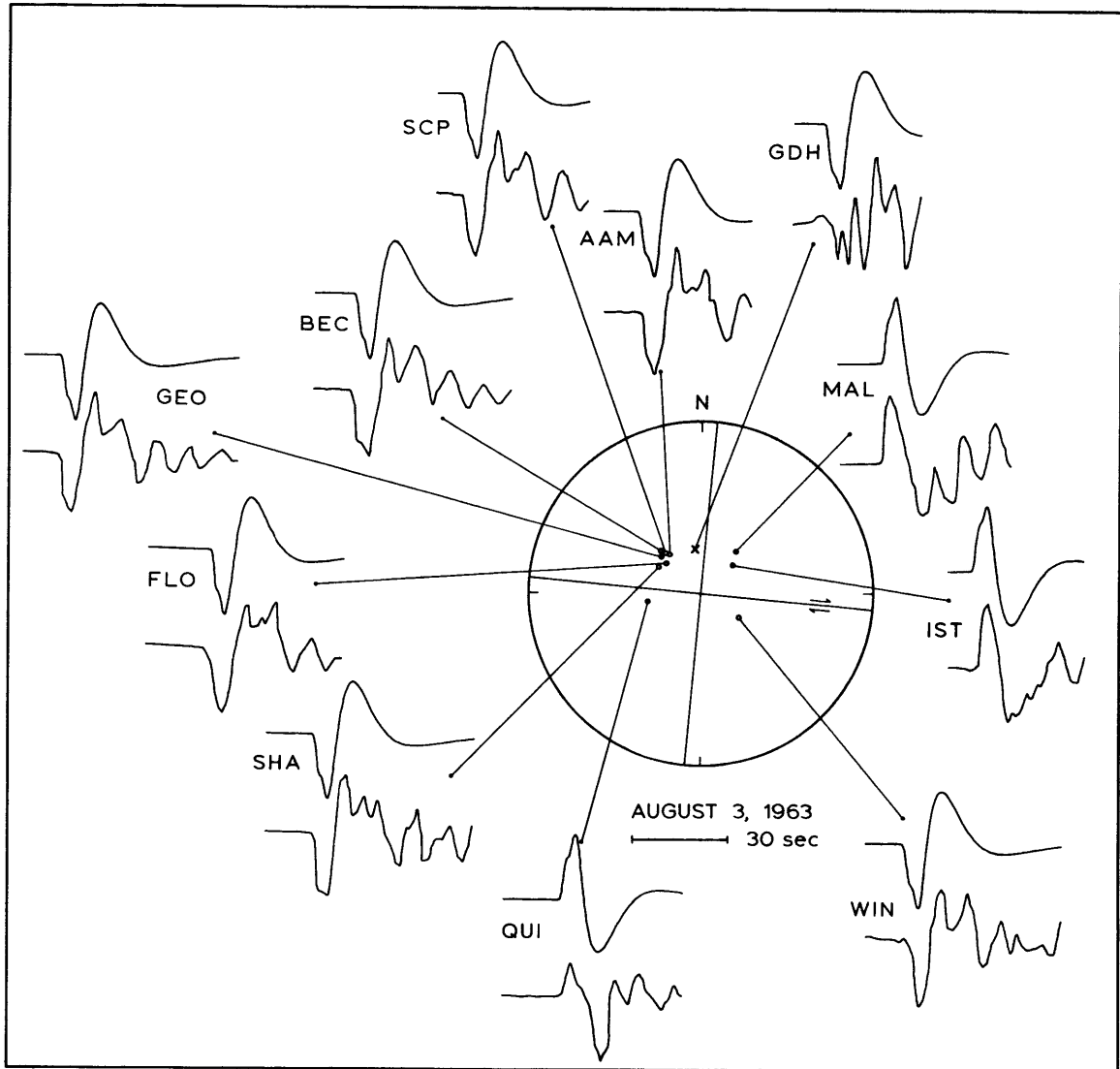


Fig. 8.3

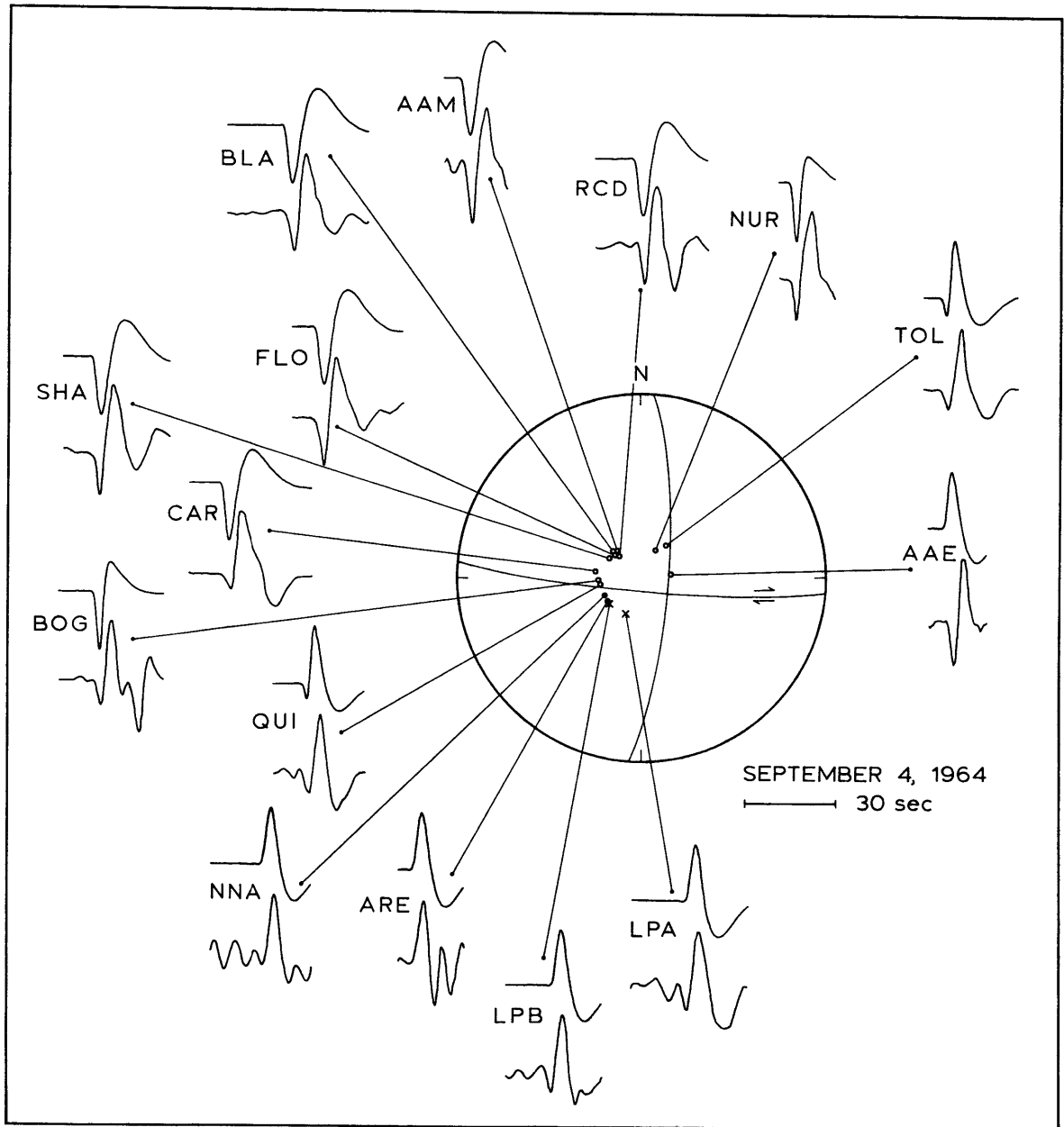


Fig. 8.4

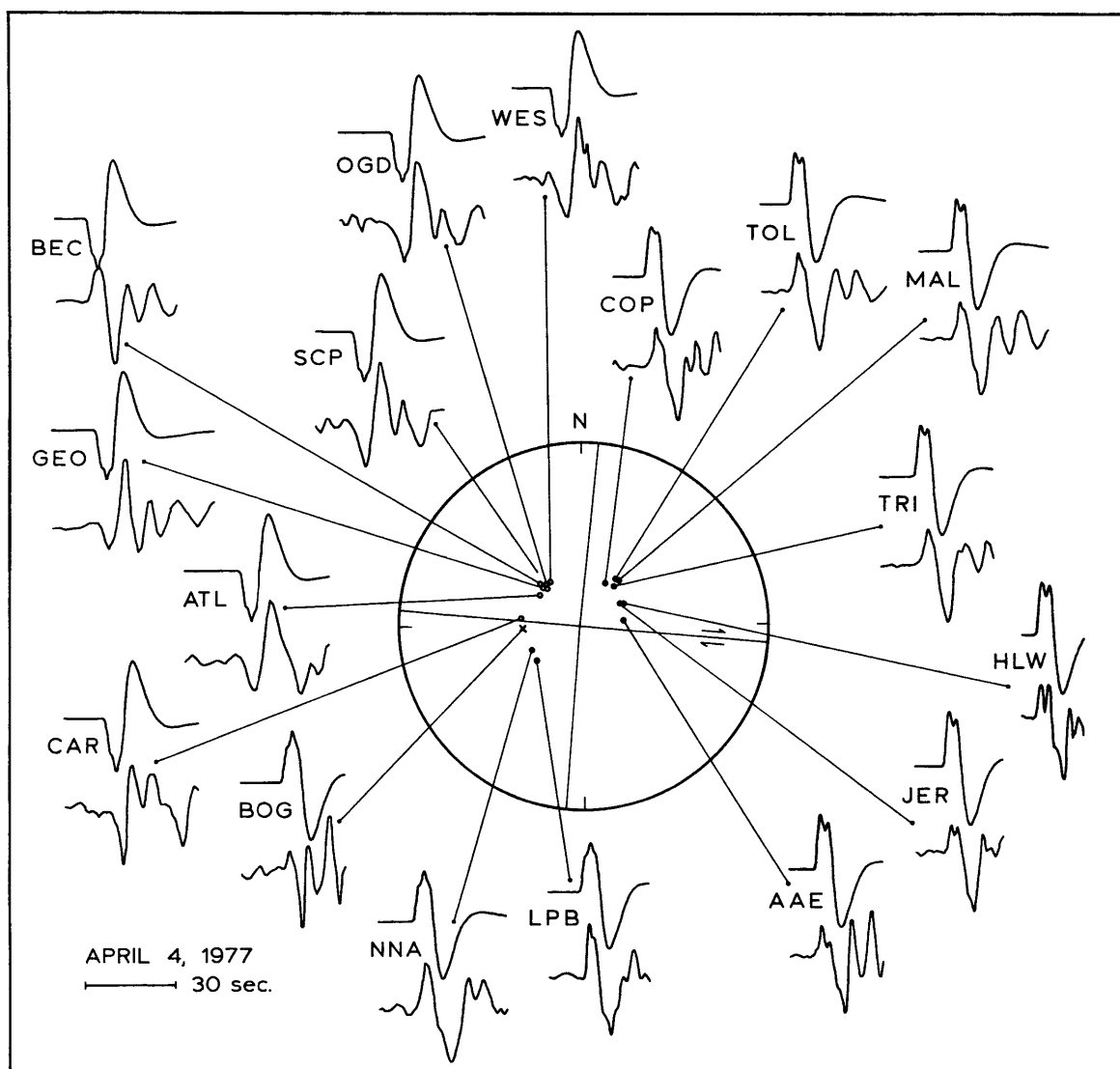


Fig. 8.5

## CHAPTER 9. CHARACTERIZATION OF GENERAL SEISMIC BEHAVIOR OF 6 ATLANTIC TRANSFORMS

In this chapter we present that part of our results obtained with data from all six transforms studied, and we discuss what can be learned about transform behavior from this and the result of the previous 6 chapters. Specifically we summarize our findings on the source characteristics of large transform earthquakes, we derive relationships among  $m_b$ ,  $M_S$ , and  $M_0$  as a way of characterizing transform seismicity, and we examine the various transforms for their similarities and differences. We also compare the seismic records of each transform to see if regional or tectonic influences have been operative over a scale large enough to affect several transforms simultaneously.

### COMPARISON OF EARTHQUAKE SOURCE PARAMETERS

Most of the source characteristics obtained from P wave synthesis for the 12 earthquakes studied here are summarized in Table 9.1. If this set of events can be considered a representative sample of major earthquakes on oceanic transforms, then some generalities may apply to other features of transform dynamics.

The first observation is that the focal depths for all of the events studied varied between 1 and 6.5 km below basement floor. This suggests that the seismic thickness of the ocean floor (that part capable of initiating brittle fracture) is limited to the crust or the upper few km of mantle. This is not unexpected since this material is presumably cooler than the lithospheric material at greater depth. The fault widths used were generally about 5 km, with only one event requiring as much as 10 km. These values, admittedly poorly constrained, support the



suggestion that faulting does not extend much further down than the upper 5 km of so of mantle material. (The reasonable agreement found between observed and expected moment rates supports this suggestion also.)

Another observation is that transform faulting shows some tendency toward unilateral rupture propagation. This was required on five of the events studied (actually used on six), and previous work on the September 4, 1964 earthquake (Bollinger, 1968; Udias, 1971) has suggested that the faulting may have been unilateral for this event also (and in the same direction as that found for the April 4, 1977 event). (The observed waveforms for the other events did not necessarily rule out some unilateral faulting.) In addition, the direction of faulting was consistent on each transform where unilateral faulting was inferred for more than one event. One suggestion is that there is a prevailing lithospheric stress field that is consistent over distances large enough to include entire transforms.

Another interesting feature we have found is that the fault lengths seem to be no more than a few tens of kilometers. This is indicated by the predominant periods of the observed seismograms, and hence the source time functions required for the synthetic seismograms, as well as by the seismic history of several of the transforms. This finding is contrary to that of Kanamori and Stewart (1976) for the Gibbs transform that large events release strain on major portions of a transform's length. The seismic history of the Gibbs transform may be unusual in this respect, but an alternate interpretation is that, since transform behavior seems to be highly uneven over the period of our observation, we may not yet have seen representative behavior on the Gibbs transform.

The stress drops we have determined range from 30 to 660 bars. These values are poorly constrained. Since stress drop varies directly with

average displacement, and since we were required to use similar fault dimensions for earthquakes whose moments varied by 2 orders of magnitude, the largest stress drops naturally were found for the largest events.

Finally, the fault orientations we found for all of the events were consistent with horizontal slip on vertical faults, with only a few exceptions. Two of the events on the Vema transform had non-vertical fault planes, dipping to the north. (The other event on the Vema transform was too complex for us to be certain of the resolution on fault dip.) This result may correlate with the observed asymmetry of the bathymetry of this transform. We also were required to use a non-vertical fault and a component of vertical slip for one event on the Doldrums transform.

#### $M_S$ VS. $m_b$

Figure 9.1 shows a plot of the surface wave magnitude versus body wave magnitude for earthquakes on the six Atlantic transforms we studied. All earthquakes for which both  $M_S$  and  $m_b$  values were independently available and which we were fairly certain had strike-slip mechanisms were included. The best fitting straight line to these values, obtained using all of the data except two (indicated in Figure 9.1) was

$$m_b = 2.2 \pm 0.2 + (0.57 \pm 0.05) M_S \quad (9.1)$$

$$\text{or} \quad M_S = -3.8 \pm 0.7 + (1.75 \pm 0.14) m_b$$

This line is also shown in the figure. The two events not used were the two largest earthquakes on the Gibbs transform, events which Kanamori and Stewart (1976) suggested might have unusually large  $M_S$  values for their body wave excitation.

The line shown in Figure 9.1 is that which produces the minimum sum of the squares of the perpendicular distances between the points and the

line, i.e., the minimum sum of the squares of the vertical distances plus the squares of the horizontal distances. This is different from the usual least-squares technique which minimizes the sum of the squares of the vertical distances only; we chose this technique because it allows the recognition that errors can exist in both dimensions in the data, rather than just the vertical direction. The major objection to this approach is that the results vary with changes of scale, and therefore cannot be considered absolute. This problem and several solutions to it are discussed by York (1966). We felt, however, that since  $M_S$  and  $m_b$  measure roughly the same quantities, our approach was justified. When we determined the best-fitting straight line using the usual least-squares technique we obtained very similar results.

With the exception of perhaps one event on the Kane transform and the largest of the three events on the Gibbs transform, the data in Figure 9.1 fit a straight line quite well over the range of  $M_S$  from 4.2 to 6.6. The scatter of these points away from this line is much less than for most  $M_S$  vs.  $m_b$  plots, (e.g., Gutenberg and Richter, 1954; Abe and Kanamori, 1980), and, in fact, increases if we include all of the earthquakes with both  $M_S$  and  $m_b$  values listed in the seismicity tables in Chapters 3 through 8, rather than just those whose location verifies them as strike-slip events. This good fit is probably due to the fact that the earthquakes all occurred in similar tectonic settings and were observed from similar directions. The largest Gibbs transform event may indeed be irregular, as mentioned earlier, in that either its  $M_S$  is anomalously large or its  $m_b$  is unusually small. The next largest Gibbs transform event does not show this irregularity to the same extent, however.

We have used Equation (9.1) to determine  $M_S$  values from the  $m_b$  values for those events listed in the seismicity tables for which only the latter magnitudes were available. The  $M_S$  values so determined are given in parentheses in the seismicity tables in Chapters 3 through 8.

#### LOG $N(M_S)$ VS. $M_S$

Figure 9.2 shows plots of Log  $N$  vs.  $M_S$  for the six transforms studied, where  $N$  is the total number of earthquakes with  $M_S$  equal to or greater than a certain value. The values shown represent all of the known earthquakes that are thought to have occurred on the transforms during the 18 years from 1964 through 1981. There may be some contamination of the data for the Gibbs and Doldrums transforms from normal faulting events on the ridge sections included within the bounds of these transforms, but this contamination is limited to the data points representing the smaller events.

We have determined best-fitting straight lines to these data using the standard least-squares technique with the equation  $\text{Log } N = a - b M_S$ , and these lines are also shown in Figure 9.2. Only the data represented by closed circles were used; we may have seen too few of the larger events to make the sample representative, and for the smaller events, the sample may be deficient due to less complete detection. Those values not used are shown in Figure 9.2 as open circles. The transform for which choosing these points was most difficult was the Oceanographer, which is not surprising since this is the smallest of the six. For the straight line fits, we normalized the values of  $N$  by dividing by 18, so they represent the number of events per year. The values of  $a$  and  $b$  we obtained, together with their standard deviations, are shown in Table 9.2.

One feature immediately apparent is that both the  $a$ -values, which represent a measure of the total number of earthquakes [actually  $\log N(M_S > 0)$ ], and the  $b$ -values, which represent the distribution of events with size, vary systematically with latitude for five of the six transforms. The values obtained for the Kane,  $15^{\circ}20'$ , and Vema transforms are only slightly dependent on the  $M_S$  range used. For the Gibbs transform, the inclusion of the higher  $M_S$  values would have resulted in  $a$  and  $b$  values closer to those of the other transforms. The fit obtained for the Doldrums transform is quite good up to the highest  $M_S$  seen ( $M_S = 6.0$ ), though the deviation for the lower  $M_S$  values is also quite abrupt. The exception to this apparent trend is that either the values for the Kane transform are too large or the values for the  $15^{\circ}20'$  transform are too small, though the deviations from the trends are not great. That the  $a$  and  $b$  values would show the same trend is not too surprising since, for roughly the same expected moment rates, larger  $b$  values imply fewer large events and more small ones, and thus the total number of events must be greater. These apparent trends suggest, however, that there is some systematic difference across the six transforms. If these trends are real, then one explanation is that some large scale variation exists in the upper mantle. This is certainly possible, particularly since the variation might be by latitude in a spinning body; if this were true, trends like these would be expected in other parts of the world. We are tempted therefore to look for explanations in local properties, particularly those which have an influence on the thermal structure.

Table 9.2 lists, in addition to the  $a$  and  $b$  values for each transform, slip rate (from Minster and Jordan, 1978), transform length, length / slip rate (i.e., total age offset), and predicted and observed

moment rate, taken from Chapters 3-8. The transform lengths vary considerably and unsystematically, and these variations dominate all of the parameters listed in Table 9.2 except slip rate. The significance of length-dependent parameters is obscured anyway for the Gibbs and Doldrums transforms since both of these have ridge segments within them. However the variation of slip rate across the transforms does agree somewhat with the trends in the  $a$  and  $b$  values, with higher slip rates tending to be associated with higher  $a$  and  $b$  values. The small deviation of the Kane and  $15^{\circ} 20'$  transforms from the trends still exists; the slip rate determined for the  $15^{\circ} 20'$  transform deviates from the trend less if we use the North American-African angular rotation vector than if we use the South American-African rotation vector. An implication of these trends is that one feature dominating transform behavior may be slip rate, rather than a thermal state dependent strictly on age or length. One qualitative model for this dependence is that a faster slip rate produces more local stress, more local fracturing of the rock, and therefore more advection of mantle material into the transform from the bottom. The resulting higher temperatures (and greater density of fractures?) would mean that the material cannot support large stresses, and thus would tend to produce more smaller events. This mechanism would dominate over the differences in temperature produced by cooling with age. This model is somewhat contradicted, however, by the fact that the largest events have been recorded on the two transforms with the fastest slip rates. We must recognize, though, that these transforms also have the highest total moment rates, and as discussed later in this chapter, we may not have seen enough of the seismic history to show the full temporal behavior of the largest events.

### $M_S$ VS. $\log M_0$

Figure 9.3 shows a plot of  $M_S$  vs.  $\log M_0$  for the earthquakes we have studied. Also included in Figure 9.3 are all other known transform fault earthquakes for which we have both  $M_0$  and  $M_S$  (Burr and Solomon, 1978, and S. C. Solomon, personal communication, 1982) with the two large Gibbs transform events labeled for easy reference. The values for the earthquakes we studied generally form a linear trend that defines the upper edge of the data, with considerably less scatter than the rest of the data. Our values have less scatter probably because they were all determined using the same method, and because all of the events occurred in similar tectonic settings. That our values define the upper edge of the data may be because of some distinctive feature of the North Atlantic such as its slow spreading rate, or it may be because, for strike-slip earthquakes, P wave techniques tend to produce higher moments than more commonly used surface wave techniques.

We have determined a best-fit straight line to our data using the same perpendicular-distance technique we described for Figure 9.1. We used this technique since there are uncertainties in both  $M_0$  and  $M_S$  values. We did not include (1) the two Gibbs transform events, since we did not determine these moment values, (2) the smaller of the two Oceanographer events, since its moment was determined using only one station. The best-fitting line we found was

$$\log M_0 = 18.6 \pm 0.6 + (1.18 \pm 0.09) M_S . \quad (9.2)$$

This line is also shown in Figure 9.3. Since the data fit a straight line reasonably well, we obtain almost the same results if we use a conventional least-squares technique. We believe that this line is representative of earthquakes on North Atlantic transform faults, at

least for moments calculated using P-wave synthesis. Using this line we calculated  $M_0$  values for all of the earthquakes given in our seismicity tables for which other moment values were not available, and these estimated values are given in parentheses in the tables. We used these estimated values for slope and intercept ( $c$  and  $d$  in Equation 3.3) to determine the rates of unobserved seismic moment in Chapters 3 through 8.

#### TOTAL $M_0$ AND ACCUMULATED $M_0$ PER YEAR

Figure 9.4 shows the total seismic moment during each year for all six transforms, for the years between the first known event on each transform through 1981. These values were obtained by simply adding the moments of all the transform earthquakes listed for each year in the seismicity tables in Chapters 3 through 8. (The unobserved background levels were too low to be seen on these plots, and in general the plots were dominated by the largest events, i.e., those with  $M_S$  of at least, say, 5.5.) Seismic activity is composed of discontinuous, discrete events, so, properly speaking, it is not correct to consider derivatives, but if we think of these plots as imperfect representations of continuous tectonic movement, then they represent the rate of moment release on each transform for each year, in units of dyne-cm/ year, i.e., the derivative of the total accumulated moment (see Figure 9.5).

Figure 9.5 shows the total accumulated moment on each transform, from the first known event through 1981, normalized so that the total equals 1 at the end of 1981. Subject to the same reservations as for Figure 9.4, these represent the integrals of the moment rates shown in Figure 9.4. They were normalized so that the transforms could be compared to each other with the effects of different total moment rates eliminated.



A number of noteworthy features are apparent in these two figures. The most obvious is that three of the six transforms had large moment rates (produced by very large events) before 1930, and these levels have not been approached since. It is possible that the magnitudes for these events (admittedly not quite the same as modern  $M_S$ ) are much larger than we would calculate today for the same events, but if this were the case then we would expect that such errors would also exist in the magnitudes of the other events before 1964. Thus it is probable that these extraordinarily large magnitudes (and therefore moments) are real.

The next implication from this view is that we probably have seen no more than one complete seismic cycle for most of the transforms, if we have seen a complete cycle at all. For example, the set of three large events on the Vema transform in 1925, 1927, and 1929 may have fractured the entire transform, but this kind of activity has certainly not been repeated since. This is compatible with the fact that the recurrence times we calculated for the earthquakes studied here ranged between roughly 50 and 300 yrs (Table 9.1). This implication is valid even if these earlier magnitudes are too large for comparison to today's since, if we must take these as actually being smaller than our figures indicate, then the other events observed between, say, 1930 and 1960 must also be considered as much smaller. Thus there must have been practically no significant seismic activity between 1930 and the early 1960's, again implying at most a fraction of a complete cycle on three of the transforms. The small fault dimensions we obtained for the earthquakes we studied, even if too low by a factor of two, support the idea that the transforms have not slipped over their entire length since, say, 1960. We can see from Table 9.2 and Figure 9.4 that the transforms

for which the observed moment rate is more than twice that expected from the slip rate are the same transforms on which one or more very large earthquakes occurred early in the period of seismic observation, and the only transform for which the observed moment rate is less than the expected rate is the Gibbs transform, which has shown a higher rate of moment release during the last 30 years or so than during the previous 30 years. (We must remember that Figures 9.4 and 9.5 contain no information about where on each transform these events occurred. If we consider that the moment released in any two events can be on different parts of a transform, then the unevenness of seismic moment rates on any single part of a transform is even greater.)

The preceeding discussion throws into doubt any conclusions obtained from comparisons of observed moment rates to moment rates calculated from slip rates. During our observed seismic history the rate of seismic moment release has been decidedly uneven. Even if tectonic movement has occurred at a constant rate over the span of our seismic observation (which, as suggested elsewhere in this work, may not be the case), and assuming that this rate is roughly equal to the long term ( $> 1$  m.y.) average obtained from such sources as sea floor magnetic anomalies, it is still possible that one large earthquake on any given part of a transform may have released strain accumulated for an indefinite period, and thus we cannot convert the total slip of this event into a value for slip rate.

The next interesting feature of Figures 9.4 and 9.5 is that there seems to be some correlation between the seismic activity on the different transforms. The most striking is the apparent correlation of the high-moment-release years on the Kane, Vema, and Doldrums transforms

between 1918 and 1929, accompanied by significant, though less dramatic, activity on the other three transforms during this same period. During the entire time of seismic observations the behavior of the Kane and  $15^{\circ} 20'$  transforms has been remarkably similar, though the  $15^{\circ} 20'$  transform has consistently lagged behind the Kane by about 5 years. All of the transforms had active years between 1939 and 1942 except the Kane transform, which had a big year in 1935, and the Vema transform, which may have been completely relaxed by its three large events in 1925, 1927, and 1929. After the "1940" activity, five of the six transforms had quiet periods. Then, in an active period beginning in 1962, all six transforms displayed major seismic activity, with the "slightly late" transforms being the  $15^{\circ} 20'$  (as usual), and the Gibbs, which had unique activity in 1954.

One must be careful, when staring at figures such as these, not to read too much into them; the human mind is a very good imaging system, quite capable of finding "virtual" correlations in data when none actually exists. The proper way to test for the existence of these correlations would be to develop some sort of probability model, in this case taking into account the event times, seismic moments, locations on the transforms, fault lengths, and the locations of the transforms themselves, and then see if the observed distribution differs significantly from what the model predicts. Such a study would be outside of the immediate goals of this work, and there probably are not enough data here for this to be done effectively since there would have to be many degrees of freedom in the probability model. Nevertheless, we must still question whether these correlations are real. Some of the correlations we might be tempted to claim could certainly be

fortuitous, such as the "1940" episode, or a new emerging episode implied by the 1979 Vema and 1980 Kane events. And it is certainly possible, given enough transforms (six?) over a short enough time span (60 years, when a cycle could span maybe 10?) that two of them could behave similarly. However, we must note that the two with similar behavior are adjacent and, in fact, all of the four southernmost transforms "seem" to have had similar behavior. Also the occurrence of the anomalously large events on three of the transforms before 1930, and the occurrence of the unusually quiet periods on five of the transforms during roughly 1940 to 1960 seem highly improbable. In the absence of a more methodical study we conclude that some correlation exists, even if it is only in the grossest level of seismic activity.

If these correlations in transform behavior are real, then we must ask why. One possibility is that a large event on one transform can trigger events on others by causing local increases of stress in the lithosphere that "diffuse" by viscoelastic relaxation in the asthenosphere and perhaps the lower lithosphere. Stress propagation has been discussed by others (Ida, 1974; Anderson, 1975; Kasahara, 1979) and was the apparent mechanism allowing for the prediction of the February 4, 1975 Haicheng earthquake (Scholz, 1977). If this mechanism is in effect, it need not necessarily produce any strong directionality of activity moving away from an initial event because the occurrence of an earthquake on any transform would still be controlled by the total local stress, old and newly acquired, and not just that acquired when the initial event occurred.

Another possible mechanism for the apparent correlation of transform behavior is that large-scale tectonic movement is episodic, with a period

of 60 years or more. This differs from the mechanism of the previous paragraph, in which an earthquake can trigger others by stress diffusion. In this case, the effect causing increased seismicity originates with an episode of increased mantle-driven tectonic movement, not with a large earthquake. Thus the large moment totals seen from 1918 to 1929 could signal a major episode of spreading along the entire mid-ocean ridge system in the central North Atlantic, with smaller episodes accounting for the other apparent active periods, and the quiet period from 1940 to 1960 could be the result of a lack of comparable tectonic movement during this time.

This interpretation suggests that tectonic movement itself is as episodic as the seismicity appears to be. Such a possibility was discussed in Chapter 6 as a mechanism whereby two large events could occur within a short time with their fault planes overlapping the same parts of a transform, even though too little time had elapsed between the events for sufficient strain to accumulate at the long-term average slip rate of the transform. We showed that this possibility was not a necessary requirement of the seismic history, merely one of several explanations of the observed seismicity. The same is true here: uneven tectonic movement is a possible, though non-unique, explanation. Such uneven tectonic movement may, of course, be on a much longer time scale, say, 100 years or more. The activity between 1918 and 1929 would then be associated with a plate-wide tectonic event which has not yet been repeated. The apparent similarity we think we see in Figures 9.4 and 9.5 in the short term behavior of the six transforms may be due to the fact that they all have similar dynamics, and thus all behaved the same way after the originating tectonic event.

## SUMMARY OF RESULTS

An analysis of P waveforms from large earthquakes on five Atlantic transforms produced the following conclusions:

1. Focal depths are shallow. Rupture initiates either in the upper few kilometers of the mantle or in the crust, though generally not directly at the sea floor.

2. The fault lengths, even of the major events, are a few tens of kilometers at most, and therefore do not fracture entire transforms.

3. Displacements are on the order of a meter, while rise times are short, so that particle velocities and stress drops are therefore high.

4. The fault planes are close to, but not necessarily vertical, except for those on the Vema transform, which seem to dip at high angles to the north.

5. The slip angles are generally close to  $0^\circ$  or  $180^\circ$ , but some small vertical component of slip cannot be ruled out.

6. The faulting shows considerable horizontal directivity, with a consistency in the direction of rupture propagation for each transform.

7. The vertical component of rupture propagation cannot be well resolved.

An analysis of seismicity on six Atlantic transforms yielded the following conclusions:

1. The transforms have shown uneven seismic behavior during the period of our observation, and we have seen no more than one complete cycle, if that much.

2. Transforms generally do not slip along their entire length in a few large events. A single connected fault trace for the active plate boundary need not characterize long oceanic transforms (though a single trace may be presently active for the Vema transform).

3. The  $b$ -values show a tendency to increase with increasing slip rate. We suggest that fracture generation in oceanic crust and rise of altered mantle material may dominate the small scale dynamics. The earthquake parameters also do not seem to depend on their position on the transform, suggesting that some broad scale feature such as the age of each side does not control movement.

4. There may be some correlation of large earthquake recurrence times between transforms. Such a correlation, if real, may be caused by one large event triggering others or by plate-scale episodes of deformation that trigger them all together.

5. Looking at one tectonic setting (from consistent viewing angles and with consistent techniques) produces good linear correlations between  $M_S$  and  $m_b$  values and between  $M_S$  and  $\log M_0$  values.

TABLE 9.1 Summary of source parameters for the 12 earthquakes studied.

Date:	5/17/64	11/18/70	3/12/77	9/24/69	6/19/70	12/9/72	3/17/62	5/14/76	8/25/79	8/3/63	9/4/64	4/4/77
Transform	Oceanographer		Kane	15°20'			Vema			Doldrums		
$m_b$	5.6	5.1	5.4	5.8	5.5	5.5	---	5.5	6.0	---	5.4	5.6
$M_s$	6.3	(5.1)	5.6	(6.4)	(5.8)	5.7	7.0	5.7	6.6	6.9	5.6	6.0
$M_0$	8.3	0.95	1.3	17	2.7	2.8	130	3.1	22	30	1.8	5.3
L(km)	12	6	10	15	10	12	30	10	60*	18	10	10
w(km)	5	5	5	5	6	5	10	5	5	4	5	3
$v_r$ (km/s)	4	3	3	3	4	3	3	3	3	4	3	4
Dir	W	W	B	E	E	E	B	B	B	B	B	E
h(km)	8/4	10.5/ 6.5	5.5/ 1.5	5/1	7/3	6/2	7.8/ 2.1	7.5/ 1.8	8/ 2.3	7.5/ 3.5	5.5/ 1.5	7.8/ 3.8
D(m)	4.0	0.9	0.7	6.3	1.3	1.3	12	1.2	2.1	12	1.0	5.1
$R_t$ (s)	1	1	0.5	1	1	1	2	1	1	1	0.5	0.8
$V_t$ (m/s)	4	0.9	1.5	6	1.3	1.3	6	1.2	2	12	2	6
$T_{rec}$ (yr)	170	90	30	200	40	40	200	40	70	350	60	190
$\Delta\sigma$ (bar)	180	40	30	280	50	60	270	50	90	660	50	380

\*Double event.

Notes:  $m_b$  and  $M_s$  are body and surface wave magnitude, respectively ( $M_s$  values in parentheses were determined from  $m_b$  using Equation 9.1);  $M_0$  is seismic moment, in  $10^{25}$  dyne-cm; L and w are fault length and width, respectively;  $v_r$  is rupture propagation speed; Dir is horizontal direction of rupture (E = east, W = west, B = bilateral); h is focal depth (first number is depth below sea level, second is below basement floor); D is average displacement;  $R_t$  is rise time;  $V_t$  is particle dislocation velocity;  $T_{rec}$  is the average recurrence time found for a similar event on the same part of the transform;  $\Delta\sigma$  is stress drop.



Table 9.2. Some features of the seismicity of the transforms included in this study.

Transform	a	Std. Dev.	b	Std. Dev.	V, cm/yr	L, km	Age, m.y.	$\Sigma M_0$ , 10 <sup>25</sup> dyne-cm/yr	
								calc	obs
Gibbs	1.7 ± 0.04		0.37 ± .01		2.3	350	15	2.9	2.6
Oceanographer	1.8 ± 0.1		0.47 ± .03		2.4	130	5.4	0.55	0.87
Kane	2.4 ± 0.1		0.60 ± .02		2.4	150	6.3	0.63	3.1
15° 20'	2.0 ± 0.2		0.52 ± .04		2.8 3.1	155	5.5 5.0	0.76 0.84	1.4
Vema	2.6 ± 0.1		0.61 ± .02		3.1	320	10	3.5	11
Doldrums	4.3 ± 0.1		0.92 ± .02		3.4	410 (760)	12 (22)	2.3	6.7

Notes: a and b values, and estimates of their standard deviations, are the empirical constants in Equation 3.2, derived from the data shown in Figure 9.2. V is the relative plate velocity (Minster and Jordan, 1978). L is the transform length, and Age denotes the age offset across the inactive portions of the fracture zone. The last two columns compare the predicted and observed annual rates of seismic moment release for the period 1920 through 1981. Values for the 15° 20' transform were calculated using both the North American-African (first line) and the South American-African angular velocity vector (second line). Age offset values for the Gibbs and Doldrums transforms are totals for both segments studied, neglecting the emplacement of younger material at the short intervening spreading center. Values for the entire four-segment length of the Doldrums transform are included in parentheses. For the Doldrums transform, the annual rate of moment release is an average for the years 1918 through 1981.

### Figure captions

Figure 9.1 Surface wave magnitude versus body wave magnitude for earthquakes on the six transforms studied. All earthquakes for which both  $M_S$  and  $m_b$  values were available and which we were fairly certain had strike-slip mechanisms were included. The best fitting straight line to these values is also shown. The two largest earthquakes on the Gibbs transform, indicated in parentheses, were not used to determine the straight line. The line shown is that which produces the minimum sum of the squares of the perpendicular distances between the points and the line, i.e., the minimum sum of the squares of the vertical distances plus the squares of the horizontal distances (see text). Symbols beside each point indicate on which transform the event(s) occurred.

Figure 9.2 Log N vs.  $M_S$  for each of the six transforms studied, where N is the total number of earthquakes during the 18 years from 1964 through 1981 with  $M_S$  equal to or greater than the given value. The values shown represent all of the known earthquakes that are thought to have occurred on the transforms during these years. There may be some contamination of the data for the Gibbs and Doldrums transforms from normal faulting events on the ridge sections included within the bounds of these transforms, but this contamination is limited to the data points representing the smaller events. The best-fitting straight lines to these data, using the standard least-squares technique with the equation  $\text{Log } N = a - b M_S$ , are also shown. Only the data represented by closed circles were used; values not used are shown as open circles. For the straight line fits, we

normalized the values of  $N$  by dividing by 18, so they represent the number of events per year. The values of  $a$  and  $b$  so obtained are given in Table 9.2.

Figure 9.3  $M_S$  vs.  $\log M_0$  in dyne-cm for the earthquakes we have studied (large closed circles, and the open circle for the November 18, 1970 event) and all other known transform fault earthquakes (small closed circles) for which we have both  $M_0$  and  $M_S$  (Burr and Solomon, 1978, and S. C. Solomon, personal communication, 1982). The two large Gibbs transform events are labeled for easy reference. The best-fit straight line to the large closed circles, using the same perpendicular-distance technique as described for Figure 9.1, is also shown. For this fit we did not include the events represented by the small closed circles, since we did not determine these moment values, or the smaller of the two indicated Oceanographer transform events (November 18, 1970), since its moment was determined using only one station.

Figure 9.4 Annual seismic moment for each of the six transforms studied, for the years between the first known event on each transform through 1981. These values were obtained by adding the moments of all the transform earthquakes listed for each year in the seismicity tables in Chapters 3 through 8.

Figure 9.5 Normalized cumulative seismic moment for each transform, for the years between the first known event on each transform through 1981. These results were obtained by adding cumulatively the moments

of all the transform earthquakes through each year listed in the seismicity tables in Chapters 3 through 8, and normalizing so that the total for 1981 equals 1.

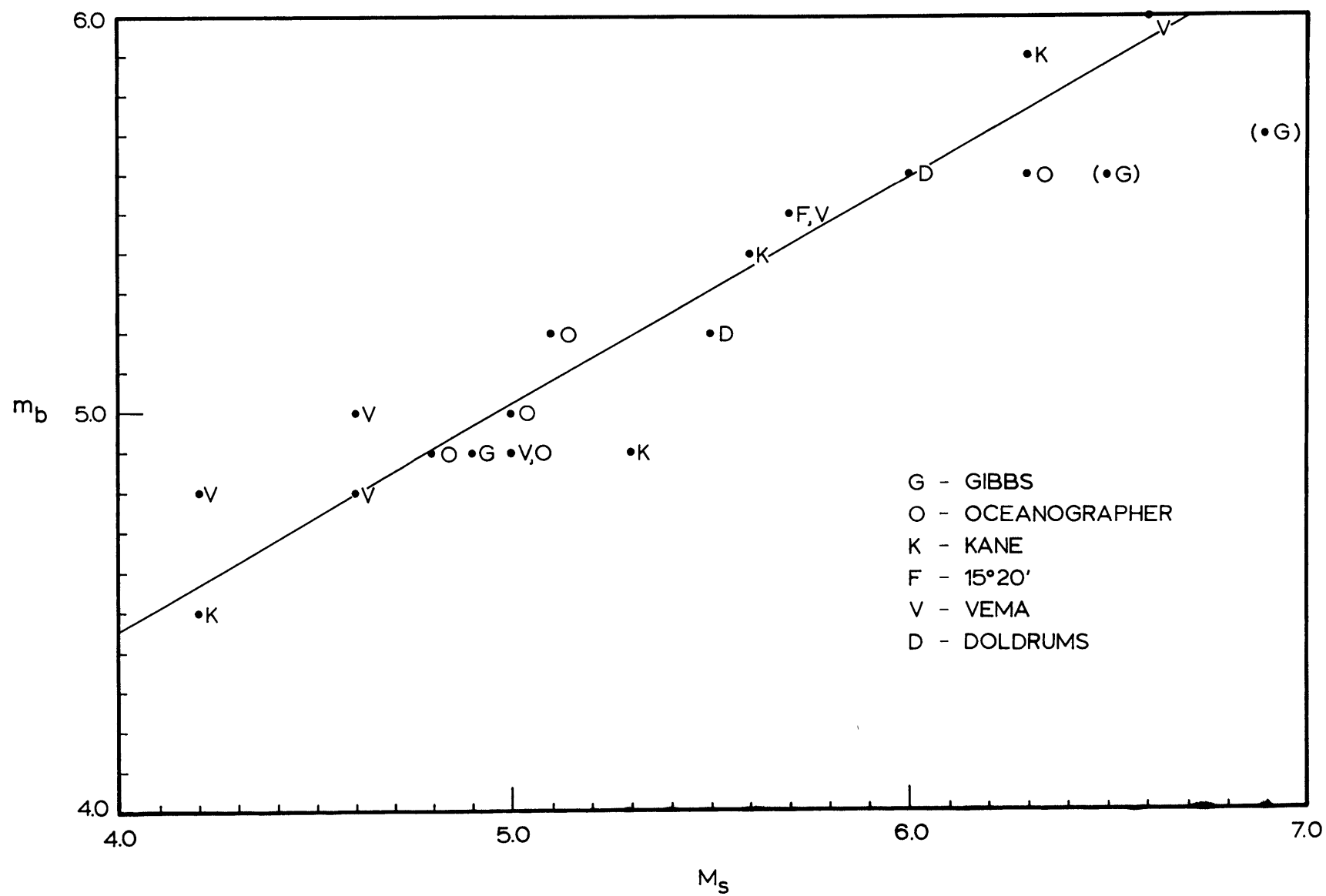


Fig a 1

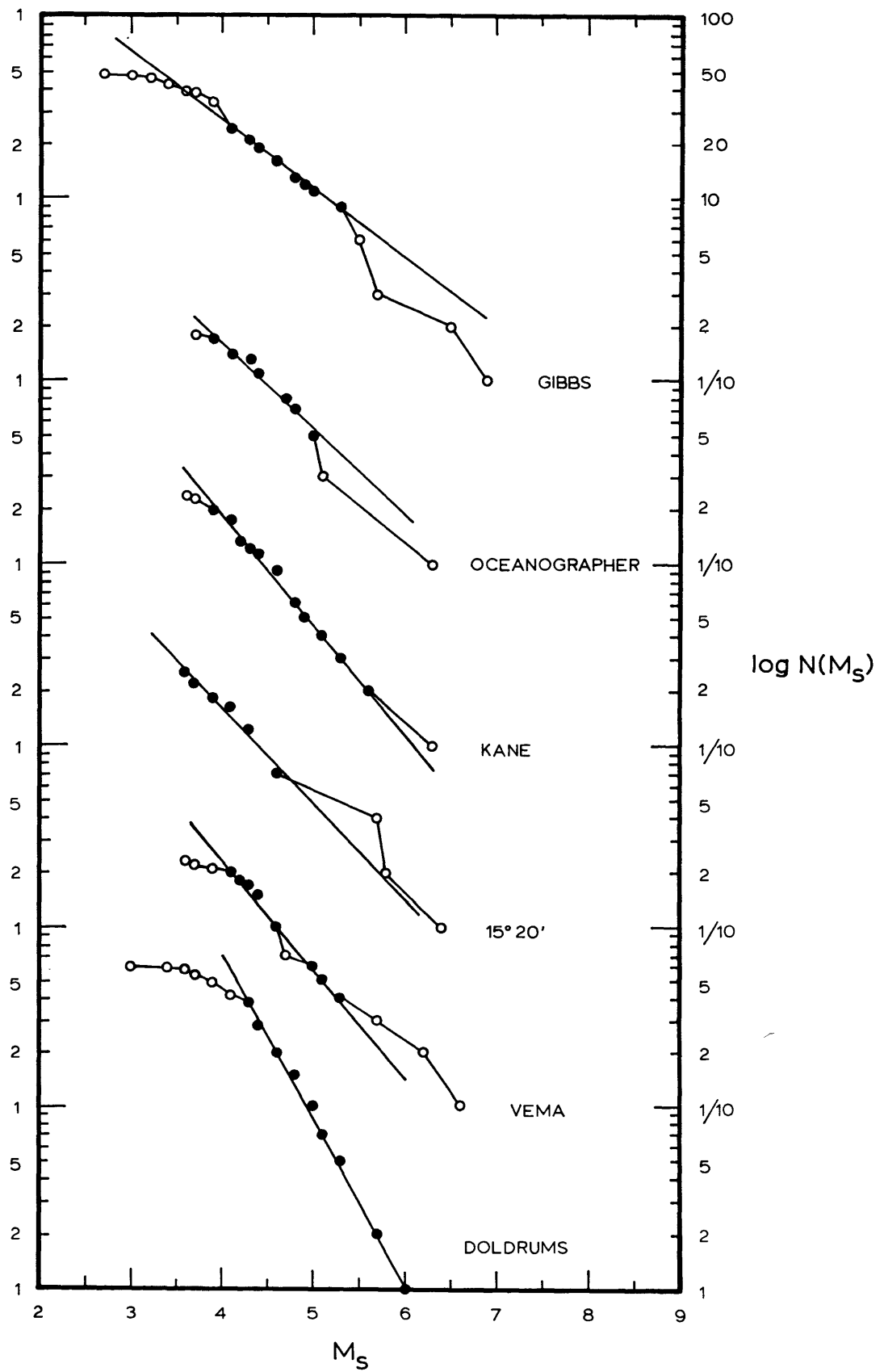
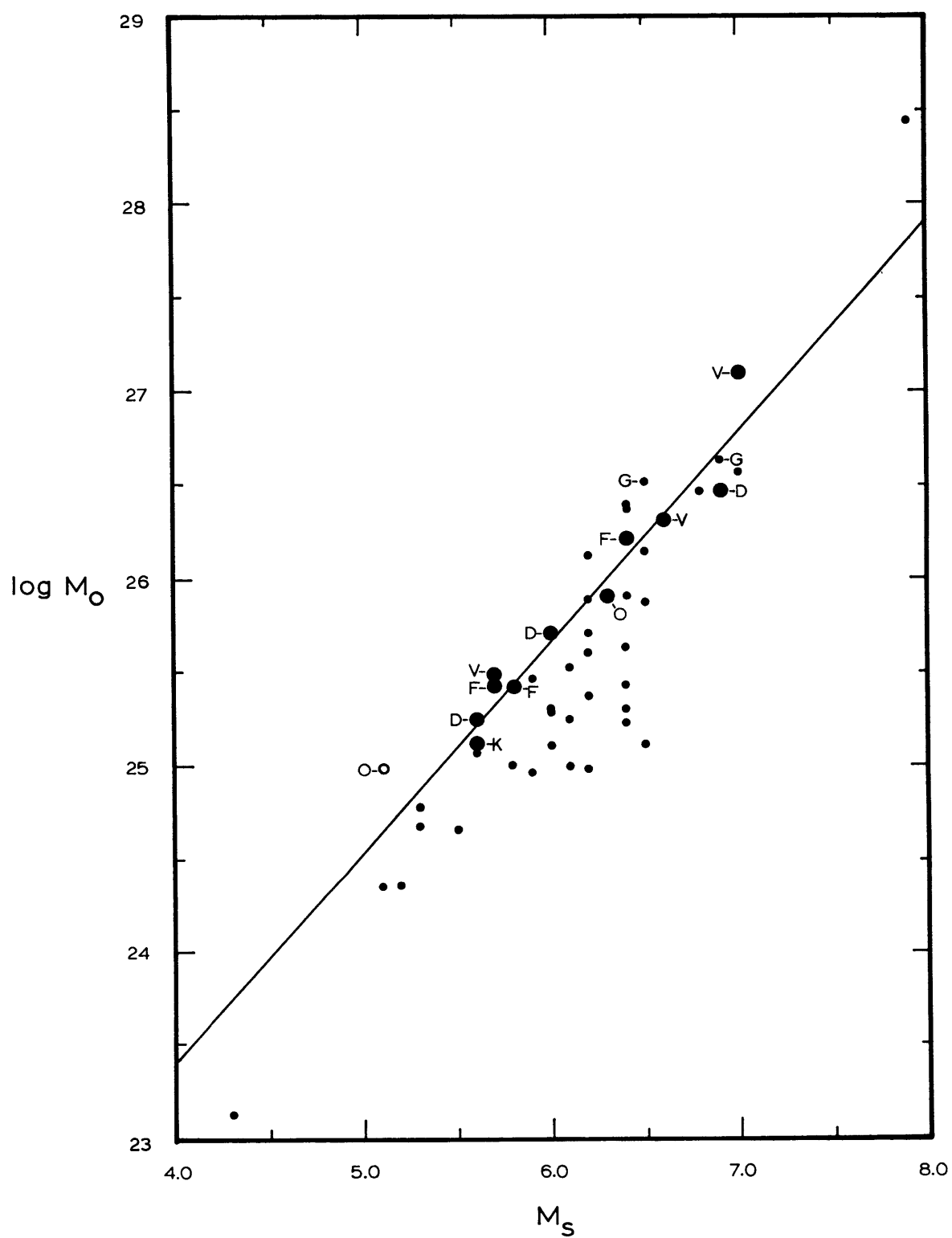


Fig. 9.2



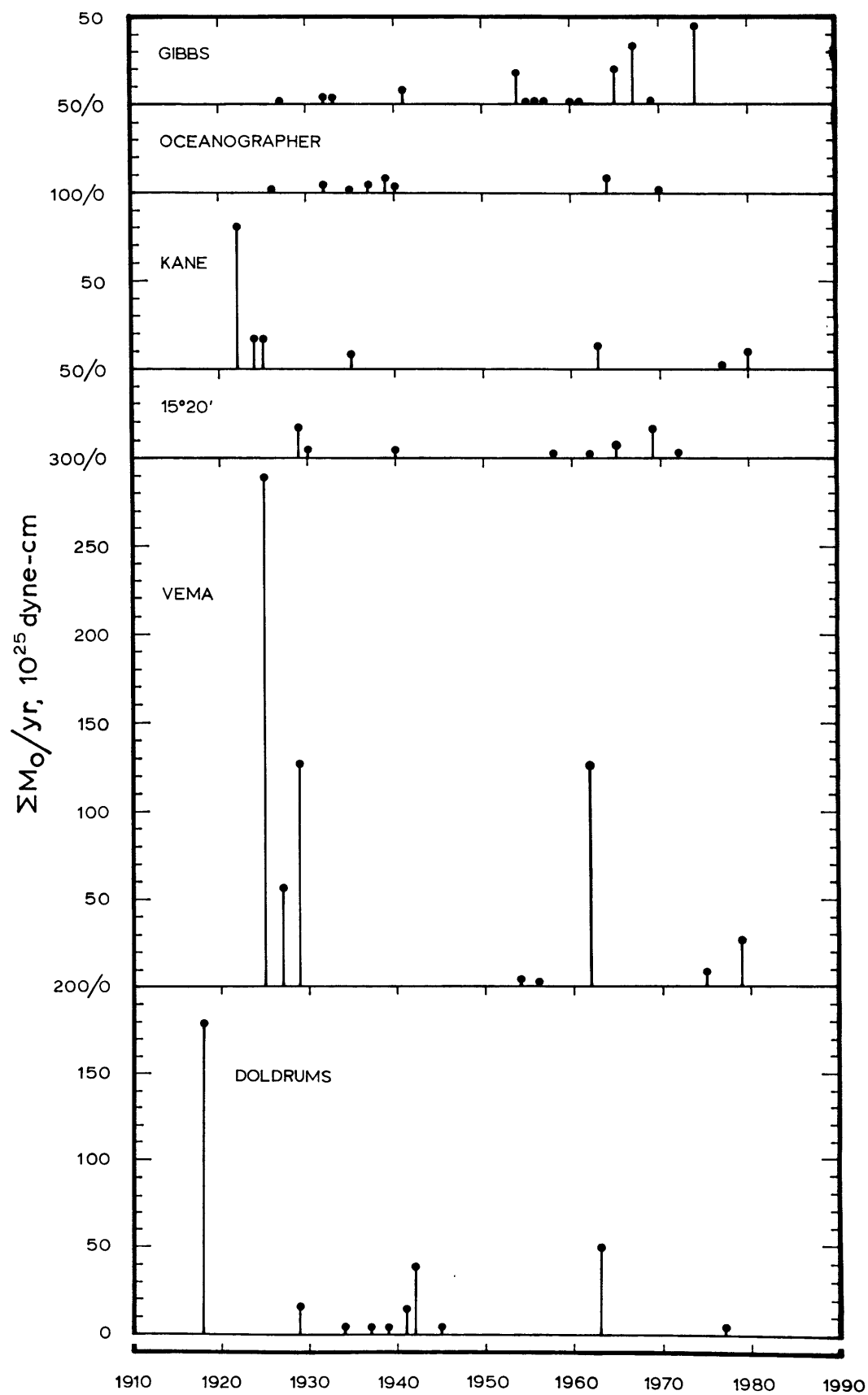


Fig. 9.4



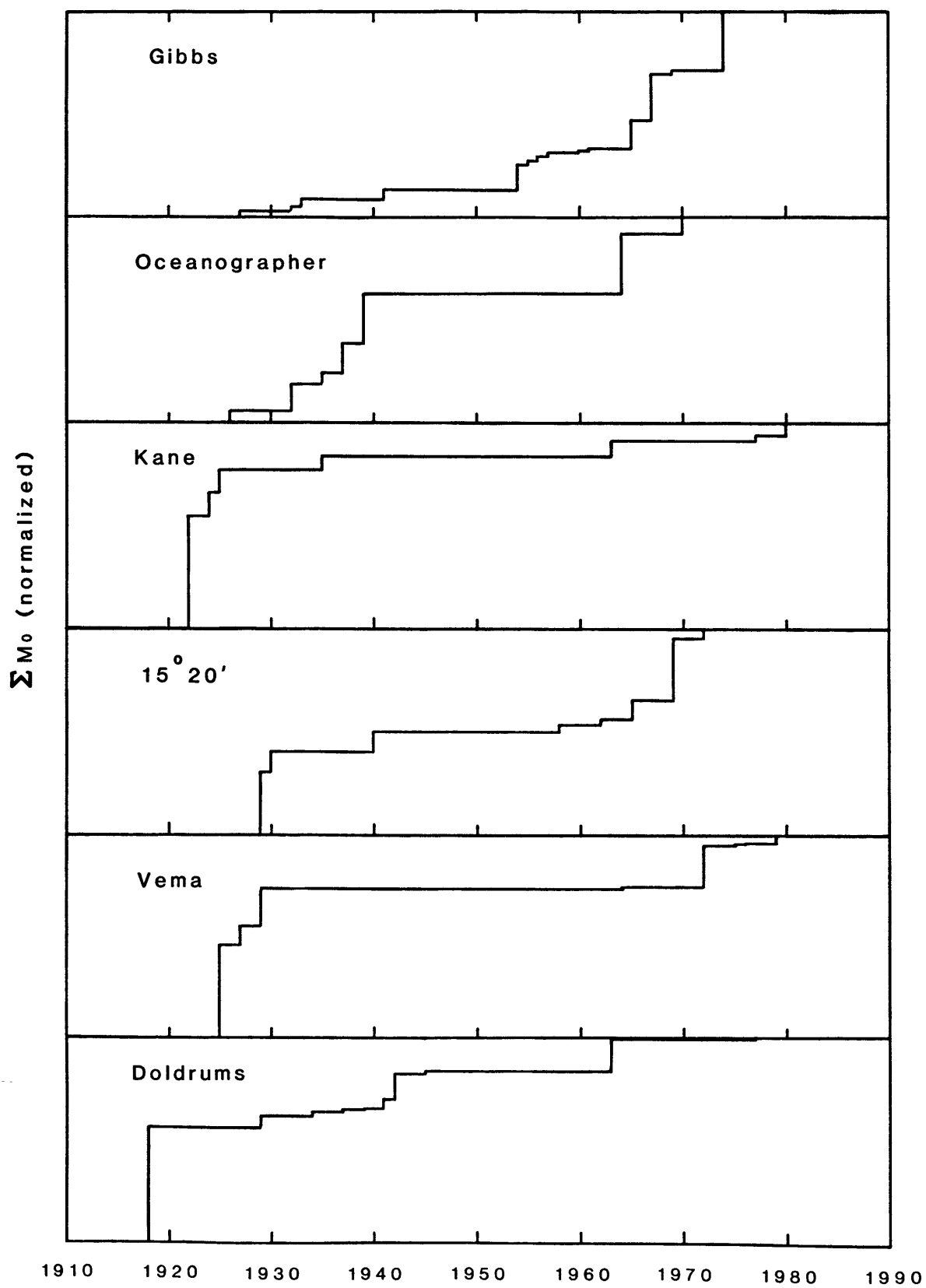


Fig. 9.5

## REFERENCES

- Abe, K., Fault parameters determined by near- and far-field data: The Wakasa Bay earthquakes of March 26, 1963, Bull. Seis. Soc. Am., 64, 1369-1382, 1974.
- Abe, K., and H. Kanamori, Magnitudes of great shallow earthquakes from 1953-1977, Tectonophysics, 62, 191-203, 1980.
- ARCYANA, Transform fault and rift valley from bathyscaph and diving saucer, Science, 190, 108-116, 1975.
- Anderson, D. L., Accelerated plate tectonics, Science, 187, 1077-1079, 1975.
- Bollinger, G. A., Determination of earthquake fault parameters from long-period P waves, J. Geophys. Res., 73, 785-807, 1968.
- Bonatti, E. and J. Honnorez, Sections of the earth's crust in the equatorial Atlantic, J. Geophys. Res., 81, 4104-4116, 1976.
- Bouchon, M., and K. Aki, Discrete wave-number representation of seismic source wave fields, Bull. Seis. Soc. Am., 67, 259-277, 1977.
- Brune, J. N., Tectonic stress and the spectra of seismic shear waves from earthquakes, J. Geophys. Res., 75, 4997-5009, 1970.
- Bryan, W. B., G. Thompson, and J. N. Ludden, Compositional variation in normal MORB from 22°-25°N: Mid-Atlantic Ridge and Kane Fracture Zone, J. Geophys. Res., 86, 11,815-11,836, 1981.
- Bullen, K. E., An Introduction to the Theory of Seismology, Cambridge University Press, Cambridge, 3rd ed., 381 pp., 1965.
- Burr, N. C., and S. C. Solomon, The relationship of source parameters of oceanic transform earthquakes to plate velocity and transform length, J. Geophys. Res., 83, 1193-1205, 1978.
- Carpenter, E. W., Absorption of elastic waves- an operator for a constant Q mechanism, AWRE Report 0-43/66, Her Majesty's Stationery Office, London, 1966.
- Choukroune, P., J. Francheteau, and X. Le Pichon, In situ structural observations along transform fault A in the FAMOUS area, Mid-Atlantic Ridge, Geol. Soc. Amer. Bull., 89, 1013-1029, 1978.
- Chung, W.-Y., and H. Kanamori, Source process and tectonic implications of the Spanish deep-focus earthquake of March 29, 1954, Phys. Earth Planet. Int., 13, 85-96, 1976. Collette, Bastiaan J., Hans Schouten, Kees Rutten, and A. Peter Slootweg, Structure of the Mid Atlantic Ridge province between 12° and 18°N, Mar. Geophys. Res., 2, 143-179, 1974.

- Collette, B. K. Rutten, J., H. Schouten, and A. Sloomweg, Continuous seismic and magnetic profiles over the Mid Atlantic Ridge between 12° and 18°N, Mar. Geophys. Res., 2, 133-142, 1974.
- Collette, B. J., H. Schouten, K. Rutten, and A. Sloomweg, Structure of the Mid Atlantic Ridge province between 12° and 18°N, Mar. Geophys. Res., 2, 143-179, 1974.
- Detrick, R. S., M. H. Cormier, R. A. Prince, and D. W. Forsyth, Seismic constraints on the crustal structure within the Vema Fracture Zone, J. Geophys. Res., 87, 10599-10612, 1982.
- Detrick, R., J. Mudie, B. Luyendyk, and K. Macdonald, Near-bottom observation of an active transform fault: Mid-Atlantic Ridge at 37° N, Nature, 246, 59-61, 1973.
- Detrick, R. S., Jr., and G. M. Purdy, The crustal structure of the Kane Fracture Zone from seismic refraction studies, J. Geophys. Res., 85, 3759-3777, 1980.
- Dziewonski, A. M., and J. H. Woodhouse, Moderate and large earthquakes of 1981 (abstract), EOS Trans. AGU, 63, 373, 1982.
- Eittreim, S., and J. Ewing, Vema Fracture Zone transform fault, Geology, 3, 555-558, 1975.
- Ewing, W. M., W. S. Jardetzky, and F. Press, Elastic Waves in Layered Media, McGraw-Hill, New York, 380 pp., 1957.
- Fleming, H. S., N. Z. Cherkis, and J. R. Heirtzler, The Gibbs Fracture Zone: A double fracture zone at 52° 30' N in the Atlantic Ocean, Mar. Geophys. Res., 1, 37-45, 1970.
- Fox, P. J., A. Lowrie, and B. C. Heezen, Oceanographer Fracture Zone, Deep Sea Res., 16, 59-66, 1969.
- Fox, P. J., E. Schreiber, H. Rowlett, and K. McCamy, The geology of the Oceanographer Fracture Zone - a model for fracture zones, J. Geophys. Res., 81, 4117-4128, 1976.
- Futterman, W. I., Dispersive body waves, J. Geophys. Res., 67, 5279-5291, 1962.
- Geller, R. J., and H. Kanamori, Magnitudes of great shallow earthquakes from 1904 to 1952, Bull. Seis. Soc. Am., 67, 587-598, 1977.
- Gutenberg, B., and C. F. Richter, Seismicity of the Earth, 2nd ed., Princeton University Press, Princeton, N. J., 1954.
- Hagiwara, T., A note on the theory of the electromagnetic seismograph, Bull. Earthq. Res. Inst., 36, 139-164, 1958.
- Heezen, B. C., M. Tharp, and M. Ewing, The floors of the oceans, 1, The North Atlantic, Geol. Soc. Am. Spec. Pap. 65, 122pp., 1959.
- Heezen, B. C., R. D. Gerard, and M. Tharp, The Vema Fracture Zone in the equatorial Atlantic, J. Geophys. Res., 69, 733-739, 1964.

- Herrin, E., Introduction to '1968 seismological tables for P phases', Bull. Seis. Soc. Am., 58, 1193-1241, 1968.
- Ida, Y., Slow-moving deformation pulses along tectonic faults, Phys. Earth Planet. Int., 9, 328-337, 1974.
- Isacks, B., J. Oliver, and L. R. Sykes, Seismology and the new global tectonics, J. Geophys. Res., 73, 5855-5899, 1968.
- Johnson, G. L., North Atlantic fracture zones near 53°, Earth Planet. Sci. Lett., 2, 445-448, 1967.
- Kanamori, H., Determination of effective tectonic stress associated with earthquake faulting, the Tottori earthquake of 1943, Phys. Earth Planet. Int., 5, 426-434, 1972.
- Kanamori, H., and D. L. Anderson, Theoretical basis of some empirical relations in seismology, Bull. Seis. Soc. Am., 65, 1073-1096, 1975.
- Kanamori, H., and G. S. Stewart, Mode of the strain release along the Gibbs fracture zone, Mid-Atlantic ridge, Phys. Earth Planet. Int., 11, 312-332, 1976.
- Kasahara, K., Migration of crustal deformation, Tectonophysics, 52, 329-341, 1979.
- Kolsky, H., The propagation of stress pulses in viscoelastic solids, Phil. Mag., (8) 1, 693-710, 1956.
- Langseth, M. G., and M. A. Hobart, Interpretation of heat flow measurements in the Vema Fracture Zone, Geophys. Res. Lett., 3, 241-244, 1976.
- Langston, C. A., and D. V. Helmberger, A procedure for modelling shallow dislocation sources, Geophys. J. Roy. Astron. Soc., 42, 117-130, 1975.
- Lonsdale, P., and A. Shor, The oblique intersection of the Mid-Atlantic Ridge with Charlie-Gibbs transform fault, Tectonophysics, 54, 195-209, 1979.
- Louden, K. E., and D. W. Forsyth, Crustal structure and isostatic compensation near the Kane Fracture Zone from topography and gravity measurements: Part I: spectral analysis approach, Geophys. J. Roy. Astron. Soc., 68, 725-750, 1982.
- Love, A. E. H., A Treatise on the Mathematical Theory of Elasticity, Cambridge, Cambridge University Press, 4th ed., 643 pp., 1934.
- Ludwig, W. J., and P. D. Rabinowitz, Structure of Vema Fracture Zone, Mar. Geol., 35, 99-110, 1980.
- Minster, J. B. and T. H. Jordan, Present-day plate motions, J. Geophys. Res., 83, 5331-5354, 1978.

- Molnar, P., Earthquake recurrence intervals and plate tectonics, Bull. Seis. Soc. Am., 69, 115-133, 1979.
- Oceanographer Transform Tectonic Research Team, The Oceanographer transform: Morphotectonic character of a ridge-transform intersection (abstract), EOS Trans. AGU, 61, 1105, 1980a.
- Oceanographer Transform Tectonic Research Team, The geology of the Oceanographer transform: Submersible and deep-towed camera investigations (abstract), EOS Trans. AGU, 61, 1105, 1980b.
- Okal, E. A., and L. M. Stewart, Slow earthquakes along oceanic fracture zones: Evidence for asthenospheric flow away from hotspots?, Earth Planet. Sci. Lett., 57, 75-87, 1982.
- Olivet, J.-L., X. Le Pichon, S. Monti, and B. Sichler, Charlie-Gibbs Fracture Zone, J. Geophys. Res., 79, 2059-2072, 1974.
- Perry, R. K., H. S. Fleming, P. R. Vogt, N. Z. Cherkis, R. H. Feden, J. Thiede, J. E. Strand, and B. J. Collette, North Atlantic Ocean: Bathymetry and plate tectonic evolution, map, Geol. Soc. Amer., Boulder, Colo., 1981.
- Prince, R. A., and D. W. Forsyth, Deepening of the median valley toward the Vema Fracture Zone: Hydrostatic head loss or crustal thinning? (abstract), EOS Trans. AGU, 62, 390, 1981.
- Project ROSE Scientists, Microearthquake activity on the Orozco Fracture Zone: Preliminary results from project ROSE, J. Geophys. Res., 86, 3783-3790, 1981.
- Purdy, G. M., P. D. Rabinowitz, and J. A. Velterop, The Kane Fracture Zone in the central Atlantic Ocean, Earth Planet. Sci. Lett., 45, 429-434, 1979.
- Rabinowitz, P. D., and G. M. Purdy, The Kane Fracture Zone in the western central Atlantic Ocean, Earth Planet. Sci. Lett., 33, 21-26, 1976.
- Robb, J. M., and M. F. Kane, Structure of the Vema Fracture Zone from gravity and magnetic intensity profiles, J. Geophys. Res., 80, 4441-4445, 1975.
- Rogan, M., Ocean Margin Drilling Area VIII-I, map, Lamont-Doherty Geological Observatory, Palisades, N.Y., 1982.
- Rona, P. A., and D. F. Gray, Structural behavior of fracture zones symmetric and asymmetric about a spreading axis: Mid-Atlantic Ridge (latitude 23°N to 27°N), Geol. Soc. Am. Bull., Part 1, 91, 484-494, 1980.
- Rothe, J. P., The Seismicity of the Earth, UNESCO, Paris, 336 pp., 1969.
- Rowlett, H., Seismicity at intersections of spreading centers and transform faults, J. Geophys. Res., 86, 3815-3820, 1981.

- Rowlett, H., and D. Forsyth, Teleseismic P-wave delay times in a major oceanic fracture zone, Geophys. Res. Lett., 6, 273-276, 1979.
- Rowlett, H. and D. W. Forsyth, Recent faulting and microearthquakes at the intersection of the Vema Fracture Zone and the Mid-Atlantic Ridge, J. Geophys. Res., in press, 1983.
- Scholz, C. H., A physical interpretation of the Haicheng earthquake prediction, Nature, 267, 121-124, 1977.
- Schouten, H., G. M. Purdy and P. R. Rabinowitz, History of the Kane Fracture Zone (abstract), EOS Trans. AGU, 60, 394, 1979.
- Schroeder, R. W., A geophysical investigation of the Oceanographer Fracture Zone and the Mid-Atlantic Ridge in the vicinity of 35 degrees north, Ph.D. Thesis, Columbia Univ., New York, 458 pp., 1977.
- Searle, R. C., Side-scan sonar studies of North Atlantic fracture zones, J. Geol. Soc. Lond., 136, 283-292, 1979.
- Searle, R., The active part of the Charlie-Gibbs Fracture Zone: A study using sonar and other geophysical techniques, J. Geophys. Res., 86, 243-262, 1981.
- Sleep, N. H., and S. Biehler, Topography and tectonics at the intersections of fracture zones with central rifts, J. Geophys. Res., 75, 2748-2752, 1970.
- Solomon, S. C., Shear wave attenuation and melting beneath the Mid-Atlantic Ridge, J. Geophys. Res., 78, 6044-6059, 1973.
- Sykes, L. R., Mechanism of earthquakes and nature of faulting on mid-ocean ridges, J. Geophys. Res., 72, 2131-2153, 1967.
- Sykes, L. R., Focal mechanism solutions for earthquakes along the world rift system, Bull. Seis. Soc. Am., 60, 1749-1752, 1970.
- Toksoz, M. N., and D. H. Johnston, eds., Seismic Wave Attenuation, Soc. Explor. Geophys., Tulsa, Okla., 459 pp., 1981.
- Trehu, A. M., Seismicity and structure of the Orozco transform fault from ocean bottom seismic observations, Ph.D. Thesis, M.I.T./W.H.O.I., 370 pp., 1982.
- Tsai, Y. B., Determination of focal depths of earthquakes in the mid-ocean ridges from amplitude spectra of surface waves, Ph. D. Thesis, M.I.T., 1969.
- Uchupi, E., Bathymetric Atlas of the Atlantic, Caribbean, and Gulf of Mexico, Woods Hole Oceanogr. Inst., Woods Hole, Mass., 1982.
- Udias, A., Source parameters of earthquakes from spectra of Rayleigh waves, Geophys. J. Roy. Astron. Soc., 22, 353-376, 1971.

- van Andel, T. H., R. P. Herzen, and J. D. Phillips, The Vema Fracture Zone and the tectonics of transverse shear zones in oceanic crustal plates, Mar. Geophys. Res., 1, 261-283, 1971.
- Vogt, P. R., C. N. Anderson, and D. R. Bracey, Mesozoic magnetic anomalies, sea-floor spreading and geomagnetic reversals in the southwestern North Atlantic, J. Geophys. Res., 76, 4796-4823, 1971.
- Weidner, D. J., and K. Aki, Focal depth and mechanism of mid-ocean ridge earthquakes, J. Geophys. Res., 78, 1818-1831, 1973.
- Wilson, J. T., A new class of faults and their bearing on continental drift, Nature, 207, 343-347, 1965.
- Wyss, M., Apparent stresses of earthquakes on ridges compared to apparent stresses of earthquakes in trenches, Geophys. J. Roy. Astron. Soc., 19, 479-484, 1970.
- York, D., Least-squares fitting of a straight line, Can. J. Phys., 44, 1079-1086, 1966.